



Structures and Bifurcations in Fluid Flows with Applications to Vortex Breakdown and Wakes

Bisgaard, Anders Villefrance; Brøns, Morten

Publication date:
2005

Document Version
Publisher's PDF, also known as Version of record

[Link back to DTU Orbit](#)

Citation (APA):
Bisgaard, A. V., & Brøns, M. (2005). *Structures and Bifurcations in Fluid Flows with Applications to Vortex Breakdown and Wakes*.

General rights

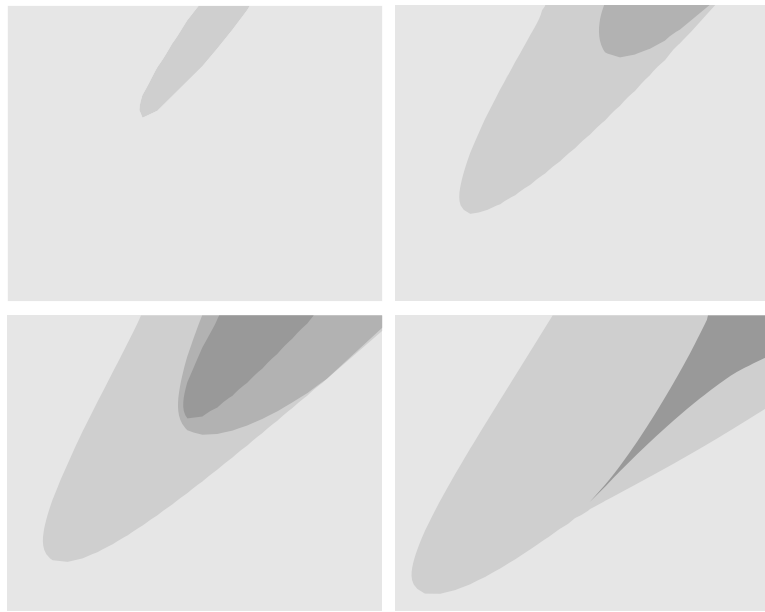
Copyright and moral rights for the publications made accessible in the public portal are retained by the authors and/or other copyright owners and it is a condition of accessing publications that users recognise and abide by the legal requirements associated with these rights.

- Users may download and print one copy of any publication from the public portal for the purpose of private study or research.
- You may not further distribute the material or use it for any profit-making activity or commercial gain
- You may freely distribute the URL identifying the publication in the public portal

If you believe that this document breaches copyright please contact us providing details, and we will remove access to the work immediately and investigate your claim.

Structures and Bifurcations in Fluid Flows

with Applications to Vortex Breakdown and Wakes



Anders V. Bisgaard

Ph.D. Thesis - 2005
Department of Mathematics
Technical University of Denmark

Title of Thesis:

Structures and Bifurcations in Fluid Flows with Applications to Vortex Breakdown and Wakes

Ph.D. Student:

Anders V. Bisgaard
Department of Mathematics
Matematiktorvet, bldg. 303
Technical University of Denmark
DK-2800 Lyngby, Denmark
E-mail: A.Bisgaard@mat.dtu.dk

Supervisor:

Professor Ph.D. Morten Brøns
Department of Mathematics
Matematiktorvet, bldg. 303
Technical University of Denmark
DK-2800 Lyngby, Denmark
E-mail: M.Brons@mat.dtu.dk

Co-supervisor:

Professor Ph.D. Jens Nørkær Sørensen
Department of Mechanical Engineering
Nils Koppels Alle, bldg. 403
Technical University of Denmark
DK-2800 Lyngby, Denmark
E-mail: jns@mek.dtu.dk



~ is a sign for one complete oscillation or one whole wave. ≍ seems to be humankind's most common sign for water in general and for streaming or flowing water in particular. In early Chinese writings ≍ represented river or stream. See www.symbols.com

Preface

This thesis is submitted in partial fulfilment of the requirements for obtaining the Ph.D.-degree. The work has been carried out at The Department of Mathematics, The Technical University of Denmark in the period from February 2002 to July 2005 under the supervision of Professor Ph.D. Morten Brøns. The Ph.D.-study was financially supported by The Technical University of Denmark. The support is most gratefully acknowledged.

Acknowledgments

First of all I would like to express my outmost sincere gratitude to my supervisor Professor Ph.D. Morten Brøns. It has been a true privilege to work together with you Morten - you have taught me so much, thank you. And to you Tom Høholdt, thank you for helping me obtaining the scholarship, for believing in the project and for your always acute advises. The computer simulations done as part of the project are conducted by using the codes `czax` and `EllipSys`, both kindly made available to me by Professor Ph.D. Jens Nørkær Sørensen at The Department of Mechanical Engineering, Technical University of Denmark. Further I am thankful to Ph.D. Lars P. Køllgaard Voigt for spending time teaching me some of the user-specifics of `EllipSys`. Although not related to this project I thank Professor Preben Graae Sørensen for teaching me the dynamical systems aspects of biological systems. Thanks goes to all my colleagues at the department for making the working conditions so pleasant. To Jens Gravesen, Poul-Erik Madsen and Wanja Andersen for helping me sorting out computer related issues and to Ulla Louring and Anna Jensen for taking good care of the administrative issues of my employment. To Atsushi Kawamoto, it has been a pleasure over the years to share office with you, and most joyful to have been introduced to Japanese culture and way of living by you and your family.

I am indebted to my family and friends for their interest and encouragement. Last but not least, thank you Søs, for your love and constant support, and for showing me that there are much more to the world than dynamical systems.

The thesis is typeset in LATEX, see Mittelbach and Goossens (2004). Most graphical plots have been created using MATLAB by MathWorks (2004), some by using Xfig by Smith et al. (2002).

Anders V. Bisgaard
July 2005

Summary

In the analysis of a fluid mechanical system the identification of the inherent flow structures is of importance. Flow structures depend on system parameters. A change in parameter values will typically alter the flow structure. Thus it is of interest to produce a catalogue of the various structures appearing. In this project we consider two types of flow systems. The vortex breakdown in the cylindrical container with rotating covers and the streamline and vorticity patterns in the near wake of a flow passing a cylinder. The two flows are assumed viscous, laminar and incompressible. Common for the two systems is the lack of a systematic description of possible flow structures. The objective of this project is, within certain parameter domains, to give such a description. A flow structure can be described by streamlines. Streamlines are found by time integrating the flow velocity field. The velocity field generates a dynamical system. Thus an understanding of the flow structure can be obtained by virtue of the bifurcation theory for dynamical systems. This theory provide tools to analyse the qualitative changes of solutions to a dynamical system caused by varying parameters. Based on this it is feasible to systematically construct a catalogue of possible flow structures. In the cylinder with rotating covers, one or several vortices are formed. It is this effect we have investigated via numerical simulations and catalogued in a certain parameter domain. To do so we have developed a systematic method by which we can handle the simulations. The method is based on knowledge drawn from the bifurcation analysis of the system. Also based on the guidance of a bifurcation analysis, the flow structures produced by numerical simulations of the cylinder wake have been catalogued.

Resumé (In Danish)

Ved en beskrivelse af et fluidmekanisk system er identificering af fluidets strømningsstrukturer af afgørende betydning. Strømningsstrukturer afhænger af systemets parametre. En ændring af parameterværdier vil typisk medføre ændringer i strukturen. Det er således af interesse at kunne opstille et katalog over de forskellige typer af strukturer. I dette projekt ser vi på to typer af fluidmekaniske systemer. Først undersøger vi hvirvlstrukturer opstået i en cylinder med roterende låg/bund, dernæst strømningsstrukturer opstået i kølvandet af en cylinder nedsænket i en strømmende væske. Vi antager at begge væskestrømninger er laminære, inkompressible og viskøse. Fælles for begge systemer er, at der ikke i alle henseender foreligger en systematisk bestemmelse af mulige strømningsstrukturer. Det er hensigten med dette projekt, indenfor visse parameterområder, at afdække disse strukturer. Et fluids strømningsstruktur kan beskrives ved en samling strømlinier. Strømlinierne er bestemt ved tidsintegration af fluidets hastighedsfelt. Hastighedsfeltet genererer et dynamisk system. En forståelse af strukturen kan da opnås ved brug af bifurkationsteorien for dynamiske systemer. Her studeres hvorledes løsninger ændres kvalitativt, som en følge af ændringer af systemparametre. Baseret på dette, er det muligt at foretage en systematisk undersøgelse af systemet og derved at opstille et katalog over mulige strukturer. Dette giver en lige så vigtig funktion nemlig mulighed for at udelukke forekomsten af visse typer strukturer. I cylinderen med roterende låg/bund opstår eller nedbrydes op til flere hvirvler. Det er denne effekt vi har undersøgt og kortlagt i et givet parameterområde. Dette har involveret udvikling af en systematisk metode til behandling af de numeriske simuleringer. Metoden er baseret på viden hentet fra bifurkationsteorien anvendt på systemet. Ligeledes er strømningsstrukturer for cylinderkølvandet kortlagt under vejledning af kataloger bestemt ved bifurkationsanalyse.

Contents

1	A World of Dynamical Systems	1
2	Introduction to Dynamical Systems and Topological Fluid Dynamics	3
2.1	The governing dynamical system	4
2.2	Stagnation points	6
2.3	Streamlines near a stagnation point	7
2.3.1	Condition for the linearized system to be governing	7
2.4	Structural stability, unfolding and codimension	9
2.4.1	Structural stability	10
2.4.2	Unfolding and codimension	11
2.5	Unfolding a degenerate stagnation point, the cusp bifurcation	12
2.5.1	Taylor expansion and generic stagnation point	12
2.5.2	Degenerate stagnation point and normal forms	12
2.5.3	Unfolding the degenerate stagnation point	13
2.6	Stagnation points at a wall	15
3	Vortex Breakdown in the Cylinder with Rotating Covers	17
3.1	Apparatus, experiments and modelling	19
3.2	Topological classification and bifurcation diagrams	25
3.2.1	Normal forms	27
3.2.2	Area-preserving near identity transformation	28
3.2.3	Normal form for the degenerate streamfunction	30
3.2.4	Calculation of the axisymmetric normal form using computer algebra	33
3.2.5	Bifurcation diagrams	37
3.2.6	The non-simple degenerate axisymmetric normal form	42
3.2.7	Brief on bifurcations taking place in a corner	44
3.2.8	Bifurcation conditions in terms of the velocity field	44
3.3	Bifurcation diagrams based on numerical investigations	46
3.3.1	Brief on the computational code	47
3.3.2	The creation and merging of recirculation zones	48
3.3.3	The post process method	53
3.3.4	Constructing creation and merging bifurcation curves	54
3.3.5	Constructing cusp bifurcation curves	63
3.3.6	Formation of one recirculation zone through an in-flow loop	67
3.3.7	The appearance of a saddle point on the center axis	67
3.3.8	The bifurcation diagrams	67
3.3.9	Interpreting the bifurcation scenarios	78
3.4	Conclusions	81

4	Laminar Flow Topology of the Cylinder Wake	83
4.1	Modelling	89
4.2	The stationary cylinder and topological classification	92
4.2.1	Symmetric unfolding of the streamfunction	93
4.2.2	Full unfolding of the streamfunction	96
4.2.3	Bifurcations in the vorticity topology	97
4.2.4	Streamline and vorticity topology together with the Hopf bifurcation	98
4.3	Numerical investigations	100
4.3.1	The computational domain and simulation code	101
4.3.2	The simulations	102
4.4	Bifurcations in the streamline topology	103
4.4.1	The steady wake and the first topological bifurcation	103
4.4.2	The periodic wake and the Hopf bifurcation	105
4.4.3	Streamline topology after the Hopf bifurcation	109
4.4.4	The periodic wake and the second topological bifurcation	110
4.4.5	The periodic wake and the third topological bifurcation	115
4.5	Bifurcations in the translated streamline topology	117
4.6	Bifurcations in the vorticity topology	120
4.7	Validating the numerical investigations	125
4.8	Conclusions	130

Bibliography	132
---------------------	------------

1

A World of Dynamical Systems

Nonlinear dynamics is a truly interdisciplinary field that binds together and draws upon all the different branches of the natural sciences, from physics over chemistry to biology and all the engineering applications thereof. Furthermore the concepts of dynamics have in the last decades received more and more attention in the social and economical sciences as well. The methods of nonlinear dynamics, or put with more justice *Nonlinear Science*, are formulated in the language of mathematics and can therefore also be regarded as a branch of applied mathematics which naturally relies on pure mathematics. In the encyclopedia assembled and edited by Scott (2005) one finds an impressive collection of 438 entries each defining and explaining aspects of Nonlinear Science.

The motivation and fascination for studying nonlinear dynamical systems is at least two-fold. The motivation lies partly in our fascination of their richly varied solutions and behaviour, beautiful structures and patterns. In fluid dynamics, in particular, one finds overwhelmingly stunning patterns. Patterns either obtained from experiments or computer simulations. But this may not be reason enough to study such systems. Nonlinear systems have a practical importance as natural phenomena and real-world engineering systems are nonlinear. It is crucial to educate scientists and engineers to understand nonlinear systems. For instance nonlinear models provide the basis for investigating the Earth's atmosphere and oceans, Olsen et al. (2005) and contribute to the debate of the global warming.

In this project we study two types of fluid mechanical systems. In our analysis we use the combination of theory and computer simulations and compare our results to experiments conducted by others. The thesis consists of two main chapters, one for each fluid mechanical system and an introduction in chapter 2. In that chapter we introduce the theory of dynamical systems with a focus on two dimensional Hamiltonian systems suitable as models for the flows we study. Further the bifurcation theory with the concepts of bifurcations and the normal form technique, that we will rely so heavily on in the later chapters, are presented. The introduction is followed by an analysis of the fluid filled cylindrical container with rotating covers in chapter 3. This chapter falls in three parts. First the problem setting is motivated based on an overview of previous work. Secondly follows the modelling and the bifurcation analysis of the system is presented. This analysis serves the basis for the numerical investigations we conduct in the second part. Here a procedure for obtaining bifurcation curves is developed and used to create the bifurcation diagrams that are the

main results of the thesis. The results and methods of this chapter are reported in:

- M. Brøns, A. Bisgaard: Bifurcation of vortex breakdown patterns. In S. N. Atluri and A. J. B. Tadeu, editors, *Proceedings of the 2004 International Conference on Computational & Experimental Engineering and Sciences*, pages 988-993. Tech Science Press, Georgia, USA, 2004.
- M. Brøns, A. V. Bisgaard: Bifurcation of vortex breakdown patterns in a circular cylinder with two rotating covers. Submitted for publication. 2005.
- A. V. Bisgaard, M. Brøns: Vortex breakdown generated by off-axis bifurcation in a cylinder with rotating covers. In preparation. 2005.

In the last chapter we turn to our investigation of the near wake of the fluid flow passing a cylinder. Also this chapter falls in three parts with a motivation followed by a modelling and a bifurcation analysis of the system. The bifurcation analysis is subsequently used to guide us in conducting numerical investigations showing the possible streamline and vorticity patterns that might appear. The results of this chapter contribute to:

- M. Brøns, K. Niss, B. Jakobsen, A. V. Bisgaard, L. K. Voigt: Streamline topology and vorticity patterns in the near-wake of a circular cylinder at low Reynolds numbers. In preparation. 2005.

2

Introduction to Dynamical Systems and Topological Fluid Dynamics

In the forthcoming chapters we will concentrate on fluid mechanical problems arising in two dimensional incompressible laminar fluid flows. Common to the understanding and description of the problem cases and to fluid mechanical systems in general is the identification and investigation of the inherent fluid flow patterns.

Fluid flow patterns can be described in various ways, one often consider one or a whole collection of fluid parcels and study their behaviour through either pathlines, streaklines or streamlines obtained in the flow domain. A pathline is the trajectory traced out by observing the movement through the flow domain over time of a given fluid parcel. If instead a fixed position in the flow domain is considered over time and lines are joined between the fluid parcels passing this position then the streaklines are obtained. Streamlines on the other hand are at a given instant in time tangential to the velocity field at every point in the flow domain. The streamlines therefore show in which direction a fluid parcel moves in that very instant. While the two first descriptions give information on material transport in the flow the latter contains information on the flow velocity field. For a steady velocity field pathlines and streamlines coincide.

The physical model of fluid mechanical problems are typically given by the Navier-Stokes equation together with the continuity condition, the initial condition of the flow for a given time instant and conditions on the flow at the boundary of the flow domain. Integration of the Navier-Stokes equation for a given problem gives the pressure field $p(t, \mathbf{x})$ and the velocity field $\mathbf{v}(t, \mathbf{x})$ as a function of time t and position \mathbf{x} . This gives information on forces and stresses on bodies submerged in the fluid which are important for engineering design purposes. If an investigation of the transport processes are the objective then the motion of fluid parcels are of interest. The motion of a fluid parcel can be obtained by integration of the velocity field as fluid parcels move according to

$$\dot{\mathbf{x}} = \mathbf{v}(t, \mathbf{x})$$

which constitute a dynamical system where a solution curve $\mathbf{x}(t)$ is a pathline. Streamlines for a

given fixed instant in time $t = t_0$ are equal to the solution curves obtained by integration of

$$\dot{\mathbf{x}} = \mathbf{v}(t_0, \mathbf{x}).$$

It is the analysis of this autonomous dynamical system and the corresponding streamlines $\mathbf{x}(t)$ given in phase space that we are concerned with in this study. The study of fluid flow patterns given in terms of streamlines is called topological fluid dynamics and in this context we denote a streamline fluid flow pattern in phase space as a flow, a flow topology, a streamline topology or simply a topology. A given fluid system typically shows structurally different streamline topologies. One streamline topology can change qualitatively by bifurcating into a different topology as system parameters are varied. The objective of topological fluid dynamics is to construct bifurcation diagrams where the set of possible streamline topologies and the transitions or bifurcations between them has been identified. The starting point for the construction of a bifurcation diagram is to identify a degenerate streamline topology appearing for a particular set of conditions on system parameters. Even though a degenerate streamline topology is by itself of little physical relevance, as it is impossible to realize in a physical system, the degenerate topology is interesting as it acts as an organizing center in parameter space for physical relevant topologies. The next step in the analysis is therefore to perturb the equations describing the degenerate streamline topology whereby an unfolding of the topology is possible resulting in a bifurcation diagram containing all physical relevant topologies appearing in a neighborhood in parameter space of the degenerate topology.

In topological fluid dynamics the qualitative theory of non-linear dynamical systems is applied to analyse and obtain bifurcation diagrams of streamline topologies. In the forthcoming chapters methods are introduced when needed and the chapters are, to a certain extent, self contained. This chapter merely serves as an introduction to the subject. Here we present, in short, the frame work we will use later. We do not go into details of all derivations but will instead give a reference to the literature or put a pointer forward to the section where a more elaborate explanation or derivation takes place.

The literature is rich on textbooks concerning dynamical systems. We refer to Guckenheimer and Holmes (1983), Grimshaw (1990), Kuznetsov (1998) and Wiggins (2003). Our approach to topological fluid dynamics follows that of Brøns (1999), Brøns and Hartnack (1999), Brøns, Voigt, and Sørensen (1999) and Hartnack (1999b). Also Bakker (1991) and Perry, Chong, and Lim (1982) work with bifurcations in flow topologies.

2.1 The governing dynamical system

A fluid in a flow domain $U \subseteq \mathbb{R}^n$ where $n = 1, 2, 3$ is described by a velocity field \mathbf{v} depending on position $\mathbf{x} \in U$ and, if the fluid flow is not steady, on time $t \in I \subseteq \mathbb{R}$, $\mathbf{v} = \mathbf{v}(t, \mathbf{x})$. The velocity field maps $U \times I$ onto U . We assume the velocity field to be known and C^r for $r \geq 1$ in \mathbf{x} and t .

Our aim is to investigate the streamlines of the velocity field, hence for a given instant $t = t_0$ in time we define the velocity field $\mathbf{v}(\mathbf{x}) = \mathbf{v}(t_0, \mathbf{x})$.

In mathematical nomenclature it is said that the vector field $\mathbf{v}(\mathbf{x})$ generates a *flow* φ mapping $U \times I$ onto U with $\varphi = \varphi(t, \mathbf{x})$. The rate of change of $\varphi(t, \mathbf{x})$ is given by

$$\left. \frac{d\varphi(t, \mathbf{x})}{dt} \right|_{t=t_1} = \mathbf{v}(\varphi(t, \mathbf{x})) \quad (2.1)$$

for all $t_1 \in I$ and $\mathbf{x} \in U$. The flow φ can loosely speaking be viewed as the total collection of streamlines in the flow domain U at time instant $t = t_0$.

A streamline passing the (initial) position \mathbf{x}_I is a trajectory $\mathbf{x}(t, \mathbf{x}_I)$ which is, so to say, picked out of the flow by setting $\mathbf{x}(t_I, \mathbf{x}_I) = \boldsymbol{\varphi}(t_I, \mathbf{x}_I)$. A streamline $\mathbf{x}(t, \mathbf{x}_I)$ can together with a specified initial condition $\mathbf{x}(t_I, \mathbf{x}_I) = \mathbf{x}_I$ be found by solving

$$\dot{\mathbf{x}} = \mathbf{v}(\mathbf{x}) \quad (2.2)$$

where $\dot{\mathbf{x}} = d\mathbf{x}/dt$. Solutions to (2.2) exists and are unique according to:

Theorem 2.1 (Existence and uniqueness) Let $\mathbf{x}_I \in U$ and $t_I \in I$. Then a solution $\mathbf{x}(t, \mathbf{x}_I)$ to (2.2) exists with $\mathbf{x}(t_I, \mathbf{x}_I) = \mathbf{x}_I$ for $|t - t_I|$ sufficiently small. The solution is unique; any other solution through \mathbf{x}_I at $t = t_I$ is the same as $\mathbf{x}(t, \mathbf{x}_I)$ in the common time interval of existence. Further $\mathbf{x}(t, \mathbf{x}_I)$ is C^r for $r \geq 1$ in t and \mathbf{x}_I .

See Wiggins (2003) for references to, or Grimshaw (1990) for, a proof of Theorem 2.1. Below we omit the explicit dependence on initial position \mathbf{x}_I on the solutions, $\mathbf{x}(t) = \mathbf{x}(t, \mathbf{x}_I)$.

Later in this introduction we will compare different flows. One speaks of flows being topologically equivalent:

Definition 2.1 (Topological equivalence) A flow $\boldsymbol{\varphi}_1 : U_1 \times I \rightarrow U_1$ of a dynamical system is called topologically equivalent in a region $U_1 \subset \mathbb{R}^n$ to a flow $\boldsymbol{\varphi}_2 : U_2 \times I \rightarrow U_2$ in a region $U_2 \subset \mathbb{R}^n$ of a second dynamical system if there exist a homeomorphism $\mathbf{h} : \mathbb{R}^n \rightarrow \mathbb{R}^n$ with $\mathbf{h}(U_1) = U_2$ mapping streamlines of the first system in U_1 onto streamlines of the second system in U_2 , preserving the direction of time.

See Kuznetsov (1998).

The time evolution of the solution curves $\mathbf{x}(t) = (x_1(t), x_2(t), \dots, x_n(t))^T$ to the system (2.2) plotted as functions of time t in the flow domain $U = \text{span}(x_1, x_2, \dots, x_n)$ quantifies the streamline topology of the fluid flow. In dynamical systems terminology this is the *phase space* representation. In this representation time does not appear explicitly but is often indicated by arrows drawn on the streamlines.

We will study (2.2) for two types of fluid flows both assumed to be viscous and incompressible. The velocity fields for the fluid flows are obtained numerically by solving the Navier-Stokes and mass conservation equations. The consequence of mass conservation of an incompressible fluid flow is that it is divergence free,

$$\nabla \cdot \mathbf{v} = 0. \quad (2.3)$$

The first fluid flow, studied in chapter 3, is a three dimensional but axisymmetric flow given in cylindrical coordinates $\mathbf{x} = (\rho, \theta, z)^T$. Although the flow is three dimensional the axisymmetric assumption implies that the flow can be considered in a meridional plane (r, z) and is essentially two dimensional with the velocity field having the components $\mathbf{v}(\rho, z) = (u(\rho, z), w(\rho, z))^T$ in the meridional plane, we will return to this in section 3.1. The second fluid flow is studied in chapter 4. We consider here a two dimensional flow given in Cartesian coordinates $\mathbf{x} = (x, y)^T$ with $\mathbf{v}(x, y) = (u(x, y), v(x, y))^T$.

We consider in the following a velocity field given in Cartesian coordinates. Similar expressions and results are valid for the velocity components in a meridional plane of an axisymmetric flow and visa versa.

For a two dimensional divergence free fluid flow in a domain U the velocity field is given in terms of a scalar valued function, a streamfunction ψ , by

$$u(x, y) = \frac{\partial \psi(x, y)}{\partial y}, \quad v(x, y) = -\frac{\partial \psi(x, y)}{\partial x} \quad (2.4)$$

where ψ maps U onto \mathbb{R} . Inspection shows that (2.4) satisfies (2.3). To prove that a streamfunction exists Green's theorem in the plane is applied. We derive (2.4) in the case of the meridional flow in section 3.1. As a consequence of (2.4) the system (2.2) is an autonomous Hamiltonian system

$$\dot{x} = \frac{\partial \psi}{\partial y}, \quad \dot{y} = -\frac{\partial \psi}{\partial x}. \quad (2.5)$$

The streamline topology for (2.5) is most conveniently determined, as streamlines are given as level sets of the streamfunction, i.e. streamlines coincide with curves $(x(t), y(t))$ in U implicitly given by solving

$$\psi(x, y) = \psi_0 \quad (2.6)$$

where ψ_0 is a constant. This can be seen by exploiting the fact that the streamfunction is time independent and by considering a streamline $(x(t), y(t))$, we have that, at the streamline

$$\frac{d}{dt}\psi(x(t), y(t)) = \frac{\partial \psi}{\partial x}\dot{x} + \frac{\partial \psi}{\partial y}\dot{y} = \frac{\partial \psi}{\partial x}\frac{\partial \psi}{\partial y} - \frac{\partial \psi}{\partial y}\frac{\partial \psi}{\partial x} = 0 \quad (2.7)$$

which shows that the streamfunction is constant along the streamline. Rewriting (2.7) as

$$\frac{\partial \psi}{\partial x}\dot{x} + \frac{\partial \psi}{\partial y}\dot{y} = \left(\frac{\partial \psi}{\partial x}, \frac{\partial \psi}{\partial y}\right) \cdot (\dot{x}, \dot{y}) = \nabla \psi \cdot (u, v) = \nabla \psi \cdot \mathbf{v} = 0 \quad (2.8)$$

using (2.4) we can also conclude that in a point on a streamline the gradient of the streamfunction is orthogonal to the velocity field thus in a point on a streamline, the streamline is tangent to the velocity field. Now we have established the governing dynamical system. We proceed with the first step in the analysis of the streamline topology, namely finding stagnation points in a fluid flow.

2.2 Stagnation points

A stagnation point of the dynamical system (2.2) is a point \mathbf{x}_0 in the flow domain U where

$$\mathbf{v}(\mathbf{x}_0) = 0. \quad (2.9)$$

A dynamical system may possess no, one or more stagnation points. In the literature stagnation points are also known as fixed points, critical points, stationary points or singular points. We may use any of these notions in later chapters. Stagnation points and their type are of crucial importance for a streamline topology. First of all the fluid has no motion at a stagnation point, a fluid parcel located at a stagnation point \mathbf{x}_0 stays at \mathbf{x}_0 . A stagnation point is in itself a streamline. Secondly a stagnation point typically organizes the streamline topology in the flow domain U in a neighborhood of the stagnation point. We turn to these issues in section 2.3.

2.3 Streamlines near a stagnation point

Streamlines in a neighborhood of a stagnation point may typically converge to or diverge from a stagnation point. To analyse this in more detail we consider a Taylor expansion at the stagnation point of the velocity field. We assume that the stagnation point is situated at the origin $\mathbf{x}_0 = (0, 0)$. If this were not the case we introduce the translation $\mathbf{x} = \bar{\mathbf{x}} - \mathbf{x}_0$ into (2.2) and consider the system in the $\bar{\mathbf{x}}$ -coordinates instead. The Taylor expansion of the velocity field \mathbf{v} for the dynamical system (2.2) is given as

$$\dot{\mathbf{x}} = \mathbf{J}\mathbf{x} + O(|\mathbf{x}|^2) \quad (2.10)$$

by using (2.9) and where \mathbf{J} is the Jacobian of \mathbf{v} evaluated at $\mathbf{x}_0 = (0, 0)$. The Jacobian is explicitly given by

$$\mathbf{J} = \begin{bmatrix} \frac{\partial u}{\partial x} & \frac{\partial u}{\partial y} \\ \frac{\partial v}{\partial x} & \frac{\partial v}{\partial y} \end{bmatrix} = \begin{bmatrix} \frac{\partial^2 \psi}{\partial x \partial y} & \frac{\partial^2 \psi}{\partial y^2} \\ -\frac{\partial^2 \psi}{\partial x^2} & -\frac{\partial^2 \psi}{\partial x \partial y} \end{bmatrix} \quad (2.11)$$

where the latter equality stems from the Hamiltonian system (2.5).

The analysis of the streamline topology in a neighborhood of the stagnation point can in some, but not all cases, be deduced from the linear part of (2.10). In section 2.3.1 we consider the needed requirements for doing so.

2.3.1 Condition for the linearized system to be governing

The linearization of (2.10) is given as

$$\dot{\mathbf{x}} = \mathbf{J}\mathbf{x}. \quad (2.12)$$

For a general linear system having a Jacobian possessing distinct eigenvalues λ_i and corresponding linear independent eigenvectors \mathbf{e}_i a solution is given as a linear combination of $\mathbf{x}_i = \mathbf{e}_i e^{\lambda_i t}$ where both eigenvalues and eigenvectors may be real or complex conjugate pairs.

From this it is seen that the behaviour of a solution to (2.12) depends on the eigenvalues of the two dimensional Jacobian \mathbf{J} given in (2.11). The eigenvalues to \mathbf{J} having the trace $Tr(\mathbf{J}) = 0$ are found by solving the characteristic equation $\lambda^2 - Tr(\mathbf{J})\lambda + Det(\mathbf{J}) = 0$ which has the solutions $\lambda_{1,2} = \pm 2\sqrt{-Det(\mathbf{J})}$. Three possibilities exists. The eigenvalues are either real, complex conjugate or zero:

$$\begin{aligned} \lambda_2 &= -\lambda_1 \neq 0 && \text{for } Det(\mathbf{J}) < 0 \text{ where } \lambda_1 > 0, \\ \lambda_{1,2} &= \pm i\omega && \text{for } Det(\mathbf{J}) > 0, \\ \lambda_{1,2} &= 0 && \text{for } Det(\mathbf{J}) = 0 \end{aligned} \quad (2.13)$$

with $\omega = 2\sqrt{Det(\mathbf{J})} \neq 0$. Based on this we have that:

Definition 2.2 Stagnation points for which $Det(\mathbf{J}) \neq 0$ are termed *generic* or *regular* whereas stagnation points having $Det(\mathbf{J}) = 0$ are denoted *degenerate*.

The solutions to (2.12) in the generic cases listed in (2.13) are

$$\mathbf{x}(t) = c_1 \mathbf{e}_1 e^{\lambda_+ t} + c_2 \mathbf{e}_2 e^{\lambda_- t} \quad (2.14)$$

for $Det(\mathbf{J}) < 0$ and

$$\mathbf{x}(t) = c_1 [Re(\mathbf{e}_1) \cos(\omega t) - Im(\mathbf{e}_1) \sin(\omega t)] + c_2 [Re(\mathbf{e}_1) \sin(\omega t) + Im(\mathbf{e}_1) \cos(\omega t)] \quad (2.15)$$

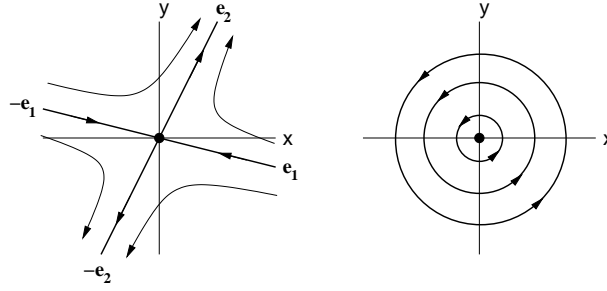


Figure 2.1: To the left a saddle point. To the right a center.

for $\text{Det}(\mathbf{J}) > 0$. The streamlines for the solutions (2.14) and (2.15) are shown in figure 2.1. In the left panel we show the phase space description of the exponential solution (2.14). The stagnation point for this case is denoted a *saddle point*. The four streamlines marked \mathbf{e}_1 , $-\mathbf{e}_1$, \mathbf{e}_2 and $-\mathbf{e}_2$ emanating from the saddle point are linear separatrices spanned by the eigenvectors \mathbf{e}_1 , $-\mathbf{e}_1$, \mathbf{e}_2 and $-\mathbf{e}_2$ for the Jacobian \mathbf{J} where $\pm\mathbf{e}_1$ corresponds to the negative eigenvalue λ_1 while $\pm\mathbf{e}_2$ corresponds to the positive eigenvalue λ_2 . The separatrices $\pm\mathbf{e}_1$ are said to span the stable subspace E^s as solutions in E^s approach the stagnation point at an exponential rate for $t \rightarrow \infty$. The separatrices $\pm\mathbf{e}_2$ span the unstable subspace E^u as solutions in E^u approach the stagnation point for $t \rightarrow -\infty$ or in other words, diverging from the stagnation point as $t \rightarrow \infty$. As the stagnation point is itself a streamline the separatrices never reach the stagnation point for either $t \rightarrow \infty$ or $t \rightarrow -\infty$. In general streamlines close to a saddle point have a minimum distance to the point. Separatrices get arbitrarily close to the saddle point for either $t \rightarrow \infty$ or $t \rightarrow -\infty$. Due to this fact and to the continuity of the streamfunction ψ the value of the streamfunction on the separatrices is equal to the value of the streamfunction evaluated at the saddle point. Since streamlines cannot cross the separatrices for a saddle point are characterized by dividing the flow domain U into subregions. A streamline starting in one region stays in that region for $t \rightarrow \pm\infty$.

In the right panel of figure 2.1 we show the phase space description of the solution (2.15). The stagnation point for this case is a *center*. All streamlines are periodic with frequency ω .

We have now considered the two generic stagnation points that appear for the linearized system (2.12). The question is, will the type and characteristics of these stagnation points i.e. the closed periodic streamlines for the center and the saddle point having four separatrices, persist in the nonlinear system (2.10). To answer this question we first introduce the notion of a *hyperbolic stagnation point*.

Definition 2.3 A stagnation point is said to be hyperbolic if the associated eigenvalues of the Jacobian evaluated at the stagnation point have non-zero real parts.

We see that a saddle point is hyperbolic as $\text{Re}(\lambda_{1,2}) = \lambda_{1,2} \neq 0$ while a center is not as $\text{Re}(\lambda_{1,2}) = \text{Re}(\pm i\omega) = 0$. We now have the Hartman-Grobman Theorem:

Theorem 2.2 (Hartman-Grobman) Let \mathbf{x}_0 be a hyperbolic stagnation point for the nonlinear system (2.10) then the flow of (2.10) and the flow of the linearized system (2.12) are topologically equivalent in a neighborhood of \mathbf{x}_0 .

References to a proof of Theorem 2.2 is found in Guckenheimer and Holmes (1983). The theorem shows that a saddle point together with the separatrices will persist in the nonlinear system. Another result also to be found in Guckenheimer and Holmes (1983) shows that the separatrices will typically not be linear though, as was the case for the linearized system, but will be invariant local manifolds. One speaks of the stable and unstable manifolds W^s and W^u . The manifold W^s will be tangent to the subspace E^s and W^u to E^u at the saddle point.

To show that the center persists in the nonlinear system we use The Second Partial Test known from calculus. In section 2.1 we argued that the streamlines for the nonlinear system (2.10) are level curves for the streamfunction ψ . Therefore a local extremum of the streamfunction ψ corresponds to a center for the nonlinear system. The Jacobian evaluated at the stagnation point was given as

$$\mathbf{J} = \begin{bmatrix} \frac{\partial^2 \psi}{\partial x \partial y} & \frac{\partial^2 \psi}{\partial y^2} \\ -\frac{\partial^2 \psi}{\partial x^2} & -\frac{\partial^2 \psi}{\partial x \partial y} \end{bmatrix} = \begin{bmatrix} 0 & 1 \\ -1 & 0 \end{bmatrix} \cdot \begin{bmatrix} \frac{\partial^2 \psi}{\partial x^2} & \frac{\partial^2 \psi}{\partial x \partial y} \\ \frac{\partial^2 \psi}{\partial x \partial y} & \frac{\partial^2 \psi}{\partial y^2} \end{bmatrix} = \mathbf{S} \cdot \mathbf{H} \quad (2.16)$$

where it is seen that \mathbf{H} is the Hessian evaluated at the stagnation point for the streamfunction ψ . From (2.16) we see that

$$\text{Det}(\mathbf{J}) = \text{Det}(\mathbf{S}) \cdot \text{Det}(\mathbf{H}) = \text{Det}(\mathbf{H}) = \lambda_1 \lambda_2. \quad (2.17)$$

Now for $\lambda_{1,2} = \pm i\omega$ we have that the linearized system has a center at the stagnation point and that $\text{Det}(\mathbf{H}) = \omega^2 > 0$. But as $\text{Det}(\mathbf{H}) > 0$ the streamfunction ψ has a local extreme at the stagnation point corresponding to a center for the nonlinear system. Thus the center persists in the nonlinear system. The streamlines for the center of the nonlinear system are closed curves but typically not elliptic curves as is the case for the linear system. With this we have all in all:

Theorem 2.3 (Generic stagnation points) Consider a two dimensional autonomous Hamiltonian system (2.5) having a stagnation point at the origin. The Jacobian \mathbf{J} evaluated at the origin is given as (2.11). If $\text{Det}(\mathbf{J}) \neq 0$ the origin is generic and for

$$\begin{aligned} \text{Det}(\mathbf{J}) < 0 & \text{ the origin is a saddle,} \\ \text{Det}(\mathbf{J}) > 0 & \text{ the origin is a center.} \end{aligned}$$

We have now found that the topology of the two cases of generic stagnation points for the nonlinear system can be deduced from the linearized system. In this respect the linearized system is interesting. Although not complicated it is not physically relevant to study the streamline topology of stagnation points for the linearized system in the degenerate cases of (2.13). Instead it becomes most relevant to study degenerate stagnation points for the nonlinear system. We will turn to this in section 2.4.

2.4 Structural stability, unfolding and codimension

The streamline topology or in other words a flow φ generated by a velocity field \mathbf{v} may be robust with respect to perturbations of the velocity field. Robust flows are termed *structurally stable*. Structurally stable flows are the flows we see in physical systems. Flows that are structurally

unstable are not robust against perturbations of the velocity field and are therefore not observed in physical systems. But, as we shall see, the structurally unstable flows plays a significant rôle in the organisation of structurally stable flows. A dynamical system

$$\dot{\mathbf{x}} = \mathbf{v}(\mathbf{x}; \mathbf{p}) \quad (2.18)$$

depending on parameters $\mathbf{p} \in \mathbb{R}^p$ may show different structurally stable flows. In going from one structurally stable flow to another structurally stable flow by varying the parameters, a structurally unstable flow has typically to be passed for certain parameter values. This set of parameter values is termed the *bifurcation set* of the dynamical system. We will typically see bifurcation sets being a discrete parameter value, a curve or surface in parameter space. The dynamical system (2.18) will for the fluid flows we investigate in the chapters 3 and 4 depend on parameters like the Reynolds number and an aspect ratio for instance.

2.4.1 Structural stability

In mathematical terms a flow is said to be structurally stable if any other flow close to the flow we consider is topologically equivalent to this. The meaning of flows being close is defined as follows:

Definition 2.4 The distance between two flows φ_1 and φ_2 generated by the C^1 velocity fields $\dot{\mathbf{x}} = \mathbf{v}_1(\mathbf{x})$ and $\dot{\mathbf{x}} = \mathbf{v}_2(\mathbf{x})$ defined in the closed domain $U \subset \mathbb{R}^n$ is given as

$$d = \|\mathbf{v}_1(\mathbf{x}) - \mathbf{v}_2(\mathbf{x})\| = \sup_{\mathbf{x} \in U} \left\{ |\mathbf{v}_1(\mathbf{x}) - \mathbf{v}_2(\mathbf{x})| + \left| \frac{\partial \mathbf{v}_1(\mathbf{x})}{\partial \mathbf{x}} - \frac{\partial \mathbf{v}_2(\mathbf{x})}{\partial \mathbf{x}} \right| \right\}. \quad (2.19)$$

See Kuznetsov (1998).

With this norm we can define structural stability more precisely:

Definition 2.5 (Structural stability) A flow φ_1 generated by a C^1 velocity field $\dot{\mathbf{x}} = \mathbf{v}_1(\mathbf{x})$ is called structural stable in $U \subset \mathbb{R}^n$ if a δ exists such that for any given flow φ_2 generated by a C^1 velocity field $\dot{\mathbf{x}} = \mathbf{v}_2(\mathbf{x})$ satisfying $d = \|\mathbf{v}_1(\mathbf{x}) - \mathbf{v}_2(\mathbf{x})\| < \delta$ is topologically equivalent to φ_1 in U .

See Kuznetsov (1998).

For two dimensional Hamiltonian systems Hartnack (1999b) proves the following two theorems by virtue of the Implicit Function Theorem. First it is shown that:

Theorem 2.4 A generic stagnation point for a two dimensional Hamiltonian system is structurally stable under a smooth perturbation preserving the Hamiltonian structure.

Secondly that:

Theorem 2.5 Homoclinic connections of generic saddle points of two dimensional Hamiltonian systems are structurally stable.



Figure 2.2: Left is seen a homoclinic connection of a saddle point, a loop. To the right a heteroclinic connection.

A homoclinic connection for a saddle point is a streamline included in both W^s and W^u for the saddle point, that is, the homoclinic connection approach the stagnation point for $t \rightarrow \pm\infty$. A homoclinic connection, often termed a *loop*, is showed in the left sketch of figure 2.2.

Structural stability depends on the perturbations, as well as the class of dynamical systems considered. If for instance a Hamiltonian system having a center, is perturbed by a dissipative velocity field not preserving the Hamiltonian structure, the center is broken, so to speak, into a spiral point. But if the perturbation falls within the class of Hamiltonian systems Theorem 2.4 says that the center is structurally stable.

From the Theorems 2.4 and 2.5 it follows that a two dimensional Hamiltonian system having solely generic stagnation points and homoclinic connections in phase space is structurally stable. A Hamiltonian system having no stagnation points at all is also structurally stable.

Examples of structurally unstable flows are flows containing degenerate stagnation points. A degenerate stagnation point is defined by having zero eigenvalues. A however small perturbation of the velocity field may change this. Another structurally unstable flow is a flow containing so-called heteroclinic connections. A heteroclinic connection involves two saddle points, as sketched in the right panel of figure 2.2. The heteroclinic connection belongs to W^u for one of the saddle points and to W^s for the other saddle point. Thus the value of the streamfunction on the heteroclinic connection and the values of the streamfunction evaluated in both the two saddle points are the same. A however small perturbation of the velocity field may change this and break the heteroclinic connection.

In most illustrations of streamline topologies in phase space we show only what we choose to call the essential streamlines i.e. the saddle point separatrices, homoclinic and heteroclinic connections together with bullets indicating the placement of stagnation points, much like seen in figure 2.2. With this, it will in most cases be sufficient to gain an overview of the topology.

2.4.2 Unfolding and codimension

The structurally stable flows of a dynamical system (2.18) are separated in parameter space by a bifurcation set corresponding to structurally unstable flows. Thus it seems natural to let a structurally unstable flow such as a degenerate stagnation point \mathbf{x}_0 at say $\mathbf{p} = \mathbf{0}$ for (2.18) be the starting point and then determine the bifurcation set by investigating perturbations of the velocity field. This is to *unfold* the structurally unstable flow:

Definition 2.6 (Unfolding) Let a family of functions $\mathbf{v}(\mathbf{x}, \mathbf{p})$ be defined in a neighborhood of \mathbf{x}_0 and $\mathbf{p} = \mathbf{0}$ and let $\mathbf{v}(\mathbf{x}, \mathbf{0}) = \mathbf{v}(\mathbf{x})$. Then $\mathbf{v}(\mathbf{x}, \mathbf{p})$ is an unfolding of $\mathbf{v}(\mathbf{x})$. If \mathbf{x}_0 is a degenerate stagnation point for $\mathbf{v}(\mathbf{x})$, the family $\mathbf{v}(\mathbf{x}, \mathbf{p})$ is said to be the unfolding of the degenerate stagnation point.

For an unfolding we say that, if all flows found by a small smooth perturbation of $\mathbf{v}(\mathbf{x}, \mathbf{0}) = \mathbf{v}(\mathbf{x})$ are topologically equivalent to a member of the family of functions in the unfolding $\mathbf{v}(\mathbf{x}, \mathbf{p})$ then

the unfolding is *versal*. Thus a versal unfolding of a degenerate stagnation point comprises all flows which occur for any small perturbation of the velocity field.

The minimum number of independent parameters needed in a versal unfolding of a degenerate stagnation point is called the *codimension*. If the number of parameters in a versal unfolding is equal to the codimension the unfolding is *miniversal*. The codimension can be thought of as a measure of how degenerate a stagnation point is.

2.5 Unfolding a degenerate stagnation point, the cusp bifurcation

In this section we will, through an example, illustrate some of the concepts we presented above and how we use them in later chapters. Moreover we will also briefly touch upon the normal form technique used to simplify high order terms in nonlinear systems. We will turn to the normal form technique in greater detail in chapter 3. When the different steps of the normal form technique are introduced below, we will give a specific reference to a forthcoming section where details are more explicitly explained.

The example here shows an unfolding to third order in the streamfunction of the cusp bifurcation taking place away from flow domain boundaries. As we will encounter the cusp bifurcation in a number of instances later on we find it appropriate to introduce it here. The example follows closely Brøns and Hartnack (1999).

2.5.1 Taylor expansion and generic stagnation point

The streamfunction ψ is expanded in a Taylor series at a point which we take to be the origin:

$$\psi = \sum_{i+j=1}^{\infty} \psi_{i,j} x^i y^j. \quad (2.20)$$

No flow domain boundaries are assumed to be in the neighborhood of the origin and thus no boundary conditions are invoked on the expansion coefficients $\psi_{i,j}$. In section 2.6 and in the chapters 3 and 4 we will see examples where a boundary impose conditions on the coefficients.

Insert (2.20) into (2.5) and consider first the linearized system (2.12) given as

$$\begin{pmatrix} \dot{x} \\ \dot{y} \end{pmatrix} = \begin{pmatrix} \psi_{0,1} \\ -\psi_{1,0} \end{pmatrix} + \begin{bmatrix} \psi_{1,1} & 2\psi_{0,2} \\ -2\psi_{2,0} & -\psi_{1,1} \end{bmatrix} \begin{pmatrix} x \\ y \end{pmatrix}. \quad (2.21)$$

If we assume that $\psi_{0,1} = 0$ and $\psi_{1,0} = 0$ it is seen that the origin is a stagnation point for (2.21). The condition on the two coefficients are termed degeneracy conditions. The determinant of the Jacobian is given as $\text{Det}(\mathbf{J}) = 4\psi_{2,0}\psi_{0,2} - \psi_{1,1}^2$. Assuming that $\text{Det}(\mathbf{J}) \neq 0$ we get from Theorem 2.3 that the origin is generic and, depending on the coefficients $\psi_{i,j}$, is either a saddle point or a center as illustrated in figure 2.1.

2.5.2 Degenerate stagnation point and normal forms

If, on the other hand, $\text{Det}(\mathbf{J}) = 0$ the origin is a degenerate stagnation point and higher order terms becomes decisive for the streamline topology. For the Jacobian of (2.21) to be singular two possibilities exists, either the Jacobian is vanishing or the Jacobian has a zero eigenvalue with geometric multiplicity one. In this example we consider the latter case for which the origin is a

simple degenerate stagnation point. We can, without loss of generality, assume that the coordinate system (x, y) is such that $\psi_{1,1} = \psi_{2,0} = 0$ but $\psi_{0,2} \neq 0$.

Before analyzing the system (2.5) where higher order terms to third order are included in the streamfunction, we conduct a normal form transformation to simplify these higher order terms, see section 3.2.1. To preserve the Hamiltonian structure *canonical transformations* are used, see section 3.2.2, where new variables are (ξ, η) . Via *generating functions*, here on the form

$$S(y, \xi) = y\xi + \sum_{i+j=3} s_{i,j} y^i \xi^j, \quad (2.22)$$

canonical transformations for $x = x(\xi, \eta)$ and $y = y(\xi, \eta)$ can be found if the equations

$$x = \frac{\partial S}{\partial y}, \quad \eta = \frac{\partial S}{\partial \xi} \quad (2.23)$$

can be solved. Inserting (2.22) into (2.23) and solving for x and y gives (see section 3.2.2 and section 3.2.4)

$$\begin{aligned} x &= \xi + s_{1,2}\xi^2 + 2s_{2,1}\xi\eta + 3s_{3,0}\eta^2 + O(|(\xi, \eta)|^3), \\ y &= \eta - 3s_{0,3}\xi^2 - 2s_{1,2}\xi\eta - s_{2,1}\eta^2 + O(|(\xi, \eta)|^3). \end{aligned}$$

With this transformation inserted into the streamfunction (2.20) we have

$$\psi = \psi_{0,2}\eta^2 + \psi_{3,0}\xi^3 + (\psi_{2,1} - 6\psi_{0,2}s_{0,3})\xi^2\eta + (\psi_{1,2} - 4\psi_{0,2}s_{1,2})\xi\eta^2 + (\psi_{0,3} - 2\psi_{0,2}s_{2,1})\eta^3 + O(|(\xi, \eta)|^4).$$

The coefficients $s_{i,j}$ of the generating function are free to choose. Thus with the choices

$$s_{2,1} = \frac{\psi_{0,3}}{2\psi_{0,2}}, \quad s_{1,2} = \frac{\psi_{1,2}}{4\psi_{0,2}}, \quad s_{0,3} = \frac{\psi_{2,1}}{6\psi_{0,2}},$$

the streamfunction is simplified to the normal form

$$\psi = \psi_{0,2}\eta^2 + \psi_{3,0}\xi^3 + O(|(\xi, \eta)|^4). \quad (2.24)$$

If $\psi_{3,0} \neq 0$ the only remaining third order term is non-degenerate. If $\psi_{3,0} = 0$ the streamfunction is degenerate to third order and higher order terms must be computed. The normal form of order three is obtained by truncating (2.23). The truncated normal form is seen to be much easier to evaluate than the original expansion. The streamline topology for the truncated normal form consists of two essential streamlines meeting in a cusp at the stagnation point. We will show a sketch of this below.

2.5.3 Unfolding the degenerate stagnation point

Above we derived the normal form for the simple degenerate stagnation point under the assumptions of the degeneracy conditions $\psi_{0,1} = 0$, $\psi_{1,0} = 0$, $\psi_{1,1} = 0$ and $\psi_{2,0} = 0$ being satisfied. Thus it is seen that the simple degenerate stagnation point is structurally unstable. To unfold the stagnation point we consider $\epsilon_{0,1} = \psi_{0,1}$, $\epsilon_{1,0} = \psi_{1,0}$, $\epsilon_{1,1} = \psi_{1,1}$ and $\epsilon_{2,0} = \psi_{2,0}$ as small parameters and, as before, we proceed to simplify the expansion of the streamfunction to normal form. The canonical transformation must now depend on the small parameters. We choose a generating function on the form

$$S(y, \xi) = y\xi + \sum_{i+j+k+l+m+n=3} s_{i,j,k,l,m,n} y^i \xi^j \epsilon_{0,1}^k \epsilon_{1,0}^l \epsilon_{1,1}^m \epsilon_{2,0}^n. \quad (2.25)$$

Inserting (2.25) into (2.23) and solving for the canonical transformations $x = x(\xi, \eta; \epsilon_{0,1}, \epsilon_{1,0}, \epsilon_{1,1}, \epsilon_{2,0})$ and $y = y(\xi, \eta; \epsilon_{0,1}, \epsilon_{1,0}, \epsilon_{1,1}, \epsilon_{2,0})$ which is then inserted into (2.20) gives

$$\begin{aligned} \psi = & \mu_1 + \mu_2\xi + \mu_3\eta + \mu_4\xi^2 + (2s_{2,1,0,0,0,0} - 4\psi_{0,2}s_{0,2,1,0,0,0})\epsilon_{1,0}\xi\eta + \\ & (-2s_{1,2,0,0,0,0} - 4\psi_{0,2}s_{0,2,0,1,0,0})\epsilon_{0,1}\xi\eta - 4\psi_{0,2}s_{0,2,0,0,1,0}\epsilon_{2,0}\xi\eta + \\ & (1 - 4\psi_{0,2}s_{0,2,0,0,0,1})\epsilon_{1,1}\xi\eta + \psi_{3,0}\xi^3 - (4\psi_{0,2}s_{1,2,0,0,0,0} - \psi_{1,2})\xi\eta^2 + \\ & (-6\psi_{0,2}s_{0,3,0,0,0,0} + \psi_{2,1})\xi^2\eta + (-2\psi_{0,2}s_{2,1,0,0,0,0} + \psi_{0,3})\eta^3 + \\ & O(|(\xi, \eta, \epsilon_{0,1}, \epsilon_{1,0}, \epsilon_{1,1}, \epsilon_{2,0})|^4). \end{aligned} \quad (2.26)$$

where μ_i , $i = 1, \dots, 4$ all depend algebraically on $\epsilon_{0,1}$, $\epsilon_{1,0}$, $\epsilon_{1,1}$ and $\epsilon_{2,0}$. Since the streamlines lie on level curves for the streamfunction we can omit μ_1 . By choosing

$$\begin{aligned} s_{1,2,0,0,0,0} &= \frac{\psi_{1,2}}{4\psi_{0,2}}, & s_{0,3,0,0,0,0} &= \frac{\psi_{2,1}}{6\psi_{0,2}}, & s_{2,1,0,0,0,0} &= \frac{\psi_{0,3}}{2\psi_{0,2}}, \\ s_{0,2,0,0,0,1} &= \frac{1}{4\psi_{0,2}}, & s_{0,2,0,1,0,0} &= -\frac{\psi_{1,2}}{8\psi_{0,2}^2}, & s_{0,2,1,0,0,0} &= \frac{\psi_{0,3}}{4\psi_{0,2}^2}, \end{aligned}$$

the streamfunction is simplified to

$$\psi = \epsilon_1\xi + \epsilon_2\eta + \epsilon_3\xi^2 + \tilde{\psi}_{0,2}\eta^2 + \psi_{3,0}\xi^3 + O(|(\xi, \eta, \epsilon_{0,1}, \epsilon_{1,0}, \epsilon_{1,1}, \epsilon_{2,0})|^4) \quad (2.27)$$

where

$$\epsilon_1 = \left(\epsilon_{1,0} - \frac{\epsilon_{0,1}\epsilon_{1,1}}{2\psi_{0,2}} + \frac{\psi_{1,2}\epsilon_{0,1}^2}{4\psi_{0,2}^2} - \frac{\psi_{0,3}\epsilon_{1,0}\epsilon_{0,1}}{2\psi_{0,2}^2} \right), \quad \epsilon_2 = \epsilon_{0,1}, \quad \epsilon_3 = \left(\epsilon_{2,0} + \frac{\psi_{1,2}\epsilon_{1,0}}{4\psi_{0,2}} - \frac{\psi_{2,1}\epsilon_{0,1}}{2\psi_{0,2}} \right)$$

and

$$\tilde{\psi}_{0,2} = \left(\psi_{0,2} - \frac{\psi_{0,3}\epsilon_{0,1}}{2\psi_{0,2}} \right).$$

If $a_{3,0} \neq 0$ the translation

$$\xi = \xi + \frac{2\psi_{2,1}\epsilon_{0,1} - \psi_{1,2}\epsilon_{1,0} - 4\psi_{0,2}\epsilon_{2,0}}{12\psi_{0,2}\psi_{3,0}}, \quad \eta = \eta + \frac{\psi_{0,2}\epsilon_{0,1}}{\psi_{0,3}\epsilon_{0,1} - 2\psi_{0,2}^2} \quad (2.28)$$

removes the terms of ξ^2 and η in (2.27) and finally dividing ψ by $2\tilde{\psi}_{0,2}$ and conducting the scaling

$$\xi \rightarrow \left(\frac{2\tilde{\psi}_{0,2}}{3\tilde{\psi}_{3,0}} \right)^{\frac{1}{3}} \xi$$

we arrive at the scaled normal form

$$\psi = \frac{1}{2}\eta^2 + c_1\xi + \frac{1}{3}\xi^3 + O(|(\xi, \eta, \epsilon_{0,1}, \epsilon_{1,0}, \epsilon_{1,1}, \epsilon_{2,0})|^4) \quad (2.29)$$

where c_1 is a new small parameter depending on $\epsilon_{0,1}$, $\epsilon_{1,0}$, $\epsilon_{1,1}$ and $\epsilon_{2,0}$. If $\psi_{3,0} = 0$ the normal form is degenerate to order three and we have to proceed considering higher order terms. The Hamiltonian system given by the normal form streamfunction (2.29) truncated at third order is

$$\dot{\xi} = \frac{\partial \psi}{\partial \eta} = \eta, \quad \dot{\eta} = -\frac{\partial \psi}{\partial \xi} = c_1 + \xi^2. \quad (2.30)$$

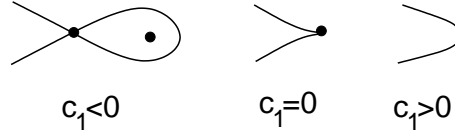


Figure 2.3: The cusp bifurcation

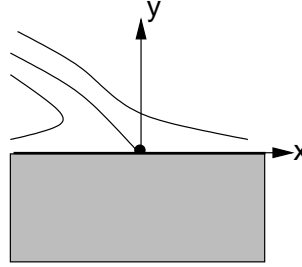


Figure 2.4: Streamline topology near a saddle point at the wall.

The stagnation points of (2.30) are $(\xi, \eta) = (\pm\sqrt{-c_1}, 0)$ for $c_1 \leq 0$ and the determinant of the Jacobian is $\text{Det}(\mathbf{J}) = -2\xi$. From this, it is seen, that no stagnation points exist for $c_1 > 0$. A stagnation point in the origin is formed at $c_1 = 0$ corresponding to the degenerate stagnation point we investigated in section 2.5.2. For $c_1 < 0$ two stagnation points exist. Theorem 2.3 shows that these two stagnation points are a center and a saddle point respectively. Thus under the given assumptions we have unfolded the degenerate stagnation point at the origin. The unfolding is shown in the bifurcation diagram sketched in figure 2.3. By virtue of Theorem 2.4 and Theorem 2.5 it is seen that the streamline topologies are structurally stable for $c_1 \neq 0$. Changing from $c_1 < 0$ to $c_1 > 0$ the structurally unstable streamline topology at the bifurcation set $c_1 = 0$ is passed. Under the given assumptions, unfolding the degenerate stagnation point requires the one parameter c_1 thus the degenerate stagnation point is of codimension 1.

2.6 Stagnation points at a wall

In section 2.5 we considered an in-flow streamline topology. In this section we will briefly introduce how to investigate the streamline topology close to a solid domain boundary, a wall, where the boundary conditions are the *no-slip condition* and the *no-flux condition*. This section is a primer to chapter 4 where we will consider the wake flow close to a cylinder.

Consider a wall as shown in figure 2.4. The no-slip and no-flux conditions are conditions on the velocity field at the wall. The no-slip condition $v(x, 0) = 0$ reflects that the fluid does not move along the wall. The no-flux condition $u(x, 0) = 0$ reflects that the fluid cannot penetrate the wall. Consider again the streamfunction (2.20) inserted into (2.5) giving to second order

$$\begin{pmatrix} \dot{x} \\ \dot{y} \end{pmatrix} = \begin{pmatrix} \psi_{0,1} \\ -\psi_{1,0} \end{pmatrix} + \begin{bmatrix} \psi_{1,1} & 2\psi_{0,2} \\ -2\psi_{2,0} & -\psi_{1,1} \end{bmatrix} \begin{pmatrix} x \\ y \end{pmatrix} + \begin{pmatrix} \psi_{2,1}x^2 + 2\psi_{1,2}xy + 3\psi_{0,3}y^2 \\ -3\psi_{3,0}x^2 - 2\psi_{2,1}xy - \psi_{1,2}y^2 \end{pmatrix}.$$

For the boundary conditions to be satisfied we see from the above system that the conditions

$$\psi_{0,1} = \psi_{1,0} = \psi_{1,1} = \psi_{2,0} = \psi_{2,1} = \psi_{3,0} = 0$$

has to be imposed on the coefficients. With these conditions the above system can be reduced to

$$\begin{pmatrix} \dot{x} \\ \dot{y} \end{pmatrix} = y \begin{pmatrix} 2\psi_{0,2} \\ 0 \end{pmatrix} + y \begin{bmatrix} 2\psi_{1,2} & 3\psi_{0,3} \\ 0 & -\psi_{1,2} \end{bmatrix} \begin{pmatrix} x \\ y \end{pmatrix}. \quad (2.31)$$

The no-slip condition implies that (2.31) has a continuous set of stagnation points for $y = 0$, at the wall. Based on the following theorem we will define a discrete set of stagnation points, the skin friction stagnation points or the stagnation points at the wall:

Theorem 2.6 Consider a continuous function $g : U \rightarrow \mathbb{R}_+$ then the systems

$$\dot{\mathbf{x}} = g(\mathbf{x}) \cdot \mathbf{v}(\mathbf{x}) \quad (2.32)$$

and

$$\dot{\mathbf{x}} = \mathbf{v}(\mathbf{x}) \quad (2.33)$$

are topologically equivalent.

A proof is found in Andersen, Hansen, and Sandqvist (1988). With Theorem 2.6 the system (2.31) is topologically equivalent to

$$\begin{pmatrix} \dot{x} \\ \dot{y} \end{pmatrix} = \begin{pmatrix} 2\psi_{0,2} \\ 0 \end{pmatrix} + \begin{bmatrix} 2\psi_{1,2} & 3\psi_{0,3} \\ 0 & -\psi_{1,2} \end{bmatrix} \begin{pmatrix} x \\ y \end{pmatrix} \quad (2.34)$$

for $g(\mathbf{x}) = y > 0$, that is, strictly above the wall. This can also be viewed as a scaling $t \mapsto yt$ of time.

Definition 2.7 Let a system (2.32) satisfy the no-slip and no-flux conditions. If the reduced system (2.33) has a stagnation point at a position that corresponds to the wall then this stagnation point is denoted a *stagnation point at the wall* for the system (2.32).

The reduced system (2.34) has a stagnation point at the origin if $\psi_{0,2} = 0$. This stagnation point is generic for $\psi_{1,2} \neq 0$ and as $\text{Det}(\mathbf{J}) = -2\psi_{1,2}^2 < 0$ Theorem 2.3 shows that this stagnation point is a saddle point. The separatrices of this saddle point are tangent to the vectors $(1, 0)^T$ and $(-\psi_{0,3}, \psi_{1,2})^T$ at the origin. Thus, according to Theorem 2.6, there exists a separatrix in the streamline topology of system (2.34). This separatrix comes arbitrarily close to the stagnation point at the wall as either $t \rightarrow \infty$ or $t \rightarrow -\infty$ (depending on the sign of $\psi_{1,2}$). Thus the streamline topology for the system (2.31) for $\psi_{0,2} = 0$ and $\psi_{1,2} \neq 0$ is given as in figure 2.4.

3

Vortex Breakdown in the Cylinder with Rotating Covers

In this chapter we contribute with some theoretical aspects and numerical results to the ongoing debate and investigations of the closed fluid-filled cylinder with rotating end-covers. The research into this particular problem was originally initiated with the purpose of gaining better understanding of the omnipresent vortex structures such as the vortex breakdown in fluid mechanics. In many vortex flows, secondary flow structures like the vortex breakdown of the bubble type develop on the vortex axis. For instance, wingtip vortices or the vortex flow in swirl burners show vortex breakdown. The wonderful book by Lugt (1983) draws perspectives on the problem at hand together with familiar problems of rotating fluid mechanical systems.

The set-up concerns a fluid-filled cylindrical tank equipped with a bottom and top lid which can be set to rotate in both directions independently from each other. The set-up has long been standard in both experimental and computational studies of the vortex breakdown. The set-up is, in principle, meant to be as simple as possible vortex generator. Together with illustrations we will give a little more detailed explanation in a later section, for now we will limit ourself to a brief introduction: The rotating bottom and lid act as pumps and drive the fluid around inside the tank creating a swirling vortex structure. For example in the special case of letting the bottom rotate and keeping the lid fixed, fluid is drawn axially down to the bottom. When reaching the bottom the fluid is driven outward in a spiralling motion towards the cylinder wall, at which it spirals upward along the wall. When reaching the top lid the fluid spirals inward along the lid towards the cylinder axis at which it is again drawn downward towards the bottom. This motion creates a vortex structure down the cylinder axis. For some system parameter values stagnation points, where the fluid velocity field is zero, appear on the cylinder axis creating closed recirculation zones of limited extent causing the vortex structure to break down. It is this vortex breakdown we will study here.

Experiments conducted on the cylinder set-up have clearly shown how formation of recirculation zones near the center axis of the cylinder may appear. The first experiments of this kind were conducted by Vogel (1968). Other more recent studies by Roesner (1989), Spohn, Mory, and

Hopfinger (1993) and Lim and Cui (2005) show that the research activity has indeed continued. The experimental observations have answered a series of questions such as whether recirculation zones can emerge and if so under which conditions these are stable. Further, experiments have revealed that there are various types of recirculation zones. In Escudier (1984) a parameter study resulting in a catalogue over the appearances of the various kinds of recirculation zones was constructed. Escudier (1984) further suggests that the flow is essentially axisymmetric in the studied parameter regime. We will here consider the same parameter regime as Escudier (1984) and assume that the flow is axisymmetric. In section 3.1 we will in more detail touching upon the study of Escudier (1984) and we will see that one consequence of the axisymmetric assumption is that an incompressible fluid can be considered two dimensional. The experimental study by Lim and Cui (2005) further advocated for the axisymmetric assumption in the parameter range that Escudier (1984) considers. Lim and Cui (2005) observes that "...attempts to produce ... [3D] vortex structures in low aspect ratio cases ... by "artificially" introducing three dimensionality into the flow, was less successful". Here, the confined environment makes a bubble-type vortex breakdown extremely robust, and the imposed asymmetry merely distorts the bubble geometry". One may argue that a closer study, if possible, of what "merely distorts" means is necessary. Others, see e.g. Spohn, Mory, and Hopfinger (1998) and Thompson and Hourigan (2003) debate the validity of the axisymmetric assumption. Outside the parameter range that Escudier (1984) considers Lim and Cui (2005) among others observe three dimensional vortex structures.

All the experimental observations have not only answered but certainly also initiated a series of questions as of why these recirculation zones appear. To this end mathematical modelling and numerical studies have been undertaken, see Sørensen (1988). Numerical simulations based on the axisymmetric assumption, see e.g. Sørensen and Loc (1989), Lopez (1990), Daube (1991) and Tsitverblit (1993), reproduce the experiments well. In the computational study by Lopez and Perry (1992) and Sørensen and Christensen (1995) stability issues for the recirculation zones are investigated and it was established that the transition to the unsteady flow regime takes place via the Hopf bifurcation.

The basic set-up of a fixed top cover and a rotating bottom cover has been varied in a number of both experimental and computational studies. In Roesner (1989), Bar-Yoseph, Solan, and Roesner (1990), Gelfat, Bar-Yoseph, and Solan (1996), Jahnke and Valentine (1998) and Brøns, Voigt, and Sørensen (1999) the fixed top cover has been replaced by a rotating cover. In Pereira and Sousa (1999) the flat rotating bottom cover has been replaced by a cone and in Spohn, Mory, and Hopfinger (1993), Lopez and Chen (1998) and Brøns, Voigt, and Sørensen (2001) the top cover has been replaced by a free surface. Mullen, Kobine, Tavener, and Cliffe (2000) added a rod at the cylinder center axis and Escudier and Cullen (1996) and Xue, Phan-Thien, and Tanner (1999) considered the flow motion of a non-Newtonian fluid. All these variations of the basic set-up result in a rich set of flow structures. Recently attention has been directed towards control issues of recirculation zones. In Mununga, Hourigan, Thompson, and Leweke (2005) the vortex breakdown in the cylinder is controlled by a small rotating disk at the bottom and in Herrada and Shtern (2003) the vortex breakdown is controlled by temperature gradients.

The purpose of this chapter is to develop a post process method by which catalogues much like the catalogues obtained experimentally by Escudier (1984) can be constructed based on a numerical parameter study. In Sørensen and Loc (1989) the axisymmetric Navier-Stokes code *czax* has been developed. We will base the numerical parameter study on *czax*. The code has, within a certain parameter regime, been successfully validated against experimental results and thus the mathematical modelling lying behind the numerical implementation has in this parameter regime shown satisfactory. We will apply the code in this parameter regime.

The chapter presents in section 3.1 the apparatus, experiments and modelling. The numerical parameter study conducted via `czax` call upon a theoretical interpretation. This interpretation is based on a two dimensional dynamical system formulated via the streamfunction and analyzed through the aid and concepts of bifurcation theory, the issue of section 3.2. The analysis is based on the bifurcation theory developed in Brøns (1999) and Brøns (2000). Bifurcation theory helps to understand and to qualitatively build up bifurcation diagrams showing the different kinds of recirculation zones. Further, as it turns out, bifurcation theory can not only help us to qualitatively build up bifurcation diagrams. It also suggests degeneracy conditions directly applicable in our quest for numerically tracing out the bifurcation curves between the various types of recirculation zones, found in the numerical parameter study. In section 3.3 we present the post process method. Further we apply the post process method resulting in a series of numerical bifurcation diagrams. The series of diagrams reveal different kind of bifurcation scenarios. These scenarios are then explained based on the theoretical bifurcation diagrams of section 3.2.

The qualitative theory of dynamical systems has been applied in several other studies in topological investigations of flows, see for instance Hunt et al. (1978), Dallmann (1988) and the reviews by Tobak and Peak (1982) and Perry and Chong (1987). Bifurcation theory is used by Bakker (1991) and Hartnack (1999a) to study the bifurcations of flows close to a wall or as in Brøns (1996) to study flows close to free and viscous interfaces and by Brøns and Hartnack (1999) to investigate general flows away from boundaries.

As with so many other research fields, a jargon has over the years been build up. When reading the literature, one stumbles over either the vortex breakdown, a recirculation zone or a recirculation bubble or simply a bubble. In the context of the cylinder with rotating end-covers they all denote the one and same entity.

3.1 Apparatus, experiments and modelling

A diagram of the closed fluid-filled cylinder with rotating end-covers is shown in figure 3.1. The left panel shows the set-up as used by Spohn et al. The inner tank, in which the actual experiments take place, is submerged into a greater tank in which fluid is circulated through a thermostat to keep the temperature constant. The two tanks are, with respect to fluid, kept isolated from each other. The working fluid in the cylinder is either plain tap water or a glycerine solution. Both tanks are made of perspex making visual recordings of the flow pattern possible. To visualize the flow pattern either an electrolytic precipitation technique is used or flouresent dye is injected into the cylinder cavity. In the electrolytic precipitation technique white powder is released from a solder wire into the fluid, when a voltage is applied to the wire. A laser light sheet forming a meridional plane through the cylinder is reflected by the dye or white powder and an image of the flow in the meridional plane of the laser light sheet can be recorded.

The right panel in figure 3.1 shows, in sketch, the cylinder having radius R and height H corresponding to the water level. The bottom and lid of the cylinder can independently be rotated with angular velocity Ω_1 respectively Ω_2 . Corresponding geometrical and mechanical system parameters are the aspect ratio $h = H/R$ and the rotation ratio $\gamma = \Omega_2/\Omega_1$.

We assume the flow is viscous and incompressible and, at the cylinder walls fulfill the no-slip boundary condition. In the case of $\gamma = 0$ the bottom rotates whereas the lid is stationary. At the bottom, sidewall and lid, boundary layers are formed. Due to the rotation of the bottom the Coriolis force will twist the streamlines of the bottom boundary layer, the Ekman layer, and an outward spiral-like flow motion occurs. At the sidewall a Stewartson boundary layer is formed and

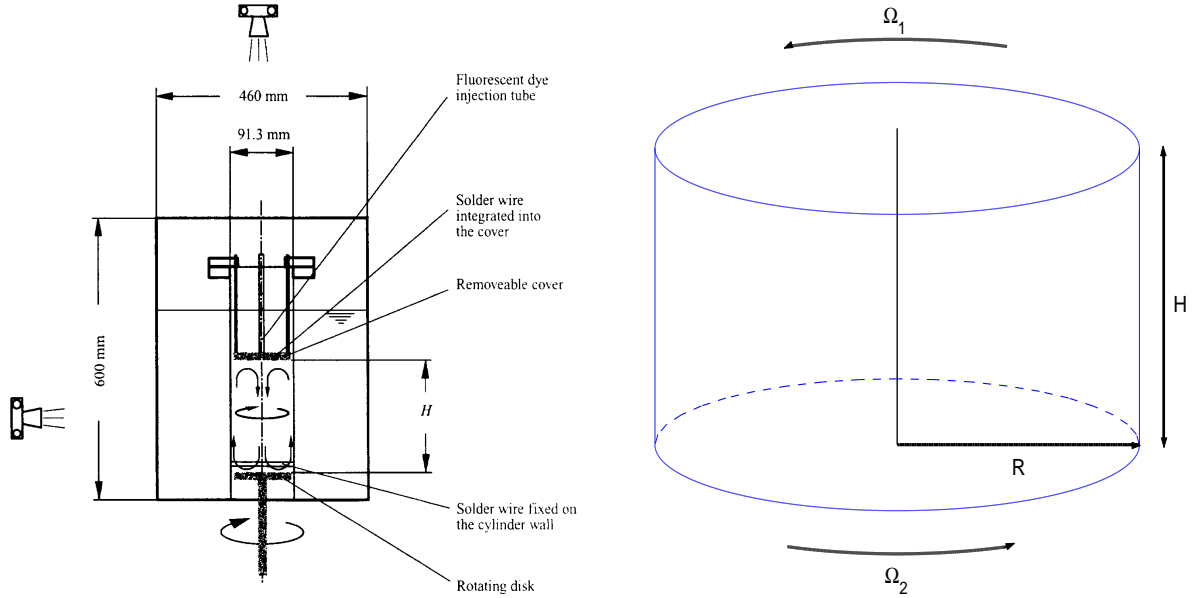


Figure 3.1: The left panel shows a diagram of the experimental apparatus used by Spohn et al. (1998). A transparent cylinder is placed inside a thermostat, which is made up by a water-filled tank and kept at constant temperature. The rotating bottom is driven by an electric motor. To visualize the fluid flow fluorescent dye is injected at the surface center. For observation the cylinder is illuminated by a laser beam sheet which is reflected by the dye. This reflection of the laser beam sheet results in an image of the flow structure. The right panel shows a schematic representation of the cylinder having radius R and height H . Further the bottom and lid of the cylinder rotate with angular velocity Ω_1 respectively Ω_2 .

the flow spirals upward along the wall. At the lid the flow starts to spiral inward and the flow swirls downward along the center axis. Thus we have the so-called primary flow and the secondary flow. The primary flow is the flow circulating around the center axis as seen from above, whereas the flow motion seen from the side, in the meridional plane, is denoted the secondary flow. Below, in figure 3.4, we will elaborate on this in connection with the mathematical model.

In figure 3.2 we show the result of a few out of many experiments conducted by Escudier (1984). In the figure we see the recording of the reflection of laser light in the meridional plane formed by the laser light sheet. What we see is the traces of dye reflected by the laser light making up the intersection of stream surfaces in the flow with the meridional plane. The left recording has been conducted for the parameter values $h = 2.0$, $\gamma = 0.0$ and $Re = 1492$ where Re is the rotational Reynolds number, we will more specifically introduce the Reynolds number below. To the right we show a close-up of the cylinder axis of a recording performed for the values $h = 2.5$, $\gamma = 0.0$ and $Re = 1994$. As $\gamma = 0.0$ the lid is stationary for the two recordings. In the left recording we see that a closed recirculation zone has been formed by two stationary saddle points situated at the center axis making up the vortex breakdown. In the recording to the right one further recirculation zone have been formed such that there are two recirculation zones. Hence by varying parameter values recirculation zones may form or disappear. To get an overview of the various recirculation zone configurations which might appear all the experiments have been collected into one single diagram shown in figure 3.3. The experimentally obtained bifurcation diagram shows for $\gamma = 0.0$ the various parameter regions of (h, Re) in which a different number of recirculation zones exists from no recirculation zones at the lower part of the diagram till a tiny region in the

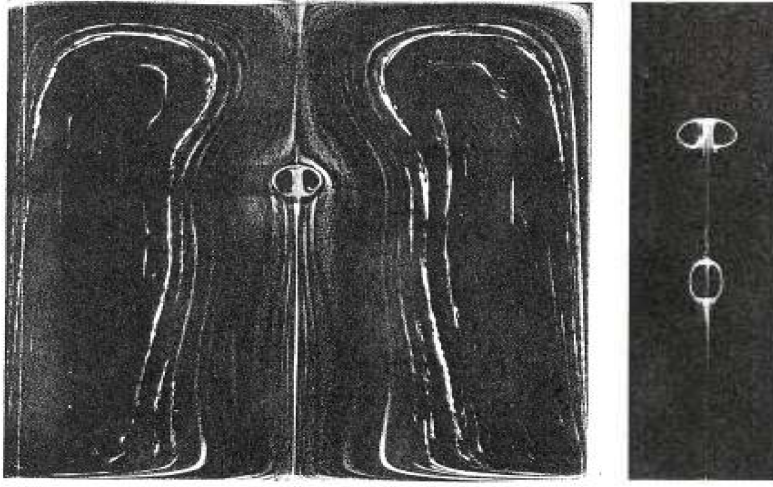


Figure 3.2: Recordings of two out of many experiments conducted by Escudier (1984). The two photographs show the traces of dye reflected by a meridional laser light sheet. The left recording is for the case of $h = 2.0$, $\gamma = 0.0$ and $Re = 1492$ and shows the existence of one recirculation zone at the center axis whereas the right recording for $h = 2.5$, $\gamma = 0.0$ and $Re = 1994$ shows the existence of two recirculation zones.

upper right part with three recirculation zones. In crossing a curve in going from one region to an adjacent, a recirculation zone emerges or disappears at the center axis of the cylinder just as shown in figure 3.2. The diagram further indicates the stability of the flow. In the lower part the flow is stable whereas in the upper part the flow is unstable. In Sørensen and Christensen (1995) it has been argued that the instability occurs through a Hopf bifurcation. In this study we will focus our attention on the stable stationary region and as we have set out to understand the emergence of the recirculation zones the diagram suggests roughly that we consider the parameter intervals $Re \in [700; 2400]$ and $h \in [1.0; 3.0]$. In the stable parameter region the flow pattern is time independent.

The mathematical model for the incompressible flow in the cylinder consists of the Navier-Stokes equations and the conservation of mass which in the laboratory coordinate system or reference frame reads

$$\frac{\partial \mathbf{v}}{\partial t} + (\mathbf{v} \cdot \nabla) \mathbf{v} = -\frac{1}{\varrho} \nabla p + \nu \Delta \mathbf{v}, \quad \nabla \cdot \mathbf{v} = 0. \quad (3.1)$$

If we were considering a rotating reference frame Coriolis force terms would have to be included. In (3.1) ν is the kinematic viscosity and ϱ the constant fluid density. Due to the geometry of the set-up, it is natural to operate in cylindrical coordinates (r, θ, z) . The velocity field is written as $\mathbf{v} = (u, v, w)^T$ with $\mathbf{v} = \mathbf{v}(r, \theta, z)$. As we consider the stable parameter region in which the flow is time independent the velocity field \mathbf{v} is modelled time independent. Following Sørensen and Loc (1989) we assume the flow to be axisymmetric hence $\mathbf{v} = \mathbf{v}(r, z)$. For the parameter range we consider here, based on the experimental results obtained in Escudier (1984), it can be argued that this is a reasonable assumption.

To non-dimensionalize (3.1) we choose the following scalings

$$\tilde{z} = \frac{z}{R}, \quad \tilde{r} = \frac{r}{R}, \quad \tilde{t} = \Omega_1 t, \quad \tilde{p} = \frac{p}{p_0}$$

with the choice of a characteristic pressure constant given as $p_0 = \varrho R^2 \Omega_1^2$. From the above scalings we get the non-dimensional velocity $\tilde{\mathbf{v}} = \frac{1}{R \Omega_1} \mathbf{v}$. Inserting the non-dimensional variables into (3.1) and leaving out the tilde-notation we get the non-dimensional Navier-Stokes and conservation of

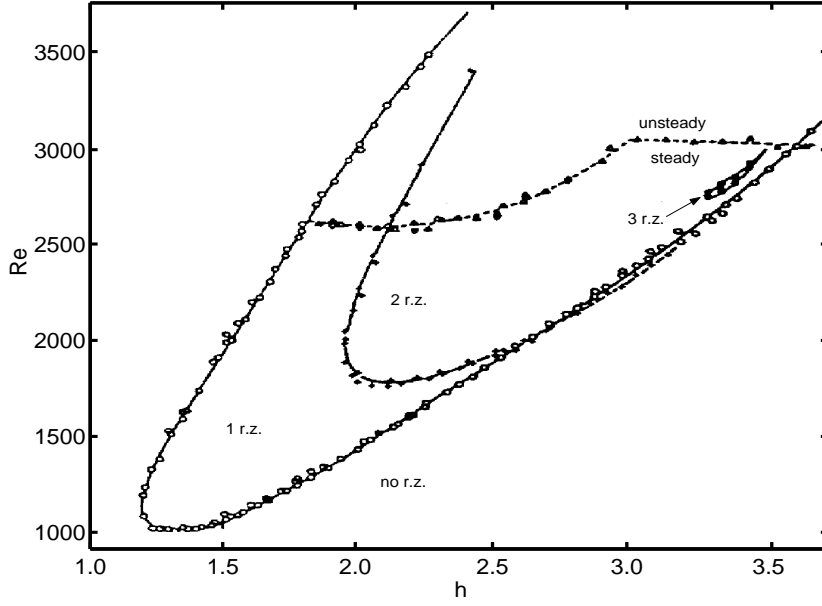


Figure 3.3: Experimentally obtained bifurcation diagram from Escudier (1984) showing regions in parameter space (h, Re) where no, 1, 2 or 3 recirculation zones exist. Each region is correspondingly labeled *no r.z.*, *1 r.z.*, *2 r.z.* or *3 r.z.* In this series of experiments the lid of the cylinder is at stand still and only the bottom is rotating thus $\gamma = 0.0$.

mass equations

$$\frac{\partial \mathbf{v}}{\partial t} + (\mathbf{v} \cdot \nabla) \mathbf{v} = -\nabla p + \frac{1}{Re} \Delta \mathbf{v}, \quad \nabla \cdot \mathbf{v} = 0. \quad (3.2)$$

The non-dimensional group $Re = \frac{\Omega_1 R^2}{\nu}$ is the Reynolds number. In mentioning the aspect ratio h and the ratio γ of angular velocities we can finally summarize all the non-dimensionalized inherent system parameters (h, Re, γ) and parameter space is consequently three dimensional. As the system is operated at constant temperature ν and ρ are constants and do not contribute to the set of system parameters. We see that in non-dimensional variables the meridional plane is given for $r \in [0; 1]$ and $z \in [0; h]$.

Applying the definition of vorticity $\boldsymbol{\omega} = (\omega_r, \omega_\theta, \omega_z)^T$ and the vector identity

$$\boldsymbol{\omega} = \nabla \times \mathbf{v} \quad \text{and} \quad \frac{1}{2} \nabla (\mathbf{v} \cdot \mathbf{v}) = (\mathbf{v} \cdot \nabla) \mathbf{v} + \mathbf{v} \times (\nabla \times \mathbf{v})$$

we can reformulate the governing equation (3.2) obtaining the vorticity equation

$$\frac{\partial \boldsymbol{\omega}}{\partial t} + \nabla \times (\boldsymbol{\omega} \times \mathbf{v}) = \frac{1}{Re} \Delta \boldsymbol{\omega}. \quad (3.3)$$

which is seen to not include the pressure gradient. Introducing the circulation $\Gamma(r, z)$, the azimuthal component of the vorticity $\omega(r, z) = \omega_\theta(r, z)$ and in the meridional plane a streamfunction $\psi(r, z)$ by

$$\Gamma = r \cdot v, \quad \omega = \frac{\partial u}{\partial z} - \frac{\partial w}{\partial r}$$

and

$$\dot{r} = u = \frac{1}{r} \frac{\partial \psi}{\partial z}, \quad \dot{z} = w = -\frac{1}{r} \frac{\partial \psi}{\partial r} \quad (3.4)$$

we obtain the streamfunction-vorticity-circulation formulation

$$\begin{aligned} r\omega &= \frac{\partial^2 \psi}{\partial z^2} + \frac{\partial^2 \psi}{\partial r^2} - \frac{1}{r} \frac{\partial \psi}{\partial r} \\ \frac{\partial \omega}{\partial t} &= \frac{1}{Re} \left(\frac{\partial^2 \omega}{\partial z^2} + \frac{\partial^2 \omega}{\partial r^2} + \frac{1}{r} \frac{\partial \omega}{\partial r} - \frac{\omega}{r^2} \right) - \left(\frac{\partial(w\omega)}{\partial z} + \frac{\partial(u\omega)}{\partial r} - \frac{\partial}{\partial z} \left(\frac{\Gamma^2}{r^3} \right) \right) \\ \frac{\partial \Gamma}{\partial t} &= \frac{1}{Re} \left(\frac{\partial^2 \Gamma}{\partial z^2} + \frac{\partial^2 \Gamma}{\partial r^2} - \frac{1}{r} \frac{\partial \Gamma}{\partial r} \right) - \left(\frac{\partial(w\Gamma)}{\partial z} + \frac{\partial(u\Gamma)}{\partial r} + \frac{u\Gamma}{r} \right). \end{aligned} \quad (3.5)$$

We assume that the circulation, the vorticity and the streamfunction are analytic. Expressing the velocity field (u, w) for the dynamical system (3.4) in the meridional plane by the streamfunction ψ is most conveniently and can be justified by considering the bijective transformation of the radial variable $\rho = \frac{1}{2}r^2$. The radial transformation leads to the dynamical system

$$\dot{z} = w(r, z) = \bar{w}(\rho, z), \quad \dot{\rho} = ru(r, z) = \bar{u}(\rho, z) \quad (3.6)$$

with the transformed velocity field $\bar{\mathbf{v}} = (\bar{u}(\rho, z), \bar{w}(\rho, z))^T$. The conservation of mass must be fulfilled hence

$$\nabla \cdot \mathbf{v} = \frac{1}{r} \frac{\partial}{\partial r}(ru) + \frac{\partial}{\partial z}w = \frac{\partial}{\partial \rho}\bar{u} + \frac{\partial}{\partial z}\bar{w} = \nabla \cdot \bar{\mathbf{v}} = 0.$$

Using Green's Theorem in the plane on the divergence of the transformed velocity field $\bar{\mathbf{v}}$ we observe that

$$\int_D \nabla \cdot \bar{\mathbf{v}} d\rho dz = \int_{\partial D} -\bar{w}(\rho, z) d\rho + \bar{u}(\rho, z) dz = 0$$

where D is a region in the plane such that the boundary ∂D is a closed piecewise C^1 -curve. As the curve integral equals zero implies that an exact differential form exists

$$d\bar{\psi}(\rho, z) = -\bar{w}(\rho, z) d\rho + \bar{u}(\rho, z) dz \quad (3.7)$$

where $d\bar{\psi}(\rho, z)$ is the differential of a scalar function, a streamfunction $\bar{\psi}(\rho, z)$. The differential of the streamfunction can also be written as

$$d\bar{\psi}(\rho, z) = \frac{\partial \bar{\psi}(\rho, z)}{\partial \rho} d\rho + \frac{\partial \bar{\psi}(\rho, z)}{\partial z} dz. \quad (3.8)$$

Equating the coefficients of $d\rho$ and dz in (3.7) and (3.8) we arrive at the Hamiltonian system

$$\dot{\rho} = \bar{u} = \frac{\partial \bar{\psi}}{\partial z}, \quad \dot{z} = \bar{w} = -\frac{\partial \bar{\psi}}{\partial \rho}. \quad (3.9)$$

The streamfunction $\bar{\psi}$ can be determined up to an arbitrary integration constant $\bar{\psi}_0$ by $\bar{\psi}(\rho, z) = \int -\bar{w}(\rho, z) d\rho + \bar{u}(\rho, z) dz + \bar{\psi}_0$. As a consequence of the axisymmetric assumption, the center axis is a solution curve to (3.9) and we conveniently choose to set $\bar{\psi}(0, z) = \bar{\psi}_0 = 0$ at the center axis. In general other solution curves also denoted trajectories or streamlines $(\rho(t), z(t))$ to the system (3.9) are implicitly given by the set of level curves for the streamfunction. Thus a set of streamlines can be found by solving $\bar{\psi}(\rho, z) = \bar{\psi}_c$ where $\bar{\psi}_c$ is some constant. We note that by continuity of the streamfunction streamlines starting or ending on the center axis have $\bar{\psi}(\rho, z) = 0$.

The dynamical system (3.4) is found by using the radial transformation $\rho = \frac{1}{2}r^2$ to transform (3.9) back to (r, z) variables.

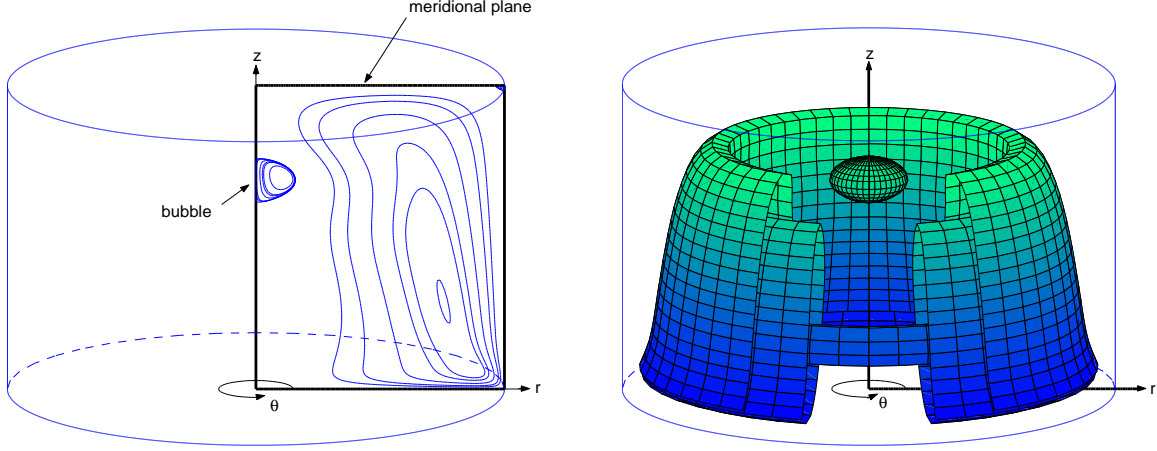


Figure 3.4: To the left is depicted the meridional plane which is the computational domain. To the right the corresponding stream surfaces. The surfaces are shown cut open to illustrate how they are embedded in each other.

The non-dimensional boundary conditions for the cylinder with rotating end-covers given for the formulation (3.5) are

$$\begin{aligned}
 \text{Center axis: } r = 0 \quad \text{and} \quad 0 \leq z \leq h, \quad \psi = u = \omega = \frac{\partial \psi}{\partial r} = 0, \quad v = 0, \quad \frac{\partial^2 \psi}{\partial r^2} = -w. \\
 \text{Cylinder wall: } r = 1 \quad \text{and} \quad 0 \leq z \leq h, \quad \psi = u = w = \frac{\partial \psi}{\partial r} = 0, \quad v = 0, \quad \frac{\partial^2 \psi}{\partial r^2} = r\omega. \\
 \text{Rotating lid: } z = 1 \quad \text{and} \quad 0 \leq r \leq 1, \quad \psi = u = w = \frac{\partial \psi}{\partial z} = 0, \quad v = \gamma r, \quad \frac{\partial^2 \psi}{\partial z^2} = r\omega. \\
 \text{Rotating bottom: } z = 0 \quad \text{and} \quad 0 \leq r \leq 1, \quad \psi = u = w = \frac{\partial \psi}{\partial z} = 0, \quad v = r, \quad \frac{\partial^2 \psi}{\partial z^2} = r\omega.
 \end{aligned} \tag{3.10}$$

These are the boundary conditions implemented in the axisymmetric Navier-Stokes code *czax* which we will comment on below. Before we do so we note that as ψ is an even function in r due to the axisymmetric assumption the boundary condition of all odd partial derivatives of ψ with respect to r are zero

$$\frac{\partial^{(2n-1)} \psi}{\partial r^{(2n-1)}} = 0 \quad \text{for } n = 1, 2, 3, \dots \tag{3.11}$$

at the center axis. We use this in the bifurcation analysis of the streamfunction in section 3.2.

The axisymmetric Navier-Stokes code *czax* has been implemented by Professor J. N. Sørensen, see Sørensen and Loc 1989. The code has kindly been put to our disposal. The code solves the problem (3.5) with given initial and boundary conditions in the computational domain $r \in [0; 1]$ and $z \in [0; h]$. With the code we have, among other entities, access to the axial velocity component $w(r, z)$. As we shall see the axial velocity component plays an important part in a set of degeneracy conditions applicable in tracing out bifurcation curves for recirculation zones in a numerical parameter study..

In figure 3.4 we show a simulation result based on *czax* for the case of $Re = 1600, h = 2.06$ and $\gamma = 0.0$. To the left we have shown the computational domain, which is the meridional

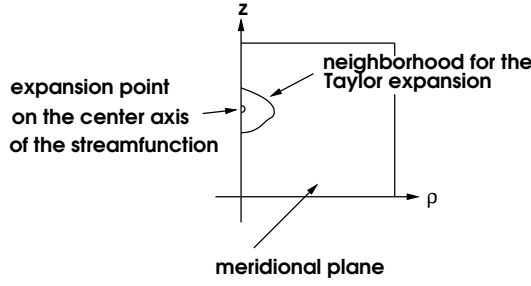


Figure 3.5: The Taylor expansion (3.13) of the streamfunction $\psi(\rho, z)$ is valid in a neighborhood of the expansion point at the center axis. As the sketch shows the neighborhood extends into the meridional plane.

plane embedded into the cylinder. In the meridional plane we see a number of streamlines of the streamfunction ψ corresponding to a series of certain constant values ψ_c . The streamlines are found by solving $\psi(r, z) = \psi_c$ for $r \in [0; 1]$ and $z \in [0; h]$. If we compare with the experimentally obtained diagram in figure 3.3 we see that, for the given set of parameters, we are in the middle of the domain where only one recirculation zone exist on the center axis. Now returning to figure 3.4 we note that, in our numerical simulation, there has been formed one recirculation zone on the center axis.

To the right in figure 3.4 we show the stream surfaces. One surface is the full rotation of the corresponding streamline shown to the left in figure 3.4. The transport of a particular fluid particle will be confined to take place on one of the stream surfaces. The figure has been included to give a better visual impression of the axisymmetric assumption of the swirl of a particle spiralling around inside the cylinder sitting on top of these surfaces.

From (3.4) or equivalently (3.9) we see that the axisymmetric assumption implies that we can consider the flow effectively two dimensional. In the section 3.2 we will analyse this dynamical system.

3.2 Topological classification and bifurcation diagrams

In the following we apply the qualitative phase space and bifurcation methods from the theory of dynamical systems (see Wiggins (2003) for a good introduction) to conduct a bifurcation analysis of the autonomous Hamiltonian system (3.9) thereby obtaining a topological classification of the axisymmetric flow structures appearing in a neighbourhood of the center axis. We leave out the bar-notation and rewrite (3.9) as

$$\dot{\rho} = u(\rho, z) = \frac{\partial \psi}{\partial z}, \quad \dot{z} = w(\rho, z) = -\frac{\partial \psi}{\partial \rho}. \quad (3.12)$$

We assume that the streamfunction $\psi(\rho, z)$ is analytic. As we see in the experimental results of figure 3.2 the recirculation zones are attached to the center axis. Hence we Taylor expand $\psi(\rho, z)$ at a given point on the center axis. We take this point to be the origin $(\rho, z) = (0, 0)$ and write

$$\psi(\rho, z) = \sum_{m+n=0}^{\infty} a_{m,n} \rho^m z^n \quad (3.13)$$

remembering that we have chosen to set $\psi(0, 0) = 0$. The Taylor expansion is valid in some neighborhood of the expansion point $(0, 0)$ where the neighborhood extends into the meridional plane, see figure 3.5.

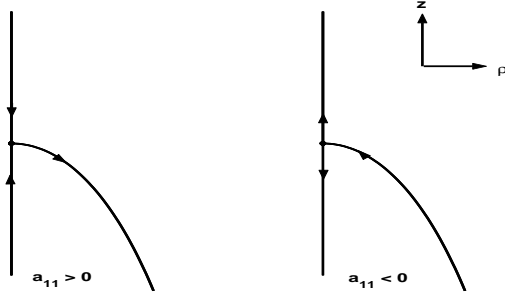


Figure 3.6: Diagram showing separation off or attachment to the center axis of a separatrix for the linear system (3.15) with $a_{1,0} = 0$. Separation takes place for $a_{1,1} > 0$ whereas attachment occurs for $a_{1,1} < 0$. The bullet (\bullet) marks the placement of a stagnation point.

From (3.11) we find that $a_{0,n} = 0$ for $n = 0, 1, 2, \dots$ and the streamfunction system (3.12) leads to

$$\begin{aligned}\dot{\rho} &= \rho(a_{1,1} + a_{2,1}\rho + 2a_{1,2}z) + O(|(\rho, z)|^3) \\ \dot{z} &= -a_{1,0} - 2a_{2,0}\rho - a_{1,1}z - 3a_{3,0}\rho^2 - 2a_{2,1}\rho z - a_{1,2}z^2 + O(|(\rho, z)|^3).\end{aligned}\quad (3.14)$$

Truncated to first order (3.14) is given as

$$\begin{pmatrix} \dot{\rho} \\ \dot{z} \end{pmatrix} = \begin{pmatrix} 0 \\ -a_{1,0} \end{pmatrix} + \begin{bmatrix} a_{1,1} & 0 \\ -2a_{2,0} & -a_{1,1} \end{bmatrix} \begin{pmatrix} \rho \\ z \end{pmatrix}.\quad (3.15)$$

According to the Hartman-Grobman Theorem the local dynamics close to a regular or generic stagnation point is governed by the linear approximation of a velocity field. But if the Jacobian is singular higher order terms in the velocity field becomes decisive for the local dynamics of the degenerate stagnation point.

If the degeneracy condition $a_{1,0} = 0$ is fulfilled for (3.15) the origin $(\rho, z) = (0, 0)$ is a stationary point. The eigenvalues for the Jacobian \mathbf{J} of (3.15) are given as $\lambda_{\pm} = \pm a_{1,1}$ hence the stationary point is a hyperbolic saddle under the condition $a_{1,1} \neq 0$. The linear approximations of the saddle separatrices are the eigenvectors of \mathbf{J} and are given as $\mathbf{u}_{-} = (0, 1)^T$ and $\mathbf{u}_{+} = (1, -a_{2,0}/a_{1,1})^T$. We see that the center axis, which is a streamline, is also a separatrix for the hyperbolic saddle and is therefore invariant. A fluid particle staying on the center axis will not flow into the flow in the meridional plane. Furthermore we see that another separatrix or invariant meridional streamline exists and is directed into the meridional plane. As illustrated in figure 3.6 we have separation from the center axis for $a_{1,1} > 0$ and attachment to the center axis for $a_{1,1} < 0$. In the figure the bullet signifies a stagnation point, this will also hold true for forthcoming bifurcation diagrams.

If both degeneracy conditions $a_{1,0} = 0$ and $a_{1,1} = 0$ are fulfilled the Jacobian \mathbf{J} is singular and we cannot analyse the system (3.14) through the linear approximation (3.15). Higher order terms in the velocity field becomes decisive for the local dynamics of the degenerate stagnation point. The system (3.14) involves to second order nine terms and a substantial number of terms are added when writing up explicitly terms of higher order. The great many number of non-linear terms complicates a bifurcation analysis. A tremendous simplification can be obtained by deriving a normal form in which only the so-called resonant terms in the expansion (3.14) are left. Brøns (1999) have formulated a theorem showing how the axisymmetric Taylor expansion of $\psi(\rho, z)$ can be simplified to normal form.

Theorem 3.1 (Axisymmetric normal form) Let $a_{1,0}, \dots, a_{1,N-1}$ be small parameters. Assuming the non-degeneracy conditions $a_{2,0} \neq 0$ and $a_{1,N} \neq 0$, then a truncated normal form of order

N for the streamfunction (3.13) is, in new coordinates (ξ, η)

$$\psi = \xi \left(-\mu + \frac{1}{2}\sigma\xi + \sum_{i=1}^N c_i \eta^i \right) \text{ with } c_{N-1} = 0 \text{ and } c_N = \frac{1}{N} \quad (3.16)$$

where

$$\sigma = \begin{cases} -1 & \text{for } N \text{ even and } a_{2,0}/a_{1,N} < 0 \\ +1 & \text{for } N \text{ even and } a_{2,0}/a_{1,N} > 0 \text{ or } N \text{ odd} \end{cases} \quad (3.17)$$

and μ and c_i for $i = 1, \dots, N-2$ are transformed small normal form parameters.

The non-degeneracy condition $a_{2,0} \neq 0$ ensures that the linear part of (3.16) is non-zero. The normal form for the degeneracy condition $a_{2,0} = 0$ fulfilled is treated in section 3.2.6.

In section 3.2.5 we will list the various bifurcation diagrams for the orders $N = 2, \dots, 4$ of the normal form (3.16) corresponding to analyzing the dynamical system

$$\dot{\xi} = \frac{\partial \psi}{\partial \eta} = \xi f'(\eta), \quad \dot{\eta} = -\frac{\partial \psi}{\partial \xi} = \mu - \sigma\xi - f(\eta). \quad (3.18)$$

We show in section 3.2.1 to section 3.2.4. Theorem 3.1

3.2.1 Normal forms

The objective of the normal form technique is to conduct a simplification of the nonlinearities in the vector field of a dynamical system. The basic idea is to perform a series of nonlinear coordinate transformations bringing the vector field on a simpler form, a normal form. The coordinate transformations are in general local near identity transformations generated in a neighborhood of an already know solution, typically a stationary point of some codimension. We note that the transformations are found by solving a series of linear problems. In most cases the near identity transformation may remove some but not all nonlinear terms in the vector field. The nonlinearities left after a transformation has been performed are denoted resonant terms. The resonant terms thereby manifest the terms essential for the dynamics of a given nonlinear system. Here we will simplify the streamfunction (3.13) for the degenerate case where $a_{1,0} = 0$ and $a_{1,1} = 0$ with $a_{2,0} \neq 0$ hence preserving a non-zero Jacobian of the system (3.14). The derivation of the normal form is conducted in a sequence where nonlinear terms of increasing order are simplified order by order. The derivation will take place in two steps. In the first step we will find a suitable near identity transformation chosen such that the area-preserving structure of the Hamiltonian system (3.12) is kept. The transformation will map the original or physical variables (ρ, z) into normal form variables (ξ, η) . In the second step we will determine a normal form at the stationary point $(\rho, z) = (0, 0)$ for the degenerate streamfunction. Due to the degeneracy conditions the second order terms are already simplified, this fact will become clear below. Therefore we start out by identifying third order resonant terms. As we shall see, it becomes clear after having identified the third order terms how we in general can identify resonant terms of any given order $i \geq 3$.

Consider the Taylor expansion of the streamfunction

$$\psi(\rho, z) = \sum_{i=0}^{N+1} \psi_i(\rho, z) + O(|(\rho, z)|^{N+2})$$

with scalar homogeneous polynomial terms of order i on the form

$$\psi_i(\rho, z) = \sum_{m+n=i} a_{m,n} \rho^m z^n \quad \text{for } m, n = 0, \dots, i.$$

The first term ψ_0 in $\psi(\rho, z)$ is a constant and as mentioned above we have chosen to set the arbitrary integration constant equal zero on the center axis thus $\psi(0, 0) = \psi_0 = 0$. Furthermore the boundary condition (3.11) leads to the condition $a_{0,n} = 0$ for $n = 0, 1, 2, \dots$ on the expansion coefficients hence no terms on the form z^n for $n = 0, 1, 2, \dots$ appear in the streamfunction. Introducing this condition we can rewrite the streamfunction as

$$\psi(\rho, z) = \rho \phi(\rho, z) = \rho \left(\sum_{i=1}^N \phi_{i-1}(\rho, z) \right) + O(|(\rho, z)|^{N+2}) \quad (3.19)$$

where

$$\phi_i(\rho, z) = \sum_{m+n=i} a_{m+1,n} \rho^m z^n \quad \text{for } m, n = 0, \dots, i \quad (3.20)$$

which we will simplify using the transformations derived in section 3.2.2.

3.2.2 Area-preserving near identity transformation

To simplify higher order terms $\psi_i(\rho, z)$ we seek a near identity transformation on the form

$$\rho = R(\xi, \eta) = \xi + \bar{R}(\xi, \eta), \quad z = Z(\xi, \eta) = \eta + \bar{Z}(\xi, \eta) \quad (3.21)$$

mapping the normal form variables (ξ, η) to the original variables (ρ, z) , where R, Z, \bar{R} and \bar{Z} are smooth functions with \bar{R} and \bar{Z} of second order or higher. We wish to preserve the Hamiltonian property of the system (3.12) under the near identity transformation (3.21). Canonical transformations preserve the Hamiltonian structure, see Grimshaw (1990). A canonical transformation is an area-preserving map of the meridional plane. Thus the near identity transformation must be area-preserving. To obtain this consider a region D in (ρ, z) -variables having area $A_{(\rho,z)}$ and let the same region D in (ξ, η) -variables have area $A_{(\xi,\eta)}$. Then the transformation (3.21) from normal form variables to original variables is area-preserving for $A_{(\rho,z)} = A_{(\xi,\eta)}$ where

$$A_{(\rho,z)} = \int \int_D 1 \cdot d\rho dz = \int_{\partial D} -z d\rho = \int_{\partial D} \rho dz \quad (3.22)$$

and

$$A_{(\xi,\eta)} = \int \int_D 1 \cdot d\xi d\eta = \int_{\partial D} -\eta d\xi = \int_{\partial D} \xi d\eta. \quad (3.23)$$

In (3.22) and (3.23) we have used the special case of Green's Theorem for the area A of a region D in the plane where we assume the boundary ∂D of D is a closed piecewise C^1 -curve. Equating $A_{(\rho,z)} = A_{(\xi,\eta)}$ in (3.22) and (3.23) gives four combinations of integrals. We choose arbitrarily one of them

$$\int_{\partial D} \rho dz + \eta d\xi = 0$$

which defines an exact differential $dS = \rho dz + \eta d\xi$ implying the existence of a generating function $S(z, \xi)$ for which the partial derivatives are given as

$$\rho = \frac{\partial S}{\partial z}(z, \xi), \quad \eta = \frac{\partial S}{\partial \xi}(z, \xi). \quad (3.24)$$

The partial derivatives serve as the basis for the near identity transformation. As we see (3.24) is not on the form (3.21) so to ensure that we can solve (3.24) for z as functions of ξ and η we assume that $\frac{\partial S}{\partial \xi \partial z}|_{(0,0)} \neq 0$ and the Implicit Function Theorem guarantees the existence of a solution in a neighborhood of $(0,0)$. We will briefly come back to this point below.

As we wish to conduct the derivation of the normal form order-wise we choose a generating function $S(z, \xi)$ on the form

$$S(z, \xi) = z\xi + S_i(z, \xi) \quad (3.25)$$

where $S_i(z, \xi)$ is a homogeneous polynomial of order $i \geq 3$ given as

$$S_i(z, \xi) = \sum_{m+n=i} s_{m,n} z^m \xi^n \quad \text{for } m, n = 0, \dots, i$$

or for clarity written in expanded form

$$S_i(z, \xi) = s_{i,0} z^i + s_{i-1,1} z^{i-1} \xi + \dots + s_{1,i-1} z \xi^{i-1} + s_{0,i} \xi^i. \quad (3.26)$$

For later convenience we write explicitly the partial derivative with respect to z and ξ of the expansion (3.26)

$$\frac{\partial S_i}{\partial z}(z, \xi) = i s_{i,0} z^{i-1} + (i-1) s_{i-1,1} z^{i-2} \xi + \dots + s_{1,i-1} \xi^{i-1} \quad (3.27)$$

$$\frac{\partial S_i}{\partial \xi}(z, \xi) = s_{i-1,1} z^{i-1} + \dots + (i-1) s_{1,i-1} z \xi^{i-2} + i s_{0,i} \xi^{i-1}. \quad (3.28)$$

The partial derivatives are of order $i-1$.

We note that (3.25) fulfills the condition $\frac{\partial^2 S}{\partial \xi \partial z}|_{(0,0)} \neq 0$. Inserting (3.25) in (3.24) we get

$$\rho = \xi + \frac{\partial S_i}{\partial z}(z, \xi), \quad z = \eta - \frac{\partial S_i}{\partial \xi}(z, \xi). \quad (3.29)$$

It is seen in (3.29) that ρ and z depends implicitly on z through the partial derivative of the monomial $S_i(z, \xi)$ in the generating function. To put (3.29) on the form (3.21) we apply the Implicit Function Theorem and introduce the smooth function f given by

$$f(\xi, \eta, z) = \frac{\partial S_i}{\partial \xi}(z, \xi) + z - \eta \quad (3.30)$$

and consider the equation $f(\xi, \eta, z) = 0$ which has the solution $(\xi, \eta, z) = (0, 0, 0)$. As

$$\left. \frac{\partial f}{\partial z} \right|_{(0,0,0)} = \left. \frac{\partial^2 S_i}{\partial \xi \partial z} \right|_{(0,0,0)} + 1 = 1 \neq 0$$

there exists a smooth function $z = Z(\xi, \eta)$ in a neighborhood of $(0,0,0)$ such that $Z(0,0) = 0$ and $f(\xi, \eta, Z(\xi, \eta)) = 0$. A Taylor expansion of Z can be found by inserting $Z(\xi, \eta)$ in (3.30) and deriving higher order partial derivatives by implicit differentiation. A similar approach can be used in (3.29) to obtain a smooth function R such that $\rho = R(\xi, \eta)$. Now by using implicit differentiation it can be shown that

$$\rho = R(\xi, \eta) = \xi + \bar{R}_{i-1}(\xi, \eta) + O(|(\xi, \eta)|^i) \quad (3.31)$$

$$z = Z(\xi, \eta) = \eta + \bar{Z}_{i-1}(\xi, \eta) + O(|(\xi, \eta)|^i) \quad (3.32)$$

where \bar{Z}_{i-1} and \bar{R}_{i-1} are homogeneous polynomials of order $i-1$. Continuing inserting the near-identity transformation (3.31) and (3.32) into (3.29) we obtain

$$\begin{aligned}\bar{R}_{i-1}(\xi, \eta) + O(|(\xi, \eta)|^i) &= \frac{\partial S_i}{\partial z}(\eta + Z_{i-1}(\xi, \eta) + O(|(\xi, \eta)|^i), \xi) = \frac{\partial S_i}{\partial z}(\eta, \xi) + O(|(\xi, \eta)|^i) \\ \bar{Z}_{i-1}(\xi, \eta) + O(|(\xi, \eta)|^i) &= -\frac{\partial S_i}{\partial \xi}(\eta + Z_{i-1}(\xi, \eta) + O(|(\xi, \eta)|^i), \xi) = -\frac{\partial S_i}{\partial \xi}(\eta, \xi) + O(|(\xi, \eta)|^i).\end{aligned}$$

We have now identified terms in the near identity transformation and the canonical transformation and we can finally write the area-preserving near identity transformation of order $i-1$ on the form

$$\rho = \xi + \frac{\partial S_i}{\partial z}(\eta, \xi) + O(|(\xi, \eta)|^i), \quad z = \eta - \frac{\partial S_i}{\partial \xi}(\eta, \xi) + O(|(\xi, \eta)|^i). \quad (3.33)$$

The near identity transformation (3.33) can be used in general to simplify two dimensional Hamiltonian systems.

To make the normal form fulfill the same boundary conditions (3.11) as the axisymmetric streamfunction we choose to impose constraints on some of the coefficients $s_{m,n}$ in the polynomial $S_i(z, \xi)$ in (3.25). To identify the relevant terms in the near identity transformation we insert (3.29) (and not (3.33) for notational reasons) in (3.19) remembering that $z = \eta + \bar{Z}_{i-1}(\xi, \eta) + O(|(\xi, \eta)|^i)$

$$\begin{aligned}\psi(\rho, z) &= \rho\phi(\rho, z) = \left(\xi + \frac{\partial S_i}{\partial z}(z, \xi)\right) \times \phi\left(\xi + \frac{\partial S_i}{\partial z}(z, \xi), \eta - \frac{\partial S_i}{\partial \xi}(z, \xi)\right) \\ &= \xi\phi\left(\xi + \frac{\partial S_i}{\partial z}(z, \eta), \xi\right) + \underbrace{\eta - \frac{\partial S_i}{\partial \xi}(z, \xi)}_{\text{must not contain any terms on the form } z^m \text{ for any } m=0,1,\dots} \times \phi\left(\xi + \frac{\partial S_i}{\partial z}(z, \xi), \eta - \frac{\partial S_i}{\partial \xi}(z, \xi)\right)\end{aligned} \quad (3.34)$$

The last product term in (3.34) must not contain any terms on the form z^m for any $m = 0, 1, 2, \dots$ implying that $s_{m,0} = 0$ for $m = 0, 1, 2, \dots$, see (3.27). From the near identity transformation of ρ in (3.33) it is seen that the boundary constraint $s_{m,0} = 0$ for $m = 0, 1, 2, \dots$ ensures that $\xi = 0$ maps to $\rho = 0$ corresponding to letting the ξ -axis map to the ρ -axis and the ξ -variable can be understood as being radial-like.

3.2.3 Normal form for the degenerate streamfunction

Let us now turn to the second step, to find the normal form for the degenerate streamfunction

$$\psi(\rho, z) = \rho\phi(\rho, z) = \rho[a_{2,0}\rho + \phi_2(\rho, z) + \phi_3(\rho, z) + \phi_4(\rho, z) + \dots] \quad (3.35)$$

with the first couple of terms given as

$$\phi_1(\rho, z) = a_{2,0}\rho \quad (3.36)$$

$$\phi_2(\rho, z) = a_{3,0}\rho^2 + a_{2,1}\rho z + a_{1,2}z^2 \quad (3.37)$$

$$\phi_3(\rho, z) = a_{4,0}\rho^3 + a_{3,1}\rho^2 z + a_{2,2}\rho z^2 + a_{1,3}z^3. \quad (3.38)$$

The first order polynomial ϕ_1 cannot be simplified further apart from a possible scaling using $a_{2,0}$ as the Jacobian \mathbf{J} of the linear part of (3.14) is on Jordan form

$$\mathbf{J} = -2a_{2,0} \begin{pmatrix} 0 & 0 \\ 1 & 0 \end{pmatrix}.$$

Having the near identity transformation (3.33) together with the boundary constraint $s_{m,0} = 0$ for $m = 0, 1, 2, \dots$ we can continue to simplify higher order terms. To illustrate the method we start out by simplifying the third order terms $\psi_3(\rho, z)$ which corresponds to simplifying the second order terms $\phi_2(\rho, z)$. To simplify $\phi_2(\rho, z)$ the near identity transformation must match in polynomial order, hence we have to choose $i = 3$ in (3.33). Inserting (3.33) in (3.35) gives

$$\begin{aligned} \psi(\xi, \eta) &= \rho\phi(\rho, z) = \\ &= \left[\xi + \frac{\partial S_3}{\partial z}(\eta, \xi) + O(|(\xi, \eta)|^3) \right] \times \\ &\quad \left[a_{2,0} \left(\xi + \frac{\partial S_3}{\partial z}(\eta, \xi) + O(|(\xi, \eta)|^3) \right) \right. \\ &\quad + \phi_2 \left(\xi + \frac{\partial S_3}{\partial z}(\eta, \xi) + O(|(\xi, \eta)|^3), \eta - \frac{\partial S_3}{\partial \xi}(\eta, \xi) + O(|(\xi, \eta)|^3) \right) \\ &\quad + \phi_3 \left(\xi + \frac{\partial S_3}{\partial z}(\eta, \xi) + O(|(\xi, \eta)|^3), \eta - \frac{\partial S_3}{\partial \xi}(\eta, \xi) + O(|(\xi, \eta)|^3) \right) \\ &\quad \left. + \phi_4 \left(\xi + \frac{\partial S_3}{\partial z}(\eta, \xi) + O(|(\xi, \eta)|^3), \eta - \frac{\partial S_3}{\partial \xi}(\eta, \xi) + O(|(\xi, \eta)|^3) \right) + \dots \right] \quad (3.39) \end{aligned}$$

$$= \xi(a_{2,0}\xi + \underbrace{a_{2,0}\frac{\partial S_3}{\partial z}(\eta, \xi) + \phi_2(\xi, \eta) + \tilde{\phi}_3(\xi, \eta) + \tilde{\phi}_4(\xi, \eta) + \dots}_{\text{polynomial of order 2}}) \quad (3.40)$$

where the higher order terms $\tilde{\phi}_i(\xi, \eta) = \phi_i(\xi, \eta) + O(|(\xi, \eta)|^i)$ for $i \geq 3$ have been modified as a consequence of expanding (3.39) resulting in (3.40). Comparing with (3.37) we also notice that the introduction of the second order near identity transformation has left the first order term $\phi_1(\xi, \eta) = a_{2,0}\xi$ unchanged.

Up until now the generating function (3.25) has, except for the boundary constraint on $s_{m,0} = 0$, been completely arbitrary. We can exploit this fact by choosing the coefficients $s_{m,n}$ such that we simplify the second order terms $\phi_2(\xi, \eta)$ in (3.39) as much as possible. The terms of second order are

$$\begin{aligned} a_{2,0}\frac{\partial S_3}{\partial z}(\eta, \xi) + \phi_2(\xi, \eta) &= a_{2,0}(2s_{2,1}\eta\xi + s_{1,2}\xi^2) + (a_{3,0}\xi^2 + a_{2,1}\xi\eta + a_{1,2}\eta^2) \\ &= (a_{2,0}s_{1,2} + a_{3,0})\xi^2 + (2a_{2,0}s_{2,1} + a_{2,1})\xi\eta + a_{1,2}\eta^2. \quad (3.41) \end{aligned}$$

Choosing the constants $s_{1,2}$ and $s_{2,1}$ as

$$s_{1,2} = -\frac{a_{3,0}}{a_{2,0}}, \quad s_{2,1} = -\frac{a_{2,1}}{2a_{2,0}}$$

in (3.41) we have, except for one term $a_{1,2}\eta^2$, simplified $\phi_2(\xi, \eta)$ as much as possible. so the term $\phi_2^{res}(\xi, \eta) = a_{1,2}\eta^2$ is resonant.

The above simplification of the second order terms $\phi_2(\xi, \eta)$ can be generalized to terms $\phi_i(\rho, z)$

of any given order i . Inserting the near identity transformation (3.33) of order i into (3.35)

$$\begin{aligned}
\psi(\xi, \eta) &= \rho\phi(\rho, z) = \\
&= \left[\xi + \frac{\partial S_{i+1}}{\partial z}(\eta, \xi) + O(|(\xi, \eta)|^{i+1}) \right] \times \\
&\quad \left[a_{2,0} \left(\xi + \frac{\partial S_{i+1}}{\partial z}(\eta, \xi) + O(|(\xi, \eta)|^{i+1}) \right) \right. \\
&\quad + \phi_2^{res} \left(\xi + \frac{\partial S_{i+1}}{\partial z}(\eta, \xi) + O(|(\xi, \eta)|^{i+1}), \eta - \frac{\partial S_{i+1}}{\partial \xi}(\eta, \xi) + O(|(\xi, \eta)|^{i+1}) \right) \\
&\quad \vdots \\
&\quad + \tilde{\phi}_i \left(\xi + \frac{\partial S_{i+1}}{\partial z}(\eta, \xi) + O(|(\xi, \eta)|^{i+1}), \eta - \frac{\partial S_{i+1}}{\partial \xi}(\eta, \xi) + O(|(\xi, \eta)|^{i+1}) \right) \\
&\quad \left. + \tilde{\phi}_{i+1} \left(\xi + \frac{\partial S_{i+1}}{\partial z}(\eta, \xi) + O(|(\xi, \eta)|^{i+1}), \eta - \frac{\partial S_{i+1}}{\partial \xi}(\eta, \xi) + O(|(\xi, \eta)|^{i+1}) \right) + \dots \right] \\
&= \underbrace{\xi(a_{2,0}\xi + \phi_2^{res}(\xi, \eta) + \dots + a_{2,0}\frac{\partial S_{i+1}}{\partial z}(\eta, \xi) + \tilde{\phi}_i(\xi, \eta) + \tilde{\phi}_{i+1}(\xi, \eta) + \dots)}_{\text{polynomial of order } i} \quad (3.42)
\end{aligned}$$

we can simplify the terms of order i down to the resonant terms $\phi_i^{res}(\xi, \eta)$ by considering

$$\begin{aligned}
a_{2,0}\frac{\partial S_{i+1}}{\partial z}(\eta, \xi) + \tilde{\phi}_i(\xi, \eta) &= a_{2,0}((i+1)s_{i+1,0}\eta^i + is_{i,1}\eta^{i-1}\xi + \dots + s_{2,i-1}\eta\xi^{i-1} + s_{1,i}\xi^i) \\
&\quad + (\tilde{a}_{i+1,0}\xi^i + \tilde{a}_{i,1}\xi^{i-1}\eta + \dots + \tilde{a}_{2,i-1}\xi\eta^{i-1} + \tilde{a}_{1,i}\eta^i) \\
&= (\tilde{a}_{1,i} + (i+1)a_{2,0}s_{i+1,0})\eta^i + (\tilde{a}_{2,i-1} + ia_{2,0}s_{i,1})\eta^{i-1}\xi + \dots \\
&\quad + (\tilde{a}_{i,1} + a_{2,0}s_{2,i-1})\eta\xi^{i-1} + (\tilde{a}_{i+1,0} + a_{2,0}s_{1,i})\xi^i. \quad (3.43)
\end{aligned}$$

By inspection of (3.43) we see that by choosing the coefficients $s_{m,n}$ as

$$s_{i,1} = -\frac{\tilde{a}_{2,i-1}}{ia_{2,0}}, \quad s_{i-1,2} = -\frac{\tilde{a}_{3,i-2}}{(i-1)a_{2,0}}, \quad \dots \quad s_{1,i} = -\frac{\tilde{a}_{i+1,0}}{a_{2,0}} \quad (3.44)$$

we can remove all terms except $\phi_i^{res}(\xi, \eta) = a_{1,i}\eta^i$. In the process of the simplification using the near identity transformation only terms of order greater than i are being modified. Already obtained resonant terms having order less than i are left unaltered and the normal form of the degenerate streamfunction becomes

$$\psi(\xi, \eta) = \xi(a_{2,0}\xi + \tilde{a}_{1,2}\eta^2 + \tilde{a}_{1,3}\eta^3 + \dots + \tilde{a}_{1,N}\eta^N) + O(|(\xi, \eta)|^{N+2}). \quad (3.45)$$

A scaling $\xi \rightarrow a\xi$, $\eta \rightarrow b\eta$ and $\psi \rightarrow c\psi$ can further simplify (3.45). Inserting the scaling we obtain

$$\psi(\xi, \eta) = \frac{a}{c}a_{2,0}\xi \left(a\xi + \frac{\tilde{a}_{1,2}}{a_{2,0}}b^2\eta^2 + \frac{\tilde{a}_{1,3}}{a_{2,0}}b^3\eta^3 + \dots + \frac{\tilde{a}_{1,N}}{a_{2,0}}b^N\eta^N \right) + O(|(\xi, \eta)|^{N+2}). \quad (3.46)$$

In choosing the scaling we have to distinguish between N being odd or even. For N odd it follows that either $b^N > 0$ or $b^N < 0$. For N even we have $b^N > 0$. Therefore we choose the scalings

$$N \text{ odd} : \frac{\tilde{a}_{1,N}}{a_{2,0}}b^N = \frac{1}{N} \Rightarrow b = \left(\frac{a_{2,0}}{\tilde{a}_{1,N}} \frac{1}{N} \right)^{1/N}, \quad N \text{ even} : \sigma \left| \frac{\tilde{a}_{1,N}}{a_{2,0}} \right| b^N = \sigma \frac{1}{N} \Rightarrow b = \left(\left| \frac{a_{2,0}}{\tilde{a}_{1,N}} \right| \frac{1}{N} \right)^{1/N}$$

where

$$\sigma = \left| \frac{a_{2,0}}{\tilde{a}_{1,N}} \right| \frac{\tilde{a}_{1,N}}{a_{2,0}} = \begin{cases} +1 & \text{for } \frac{\tilde{a}_{1,N}}{a_{2,0}} > 0 \\ -1 & \text{for } \frac{\tilde{a}_{1,N}}{a_{2,0}} < 0. \end{cases}$$

Choosing $a = 1/2$ and $c = 2\sigma/a_{2,0}$ we get the normal form for the degenerate streamfunction

$$\psi(\xi, \eta) = \xi \left(\frac{1}{2}\sigma\xi + c_{1,2}\eta^2 + c_{1,3}\eta^3 + \dots + c_{1,N-1}\eta^{(N-1)} + \frac{1}{N}\eta^N \right) + O(|(\xi, \eta)^{N+2}|) \quad (3.47)$$

where $c_{1,i} = \sigma \frac{\tilde{a}_{1,i}}{a_{2,0}}$ for $i = 2, \dots, N-1$ are small parameters.

In principle the normal form for the unfolding of the degenerate streamfunction can be derived in a similar manner as above by adding parameter dependent perturbation terms on the form

$$\epsilon(\xi, \eta) = \xi \left(\sum_{i=1}^N \epsilon_{i-1}(\xi, \eta) \right) + O(|(\xi, \eta)^{N+2}|) \quad (3.48)$$

to (3.47) where the polynomial $\epsilon_i(\xi, \eta)$ of order i is given as

$$\epsilon_i(\xi, \eta) = \sum_{m+n=k} \epsilon_{m+1,n} \xi^m \eta^n \quad \text{for } m, n = 0, \dots, k.$$

with parameters $|\epsilon_{m,n}| \ll 1$. This unfolded system can then be transformed by a parameter dependent near identity transformation on the same form as (3.33). Algebraically it is cumbersome to conduct this transformation for a given polynomial order i as inserting the parameter dependent near identity transformation into the perturbed streamfunction yields terms of order $i-1$, i and $i+1$. A way to circumvent this is to turn to symbolic computer algebra. We will consider this approach in section 3.2.4.

3.2.4 Calculation of the axisymmetric normal form using computer algebra

In the previous sections we showed how the degenerate normal form (3.46) for any given order N can be derived. But it turned out to be unfeasible to conduct the unfolding in a similar manner. Thus we turn to computer algebra. The approach has other advantages. For instance in applying normal forms we may need to know how the normal form constants μ and c_i from Theorem 3.1 depend explicitly on the coefficients $a_{m,n}$ in the Taylor expansion of the streamfunction (3.13). These are quite involved relations unfeasible to derive without computer algebra. Furthermore as the normal forms are formulated in terms of the normal form variables (ξ, η) and not the original or physical variables (ρ, z) it becomes important, in some applications of normal forms, to be able to map back and forth between the sets of variables (ξ, η) and (ρ, z) using the near identity transformation. This approach has been taken in Brøns (1999).

In the practical usage of normal forms it is typically sufficient to conduct an analysis of the first four orders of the normal form depending on the inherent codimension of the problem. In the case of the cylinder with rotating covers we have seen that the parameter space (h, Re, γ) is three dimensional and thus expect the problem to be at most of codimension 3. Theorem 3.1 shows that to analyse the axisymmetric normal form of codimension 3 we need to consider the normal form of order $N = 4$ having the three normal form parameters μ , c_1 and c_2 .

A feasible way to handle the mapping back and forth between (ξ, η) and (ρ, z) or to derive the algebraic relations between the normal form parameters and the Taylor coefficients for the streamfunction is, for some given low order, to derive a so-called complete near identity transformation by collecting the sequence of near identity transformations of increasing order into one transformation and perform the complete near identity transformation in one step up to the chosen order of the normal form considered. Algebraic computer programs such as Maple are well suited for this purpose.

In section 3.2.8 we will need to know how the normal form parameters μ , c_1 and c_2 depend explicitly on the Taylor coefficients $a_{m,n}$ for the third and fourth order normal form of the streamfunction (3.13). As the derivation of these algebraic relations for the fourth order streamfunction is elaborate we will merely state the results. But as the method is very convenient in applications we will illustrate the approach by deriving the normal form for the third order streamfunction. Calculations of the subsequent higher orders are conducted in a similar fashion.

Example 3.1 (The third order normal form) The calculation is based on the area-preserving canonical transformation (3.24). We consider the small parameters $\epsilon_{1,0} = a_{1,0}$ and $\epsilon_{1,1} = a_{1,1}$ and choose a generating function on the form

$$S(z, \xi, \epsilon_{1,0}, \epsilon_{1,1}) = z\xi + S_3(z, \xi, \epsilon_{1,0}, \epsilon_{1,1}) = z\xi + \sum_{m+n+p+q=3} s_{m,n,p,q} z^m \xi^n \epsilon_{1,0}^p \epsilon_{1,1}^q. \quad (3.49)$$

which we insert in the canonical transformation

$$\rho = \frac{\partial S}{\partial z}(z, \xi, \epsilon_{1,0}, \epsilon_{1,1}), \quad \eta = \frac{\partial S}{\partial \xi}(z, \xi, \epsilon_{1,0}, \epsilon_{1,1}) \quad (3.50)$$

giving

$$\begin{aligned} \rho &= \xi + s_{1,0,0,2}\epsilon_{1,1}^2 + s_{1,0,1,1}\epsilon_{1,0}\epsilon_{1,1} + s_{1,0,2,0}\epsilon_{1,0}^2 + s_{1,1,0,1}\xi\epsilon_{1,1} + s_{1,1,1,0}\xi\epsilon_{1,0} \\ &\quad + s_{1,2,0,0}\xi^2 + 2s_{2,0,0,1}z\epsilon_{1,1} + 2s_{2,0,1,0}z\epsilon_{1,0} + 2s_{2,1,0,0}\xi z + 3s_{3,0,0,0}z^2 \\ \eta &= z + s_{0,1,0,2}\epsilon_{1,1}^2 + s_{0,1,1,1}\epsilon_{1,0}\epsilon_{1,1} + s_{0,1,2,0}\epsilon_{1,0}^2 + 2s_{0,2,0,1}\xi\epsilon_{1,1} + 2s_{0,2,1,0}\xi\epsilon_{1,0} \\ &\quad + 3s_{0,3,0,0}\xi^2 + s_{1,1,0,1}z\epsilon_{1,1} + s_{1,1,1,0}z\epsilon_{1,0} + 2s_{1,2,0,0}\xi z + s_{2,1,0,0}z^2 \end{aligned} \quad (3.51)$$

A solution to (3.51) for the normal form variables $\xi(\rho, z)$ and $\eta(\rho, z)$ is sought in the form of Taylor expansions

$$\rho = \sum_{m+n=2} \alpha_{m,n} \xi^m \eta^n, \quad z = \sum_{m+n=2} \beta_{m,n} \xi^m \eta^n. \quad (3.52)$$

Inserting (3.52) in (3.51) and collecting terms of the same polynomial order in ξ and η yields a set of linear equations for the Taylor coefficients which solves to

$$\begin{aligned} \rho &= \xi + s_{1,0,0,2}\epsilon_{1,1}^2 + s_{1,0,1,1}\epsilon_{1,0}\epsilon_{1,1} + s_{1,0,2,0}\epsilon_{1,0}^2 + s_{1,1,0,1}\xi\epsilon_{1,1} + s_{1,1,1,0}\xi\epsilon_{1,0} \\ &\quad + s_{1,2,0,0}\xi^2 + 2s_{2,0,0,1}\eta\epsilon_{1,1} + 2s_{2,0,1,0}\eta\epsilon_{1,0} + 2s_{2,1,0,0}\xi\eta + 3s_{3,0,0,0}\eta^2 + O(|(\xi, \eta, \epsilon_{1,0}, \epsilon_{1,1})|^3) \\ z &= \eta - s_{0,1,0,2}\epsilon_{1,1}^2 - s_{0,1,1,1}\epsilon_{1,0}\epsilon_{1,1} - s_{0,1,2,0}\epsilon_{1,0}^2 - 2s_{0,2,0,1}\xi\epsilon_{1,1} - 2s_{0,2,1,0}\xi\epsilon_{1,0} \\ &\quad - 3s_{0,3,0,0}\xi^2 - s_{1,1,0,1}\eta\epsilon_{1,1} - s_{1,1,1,0}\eta\epsilon_{1,0} - 2s_{1,2,0,0}\xi\eta - s_{2,1,0,0}\eta^2 + O(|(\xi, \eta, \epsilon_{1,0}, \epsilon_{1,1})|^3). \end{aligned} \quad (3.53)$$

As for the near identity transformation (3.34) we also here need to impose the boundary conditions (3.11) on (3.53). We can use a similar argument as for (3.34) and choose ξ to be radial-like such that the near identity transformation (3.53) map the center axis $\rho = 0$ to $\xi = 0$. We impose the conditions

$$s_{1,0,0,2} = 0, \quad s_{1,0,1,1} = 0, \quad s_{1,0,2,0} = 0, \quad s_{2,0,0,1} = 0, \quad s_{2,0,1,0} = 0, \quad s_{3,0,0,0} = 0. \quad (3.54)$$

on the coefficients of the generating function. Inserting (3.53) with (3.54) into the streamfunction (3.13) we obtain

$$\begin{aligned} \psi(\xi, \eta) = & \xi\epsilon_{1,0} + a_{2,0}\xi^2 + (a_{2,1} + 4a_{2,0}s_{2,1,0,0})\xi^2\eta + (2a_{2,0}s_{1,1,1,0} + s_{1,2,0,0})\xi^2\epsilon_{1,0} \\ & + 2a_{2,0}s_{1,1,0,1}\xi^2\epsilon_{1,1} + a_{1,2}\xi\eta^2 + \xi\eta\epsilon_{1,1} + 2s_{2,1,0,0}\xi\eta\epsilon_{1,0} + s_{1,1,1,0}\xi\epsilon_{1,0}^2 \\ & + s_{1,1,0,1}\xi\epsilon_{1,0}\epsilon_{1,1} + (a_{3,0} + 2a_{2,0}s_{1,2,0,0})\xi^3 + O(|(\xi, \eta, \epsilon_{1,0}, \epsilon_{1,1})|^4) \end{aligned} \quad (3.55)$$

and again exploiting the fact that the coefficients for the generating function are arbitrary we can simplify $\psi(\xi, \eta)$ by choosing

$$s_{2,1,0,0} = -\frac{a_{2,1}}{4a_{2,0}}, \quad s_{1,2,0,0} = -\frac{a_{3,0}}{2a_{2,0}}, \quad s_{1,1,1,0} = \frac{a_{3,0}}{4a_{2,0}^2}, \quad s_{1,1,0,1} = 0. \quad (3.56)$$

Inspecting the near identity transformation (3.53) for z and comparing with (3.55) we see that the following set of coefficients has no influence on the simplification of the streamfunction and can choose to set

$$s_{0,1,0,2} = 0, \quad s_{0,1,1,1} = 0, \quad s_{0,1,2,0} = 0, \quad s_{0,2,0,1} = 0, \quad s_{0,2,1,0} = 0, \quad s_{0,3,0,0} = 0. \quad (3.57)$$

With (3.56) the streamfunction reduces to

$$\psi(\xi, \eta) = \tilde{\epsilon}_1\xi + \tilde{\epsilon}_2\xi\eta + a_{2,0}\xi^2 + a_{1,2}\xi\eta^2 + O(|(\xi, \eta, \epsilon_{1,0}, \epsilon_{1,1})|^4) \quad (3.58)$$

where

$$\tilde{\epsilon}_1 = \epsilon_{1,0} + \frac{a_{3,0}}{4a_{2,0}^2}\epsilon_{1,0}^2 \quad \text{and} \quad \tilde{\epsilon}_2 = \epsilon_{1,1} - \frac{a_{2,1}}{2a_{2,0}}\epsilon_{1,0}. \quad (3.59)$$

We assume that $a_{1,2} \neq 0$ which is a generic condition for the third order normal form. If the degeneracy condition $a_{1,2} = 0$ is fulfilled the cubic term vanishes and a normal form of order four would have to be derived for further investigation. With the assumptions $a_{1,2} \neq 0$ and $a_{2,0} \neq 0$ fulfilled we continue choosing the scalings

$$\xi \mapsto \frac{a_{1,2}}{a_{2,0}}\xi, \quad \eta \mapsto \eta - \frac{\tilde{\epsilon}_2}{2a_{1,2}}\eta \quad \text{and} \quad \psi \mapsto \frac{a_{2,0}}{2a_{1,2}^2}\psi. \quad (3.60)$$

Introducing the scalings into (3.58) we finally arrive at the scaled third order normal form

$$\psi(\xi, \eta) = -\mu\xi + \frac{1}{2}\xi^2 + \frac{1}{2}\xi\eta^2 + O(|(\xi, \eta, \epsilon_{1,0}, \epsilon_{1,1})|^4) \quad (3.61)$$

where

$$\mu = \frac{\tilde{\epsilon}_2^2}{8a_{1,2}^2} - \frac{\tilde{\epsilon}_1 a_{1,2}}{2a_{1,2}^2}. \quad (3.62)$$

which is the algebraic relation between the scaled normal form parameter μ and the Taylor coefficients for the streamfunction where ϵ_1 and ϵ_2 are found in (3.59). With the choice of constants (3.54), (3.56) and (3.57) we get the complete near identity transformation to second order

$$\begin{aligned}\rho &= \left(\frac{a_{1,2}}{a_{2,0}}\right) \left[\left(1 + \frac{a_{3,0}}{4a_{2,0}^2}\epsilon_{1,0}\right) \xi - \frac{a_{1,2}a_{3,0}}{2a_{2,0}^2}\xi^2 - \frac{a_{2,1}}{2a_{2,0}} \left(1 - \frac{\tilde{\epsilon}_2}{2a_{1,2}}\right) \xi\eta \right] + O(|(\xi, \eta, \epsilon_{1,0}, \epsilon_{1,1})|^3) \\ z &= \left(1 - \frac{\tilde{\epsilon}_2}{2a_{1,2}}\right) \left[\left(1 - \frac{a_{3,0}}{4a_{2,0}^2}\epsilon_{1,0}\right) \eta + \left(1 - \frac{\tilde{\epsilon}_2}{2a_{1,2}}\right) \frac{a_{1,2}}{4a_{2,0}}\eta^2 + \frac{a_{1,2}a_{3,0}}{a_{2,0}^2}\xi\eta \right] + O(|(\xi, \eta, \epsilon_{1,0}, \epsilon_{1,1})|^3).\end{aligned}$$

In the above example we illustrated the line of approach used by Brøns (1999) to effectively calculate normal forms. In summary, choose a generating function on polynomial form similar to (3.49) including nonlinear terms up to the same order as the order of the streamfunction to which we have set out to determine a normal form. In the generating function include small parameters corresponding to unfold the considered degeneracy conditions. Solve, using Taylor expansions and identification of nonlinear terms, the equations (3.50) for the physical variables (ρ, z) as functions of the normal form variables (ξ, η) and insert this near identity transformation into the streamfunction and simplify high order nonlinear terms using the fact that the coefficients in the generating function are arbitrary. After an appropriate scaling of variables one obtains the scaled normal form with corresponding expressions for the complete near identity transformation and algebraic relations for the dependence of the normal form parameters on the Taylor coefficients of the streamfunction.

Example 3.2 (The fourth order normal form) We will in section 3.2.8 refer to the algebraic relations for the dependence of the normal form parameters on the Taylor coefficients of the fourth order streamfunction. We will merely state the results here.

The derivation is based on the generating function with third and fourth order terms

$$\begin{aligned}S(z, \xi, \epsilon_{1,0}, \epsilon_{1,1}) &= z\xi + S_3(z, \xi, \epsilon_{1,0}, \epsilon_{1,1}) + S_4(z, \xi, \epsilon_{1,0}, \epsilon_{1,1}) \\ &= z\xi + \sum_{m+n+p+q=3} s_{m,n,p,q} z^m \xi^n \epsilon_{1,0}^p \epsilon_{1,1}^q \\ &\quad + \sum_{m+n+p+q=4} s_{m,n,p,q} z^m \xi^n \epsilon_{1,0}^p \epsilon_{1,1}^q.\end{aligned}$$

Inserting this in (3.50) and solving for ρ and z gives a near identity transformation which with the following choice of non-zero coefficients

$$\begin{aligned}s_{2,1,0,0} &= \frac{a_{3,0}}{2a_{2,0}}, & s_{1,3,0,0} &= \frac{a_{2,1}^2}{12a_{2,0}^2} + \frac{a_{2,2}}{6a_{2,0}}, & s_{2,2,0,0} &= \frac{a_{2,1}a_{3,0}}{4a_{2,0}^2} + \frac{a_{3,1}}{4a_{2,0}}, & s_{1,1,1,0} &= \frac{-a_{3,0}}{4a_{2,0}^2} \\ s_{1,2,0,0} &= \frac{a_{2,1}}{4a_{2,0}}, & s_{1,2,1,0} &= \frac{a_{2,1}a_{3,0}}{4a_{2,0}^3} - \frac{a_{3,1}}{8a_{2,0}^2}, & s_{3,1,0,0} &= \frac{-a_{3,0}^2}{8a_{2,0}^2} + \frac{a_{4,0}}{2a_{2,0}}, & s_{1,2,0,1} &= \frac{a_{3,0}}{8a_{2,0}^2} \\ s_{1,1,2,0} &= \frac{a_{4,0}}{8a_{2,0}^3}, & s_{2,1,1,0} &= \frac{a_{4,0}}{4a_{2,0}^2} - \frac{a_{3,0}^2}{16a_{2,0}^2}\end{aligned}$$

results in the truncated normal form

$$\psi(\xi, \eta) = \left(\epsilon_{1,0} + \frac{a_{3,0}\epsilon_{1,0}^2}{4a_{2,0}^2} - \frac{a_{4,0}\epsilon_{1,0}^3}{8a_{2,0}^3} \right) \xi + a_{2,0}\xi^2 + d_{1,1}\xi\eta + d_{1,2}\xi\eta^2 + a_{1,3}\xi\eta^3 \quad (3.63)$$

where

$$d_{1,1} = \epsilon_{1,1} - \frac{a_{2,1}\epsilon_{1,0}}{2a_{2,0}} - \frac{a_{3,0}\epsilon_{1,0}\epsilon_{1,1}}{4a_{2,0}^2} + \frac{a_{2,1}a_{3,0}\epsilon_{1,0}^2}{2a_{2,0}^3} + \frac{a_{3,1}\epsilon_{1,0}^2}{4a_{2,0}} \quad (3.64)$$

and

$$d_{1,2} = a_{1,2} - \frac{a_{2,1}\epsilon_{1,1}}{4a_{2,0}} - \frac{a_{2,1}^2\epsilon_{1,0}}{4a_{2,0}^2} - \frac{a_{2,2}\epsilon_{1,0}}{2a_{2,0}}. \quad (3.65)$$

We assume that $a_{1,2}$ is small and that $a_{1,3}$ fulfills the non-degeneracy condition $a_{1,3} \neq 0$. If instead the degeneracy condition $a_{1,3} = 0$ is fulfilled the quadratic term vanishes and a normal form of order five would have to be derived. Introducing the scaling

$$\xi \mapsto \frac{3a_{1,3}}{2a_{2,0}}\xi, \quad \eta \mapsto \eta - \frac{d_{1,2}}{3a_{1,3}} \quad \text{and} \quad \psi \mapsto \frac{2a_{2,0}}{9a_{1,3}}\psi \quad (3.66)$$

in the normal form yields the truncated scaled normal form

$$\psi(\xi, \eta) = -\mu\xi + \frac{1}{2}\xi^2 + c_1\xi\eta^2 + \frac{1}{3}\xi\eta^3 \quad (3.67)$$

with the normal form constants

$$\mu = \frac{d_{1,1}d_{1,2}}{9a_{1,3}^2} - \frac{2d_{1,2}^2}{81a_{1,3}^3} - \frac{\epsilon_{1,0}}{3a_{1,3}} - \frac{a_{3,0}\epsilon_{1,0}^2}{12a_{1,3}a_{2,0}^2} + \frac{a_{4,0}\epsilon_{1,0}^3}{24a_{1,3}a_{2,0}^3} \quad (3.68)$$

and

$$c_1 = \frac{d_{1,1}}{3a_{1,3}} - \frac{d_{1,2}^2}{9a_{1,3}^2}. \quad (3.69)$$

This approach can be continued to any order, hence Theorem 3.1 has been showed.

3.2.5 Bifurcation diagrams

In this section we display the various bifurcation diagrams for the orders $N = 2, 3, 4$ of the normal form (3.16). We base the analysis on the dynamical system (3.18) rewritten here for convenience

$$\dot{\xi} = \xi f'(\eta), \quad \dot{\eta} = \mu - \sigma\xi - f(\eta) \quad (3.70)$$

where $f(\eta) = \sum_{i=1}^N c_i \eta^i$ with $c_{N-1} = 0$ and $c_N = 1/N$. It follows that $f(0) = 0$. With the bifurcation diagrams we obtain a catalogue of the possible set of topologies emerging the recirculation zones can take. We will see how several recirculation zones can exist simultaneously for given parameter values and we will see how they can merge forming a new recirculation zone with inner structure. The bifurcation diagrams can also be found in Brøns (1999). The Jacobian \mathbf{J} of the system (3.70) is given as

$$\mathbf{J} = \begin{bmatrix} f'(\eta) & \xi f''(\eta) \\ -\sigma & -f'(\eta) \end{bmatrix}.$$

As the system (3.70) is Hamiltonian the trace $Tr(\mathbf{J}) = 0$. The eigenvalues of \mathbf{J} are given by $\lambda_{\pm} = \pm\sqrt{-Det(\mathbf{J})}$ where

$$Det(\mathbf{J}) = -(f'(\eta))^2 + \sigma\xi f''(\eta). \quad (3.71)$$

The stationary points of (3.70) are found by

$$\xi f'(\eta) = 0 \Rightarrow \xi = 0 \vee f'(\eta) = 0 \quad (3.72)$$

$$\mu - \sigma\xi - f(\eta) = 0. \quad (3.73)$$

For two dimensional autonomous Hamiltonian systems (3.12) the classification of a stationary point can be determined by the sign of the determinant of the Jacobian \mathbf{J} evaluated at the stationary point. The following holds, see Theorem 2.3:

$$\text{If } \text{Det}(\mathbf{J}) < 0 \text{ the stationary point is a saddle.} \quad (3.74)$$

$$\text{If } \text{Det}(\mathbf{J}) > 0 \text{ the stationary point is a center.}$$

For $\text{Det}(\mathbf{J}) = 0$ a bifurcation of the stationary point takes place. The bifurcations of stationary points that we consider here can take place either on the center axis or off, but in a vicinity of, the center axis. Below we will determine conditions needed for identifying parameter relations for the on and off axis bifurcations.

Bifurcations taking place on the center axis are found at $\xi = 0$ for $\lambda_{\pm} = 0$. Under these conditions we have from (3.71) and (3.73) that $f'(\eta) = 0$ together with $\mu - f(\eta) = 0$ must be fulfilled. It is seen from (3.70) that for $\xi = 0$ and $\mu \neq 0$ we have that $\eta \neq 0$ for stationary points to exist and

$$\mu - f(\eta) = 0, \quad f'(\eta) = 0 \quad (3.75)$$

must be solved for determining bifurcations on the center axis. It may be helpful, for $\eta \neq 0$, to consider $\eta f'(\eta) + (\mu - f(\eta)) = 0$. For $N \geq 2$ center axis bifurcations take place.

For bifurcations taking place off the center axis we have that $\xi \neq 0$ and from (3.72) we see that $f'(\eta) = 0$ and for $\lambda_{\pm} = 0$ (3.71) gives $\sigma\xi f''(\eta) = 0$ hence we have $f''(\eta) = 0$. So to determine off axis bifurcation points we need to consider the equations

$$\mu - f(\eta) = \sigma\xi, \quad f'(\eta) = 0 \quad \text{and} \quad f''(\eta) = 0. \quad (3.76)$$

For $N = 2$ the two latter conditions in (3.76) cannot be fulfilled which implies that no off axis bifurcations takes place, even though off axis stationary points do exists for $N = 2$. For $N \geq 3$ off axis bifurcations do occur.

As we will see in the following the relations (3.75) and (3.76) for the on and off axis bifurcations defines sets of bifurcations surfaces in parameter space (μ, c_1, \dots, c_N) . The surfaces acts as boundaries between different flow topologies.

The second order normal form

For order $N = 2$ we have the normal form

$$\dot{\xi} = \xi\eta, \quad \dot{\eta} = \mu - \sigma\xi - \frac{1}{2}\eta^2 \quad (3.77)$$

with $\sigma = \pm 1$ and we have two different bifurcation scenarios, each depending on the bifurcation parameter μ . An analysis of the existence of stagnation points as μ is varied reveals the bifurcation diagrams shown in figure 3.7. From (3.75) we see that a bifurcation on the center axis takes place at $\mu = 0$ and two center axis stationary points are formed at $\eta^2 = 2\mu$ thus exist for $\mu \geq 0$. As the center axis is invariant the formed stationary points on the center axis must consequently be

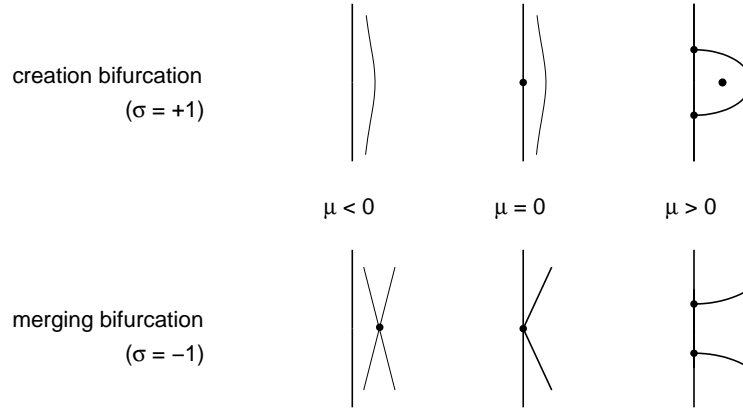


Figure 3.7: Bifurcation diagrams for the normal form (3.77). For $N = 2$ we have two possible bifurcation diagrams, both depending on the bifurcation parameter μ .

of the saddle type, this classification can also be deduced from (3.74). An off axis stationary point exists for $\eta = 0$ at $\sigma\xi = \mu$. Thus, as $\xi \geq 0$ in physical space, we have for the case $\sigma = +1$ an off axis stationary point situated at $\xi = \mu$ which exists only for $\mu \geq 0$ and is formed at the center axis for $\mu = 0$. Further (3.74) shows that the stationary point is a center. For $\sigma = -1$ the off axis stationary point is situated at $\xi = -\mu$ and exists only for $\mu \leq 0$. The stationary point is found to be a saddle.

We denote the bifurcation scenario for $\sigma = +1$ a creation bifurcation as recirculation zone is created. For $\sigma = -1$ we denote the scenario a merging bifurcation as the scenario can be understood as two recirculation zones merging in to one having inner structure.

The third order normal form

For order $N = 3$ the Axisymmetric Normal Form Theorem leads us to

$$\dot{\xi} = \xi(c_1 + \eta^2), \quad \dot{\eta} = \mu + \xi - c_1\eta - \frac{1}{3}\eta^3. \quad (3.78)$$

As N is odd we obtain only one bifurcation diagram which depends on the two bifurcation parameters μ and c_1 . Figure 3.8 shows the bifurcation diagram with codimension 1 bifurcation lines and a codimension 2 bifurcation point.

The bifurcations of stationary points on the center axis are found by using (3.75). The result is the two bifurcation lines given by $\mu^2 = -(4/9)c_1^3$ for $c_1 \leq 0$. Off axis bifurcations are determined using (3.76) and it is found that for $c_1 = 0$ with $\mu \leq 0$ a cusp bifurcation takes place. At a cusp bifurcation a center-saddle is formed. The center-saddle develops into a center and a saddle point as bifurcation parameters are varied. The saddle point has a homoclinic connection surrounding the center. The homoclinic connection is sometimes referred to as a loop.

The fourth order normal form

For order $N = 4$ we obtain the dynamical system

$$\dot{\xi} = \xi(c_1 + 2c_2\eta + \eta^3), \quad \dot{\eta} = \mu - \sigma\xi - c_1\eta - c_2\eta^2 - \frac{1}{4}\eta^4. \quad (3.79)$$

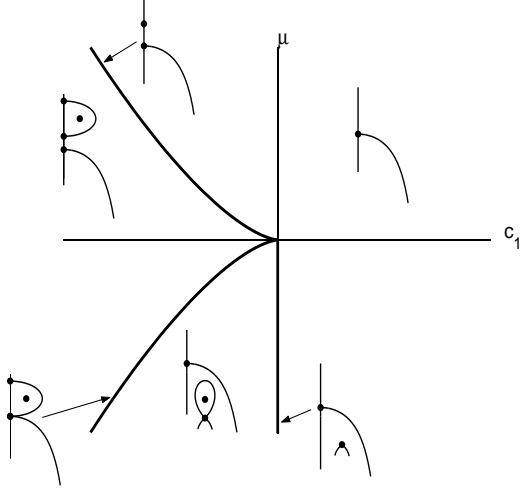


Figure 3.8: Bifurcation diagram for the normal form (3.78). In the figure we have shown the corresponding bifurcation lines and codimension 2 point in parameter space $(c_1, \mu) \in \mathbb{R}^2$.

As $N = 4$ is even $\sigma = \pm 1$. We consider the case of $\sigma = +1$. Bifurcations taking place on the center axis are again found by (3.75). It is helpful to consider $\eta f'(\eta) + (\mu - f(\eta)) = \frac{3}{4}\eta^4 + c_2\eta^2 + \mu = 0$ and instead of using the bifurcation parameter μ it is convenient to work with the discriminant $\lambda = c_2^2 - 3\mu$. The above quadratic equation has for $\lambda \geq 0$ the real solutions $\eta^2 = \frac{2}{3}(-c_2 \pm \sqrt{\lambda})$. Inserting these solutions into the condition $f'(\eta) = 0$ we get the relation $c_1^2 = (\frac{2}{3})^3(-c_2 \pm \sqrt{\lambda})(2c_2 \pm \sqrt{\lambda})^2$ which defines the surfaces in parameter space (c_1, c_2, λ) where center axis bifurcations occurs. No center axis bifurcations will take place for $\lambda < 0$.

Off axis bifurcations are determined again by (3.76). The two conditions $f'(\eta) = f''(\eta) = 0$ implies that at $c_1^2 = -4(\frac{2}{3}c_2)^3$ for $c_2 \leq 0$ and $\lambda \leq 0$ a cusp bifurcation takes place. The cusp bifurcation cannot take place for $\lambda > 0$. This can be seen from (3.76) by considering the quadratic equation $\eta f'(\eta) + (\mu - f(\eta)) = \frac{3}{4}\eta^4 + c_2\eta^2 + \mu = \xi \geq 0$ for $\eta \neq 0$. The inequality must hold implying that the top point $T = (\frac{-3c_2}{2}, \frac{-\lambda}{3})$ of the convex parabola must be situated in the first respectively second quadrant hence $\lambda \leq 0$.

The parameter space (c_1, c_2, λ) for the normal form (3.79) is three dimensional. In figure 3.9 we have, based on the above parameter relations, shown the codimension 1 bifurcation surfaces, codimension 2 bifurcation lines and as it turns out a codimension 3 bifurcation point at $c_1 = c_2 = \lambda = 0$. Figure 3.9 shows us how a recirculation zone with inner structure is formed. When traversing the parameter space a recirculation zone is first developed through a creation bifurcation by crossing the green paraboloid-like shaped surface. Then if $\lambda > 0$ a second recirculation zone is created by crossing the green surfaces acting as wings of the paraboloid-like shaped surface. These two recirculation zones can then merge to form a recirculation zone with inner structure when crossing the blue surface constituting a merging bifurcation. On the other hand an existing recirculation zone can for $\lambda < 0$ develop directly into a recirculation zone with inner structure when crossing the red cusp bifurcation surface. In section 3.3.8 numerically obtained bifurcation diagrams will comply with this color coding with the one exception that the creation bifurcation forming the first recirculation zone will be colored black.

There is another diagram for $\sigma = -1$, but as we do not find the streamline topologies for this case in the numerical simulations it is omitted here.

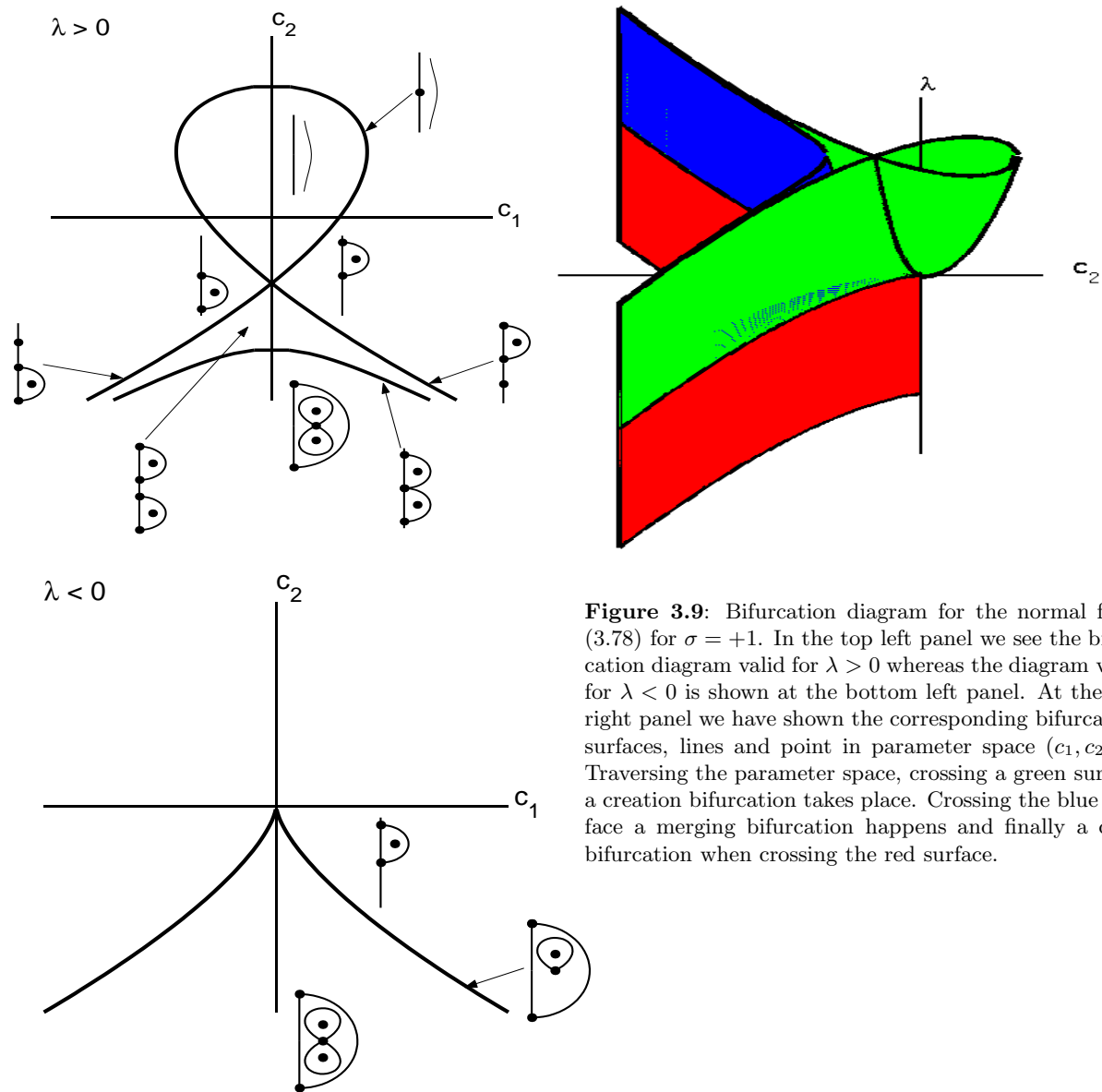


Figure 3.9: Bifurcation diagram for the normal form (3.78) for $\sigma = +1$. In the top left panel we see the bifurcation diagram valid for $\lambda > 0$ whereas the diagram valid for $\lambda < 0$ is shown at the bottom left panel. At the top right panel we have shown the corresponding bifurcation surfaces, lines and point in parameter space (c_1, c_2, λ) . Traversing the parameter space, crossing a green surface a creation bifurcation takes place. Crossing the blue surface a merging bifurcation happens and finally a cusp bifurcation when crossing the red surface.

3.2.6 The non-simple degenerate axisymmetric normal form

In the sections 3.2.1 to 3.2.5 we analysed the normal form for (3.14) in the case where $\epsilon_{1,0} = \psi_{1,0}$ and $\epsilon_{1,1} = \psi_{1,1}$ are considered small parameters while keeping $\psi_{2,0}$ a non-zero constant. Here we consider the case where $\epsilon_{1,0} = \psi_{1,0}$, $\epsilon_{1,1} = \psi_{1,1}$ and $\epsilon_{2,0} = \psi_{2,0}$ all are regarded as small parameters and analyse the corresponding normal form to third order. With the small parameters the streamfunction reads

$$\psi(\rho, z) = \rho (\epsilon_{1,0} + \epsilon_{2,0}\rho + \epsilon_{1,1}z + \psi_{3,0}\rho^2 + \psi_{2,1}\rho z + \psi_{1,2}z^2) + O(|\rho, z|^4). \quad (3.80)$$

Assuming that $\psi_{1,2} \neq 0$ and introducing a translation along the center axis and a linear transformation by

$$\begin{pmatrix} \rho \\ z \end{pmatrix} = - \begin{pmatrix} 0 \\ \frac{\epsilon}{2\psi_{1,2}} \end{pmatrix} + \begin{bmatrix} 1 & 0 \\ -\frac{\psi_{2,1}}{2\psi_{1,2}} & 1 \end{bmatrix} \begin{pmatrix} \xi \\ \eta \end{pmatrix} \quad (3.81)$$

brings (3.82) into

$$\psi(\xi, \eta) = \xi (\bar{\epsilon}_{1,0} + \bar{\epsilon}_{2,0}\xi + \bar{\psi}_{3,0}\xi^2 + \psi_{1,2}\eta^2) + O(|\xi, \eta|^4) \quad (3.82)$$

where

$$\bar{\epsilon}_{1,0} = \left(\epsilon_{1,0} - \frac{\epsilon_{1,1}^2}{4\psi_{1,2}} \right), \quad \bar{\epsilon}_{2,0} = \left(\epsilon_{2,0} - \frac{\epsilon_{1,1}\psi_{2,1}}{\psi_{1,2}} \right), \quad \bar{\psi}_{3,0} = \left(\psi_{3,0} - \frac{\psi_{2,1}^2}{1\psi_{1,2}} \right).$$

Further assuming that $\bar{\psi}_{3,0} \neq 0$ allows us to introduce the scaling

$$\eta \rightarrow \left(\sqrt{\left| \frac{\bar{\psi}_{3,0}}{\psi_{1,2}} \right|} \right) \eta \quad (3.83)$$

into (3.82) and finally dividing by $\bar{\psi}_{3,0}$ we arrive at the normal form

$$\psi(\xi, \eta) = \xi (c_1 + c_2\xi + \xi^2 + \sigma\eta^2) + O(|\xi, \eta|^4) \quad (3.84)$$

where c_1 and c_2 are transformed small parameters and

$$\sigma = \begin{cases} +1 & \text{for } \bar{\psi}_{3,0}/\psi_{1,2} > 0 \\ -1 & \text{for } \bar{\psi}_{3,0}/\psi_{1,2} < 0 \end{cases} \quad (3.85)$$

which stem from the scaling (3.83). The normal form (3.84) leads to the dynamical system

$$\dot{\xi} = 2\sigma\xi\eta, \quad \dot{\eta} = -c_1 - 2c_2\xi - 3\xi^2 - \sigma\eta \quad (3.86)$$

truncated at third order. The systems has the Jacobian \mathbf{J} with determinant $Det(\mathbf{J})$ given by

$$\mathbf{J} = \begin{bmatrix} 2\sigma\eta & 2\sigma\xi \\ -c_2 - 6\xi & -2\sigma\eta \end{bmatrix} \quad \text{and} \quad Det(\mathbf{J}) = 4\sigma(c_2 + 3\xi) - 4\eta^2. \quad (3.87)$$

In the case $c_1 = c_2 = 0$ the dynamical system (3.86) has a stagnation point at the origin with a vanishing Jacobian thus the stagnation point is non-simple degenerated. The separatrices for the stagnation point are found by setting $\phi(\xi, \eta) = 0$ for $c_1 = c_2 = 0$ in (3.84). It is found that

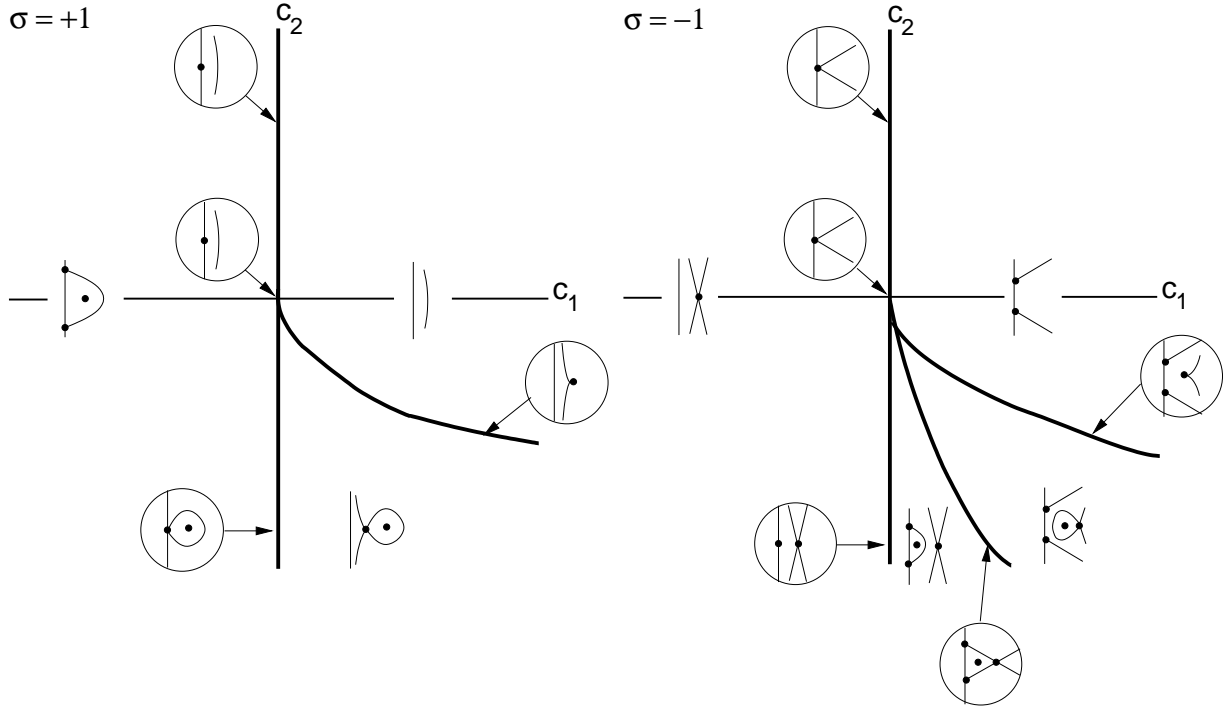


Figure 3.10: Bifurcation diagram for the normal form (3.84).

for $\sigma = +1$ the stagnation point has no separatrices except from the center axis. For $\sigma = -1$ the stagnation point has besides the center axis the two separatrices $\eta = \pm\xi + O(\xi^2)$, see figure 3.10 for $\sigma = \pm 1$ and $c_1 = c_2 = 0$.

For $c_2 \neq 0$ stagnation points on the center axis are found from (3.86) for $\xi = 0$ thus

$$-c_1 - \sigma\eta^2 = 0 \quad (3.88)$$

must be fulfilled. It is seen that for $\sigma = -1$ two stagnation points exist for $c_1 > 0$ and for $\sigma = +1$ two stagnation points exist for $c_1 < 0$ on the center axis. As $\text{Det}(\mathbf{J}) = 0$ in the origin it follows from (3.88) that the stagnation points bifurcate at $c_1 = 0$.

In-flow stagnation points are found from (3.86) for $\xi \neq 0$ and it follows that

$$\eta = 0 \quad \text{and} \quad 3\xi^2 + 2c_2\xi + c_1 = 0 \quad (3.89)$$

must be satisfied. Solving (3.89) for in-flow stagnation points it follows that only one stagnation point exists for $c_1 < 0$. Two in-flow stagnation points exist for $c_2 < -\sqrt{3c_1}$ with $c_1 > 0$. Stagnation points are either formed on the center axis for $c_1 = 0$ and moves in-flow for $c_1 \neq 0$ or in-flow in a cusp bifurcation at $c_2 = -\sqrt{3c_1}$ with $c_1 > 0$ where both (3.89) and $\text{Det}(\mathbf{J}) = 0$ are fulfilled.

The type of the stagnation points in the various parts of parameter space (c_1, c_2) are found by virtue of (3.74) and (3.87) and are shown in the bifurcation diagrams of figure 3.10.

In the case of $\sigma = -1$ for $c_2 < -\sqrt{3c_1}$ and $c_1 > 0$ four stagnation points exist; two saddle points on the center axis, one in-flow center and one in-flow saddle point, see right panel of figure 3.10. This constellation of stagnation points gives at least the possibility of two topologies. Either a recirculation zone exists together with an in-flow saddle point or an in-flow homoclinic loop exists

together with two separatrices emanating from the center axis. A global bifurcation involving heteroclinic connections between the saddle points separates the two topologies. The global bifurcation curve is determined by using the fact that due to the heteroclinic connections the value of the streamfunction at the in-flow saddle point is the same as the value of the streamfunction on the center axis i.e. (3.89) together with

$$\psi(\xi, \eta) = \xi(c_1 + c_2\xi + \xi^2) = 0 \quad (3.90)$$

must be satisfied simultaneously. By solving (3.89) and (3.90) discarding the solution $\xi = 0$ and $c_1 = 0$ it is found that the global bifurcation takes place at $c_2 = -2\sqrt{c_1}$ for $c_1 > 0$.

The bifurcation diagrams in figure 3.10 show that a recirculation zone can be formed not only by the bifurcation of a stagnation point on the center axis but also as a result of a global bifurcation where an in-flow loop interacts with center axis separatrices or as a result of an in-flow loop attaching directly to the center axis. The latter case has been observed in numerical simulations, see section 3.3.6.

3.2.7 Brief on bifurcations taking place in a corner

Later in section 3.3.7 we will see that in the top left corner formed by the lid and the center axis a saddle point can cross from the lid and onto the center axis. To understand this we can again consider the flow close to a wall as we did in section 2.6. The flow close to the corner of the meridional plane has to both satisfy the no-slip and no-flux condition at the lid and the boundary condition (3.11) at the axis. Expanding the streamfunction to third order and imposing the boundary conditions it can be shown that the system

$$\dot{\rho} = \rho(2a_{1,2} + 2a_{2,2}\rho + 3a_{1,3}z), \quad \dot{z} = -z(a_{1,2} + 2a_{2,2}\rho + a_{1,3}z) \quad (3.91)$$

describes the streamline topology. In (3.91) the corner is taken to be the origin and the streamline topology that we are interested in appear for $\rho \geq 0$ and $z \leq 0$.

If $a_{1,2} \neq 0$ the corner is a generic saddle point. If on the other hand $a_{1,2} = 0$ the corner is a degenerate stagnation point. In this case we consider $\epsilon_{1,2} = a_{1,2}$ a small parameter and assume $a_{2,2} \neq 0$ and $a_{1,3} \neq 0$ in (3.91). With this it is seen that the corner is always a stagnation point. A stagnation point on the center axis is found for $\rho = 0$ and $z = -\epsilon_{1,2}/a_{1,3}$. A stagnation point on the lid is found for $z = 0$ and $\rho = -\epsilon_{1,2}/a_{2,2}$. An in-flow stagnation point is found for

$$\rho = -\frac{\epsilon_{1,2}}{3a_{2,2}}, \quad z = -\frac{\epsilon_{1,2}}{3a_{1,3}}.$$

The bifurcation diagrams for this codimension 1 scenario is shown in figure 3.11. For $a_{1,3} > 0$ and $a_{2,2} > 0$ a saddle crosses the corner while for $a_{1,3} > 0$ and $a_{2,2} < 0$ a corner recirculation zone is created. If $a_{1,3} < 0$ the same two scenarios repeat but for the reverse order of $\epsilon_{1,2}$.

If one or both of $a_{2,2}$ and $a_{1,3}$ becomes zero higher order terms becomes decisive in (3.91) and a normal form simplification is required.

A topological equivalent bifurcation scenario has been reported by Brøns, Voigt, and Sørensen (2001) for the fluid filled cylinder with a free surface and a rotating bottom.

3.2.8 Bifurcation conditions in terms of the velocity field

In section 3.2.5 we analyzed the first few orders of the normal form (3.16) and presented the bifurcation diagrams. In this section we will first, based on the diagrams deduce degeneracy

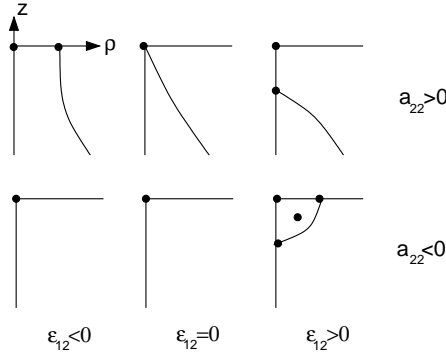


Figure 3.11: Bifurcation diagram for (3.91) for $a_{1,3} > 0$ and where $\epsilon_{1,2} = a_{1,2}$ is a small parameter.

conditions using the normal form axial velocity component. The degeneracy conditions are satisfied when the creation and merging bifurcations take place. Then we will reformulate the conditions in the physical axial velocity field component and derivatives thereof. The conditions will be used in section 3.3 to guide us in locating and interpreting the various bifurcations found in connection with numerical simulations.

To not confuse the physical velocity component $w(\rho, z)$ with the normal form velocity component $w(\xi, \eta)$ we introduce a tilde-notation $w(\xi, \eta) = \tilde{w}(\xi, \eta)$.

The normal form velocity component $\tilde{w}(\xi, \eta)$ is given as

$$\tilde{w}(\xi, \eta) = \dot{\eta} = \mu - \sigma\xi - f(\eta), \quad (3.92)$$

see (3.18). The derivation of the degeneracy conditions involves differentiating and evaluating $\tilde{w}(\rho, \eta)$ and partial derivatives thereof at the origin $(\rho, \eta) = (0, 0)$.

Based on this the conditions are formulated in the physical velocity component $w(\rho, z)$ by using the previously derived algebraic relations for the dependence of the normal form parameters on the Taylor coefficients of the streamfunction. The physical velocity component $w(\rho, z)$ is given as

$$\begin{aligned} w(\rho, z) = \dot{z} = & -\epsilon_{1,0} - 2a_{2,0}\rho - \epsilon_{1,1}z - 3a_{3,0}\rho^2 - 2a_{2,1}\rho z - a_{1,2}z^2 \\ & - 4a_{4,0}\rho^3 - 3a_{3,1}\rho^2 z - 2a_{2,2}\rho z^2 - a_{1,3}z^3 + O(|(\rho, z)|^4), \end{aligned} \quad (3.93)$$

see (3.14).

For the second order normal form (3.77) at $\xi = 0$ we get

$$\tilde{w}(0, \eta) = \mu - \frac{1}{2}\eta^2, \quad \tilde{w}_\eta(0, \eta) = -\eta, \quad \tilde{w}_{\eta\eta}(0, \eta) = -1.$$

For $\eta = 0$ we have that $\tilde{w}(0, 0) = \mu$, $\tilde{w}_\eta(0, 0) = 0$ and $\tilde{w}_{\eta\eta}(0, 0) \neq 0$. From the bifurcation diagram 3.7 we can deduce that the creation or merging bifurcation takes place for $\mu = 0$ at $(\xi, \eta) = (0, 0)$ and we have the codimension 1 condition $\tilde{w}(0, 0) = 0$, $\tilde{w}_\eta(0, 0) = 0$ with $\tilde{w}_{\eta\eta}(0, 0) \neq 0$. As the near identity transformation maps the origin in normal form variables (ξ, η) to the origin in physical variables (ρ, z) and as the creation and merging bifurcations takes place for $(\xi, \eta) = (0, 0)$ at $\mu = 0$ implies that the bifurcations in physical variables takes place at $(\rho, z) = (0, 0)$ for $\mu = 0$. From (3.93) we see that $w(0, 0) = -\epsilon_{1,0}$, $w_z(0, 0) = -\epsilon_{1,1}$ and $w(0, 0) = -2a_{1,2} \neq 0$. Hence $\epsilon_{1,0} = 0$ and $\epsilon_{1,1} = 0$ fulfills the condition $\mu = 0$ in (3.62) and we have the codimension 1 condition in the

physical axial velocity component

$$\text{Codim. 1 condition: } w(0,0) = w_z(0,0) = 0, \quad w_{zz}(0,0) \neq 0. \quad (3.94)$$

For the third order normal form (3.78) at $\xi = 0$ we get

$$\tilde{w}(0,\eta) = \mu - c_1\eta - \frac{1}{3}\eta^3, \quad \tilde{w}_\eta(0,\eta) = -c_1 - \eta^2, \quad \tilde{w}_{\eta\eta}(0,\eta) = -2\eta, \quad \tilde{w}_{\eta\eta\eta}(0,\eta) = -2. \quad (3.95)$$

Setting $\eta = 0$ we obtain $\tilde{w}(0,0) = \mu$, $\tilde{w}_\eta(0,0) = -c_1$, $\tilde{w}_{\eta\eta}(0,0) = 0$ and $\tilde{w}_{\eta\eta\eta} \neq 0$. From the bifurcation diagram in figure 3.8 we see that a codimension 2 bifurcation happens for $c_1 = \mu = 0$. Inserting this in (3.95) we have the condition for the codimension 2 bifurcation $\tilde{w}(0,0) = 0$, $\tilde{w}_\eta(0,0) = 0$, $\tilde{w}_{\eta\eta}(0,0) = 0$ and $\tilde{w}_{\eta\eta\eta}(0,0) \neq 0$ for the normal form velocity component. By inspection we notice that the conditions $\mu = 0$ and $c_1 = 0$ on the normal form parameters are fulfilled for the algebraic relations (3.68) and (3.69) using (3.64) and (3.65) for $\epsilon_{1,0} = 0$, $\epsilon_{1,1} = 0$ and $a_{1,2} = 0$. From (3.93) we see that $w(0,0) = -\epsilon_{1,0}$, $w_{zz}(0,0) = -\epsilon_{1,1}$, $w_{zzz}(0,0) = -2a_{1,2}$ and $w_{zzzz}(0,0) = -6a_{1,3}$. With the non-degeneracy condition $a_{1,3} \neq 0$ we have the codimension 2 condition formulated for the physical axial velocity component

$$\text{Codim. 2 condition: } w(0,0) = w_z(0,0) = w_{zz}(0,0) = 0 \text{ and } w_{zzz}(0,0) \neq 0. \quad (3.96)$$

We now have local conditions formulated in terms of the physical velocity component w for the creation and merging bifurcations that the previous bifurcation analysis shows we will encounter on the center axis.

Before closing this section we will make a remark on the cusp bifurcation. It seems tempting to set up a condition like above for the cusp bifurcation. From the bifurcation diagram in figure 3.8 we see that the cusp bifurcation occurs at $c_1 = 0$ for $\mu < 0$ and a condition for the normal form velocity field would be $\tilde{w}(0,0) = \mu \neq 0$, $\tilde{w}_\eta(0,0) = 0$, $\tilde{w}_{\eta\eta}(0,0) = 0$ and $\tilde{w}_{\eta\eta\eta}(0,0) \neq 0$. The condition do holds true but as it turns out only in a small neighborhood of the codimension 2 point in parameter space. The condition cannot be used to determine the cusp bifurcation curve when considering a part of parameter space away from the codimension 2 point. The reason is that the cusp condition written above is only valid in a neighborhood of the center axis. Contrary to the other types of bifurcations we consider, the cusp bifurcation takes place not only at the center axis but also in-flow in the meridional plane. In section 3.3.5 we show how to determine the cusp bifurcation.

3.3 Bifurcation diagrams based on numerical investigations

The purpose of this section is to construct a series of bifurcation diagrams showing in parameter space the regions where one recirculation zone, two recirculation zones or a recirculation zone with inner structure exist. The bifurcation diagrams are based on direct numerical simulations solving the equations (3.5). A post process procedure is developed for extracting the necessary data from the simulations needed for the bifurcation diagrams. The section ends with an explanation of the scenario observed in the bifurcation diagrams. First we comment on the computational code.

3.3.1 Brief on the computational code

The axisymmetric streamfunction-vorticity-circulation formulation (3.5) has been implemented in the dynamic simulation code *czax* by Sørensen and Loc (1989). The implementation solves for among other entities ω , Γ , ψ as well as the radial and axial velocity components u and w in the computational domain $r \in [0; 1]$ and $z \in [0; h]$ on a time interval $t \in [t_0; t_N]$. The equations (3.5) are solved using the finite difference method with an equidistantly discretized domain and time interval. The discretized time steps are given as $t_{n+1} = t_n + \Delta t$ for $n = 0, \dots, N-1$ with a chosen time increment of $\Delta t = 0.05$. We have chosen to use a finite difference domain grid of a fixed resolution $(\Delta r, \Delta z) = (0.01, 0.01)$ implying a fixed number of $1/\Delta r = 100$ discrete grid points in the radial direction and a number of $h/\Delta z$ grid points in the axial direction varying with the choice of h . Hence when conducting the simulations we must choose h such that the ratio $h/\Delta z$ is an integer number. This has not caused any limitations in constructing the bifurcation diagrams. The choice of the grid resolution is based on earlier work conducted by Sørensen and Loc (1989), Sørensen and Christensen (1995) and Westergaard, Buchhave, and Sørensen (1993), where direct numerical simulations using *czax* have been validated against experimental results. The above three studies were concentrating on the case $h = 2.0$ and $\gamma = 0$ and the conclusions were that to within experimental accuracy a grid resolution of $(\Delta r, \Delta z) = (0.01, 0.01)$ were sufficient. This result was further confirmed in Brøns, Voigt, and Sørensen (1999).

In *czax* the two transport equations in (3.5) are discretized using second order central differences which are then solved by using the alternating direction implicit method (ADI), see for instance Press et al. (1993). The Poisson equation in (3.5) is discretized using fourth order finite differences, see Sørensen and Loc (1989). The solution procedure in *czax* starts with providing initial conditions for ω , Γ , ψ , u and w at time t_s . The initial conditions can be results obtained from an earlier simulation. In each time step t_n for $n = 1, \dots, N-1$ the entities ω , Γ , ψ , u and w are updated. First the transport equations are solved for the circulation Γ and vorticity ω . Using the new updated vorticity ω the Poisson equation is next solved for the streamfunction ψ by iteration. When having the updated streamfunction ψ new values of the velocity field can be found from (3.4). Having all the updated values the procedure continues with the next time step t_{n+1} until $n = N-1$.

To investigate whether a simulation is converging towards a steady state we consider the time series $\psi(t)$ at the grid point with index $(i, j) = (50, 50)$ which in the flow domain corresponds to $(r, z) = (0.5, 0.5h)$. In the grid point we calculate the time series $\Delta\psi = \psi(t) - \psi(t_N)$. When $|\Delta\psi| \leq 0.5 \cdot 10^{-5}$ for the latest oscillation of $\Delta\psi$ we consider a simulation converged. In this study all simulations are run in the time interval from $t_0 = 0$ to $t_N = 800$. In this time interval the convergence is fulfilled for all simulations on the boundary of the part of parameter space for $Re \in [800; 2400]$, $h \in [1.0; 3.0]$ and for the γ -values that we consider. Figure 3.12 shows an example of a converged simulation. In the right panel is seen the time series $\psi(t)$ and in the left panel $\Delta\psi(t)$.

With *czax* we have access to a numerical solution of the axial velocity component $w(0, z)$ at the center axis $z \in [0; h]$ for a given set of parameter values Re , h and γ . To apply the codimension 1 condition (3.94) we need to calculate the first and second order partial derivatives of the numerical solution of w at the center axis. This is done by using the second order finite differences, see Barker (1997),

$$\left(\frac{\partial w}{\partial z}\right)_{i,j} \simeq \frac{1}{2\Delta z}(w_{i+1,j} - w_{i-1,j}) \quad \text{and} \quad \left(\frac{\partial^2 w}{\partial z^2}\right)_{i,j} \simeq \frac{1}{\Delta z^2}(w_{i+1,j} - 2w_{i,j} + w_{i-1,j}).$$

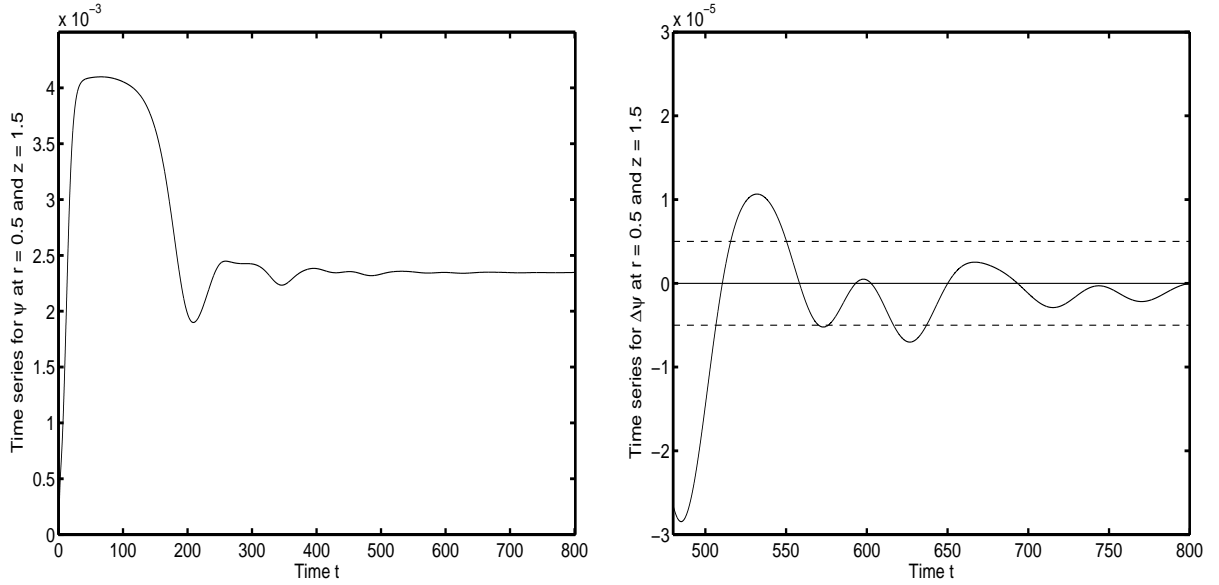


Figure 3.12: Convergence of the simulation for $Re = 2400$, $h = 3.0$ and $\gamma = 0.03$. In the left panel is seen the time series $\psi(t)$ and in the right panel is seen the time series $\Delta\psi(t) = \psi(t) - \psi(800)$. The time series are for the grid point $(r, z) = (0.5, 1.5)$. It is seen that for the last period of $\Delta\psi$ we have $|\Delta\psi| \leq 0.5 \cdot 10^{-5}$.

3.3.2 The creation and merging of recirculation zones

Here we show examples of numerical obtained streamline patterns in the meridional plane where one recirculation zone, two recirculation zones or a recirculation zone having inner structure exist. The examples illustrate how they are formed via the creation or merging bifurcation. Furthermore the examples illustrate how the codimension 1 condition (3.94) is satisfied at a bifurcation point. The particular Reynolds number at which the creation or merging bifurcation takes place is determined by a procedure which we will develop in section 3.3.4.

Formation of one recirculation zone

We start out by conducting a series of simulations where we vary the Reynolds number discretely in the interval $Re \in [1450; 1515]$ for fixed parameter values of $h = 2.2$ and $\gamma = 0.03$. The results of the simulations are shown in figure 3.13. In the top panels we show level curves for the streamfunction $\psi(r, z)$. To the left is shown a simulation for $Re = 1490$ and to the right for $Re = 1515$. In the panels the z -axis is depicted vertically and the r -axis is shown horizontally. This orientation agrees with the coordinate system for the experimental cylinder set-up. We see that in the top left panel in figure 3.13 no recirculation zone exists whereas in the panel to the right a recirculation zone has developed on the center axis. The recirculation zone is characterized by a heteroclinic connection between two stagnation points situated on the center axis and further the heteroclinic connection surrounds a center. We conclude that for a Reynolds number between $Re = 1490$ and $Re = 1515$ a creation bifurcation takes place.

To pin point the Reynolds number at which the bifurcation takes place we apply the codimension 1 condition (3.94) and consider the axial velocity component $w(0, z)$ and derivatives thereof. The two middle row panels of figure 3.13 show the plots of the axial velocity component at the center axis.

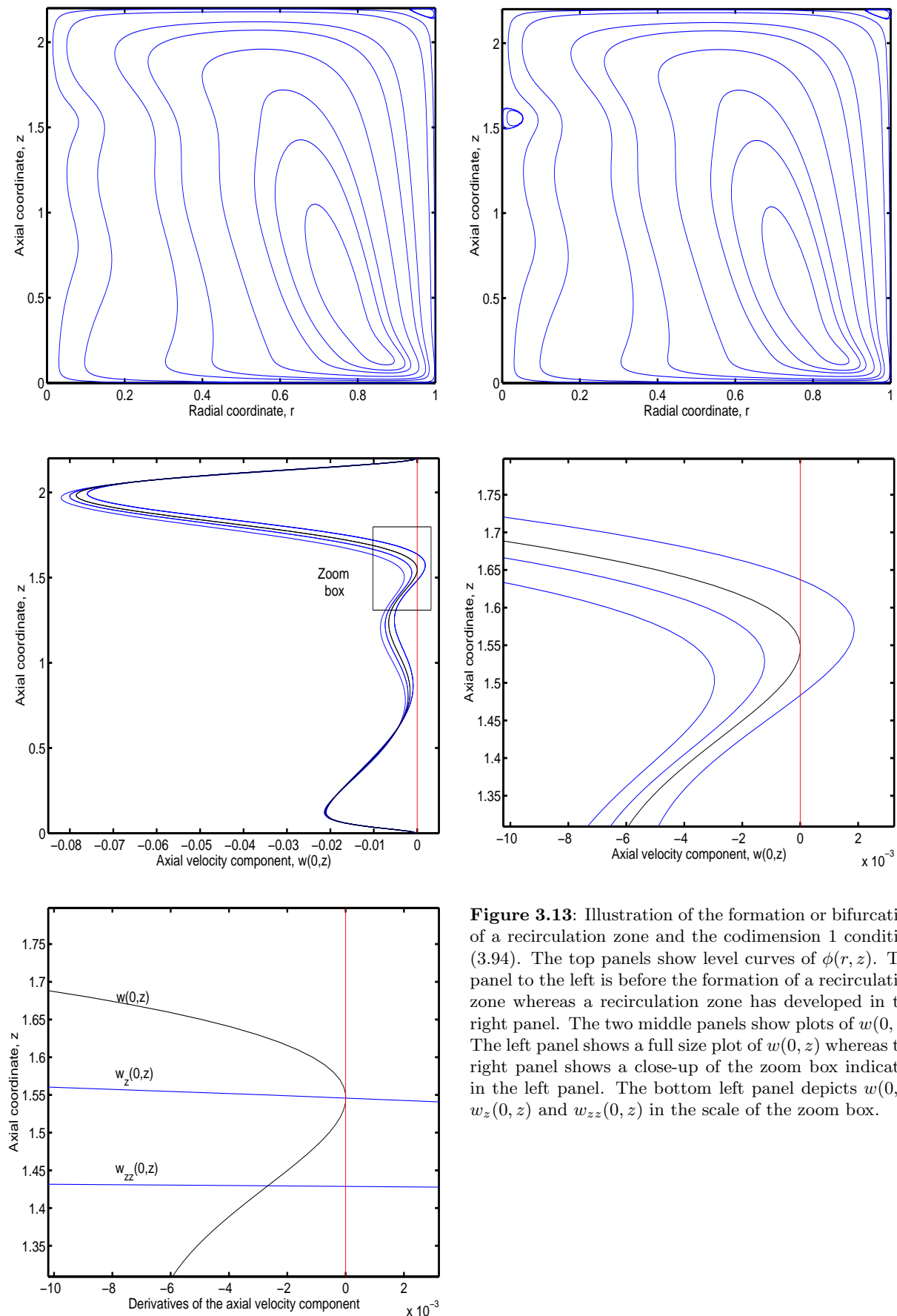


Figure 3.13: Illustration of the formation or bifurcation of a recirculation zone and the codimension 1 condition (3.94). The top panels show level curves of $\phi(r, z)$. The panel to the left is before the formation of a recirculation zone whereas a recirculation zone has developed in the right panel. The two middle panels show plots of $w(0, z)$. The left panel shows a full size plot of $w(0, z)$ whereas the right panel shows a close-up of the zoom box indicated in the left panel. The bottom left panel depicts $w(0, z)$, $w_z(0, z)$ and $w_{zz}(0, z)$ in the scale of the zoom box.

Again the z -axis is depicted vertically and the axial velocity component $w(0, z)$ is therefore plotted horizontally. This is to comply with the above chosen orientation of the coordinate system for the streamfunction. The middle right panel in figure 3.13 is an enlargement of the zoom box indicated in the middle left panel. The blue curves given from left to right are simulations for $Re = 1450, 1475$ and 1500 . In the panel to the left we see that the axial velocity component $w(0, z)$ has five extrema. The zoom box shows how, counted from below in the interval $z \in [0; h]$, the value of the fourth local extremum of $w(0, z)$ develops from being negative to becoming positive. The black curve shows the case at which $w(0, z_{OB}) = 0$ at $z_{OB} = 1.546$, which happens for $Re_{OB} = 1494.05$. The bottom left panel shows the axial velocity $w(0, z)$ together with the derivatives $w_z(0, z)$ and $w_{zz}(0, z)$ for the case of $Re_{OB} = 1494.05$ and we see that the codimension 1 condition (3.94) is fulfilled at $z_{OB} = 1.546$, that is we see that $w(0, z_{OB}) = 0$ and $w_z(0, z_{OB}) = 0$ whereas $w_{zz}(0, z_{OB}) \neq 0$. The numerically observed creation bifurcation is topologically equivalent to the creation bifurcation in figure 3.7 for the normal form (3.77).

Formation of yet a recirculation zone

We continue to consider $h = 2.2$ and $\gamma = 0.03$ and increase the Reynolds number interval to $Re = [1525; 1625]$. Simulations depicted in the two top panels of figure 3.14 show that a second recirculation zone has been formed on the center axis below the first recirculation zone. Locally the formation of the second recirculation zone is topologically equivalent to the formation of the first recirculation zone and takes place via the creation bifurcation. To locate the creation bifurcation for the second recirculation zone we again monitor in the two middle panels of figure 3.14, when a local extreme of $w(0, z)$ changes sign from being negative to becoming positive. The three curves are for the cases of $Re = 1525, 1569.4$ and 1625 from left to right. The panel to the right is a close-up of the left panel zoom box. We see that the fourth extreme of $w(0, z)$, which changed sign at the formation of the first bubble, stays positive whereas the second extreme counted from below in the interval $z \in [0; h]$ changes sign and becomes positive. Further we see in the right middle panel that the second extreme for the black curve for the case of $Re = 1569.4$, is zero at $z_{TB} = 0.914$. Hence the creation bifurcation forming the second recirculation zone takes place for $Re_{TB} = 1569.4$. In the bottom left panel in figure 3.14 we have for $Re_{TB} = 1569.4$ shown the axial velocity component $w(0, z)$ together with the derivatives $w_z(0, z)$ and $w_{zz}(0, z)$. We see that $w(0, z_{TB}) = 0$ and $w_z(0, z_{TB}) = 0$ but $w_{zz}(0, z_{TB}) \neq 0$ showing that the codimension 1 condition (3.94) is fulfilled in a neighborhood of $z_{TB} = 0.914$.

Formation of a recirculation zone having inner structure

If we further increase the Reynolds number and consider $Re = [1625; 1700]$ still with $h = 2.2$ and $\gamma = 0.03$ the two recirculation zones we discovered above merge together into one recirculation zone with inner structure as seen for $Re = 1700$ in the top right panel in figure 3.15.

The inner structure recirculation zone is a heteroclinic connection between two stagnation points situated on the center axis containing two centers and a saddle point. The saddle point is located in the middle between the two centers such that there is one center in the upper part and an another center at the lower part of the inner structure. The two separatrices of the saddle are homoclinic connections each surrounding a center.

This numerically observed merging bifurcation is topologically equivalent to the merging bifurcation for the normal form (3.77) with the topology shown in figure 3.7.

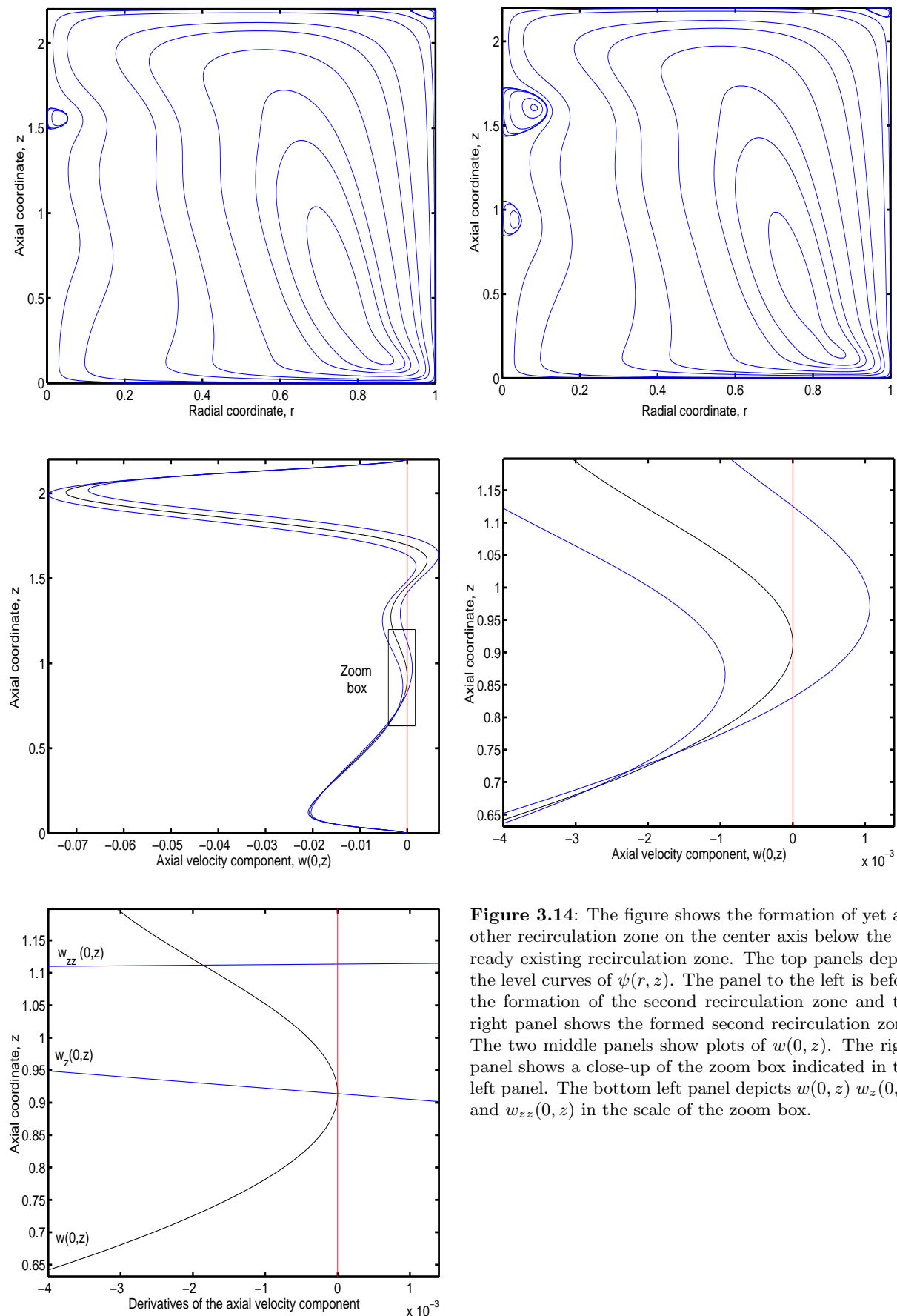


Figure 3.14: The figure shows the formation of yet another recirculation zone on the center axis below the already existing recirculation zone. The top panels depict the level curves of $\psi(r, z)$. The panel to the left is before the formation of the second recirculation zone and the right panel shows the formed second recirculation zone. The two middle panels show plots of $w(0, z)$. The right panel shows a close-up of the zoom box indicated in the left panel. The bottom left panel depicts $w(0, z)$, $w_z(0, z)$ and $w_{zz}(0, z)$ in the scale of the zoom box.

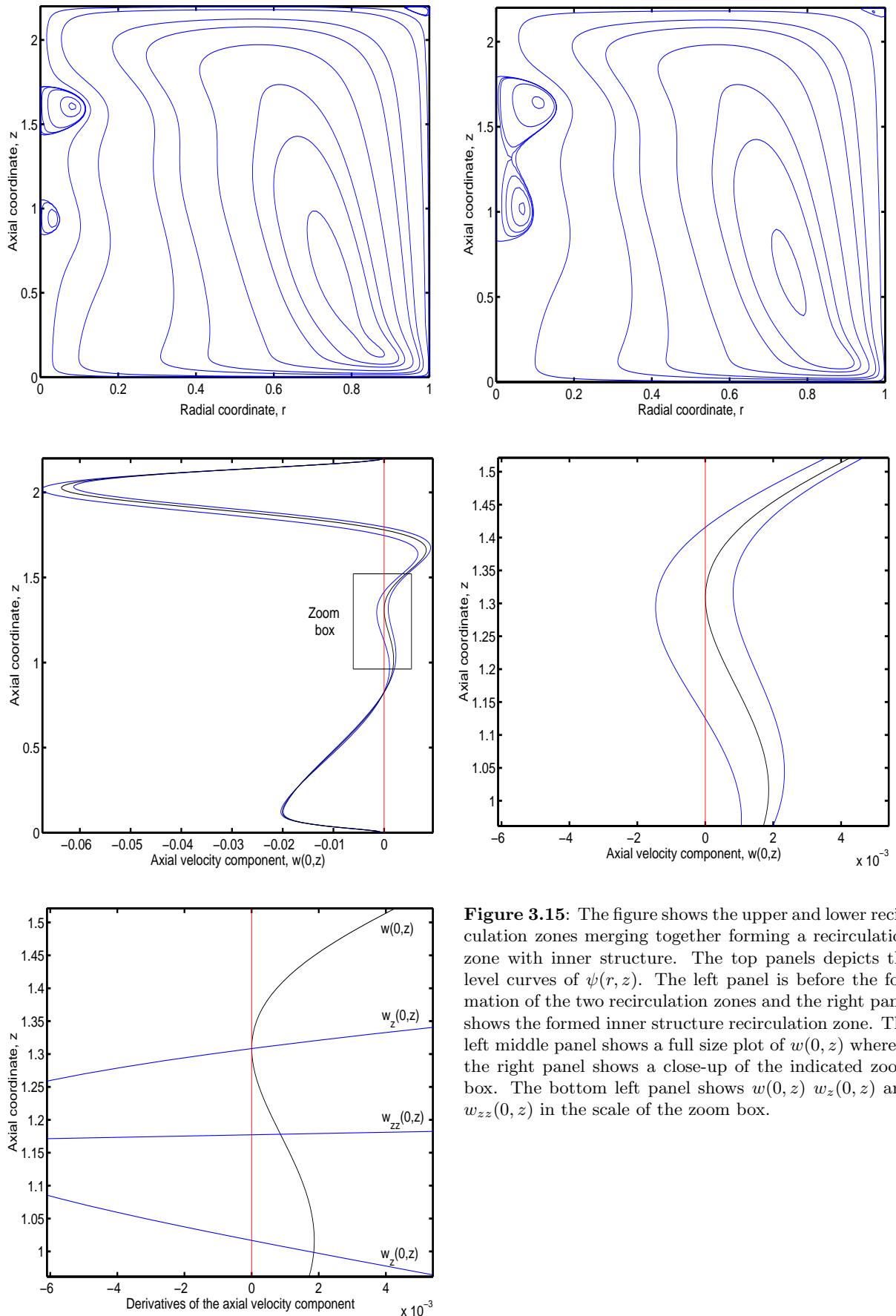


Figure 3.15: The figure shows the upper and lower recirculation zones merging together forming a recirculation zone with inner structure. The top panels depicts the level curves of $\psi(r, z)$. The left panel is before the formation of the two recirculation zones and the right panel shows the formed inner structure recirculation zone. The left middle panel shows a full size plot of $w(0, z)$ whereas the right panel shows a close-up of the indicated zoom box. The bottom left panel shows $w(0, z)$, $w_z(0, z)$ and $w_{zz}(0, z)$ in the scale of the zoom box.

To locate the merging bifurcation forming the inner structure we again consider the axial velocity component $w(0, z)$ shown in the middle panels of figure 3.15. The right panel is a close-up of the zoom box in the left middle panel. We notice that the second and fourth extreme of $w(0, z)$ stays positive in $Re = [1625; 1700]$ whereas the third extreme now changes sign from being negative to becoming positive. The third extreme is zero for $Re_{IS} = 1671.16$ which corresponds to the black curve in the middle panels of figure 3.15. Hence the merging bifurcation takes place for $Re_{IS} = 1671.16$ at $z_{IS} = 1.308$. The bottom left panel in figure 3.15 shows the axial velocity component together with the first and second derivatives thereof. In the panel we see that at $z_{IS} = 1.308$ we have that $w(0, z_{IS}) = 0$ and $w_z(0, z_{IS}) = 0$ whereas $w_{zz}(0, z_{IS}) \neq 0$ and the codimension 1 condition (3.94) is hereby fulfilled.

We have now seen how recirculation zones are formed by the creation or merging bifurcation. In section 3.3.3 and 3.3.4 we consider how to compute the curves in parameter space for these bifurcations.

3.3.3 The post process method

Here we present a method to find bifurcations of stagnation points in two dimensional flows, based on the concept of 0- and ∞ -isoclines. The method requires that the velocity field (u, w) given as function of system parameters is known either analytically or numerically. The 0- and ∞ -isoclines are curves in phase space here the meridional plane for the dynamical system (3.4). The ∞ -isocline is the set of points (ρ_∞, z_∞) where $u(\rho_\infty, z_\infty) = 0$. Thus an ∞ -isocline traverse the meridional plane exactly where the velocity field is vertical. Similarly, the 0-isoclines is the set of points (ρ_0, z_0) where $w(\rho_0, z_0) = 0$ implying that a 0-isocline goes through the meridional plane exactly where the velocity field is horizontal. Typically, a set of isoclines consists of a number of curves. In MATLAB the isoclines can be determined by calculating the zero contour of the velocity field components using the *contour*-function. For instance *contour*($r, z, w, [0 \ 0]$) calculates the 0-isoclines. The position of a stagnation point is found by solving $u(\rho_\infty, z_\infty) = w(\rho_0, z_0) = 0$ and it is seen that stagnation points are points of intersection of the 0- and ∞ -isoclines.

A bifurcation where stagnation points are created as a system parameter is varied is illustrated in figure 3.16. The bifurcation can be determined as follows: Let a branch of the 0-isocline be parametrized by arc length s , $(\rho, z) = (\rho_0(s), z_0(s))$ and let a function $G(s) = u(\rho_0(s), z_0(s))$ be the variation of u along the considered branch of the 0-isocline. The function $G(s)$ is shown in figure 3.16. Then a bifurcation occurs when the number of zeros of $G(s)$ changes. Typically, this happens when an extremum of $G(s)$ crosses the s -axis. Hence we locate a point s_f where $G'(s_f) = 0$ and consider $G(s_f)$. The sign of $G(s_f)$ will depend on the system parameters. Bifurcation can thus be found by solving $G(s_f) = 0$ with respect to the parameters. There may be several extrema of G , and each may give rise to bifurcation and must be treated individually. Furthermore, the number of extrema of G may vary. This requires attention in the implementation of this method. We return to this in section 3.3.4 and 3.3.5. We note that one can equally well consider a branch of the ∞ -isocline and parametrize this by arc length s , $(\rho, z) = (\rho_\infty(s), z_\infty(s))$ and consider the function $G(s) = w(\rho_\infty(s), z_\infty(s))$ of the variation of w along the considered branch of the ∞ -isocline instead. We do both. In section 3.3.4 we use the second approach to develop a procedure by which we compute the creation and merging bifurcation curves: The center axis is always an ∞ -isocline on which the arc length is z . To locate creation and merging bifurcations we define a function $G(z) = w(0, z)$ and apply the codimension 1 condition (3.94). In section 3.3.5 we devise a procedure by which we can compute the cusp bifurcation curves. To locate the cusp

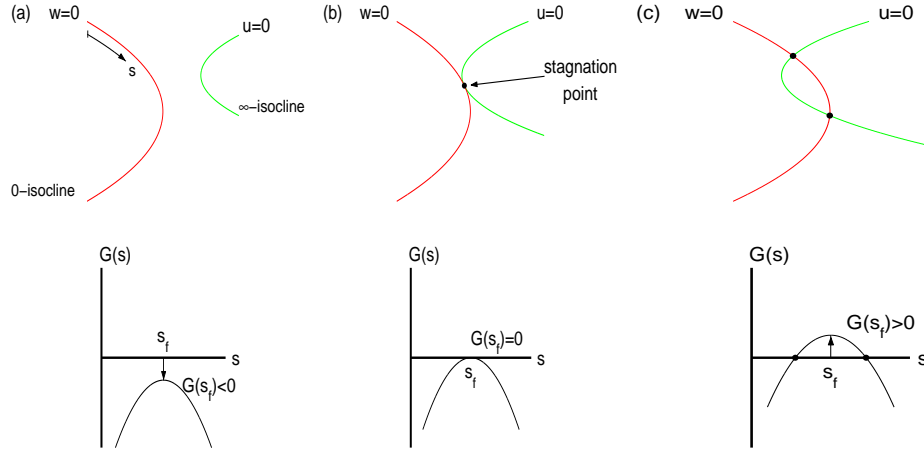


Figure 3.16: A branch of the 0-isocline is parametrized by s . A function $G(s) = u(\rho(s), z(s))$ is defined on the isocline. At an extremum s_f the function has the value $G(s_f)$. A bifurcation takes place when $G(s_f) = 0$. Case (a) is before a bifurcation. Case (b) and (c) are at and after a bifurcation where stagnation points are formed as a system parameter is varied.

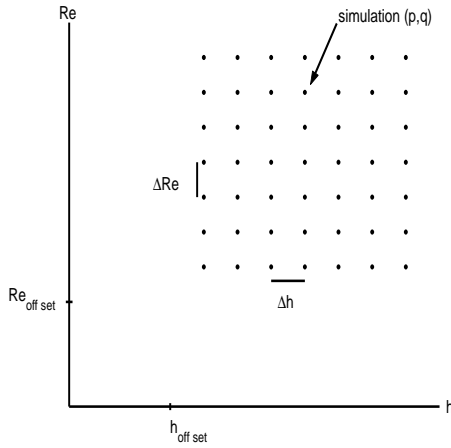


Figure 3.17: The figure illustrates the discrete grid in parameter space (h, Re) at which we conduct simulations to be used in the construction of the bifurcation diagrams.

bifurcation it turns out to be most convenient to use the first approach and consider a function $G(s) = u(\rho_0(s), z_0(s))$ defined on a branch of the 0-isocline.

We compute the creation, merging and cusp bifurcation curves in the parameter domain (h, Re) while keeping γ fixed thus resulting in diagrams similar to the experimentally obtained bifurcation diagram shown in figure 3.3.

3.3.4 Constructing creation and merging bifurcation curves

The creation or merging bifurcation curves C_{bif} are sets of parameter values $C_{\text{bif}} : \{(h_{\text{bif}}, Re_{\text{bif}})\}$ in parameter space. To compute the bifurcation curves we have been using MATLAB which is reflected in the text. We emphasize the build-in MATLAB functions and the data structure that we have applied. See MathWorks (2004) for documentation of the MATLAB functions.

The bifurcation curves are constructed on the basis of simulations conducted on a discrete grid in parameter space, see figure 3.17. Typically a parameter grid is chosen in the interval of

$h \in [1.0; 3.0]$ and $Re \in [700; 2400]$ with parameter increments in the range of $\Delta h \in [0.02; 0.08]$ and $\Delta Re \in [10; 25]$. The choice of these parameter intervals was motivated in section 3.1 and the choice of increments are based on the numerical considerations in Brøns, Voigt, and Sørensen (1999). The parameter values in the discrete parameter grid at which we conduct simulations are given as

$$h_p = p\Delta h + h_{\text{off set}} \quad \text{and} \quad Re_q = q\Delta Re + Re_{\text{off set}} \quad (3.97)$$

for $p = 1, \dots, P$ and $q = 1, \dots, Q$. A simulation is characterized by the parameter values (h_p, Re_q) and can thus via (3.97) be identified with the pair (p, q) . We define the set L of simulations in the discrete parameter grid as $L = \{(1, 1), (1, 2), (1, 3), \dots, (P, Q)\}$.

For some of the bifurcation diagrams we see later we choose for instance $h_{\text{off set}} = 0.98$ and $Re_{\text{off set}} = 675.0$ for $\Delta h = 0.08$ and $\Delta Re = 25$ with $P = 25$ and $Q = 68$. For a later use in connection with MATLAB we arrange the parameter values (h_p, Re_q) in the discrete parameter grid into two matrices $\mathbf{M}_h \in \mathbb{R}^{P \times Q}$ and $\mathbf{M}_{Re} \in \mathbb{R}^{Q \times P}$ by

$$\mathbf{M}_h = \begin{bmatrix} h_1 & \dots & h_1 \\ \vdots & & \vdots \\ h_P & \dots & h_P \end{bmatrix} \quad \text{and} \quad \mathbf{M}_{Re} = \begin{bmatrix} Re_1 & \dots & Re_1 \\ \vdots & & \vdots \\ Re_Q & \dots & Re_Q \end{bmatrix}. \quad (3.98)$$

The method for determining the bifurcation curves is based on the codimension 1 condition together with the introduction of the function $G(z) = w(0, z)$ as described in section 3.3.3. With the introduction of G we write the codimension 1 condition (3.94) on the form

$$G(0) = G'(0) = 0, \quad G(0)'' \neq 0. \quad (3.99)$$

where $G'(z) = w_z(0, z)$ and $G''(z) = w_{zz}(0, z)$.

The method involves finding the zeros of $G(z)$ and $G'(z)$. Thus we introduce z_z denoting a zero of $G(z)$ with the subindex indicating that z_z is a zero of the zero derivative of $G(z)$. Further we introduce z_f as a zero for $G'(z)$ where the subindex indicates a zero of the first derivative. Finally we let z_s denote a zero of $G''(0, z)$ with the subindex indicating a zero of the second derivative.

The functions $G(z)$, $G'(z)$ and $G''(z)$ depend on the bifurcation parameters Re and h thus $G(z) = G(z; h, Re)$, $G'(z) = G'(z; h, Re)$ and $G''(z) = G''(z; h, Re)$. Further the zeros z_z , z_f and z_s also vary with the bifurcation parameters (h, Re) and we have $z_z = z_z(h, Re)$, $z_f = z_f(h, Re)$ and $z_s = z_s(h, Re)$.

In principle, the creation or merging bifurcation curves C_{bif} can be found by solving the equations in the codimension 1 condition (3.99) as for each point $(h_{\text{bif}}, Re_{\text{bif}})$ on C_{bif} the two equations

$$G(z_{\text{bif}}; h_{\text{bif}}, Re_{\text{bif}}) = 0 \quad \text{and} \quad G'(z_{\text{bif}}; h_{\text{bif}}, Re_{\text{bif}}) = 0 \quad (3.100)$$

together with the codimension 1 non-degeneracy condition

$$G''(z_{\text{bif}}; h_{\text{bif}}, Re_{\text{bif}}) \neq 0 \quad (3.101)$$

must be fulfilled, with $z_{\text{bif}} = z_z(h_{\text{bif}}, Re_{\text{bif}}) = z_f(h_{\text{bif}}, Re_{\text{bif}})$. Thus to determine the bifurcation curves C_{bif} we can consider to either compute the zeros $z_f(h, Re)$ and then determine $(h_{\text{bif}}, Re_{\text{bif}})$ by evaluating $G(z; h, Re)$ at $z_f(h, Re)$ and then solving the first equation $G(z_f; h, Re) = 0$ in (3.100) or we can consider to compute the zeros $z_z(h, Re)$ and then determine $(h_{\text{bif}}, Re_{\text{bif}})$ by solving the second equation $G'(z_z; h, Re) = 0$ in (3.100). The former approach is feasible while the latter is not. The reason is illustrated for the case of the creation bifurcation. We saw in the middle

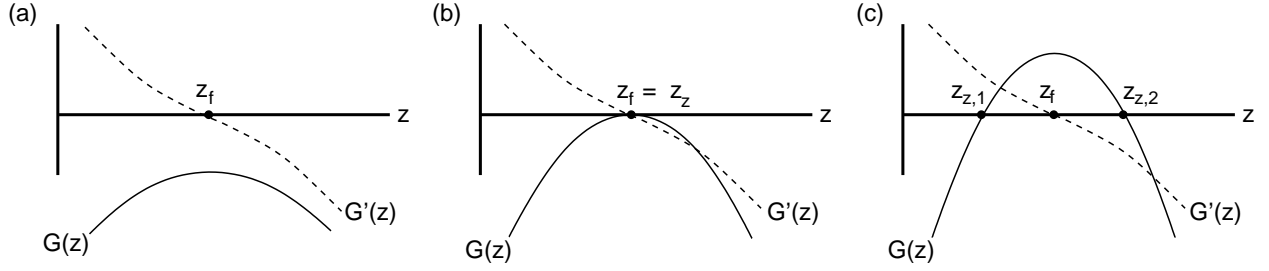


Figure 3.18: Illustration showing that in a neighborhood in parameter space of a creation bifurcation the zero $z_f(h, Re)$ exist both before, at and after a creation bifurcation whereas $z_z(h, Re)$ only exist at and after the bifurcation.

right panel of figure 3.13 that locally at the creation bifurcation the axial velocity component $G(z; h, Re) = w(0, z; h, Re)$ from being negative becomes positive. This is also sketched in figure 3.18 where the panel (a) is before the bifurcation, panel (b) is at the bifurcation and panel (c) is after the bifurcation. We see in figure 3.18 that the zero $z_f(h, Re)$ exist both before, at and after the creation bifurcation which implies that we can evaluate $G(z_f; h, Re)$ both before, at and after the bifurcation which again makes determining h_{bif} and Re_{bif} by solving $G(z_f; h, Re) = 0$ more robust numerically. In the latter choice no zeros $z_z(h, Re)$ exists before the bifurcation takes place, as seen in panel (a) in figure 3.18. A zero $z_z(h, Re)$ is formed at the bifurcation point, see (b) in figure 3.18 and splits into $z_{z,1}(h, Re)$ and $z_{z,2}(h, Re)$ after the bifurcation, see (c) in figure 3.18. Thus zeros $z_z(h, Re)$ exists only at and after the bifurcation has taken place implying that $G'(z; h, Re)$ can only be evaluated in the zero $z_z(h, Re)$ at and after the bifurcation which is not numerically advantageous when solving $G'(z_z; h, Re) = 0$.

To check that the non-degeneracy condition is fulfilled on a bifurcation curve C_{bif} we can in principle check that either $G''(z_f; h_{bif}, Re_{bif}) \neq 0$ or $G''(z_z; h_{bif}, Re_{bif}) \neq 0$. But with this approach we face a similar problem as sketched in figure 3.18. Instead we choose to compute the zeros $z_s(h, Re)$ and solve the equation $G(z_s; h, Re) = 0$ giving the curve $C_{d,1} : (h_{d,1}, Re_{d,1})$ together with the equation $G'(z_s; h, Re) = 0$ giving the curve $C_{d,2} : (h_{d,2}, Re_{d,2})$ where the subindex denotes degeneracy curve.

Now on the curve $C_{d,1}$ we have that both $G(z_s; h_{d,1}, Re_{d,1}) = 0$ and $G''(z_s; h_{d,1}, Re_{d,1}) = 0$ are fulfilled. And on $C_{d,2}$ we have that both $G'(z_s; h_{d,2}, Re_{d,2}) = 0$ and $G''(z_s; h_{d,2}, Re_{d,2}) = 0$ are fulfilled. Thus for (3.100) to be fulfilled on the bifurcation curve C_{bif} the curves $C_{d,1}$ and $C_{d,2}$ must not both intersect C_{bif} . If the curves $C_{d,1}$ and $C_{d,2}$ intersect C_{bif} at some point $(h_{codim\ 2}, Re_{codim\ 2})$ in parameter space, this point will be a codimension 2 point. The creation and merging bifurcation curves will terminate at $(h_{codim\ 2}, Re_{codim\ 2})$.

To sum up, the bifurcation curves C_{bif} can be determined by the following steps:

Procedure 3.1 (Creation and merging bifurcation curves)

- 1) Compute the zeros $z_f(h, Re)$.
- 2) Evaluate $G'(z)$ at the zeros $z_f(h, Re)$.
- 3) If a zero $z_f(h_{bif}, Re_{bif})$ solves $G(z_f; h, Re) = 0$ the point (h_{bif}, Re_{bif}) belongs to the bifurcation curve C_{bif} .
- 4) Compute the zeros $z_s(h, Re)$ and solve the equations $G(z_s; h, Re) = 0$ and $G'(z_s; h, Re) = 0$ giving the curves $C_{d,1}$ and $C_{d,2}$. Check that $C_{d,1}$ and $C_{d,2}$ do not intersect C_{bif} . If the curves

$C_{d,2}$ and $C_{d,2}$ intersect C_{bif} at the point $(h_{\text{codim } 2}, Re_{\text{codim } 2})$ in parameter space, this point is a codimension 2 point.

In practice, the set of points $(h_{\text{bif}}, Re_{\text{bif}})$ on a bifurcation curve C_{bif} will not belong to the discrete set of parameter values (h_p, Re_q) . To compute an approximation to C_{bif} via (3.100) with (3.101) based on the data obtained from the simulations at $(p, q) \in L$ we do interpolation of the numerical data. We perform this interpolation by implementing Procedure 3.1 in MATLAB. To this end we need to establish some data structures.

Via the numerical simulations conducted for h_p and Re_q at $(p, q) \in L$ we know $G(z)$ at $G(z; h_p, Re_q)$, $G'(z)$ at $G'(z; h_p, Re_q)$ and $G''(z)$ at $G''(z; h_p, Re_q)$. To handle step 1) in Procedure 3.1 we calculate the zeros $z_f(h_p, Re_q)$ for $(p, q) \in L$.

The zeros for a single simulation (p, q) are calculated using the MATLAB *spline*- and *fzero*-functions. For example, from a simulation (p, q) we know the values of $G'(z; h_p, Re_q)$ in the discrete computational grid points z_j with $j = 1, \dots, J$ in the interval $z \in [0; h]$, see section 3.3.1. For each pair z_j and z_{j+1} for $j = 1, \dots, J-1$ we calculate $G'(z_j; h_p, Re_q) \cdot G'(z_{j+1}; h_p, Re_q)$ and for $G'(z_j; h_p, Re_q) \cdot G'(z_{j+1}; h_p, Re_q) < 0$ we have identified an interval in which $G'(z; h_p, Re_q)$ changes sign and thus contains a zero $z_f(h_p, Re_q) \in [z_j; z_{j+1}]$. The *fzero*-function computes the zero of a given single-valued continuous function in a given interval. To meet this requirement we conduct a cubic spline fit of $G'(z; h_p, Re_q)$ in the entire interval $z \in [0; h]$ and provide the *fzero*-function this spline fit function together with the interval $[z_j; z_{j+1}]$ and the *fzero*-function is able to compute $z_f(h_p, Re_q)$. We have found it convenient to conduct the cubic spline fit of $G'(z; h_p, Re_q)$ in the full interval $z \in [0; h]$ as $G'(z; h_p, Re_q)$ might have a number of zeros, which we will see below. Now the cubic spline fit is re-used to determine each possible zero in $z \in [0; h]$.

Based on the approach to determine zeros we have, as an example, computed the zeros $z_f(h_p, Re_q)$ of a set of simulations conducted in the parameter range $h \in [1.5; 2.06]$ and $Re \in [1200; 2400]$ with resolution $\Delta h = 0.02$ and $\Delta Re = 25$ for a fixed $\gamma = 0.012$. The result is shown in figure 3.19. The figure shows how the number l of zeros vary with h_p and Re_q . The figure marks the regions in the discrete parameter grid where simulations (p, q) have the same number l of zeros $z_{f,i}(h_p, Re_q)$, $i = 1, \dots, l$. The curves separating the regions are seen to be piecewise linear. This is due to the discretization of the parameter space into the discrete parameter grid together with the choice of resolution Δh and ΔRe . The piecewise curves are approximations to the curves in parameter space separating the regions.

It is most convenient to compute the curves C_{bif} separately in each region characterized by a constant number l of zeros and then afterwards patch the bifurcations curves from each of the regions together. We therefore split the set L of simulations into subsets $L_{f,l}$ where each subset corresponds to a region in the discrete parameter grid having a given number l of zeros. In figure 3.19 the simulations are grouped into the three subsets $L_{f,7}$, $L_{f,5}$ and $L_{f,3}$. We note that $L_{f,3}$ consists of two disjoint regions. The simulations in the region with $l = 7$ zeros, $z_{f,i}(h_p, Re_q)$, $i = 1, \dots, 7$ are grouped into the subset $L_{f,7}$ etc.

To prepare for step 2) in Procedure 3.1 the zeros $z_{f,i}(h_p, Re_q)$, $i = 1, \dots, l$ from each subset $L_{f,l}$ of simulations are collected into l matrices $\mathbf{M}_{l,i}$ for $i = 1, \dots, l$. A matrix $\mathbf{M}_{l,i} \in \mathbb{R}^{P \times Q}$ is defined as

$$\mathbf{M}_{l,i}(p, q) = \begin{cases} z_{f,i}(h_p, Re_q) & \text{for } (p, q) \in L_{f,l} \\ NaN & \text{for } (p, q) \notin L_{f,l}. \end{cases}$$

A matrix $\mathbf{M}_{l,i}$ is defined to have $P \times Q$ elements, which are more or equal to the number of elements that are given in $L_{f,l}$ as $L_{f,l} \subseteq L$. Thus we need to fill up the left-over elements in the matrix. To

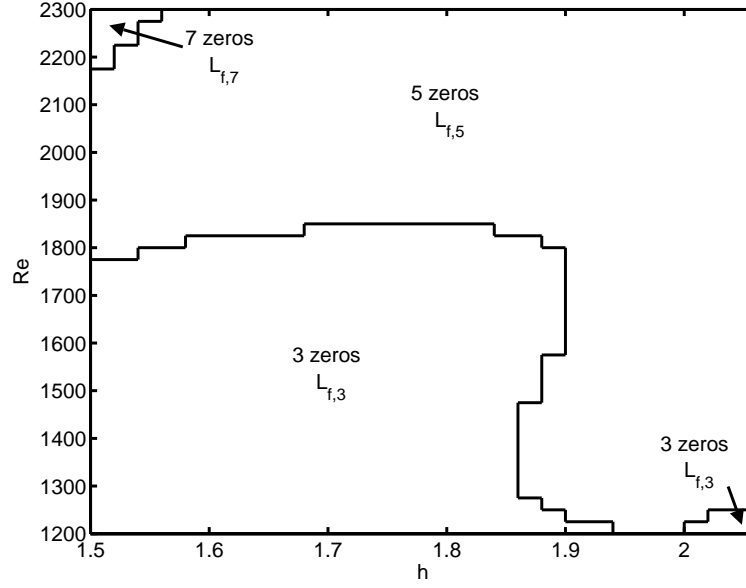


Figure 3.19: Division of (h, Re) for $\gamma = 0.012$ into subdomains $L_{f,l}$ here $L_{f,3}$, $L_{f,5}$ and $L_{f,7}$ each having a constant number of zeros $z_{f,i}$ for $i = 1, \dots, l$. Parameter space resolution is $\Delta h = 0.02$ and $\Delta Re = 25$.

do so we have introduced what we call void elements. By a void element we think of a so-called not-a-number. We denote the not-a-number void element NaN . The not-a-number concept exists in MATLAB (and FORTRAN) and has the syntax NaN . The advantage of using the not-a-number facility in MATLAB is that the various types of plotting functions ignores a NaN , we comment on this in connection with figure 3.20.

For example the zeros $z_{f,i}(h_p, Re_q)$, $i = 1, \dots, 5$ for the simulations of subset $L_{f,5}$ in figure 3.19 are collected into the five matrices $\mathbf{M}_{5,1}$, $\mathbf{M}_{5,2}$, $\mathbf{M}_{5,3}$, $\mathbf{M}_{5,4}$ and $\mathbf{M}_{5,5}$, where the first matrix $\mathbf{M}_{5,1}$ has the elements

$$\mathbf{M}_{5,1}(p, q) = \begin{cases} z_{f,1}(h_p, Re_q) & \text{for } (p, q) \in L_{f,5} \\ NaN & \text{for } (p, q) \notin L_{f,5}. \end{cases}$$

In figure 3.20 we visualize the matrices $\mathbf{M}_{5,i}$, $i = 1, \dots, 5$ of the simulations in subset $L_{f,5}$. In the figure the matrices $\mathbf{M}_{5,i}(p, q)$ are mapped as functions of $\mathbf{M}_h(p, q)$ and $\mathbf{M}_{Re}(p, q)$ for $(p, q) \in L$. The MATLAB command to visualize $\mathbf{M}_{5,i}$ is `mesh(M_h, M_Re, M_{5,i})`. We notice in figure 3.20 that even though for instance $\mathbf{M}_{5,1}$ has $P \times Q$ elements the `mesh` function has only plotted the elements $(p, q) \in L_{f,5}$. The elements $(p, q) \notin L_{f,5}$ of $\mathbf{M}_{5,1}$ were defined not-a-number and are seen ignored by the `mesh`-function.

Now we can conduct step 2) in Procedure 3.1. For a given subset $L_{f,l}$ of simulations we evaluate $G(z; h_p, Re_q)$ in each element of the matrices $\mathbf{M}_{l,i}$, $i = 1, \dots, l$. This is done by conducting a cubic spline fit of $G(z; h_p, Re_q)$ on the interval $z \in [0, h]$ for each $(p, q) \in L$. We arrange the evaluations in the matrices $\mathbf{W}_{l,i}$, $i = 1, \dots, l$ where $\mathbf{W}_{l,i} \in \mathbb{R}^{P \times Q}$ is given by

$$\mathbf{W}_{l,i}(p, q) = \begin{cases} G(z_{f,i}; h_p, Re_q) & \text{for } (p, q) \in L_{f,l} \\ NaN & \text{for } (p, q) \notin L_{f,l}. \end{cases}$$

In the top panel of figure 3.21 we have visualized the matrices $\mathbf{W}_{5,i}$, $i = 1, \dots, 5$ again for the simulations in subset $L_{f,5}$. In the top panel of figure 3.21 the matrices $\mathbf{W}_{l,i}(p, q)$ are mapped as

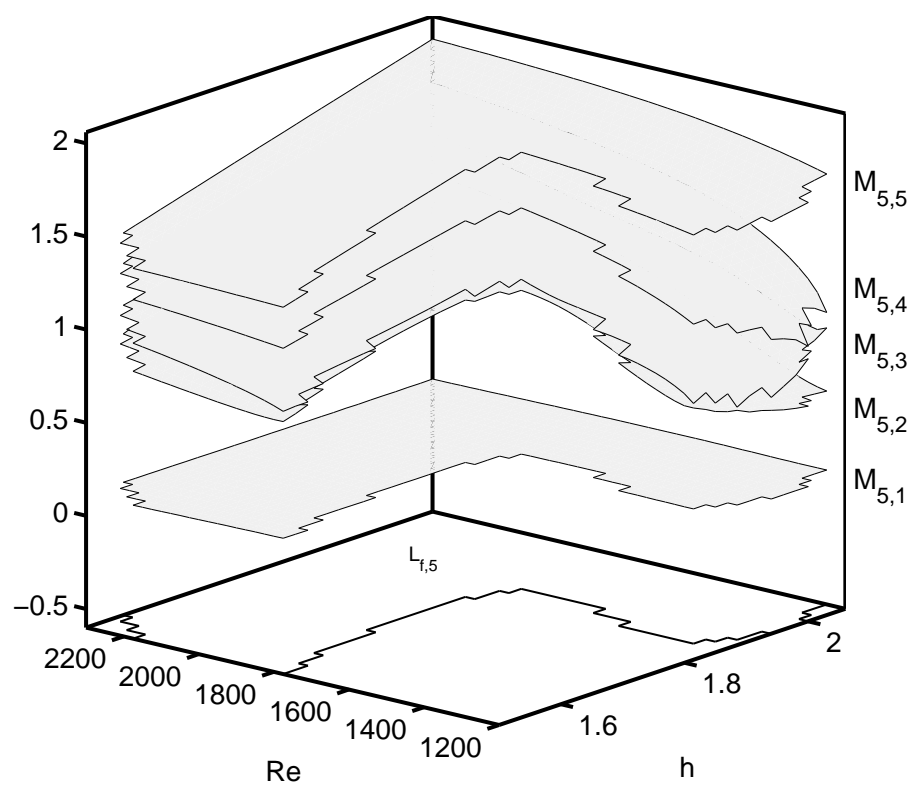


Figure 3.20: Plots for $\gamma = 0.012$ of the matrices $M_{5,i}$, $i = 1, \dots, 5$ mapped as functions of M_h and M_{Re} .

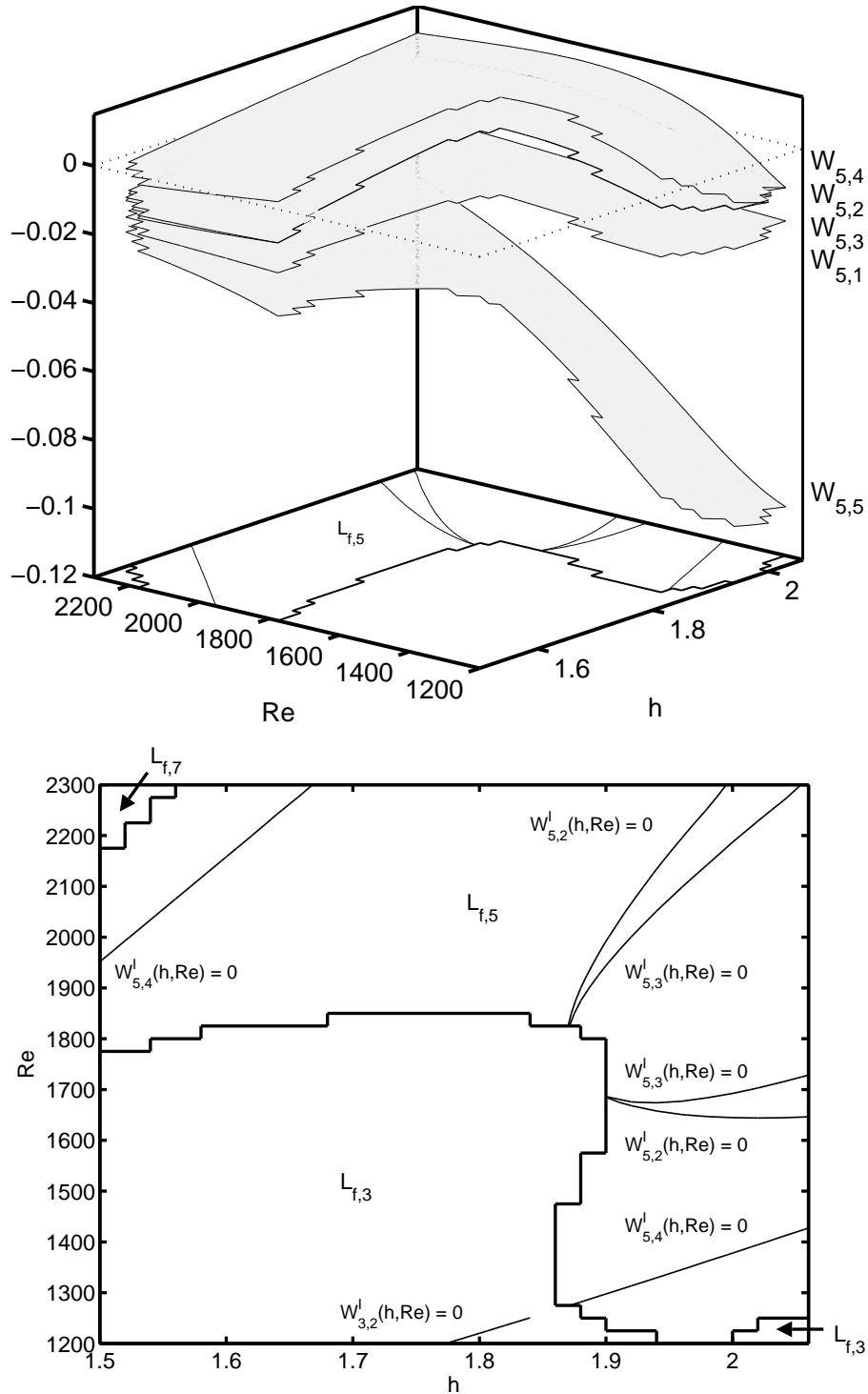


Figure 3.21: Top panel: Plots for $\gamma = 0.012$ of the matrices $\mathbf{W}_{5,i}$, $i = 1, \dots, 5$ mapped as functions of \mathbf{M}_h and \mathbf{M}_{Re} . Bottom panel: Plots of the solutions to $W_{i,j}^I(h, Re) = 0$ for the interpolation functions $W_{i,j}^I$ for $i, j = 1, \dots, 7$. The solutions constitute the creation and merging bifurcation curves denoted $C_{bif,i}$, $i = 1, \dots, 6$ in figure 3.23.

functions of $\mathbf{M}_h(p, q)$ and $\mathbf{M}_{Re}(p, q)$ for $(p, q) \in L$ with $i = 1, \dots, 5$.

We now have the data structures we need to compute the bifurcation curves C_{bif} in step 3) of Procedure 3.1. Based on the matrices \mathbf{M}_h and \mathbf{M}_{Re} in (3.98) together with $\mathbf{W}_{l,i}$, $i = 1, \dots, l$ for each subset $L_{f,l}$ of simulations, step 3) is performed by determining an interpolation function $W_{l,i}^I : \mathbb{R}^2 \rightarrow \mathbb{R}$ such that $W_{l,i}^I(\mathbf{M}_h(p, q), \mathbf{M}_{Re}(p, q)) = \mathbf{W}_{l,i}(p, q)$. Then based on the interpolation function $W_{l,i}^I(h, Re)$ investigate whether $W_{l,i}^I(h, Re) = 0$ has a solution, if so the solution $(h_{\text{bif}}, Re_{\text{bif}})$ belongs to the bifurcation curve C_{bif} . In MATLAB this can be done all-in-one with the *contour*-function. The command to issue a MATLAB calculation is *contour*($\mathbf{M}_h, \mathbf{M}_{Re}, \mathbf{W}_{l,i}, [0 \ 0]$). The *contour*-function conducts a linear interpolation within each block of four neighboring elements in $\mathbf{W}_{l,i}$. The function compares the values of each block in the matrix $\mathbf{W}_{l,i}$ to the given contour level, here zero. If a contour level falls within a block, the *contour*-function performs the linear interpolation to locate the point at which the contour crosses the edges of the cell composed by the four neighboring elements in the block. The *contour*-function connects these points to produce a piece of a contour line, corresponding to a solution to $W_{l,i}^I(h, Re) = 0$.

The consequence of using the *contour*-function conducting linear interpolation is that some of the bifurcation curves in the bifurcation diagrams we present later are not smooth especially where the curves possess high curvature. We accept this.

In the bottom panel of figure 3.21 we show the resulting bifurcation curves C_{bif} . It is seen in the top panel that the bifurcation curves are solutions to $W_{5,2}^I(h, Re) = 0$, $W_{5,3}^I(h, Re) = 0$ and $W_{5,4}^I(h, Re) = 0$ whereas no solutions exist to $W_{5,1}^I(h, Re) = 0$ and $W_{5,5}^I(h, Re) = 0$. In the bottom panel of figure 3.21 we have also added the bifurcation curve C_{bif} of the $L_{f,3}$ region. The curve is the solution to $W_{3,2}^I(h, Re) = 0$ and has been determined in a similar manner as the bifurcation curves in region $L_{f,5}$. In the $L_{f,7}$ region no bifurcation curves exists. Thus for the considered parameter range we have identified all the creation and merging bifurcation curves in the regions $L_{f,3}$ and $L_{f,5}$. Now we have to patch together bifurcation curves from different regions, bifurcation curves that corresponds to each other. For the parameter range we have studied in the case of figure 3.21 we patch together the curves found in the lower part of the diagram which are solutions to $W_{3,2}^I(h, Re) = 0$ and $W_{5,4}^I(h, Re) = 0$. These two patched bifurcation curves we denote $C_{\text{bif},6}$ in figure 3.23. The curve in the upper left part also given as solution to $W_{5,4}^I(h, Re) = 0$ we denote $C_{\text{bif},1}$ in figure 3.23. Further the two curves given as solutions to $W_{5,2}^I(h, Re) = 0$ are denoted $C_{\text{bif},2}$ and $C_{\text{bif},5}$ and finally the two curves given as solutions to $W_{5,3}^I(h, Re) = 0$ are denoted $C_{\text{bif},2}$ and $C_{\text{bif},5}$.

Finally we have reached step 4) in Procedure 3.1. To start with we compute in a similar fashion as above the zeros $z_s(h_p, Re_q)$. The result is shown in figure 3.22. Figure 3.22 shows how the number l of zeros $z_{s,i}(h_p, Re_q)$ for $i = 1, \dots, l$ depends on $(p, q) \in L$. We see that there are two regions in the parameter space containing a different number of zeros. An upper most region containing $l = 8$ zeros and a lower most region containing $l = 6$ zeros. Again we split the set of simulations $(p, q) \in L$ into to subsets and for figure 3.22 we have the two subsets $L_{s,8}$ and $L_{s,6}$. In each subset we organize the zeros $z_{s,i}(h_p, Re_q)$ into matrices $\mathbf{N}_{l,i} \in \mathbb{R}^{P \times Q}$ for $i = 1, \dots, l$ defined by

$$\mathbf{N}_{l,i}(p, q) = \begin{cases} z_{s,i}(h_p, Re_q) & \text{for } (p, q) \in L_{s,l} \\ NaN & \text{for } (p, q) \notin L_{s,l}. \end{cases}$$

Now for a given subset $L_{s,l}$ of simulations we evaluate $G(z; h_p, Re_q)$ and $G'(z; h_p, Re_q)$ in each element of $\mathbf{N}_{l,i}$, $i = 1, \dots, l$. Here we re-use the already obtained cubic spline fit of $G(z; h_p, Re_q)$ together with a cubic spline fit of $G'(z; h_p, Re_q)$ on the whole of the interval $z \in [0; h]$ for all $(p, q) \in L$.

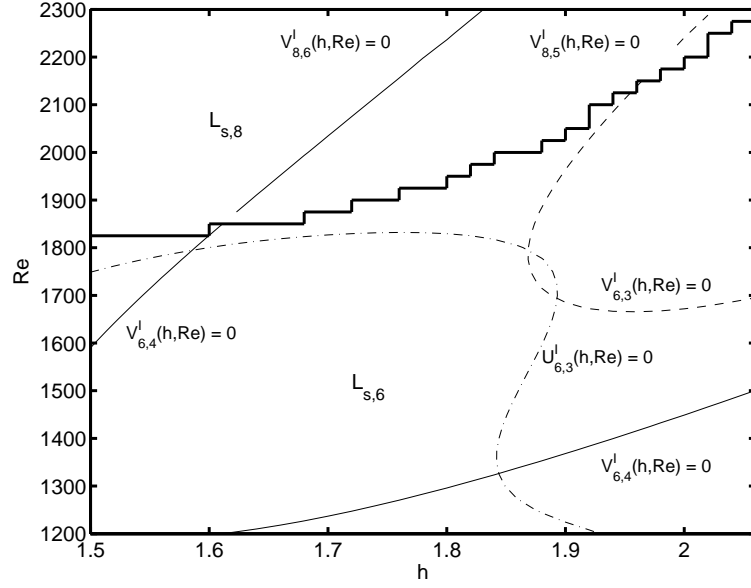


Figure 3.22: Solutions for $\gamma = 0.012$ to $V_{i,j}^I(h, Re) = 0$ and $U_{i,j}^I(h, Re) = 0$ for the interpolation functions $V_{i,j}^I$ and $U_{i,j}^I$ with $i, j = 1, \dots, 7$. The solutions to $V_{6,3}^I(h, Re) = 0$, $V_{8,5}^I(h, Re) = 0$ and $U_{6,3}^I(h, Re) = 0$ constitute the non-degenerate curves denoted $C_{d,1}$ and $C_{d,2}$ in figure 3.23.

We arrange the evaluations in the matrices $\mathbf{V}_{l,i} \in \mathbb{R}^{P \times Q}$ and $\mathbf{U}_{l,i} \in \mathbb{R}^{P \times Q}$ which are defined as

$$\mathbf{V}_{l,i}(p, q) = \begin{cases} G(z_{s,i}; h_p, Re_q) & \text{for } (p, q) \in L_{s,l} \\ NaN & \text{for } (p, q) \notin L_{s,l} \end{cases} \quad (3.102)$$

and

$$\mathbf{U}_{l,i}(p, q) = \begin{cases} G'(z_{s,i}; h_p, Re_q) & \text{for } (p, q) \in L_{s,l} \\ NaN & \text{for } (p, q) \notin L_{s,l}. \end{cases} \quad (3.103)$$

To determine the curves $C_{d,1}$ and $C_{d,2}$ for a given subset $L_{s,l}$ we again compute interpolation functions $V_{l,i}^I : \mathbb{R}^2 \rightarrow \mathbb{R}$ and $U_{l,i}^I : \mathbb{R}^2 \rightarrow \mathbb{R}$ such that $V_{l,i}^I(\mathbf{M}_h(p, q), \mathbf{M}_{Re}(p, q)) = \mathbf{V}_{l,i}(p, q)$ and $U_{l,i}^I(\mathbf{M}_h(p, q), \mathbf{M}_{Re}(p, q)) = \mathbf{U}_{l,i}(p, q)$. Then based on the interpolation functions $V_{l,i}^I(h, Re)$ and $U_{l,i}^I(h, Re)$ we investigate whether $V_{l,i}^I(h, Re) = 0$ and $U_{l,i}^I(h, Re) = 0$ have solutions. If so, the solutions $(h_{d,1}, Re_{d,1})$ and $(h_{d,2}, Re_{d,2})$ belongs to the curves $C_{d,1}$ and $C_{d,2}$. To solve $V_{l,i}^I(h, Re) = 0$ and $U_{l,i}^I(h, Re) = 0$ we again apply the *contour*-function.

In figure 3.22 we have shown the curves $C_{d,1}$ and $C_{d,2}$ for the example we have been considering. The curves $C_{d,1}$ are found as solutions to $V_{6,3}^I(h, Re) = 0$ and $V_{6,4}^I(h, Re) = 0$ for the simulations in $L_{s,6}$ and $V_{8,5}^I(h, Re) = 0$ and $V_{8,6}^I(h, Re) = 0$ for the simulations in $L_{s,8}$. The curve $C_{d,2}$ is found as solution to $U_{6,3}^I(h, Re) = 0$ for the simulations in $L_{s,6}$. We notice that the curves given by $U_{6,3}^I(h, Re) = 0$ and $V_{6,3}^I(h, Re) = 0$ intersect twice. As $U_{6,3}^I(h, Re)$ and $V_{6,3}^I(h, Re)$ both are associated with the same zero $z_{s,3}(h_{d,2}, Re_{d,2})$ via (3.102) and (3.103) implies that the two intersection points are codimension 2 points in parameter space. The curves given by $U_{6,3}^I(h, Re) = 0$ and $V_{6,4}^I(h, Re) = 0$ also intersect but the intersection point is *not* a codimension 2 point as the curve $U_{6,3}^I(h, Re) = 0$ is associated with the third zero $z_{s,3}(h_{d,2}, Re_{d,2})$ whereas the curve $V_{6,4}^I(h, Re) = 0$ is associated with the fourth zero $z_{s,4}(h_{d,2}, Re_{d,2})$. The zeros $z_{s,3}(h_{d,2}, Re_{d,2})$ and

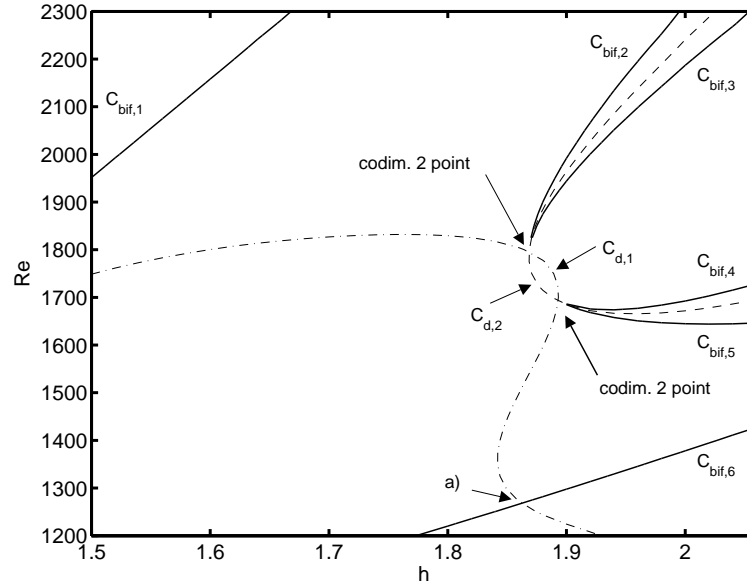


Figure 3.23: Plot for $\gamma = 0.012$ showing the creation bifurcation curves $C_{\text{bif},1}$, $C_{\text{bif},2}$, $C_{\text{bif},5}$ and $C_{\text{bif},6}$ and the merging bifurcation curves $C_{\text{bif},3}$ and $C_{\text{bif},4}$ together with the non-degenerate curves $C_{d,1}$ and $C_{d,2}$. The intersection points of $C_{d,1}$ and $C_{d,2}$ constitute codimension 2 points.

$z_{s,4}(h_{d,2}, Re_{d,2})$ are situated in different positions on the center axis. The part $V_{6,3}^I(h, Re) = 0$ of the curve $C_{d,1}$ and the part $U_{6,3}^I(h, Re) = 0$ of the curve $C_{d,2}$ are also shown in figure 3.23.

The figure 3.23 shows the bifurcation curves $C_{\text{bif},1}, \dots, C_{\text{bif},6}$ together with part of the curves $C_{d,1}$ and $C_{d,2}$. It is seen that the bifurcation curves $C_{\text{bif},1}, \dots, C_{\text{bif},6}$ are not intersected by both $C_{d,1}$ and $C_{d,2}$ thus the codimension 1 condition is fulfilled on the curves. But we can also see that the bifurcation curves $C_{\text{bif},2}$, $C_{\text{bif},3}$, $C_{\text{bif},4}$ and $C_{\text{bif},5}$ are close to the two codimension 2 points. These bifurcation curves do not end at the codimension 2 points, as they are supposed to, but this is due to the choice of resolution of our discrete parameter grid. If we had chosen a finer resolution the bifurcation curves would come closer to the codimension 2 points. In the bifurcation diagrams to come we extrapolate the bifurcation curves such that they end at the codimension 2 points. The intersection point marked a) in figure 3.23 involved different zeros on the center axis and hence has no topological relevance in the bifurcation diagram.

By inspection of the level curves for the stream function for a series of simulations we note that the curves $C_{\text{bif},1}$ and $C_{\text{bif},6}$ are creation bifurcation curves forming one recirculation zone. The curves $C_{\text{bif},2}$ and $C_{\text{bif},5}$ are also creation bifurcation curves forming yet a recirculation zone such that we have two recirculation zones. The curves $C_{\text{bif},3}$ and $C_{\text{bif},4}$ are merging bifurcation curves forming an inner structure recirculation zone. Despite having obtained these bifurcation curves the bifurcation diagram is not yet complete. In section 3.3.5 we consider how to complete the bifurcation diagram.

3.3.5 Constructing cusp bifurcation curves

In figure 3.23 in section 3.3.4 we saw that for certain parameter values codimension 2 points occur in the present flow. The creation and merging bifurcation curves end at the codimension 2 point. But these are not the only bifurcation curves ending at the codimension 2 point. The bifurcation

diagram in figure 3.8 showing an unfolding of the codimension 2 point includes a curve of cusp bifurcations. Thus the bifurcation diagram in figure 3.23 is incomplete, a cusp bifurcation curve is missing. The advantage of having determined the codimension 2 points and the creation and merging bifurcation curves is that, it gives some guidance of where to search for cusp bifurcation curves.

The cusp bifurcation takes place in the flow. Exactly at the cusp bifurcation a center-saddle appears. The center-saddle develops into a center and a saddle point as system parameters are varied exactly as shown in figure 3.16. As described in section 3.3.3 a way to determine the cusp bifurcation is to parametrize for instance the 0-isocline by the arc length s and consider the function $G(s) = u(\rho_0(s), z_0(s))$. A cusp bifurcation occurs when an extremum of $G(s)$ crosses the s -axis. We denote a zero of $G(s)$ by s_z and a zero of the derivative $G'(s)$ by s_f . A numerical example of a cusp bifurcation is given in figure 3.24 showing the result of three simulations where we have kept Re and γ fixed and varied h . The left top, middle and bottom panels show the 0- and ∞ -isoclines together with level-curves for the streamfunction $\psi(r, z)$ inside a recirculation zone before, at and after the cusp bifurcation. The right top, middle and bottom panels show the corresponding plots of the function $G(s)$ where the starting point for the arc length s is chosen to be the uppermost point of the 0-isocline. In the top left panel $G(s)$ has one zero $s_{z,1}$. This zero corresponds to the center seen in the top right panel. By increasing h we see in the middle right panel that $G'(s) = 0$ at s_f corresponding to the formation of a center-saddle seen in the left middle panel. By further increasing h the center-saddle splits into a saddle and a center corresponding to the zeros $s_{z,2}$ and $s_{z,3}$ of $G(s)$. Together with the persisting center corresponding to the zero at $s_{z,1}$ an inner-structure inside the recirculation zone has been formed.

In the computation of a cusp bifurcation curve $C_{\text{bif}} : (h_{\text{bif}}, Re_{\text{bif}})$ we take advantage of the fact that the bifurcation takes place when the degeneracy condition

$$G(s) = 0 \text{ and } G'(s) = 0 \quad (3.104)$$

is fulfilled. The derivative $G'(s)$ may have several zeros, each will be distinguished by a subindex $s_{f,i}$, $i = 1, 2, \dots, l$. Furthermore $G(s)$ and $G'(s)$ as well as $s_{f,i}$ all depend on system parameters thus we have that $G = G(s; h, Re)$ and $G' = G'(s; h, Re)$ together with $s_{f,i} = s_{f,i}(h, Re)$. Based on (3.104) a procedure to compute the cusp bifurcation curve C_{bif} is:

Procedure 3.2 (Cusp bifurcation curves)

- 1) Compute the zeros $s_f(h, Re)$ of $G'(s; h, Re)$.
- 2) Evaluate $G(s; h, Re)$ at the zeros $s_f(h, Re)$.
- 3) If a zero $s_f(h_{\text{bif}}, Re_{\text{bif}})$ solves $G(s_f; h, Re) = 0$ the point $(h_{\text{bif}}, Re_{\text{bif}})$ belongs to the cusp bifurcation curve C_{bif} .

The cusp bifurcation curves will be constructed on the basis of simulations conducted on a discrete parameter grid in parameter space, see (3.97), where a simulation is characterized by the pair (p, q) for $p = 1, \dots, P$ and $q = 1, \dots, Q$, with the set of simulations $(p, q) \in L$. The set of points $(h_{\text{bif}}, Re_{\text{bif}})$ on the cusp bifurcation curves C_{bif} will not belong to the discrete set of parameter values (h_p, Re_q) with $(p, q) \in L$ and we will have to do interpolation. From the simulations we know $G(s)$ at $G(s; h_p, Re_q)$ and $G'(s)$ at $G'(s; h_p, Re_q)$. The zeros $s_{f,i}(h_p, Re_q)$, $i = 1, \dots, l$ for a simulation (p, q)

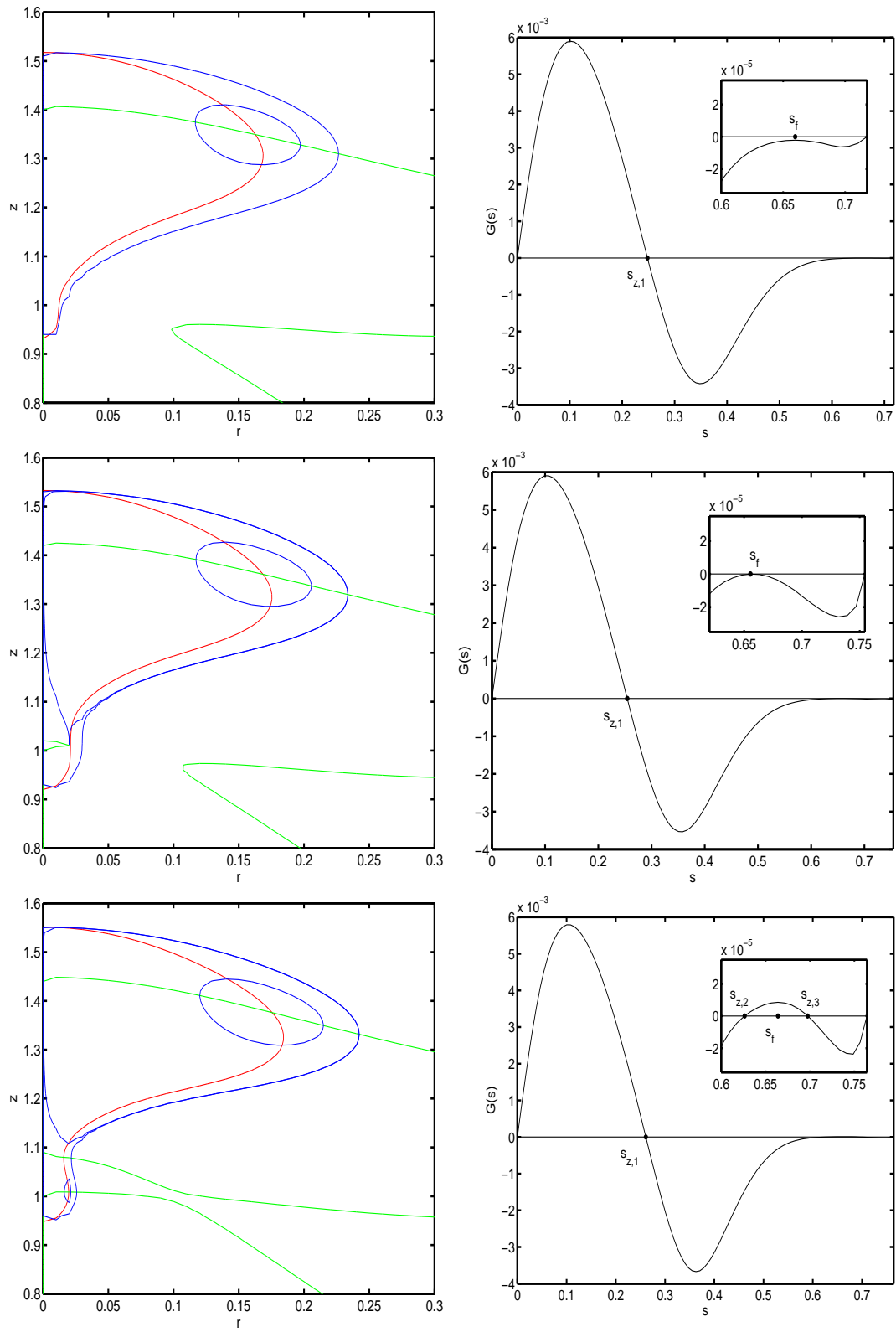


Figure 3.24: The figure illustrates the occurrence of the cusp bifurcation for $h = 1.88$ and $\gamma = 0.012$ kept fixed and Re varied. The top panels are for $Re = 1730$. The middle panels for $Re = 1780.2$ and the bottom panels for $Re = 1850$. The left column panels show the blue streamfunction and the red 0- and green ∞ -isoclines. The right column panels show $G(s)$.

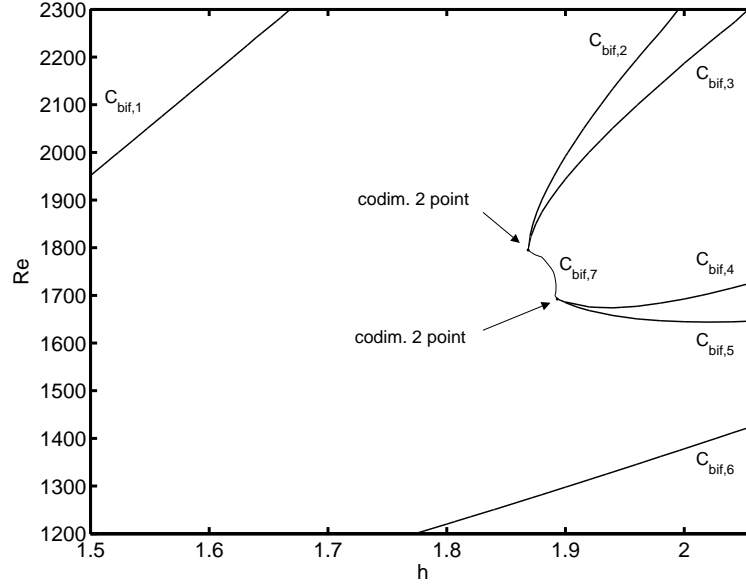


Figure 3.25: The full set of bifurcation curves and codimension 2 points for $\gamma = 0.012$. Creation curves: $C_{\text{bif},1}$, $C_{\text{bif},2}$, $C_{\text{bif},5}$ and $C_{\text{bif},6}$. Merging curves: $C_{\text{bif},3}$ and $C_{\text{bif},4}$. Cusp curve: $C_{\text{bif},7}$.

are calculated using the MATLAB *spline*- and *fzero*-functions in a similar fashion as described in section 3.3.4. The number l of zeros $s_{f,i}(h_p, Re_q)$ will vary with (h_p, Re_q) and we will compute C_{bif} separately in each region characterized by a constant number l of zeros and then afterwards patch the cusp bifurcation curves from each of the regions together. Thus we split the set L of simulations into subsets $L_{f,l}$ where each subset corresponds to a region in the discrete parameter grid having a given constant number l of zeros $s_{f,i}(h_p, Re_q)$ for $i = 1, \dots, l$ with $(p, q) \in L_{f,l}$. Complying with step 1) in the procedure 3.2 we compute and collect the zeros $s_{f,i}(h_p, Re_q)$, $i = 1, \dots, l$ from each subset $L_{f,l}$ of simulations into l matrices $\mathbf{S}_{l,i}$, $i = 1, \dots, l$ where each $\mathbf{S}_{l,i} \in \mathbb{R}^{P \times Q}$ is defined by

$$\mathbf{S}_{l,i}(p, q) = \begin{cases} s_{f,i}(h_p, Re_q) & \text{for } (p, q) \in L_{f,l} \\ NaN & \text{for } (p, q) \notin L_{f,l}. \end{cases}$$

Having determined the zeros $s_{f,i}(h_p, Re_q)$, $i = 1, \dots, l$ in $L_{f,l}$ we continue with step 2) in procedure 3.2 and evaluate $G(s; h_p, Re_q)$ in each element of the matrices $\mathbf{S}_{l,i}$. Again this is conducted by virtue of cubic spline fits. The evaluations are collected in the matrices $\mathbf{C}_{l,i}$, $i = 1, \dots, l$ where $\mathbf{C}_{l,i} \in \mathbb{R}^{P \times Q}$ is given by

$$\mathbf{C}_{l,i}(p, q) = \begin{cases} G(s_{f,i}; h_p, Re_q) & \text{for } (p, q) \in L_{f,l} \\ NaN & \text{for } (p, q) \notin L_{f,l}. \end{cases}$$

Corresponding to step 3) in procedure 3.2 we can now compute the cusp bifurcation curve based on \mathbf{M}_h and \mathbf{M}_{Re} in (3.98) together with $\mathbf{C}_{l,i}$, $i = 1, \dots, l$ by determining interpolation functions $C_{l,i}^I: \mathbb{R}^2 \rightarrow \mathbb{R}$ such that $C_{l,i}^I(\mathbf{M}_h(p, q), \mathbf{M}_{Re}(p, q)) = \mathbf{C}_{l,i}(p, q)$. Then if $C_{l,i}^I(h, Re) = 0$ for $i = 1, \dots, l$ has a solution, the solution $(h_{\text{bif}}, Re_{\text{bif}})$ belongs to the cusp bifurcation curve C_{bif} . This computation is issued in MATLAB by the *contour*-function as *contour*($\mathbf{M}_h, \mathbf{M}_{Re}, \mathbf{C}_{l,i}, [0 \ 0]$). In figure 3.25 we have computed the cusp bifurcation curve $C_{\text{bif},7}$ for $\gamma = 0.012$ and added the curve to the bifurcation diagram in figure 3.23 containing the creation and merging bifurcation curves

$C_{\text{bif},1}, \dots, C_{\text{bif},6}$ together with the two codimension 2 points. The cusp curve $C_{\text{bif},7}$ is the solution to $C_{4,3}^I(h, Re) = 0$. With the addition of the cusp bifurcation curve $C_{\text{bif},7}$ the bifurcation diagram in figure 3.25 is complete.

The choice of parameter values in figure 3.24 is actually based on the cusp bifurcation curve $C_{\text{bif},7}$ in figure 3.25.

3.3.6 Formation of one recirculation zone through an in-flow loop

The method devised in section 3.3.5 finds an application in the scenario seen in figure 3.26. as the scenario involves a cusp bifurcation.

The scenario is topologically equivalent to the bifurcation scenario seen in the left panel of figure 3.10. The bifurcation diagram was found for the non-simple degenerate normal form (3.84) analysed in section 3.2.6. The scenario in figure 3.26 corresponds to the case of $\sigma = +1$.

In the scenario a recirculation zone is formed as an in-flow loop attaches to the center axis. The loop is created by a cusp bifurcation taking place close to the axis. This shows that recirculation zones may not only be formed by the creation bifurcation taking place on the center axis but may also be the result of in-flow bifurcations. This constitute a new aspect of vortex breakdown.

3.3.7 The appearance of a saddle point on the center axis

A saddle point has been observed crossing the top left corner of the meridional plane. This is illustrated in figure 3.27. The crossing corresponds to the bifurcation diagram seen in figure 3.11 found in section 3.2.7.

3.3.8 The bifurcation diagrams

We have now devised a post processing strategy on how to determine the creation, merging and cusp bifurcation curves and finally the point has been reached where we can show the full bifurcation diagrams in the (h, Re) parameter plane. The diagrams are shown in the figures from 3.28 to 3.39. In the numerical simulations we have for our choice of parameters encountered the existence of either one recirculation zone or two recirculation zones as well as a recirculation zone with inner structure. Further an in-flow loop attachment to the center axis has been observed and also the occurrence of a saddle point crossing the top left corner has been found.

In the bifurcation diagrams, a black line denotes a creation bifurcation curve and shows where one recirculation zones is formed when traversing the diagram, a green line marks another creation bifurcation curve showing when yet a recirculation zones is formed such that two recirculation zones exist. A blue curve indicates a merging bifurcation. A red line denotes a cusp bifurcation. The magenta shows the cusp bifurcation forming the loop which attach to the center axis and finally the cyan shows where the saddle point crosses the top left corner and appears on the center axis.

This color coding complies with the color legend used for the bifurcation diagram of the fourth order normal form shown in figure 3.9. In the series of diagrams we have included the explanatory labels *no r.z.* meaning that no recirculation zones exists, *1 r.z.* showing the area where one recirculation zone exists, *2 r.z.* showing an area with two recirculation zones and *1 i.s.* indicating an area where a recirculation zone has inner structure. Further *1 l.s.* shows where a loop structure exists and *1 s.p.* shows the domain where the saddle point on the center axis exists.

Consider the bifurcation diagram of figure 3.28 that is for the case of $\gamma = -0.04$ we see that no recirculation zones exist in the lower as well as the leftmost and rightmost part of the diagram. A domain where only one recirculation zone exists is situated in the center part of the diagram.

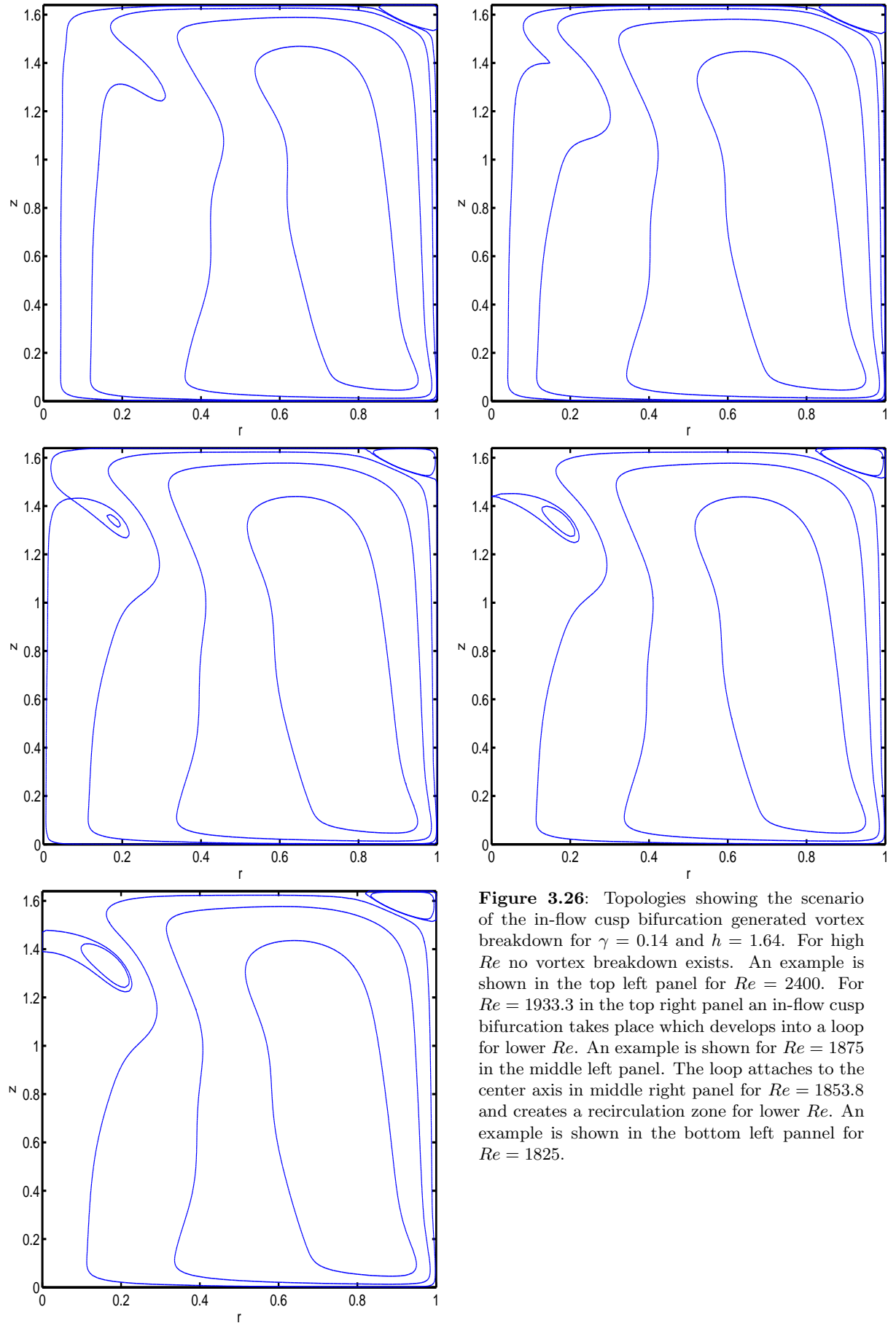


Figure 3.26: Topologies showing the scenario of the in-flow cusp bifurcation generated vortex breakdown for $\gamma = 0.14$ and $h = 1.64$. For high Re no vortex breakdown exists. An example is shown in the top left panel for $Re = 2400$. For $Re = 1933.3$ in the top right panel an in-flow cusp bifurcation takes place which develops into a loop for lower Re . An example is shown for $Re = 1875$ in the middle left panel. The loop attaches to the center axis in middle right panel for $Re = 1853.8$ and creates a recirculation zone for lower Re . An example is shown in the bottom left panel for $Re = 1825$.

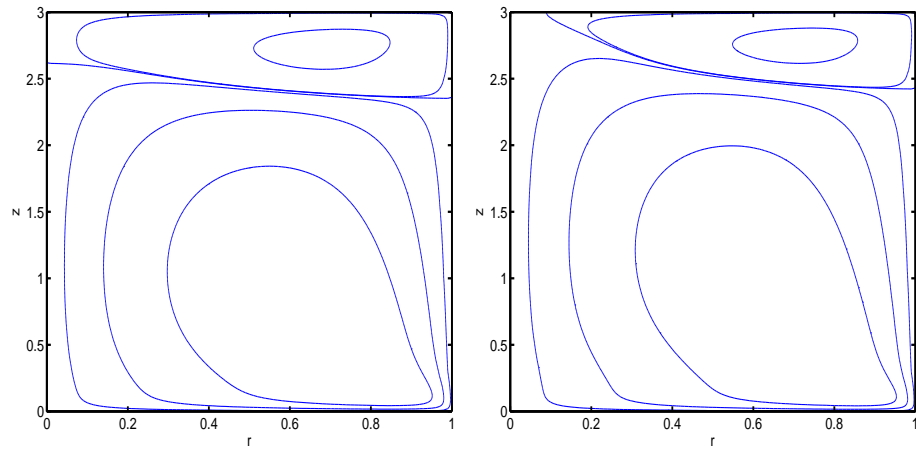


Figure 3.27: Corner crossing of a saddle point. Left panel is for $Re = 800$, right panel is for $Re = 940$. Both cases for $h = 3.0$ and $\gamma = 0.14$.

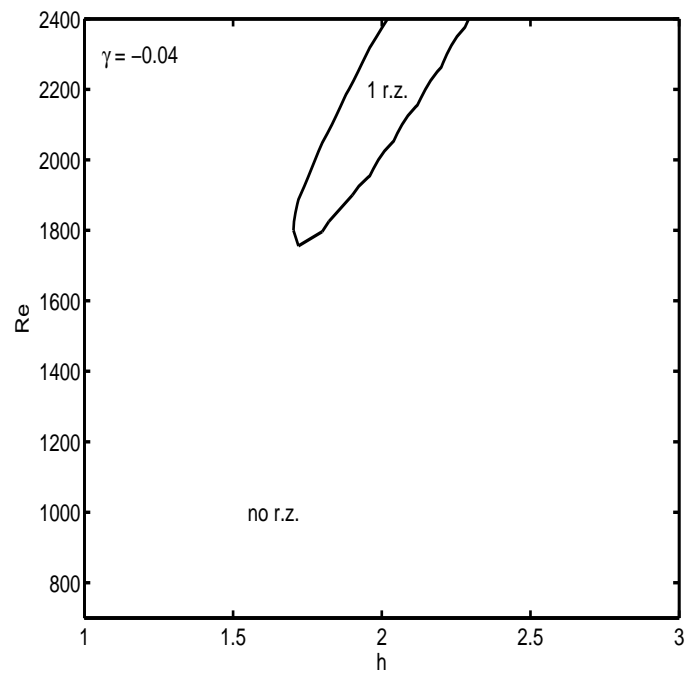


Figure 3.28: Numerically obtained bifurcation diagram for $\gamma = -0.04$.

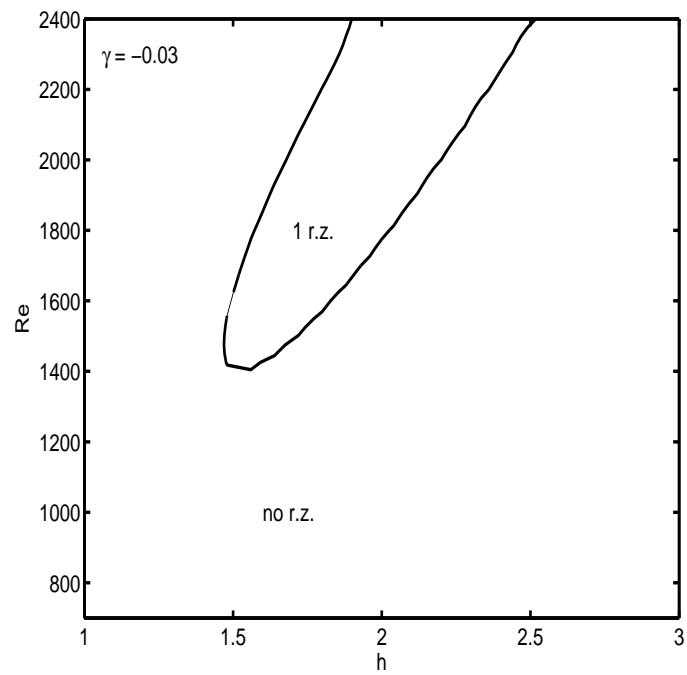


Figure 3.29: Numerically obtained bifurcation diagram for $\gamma = -0.03$.

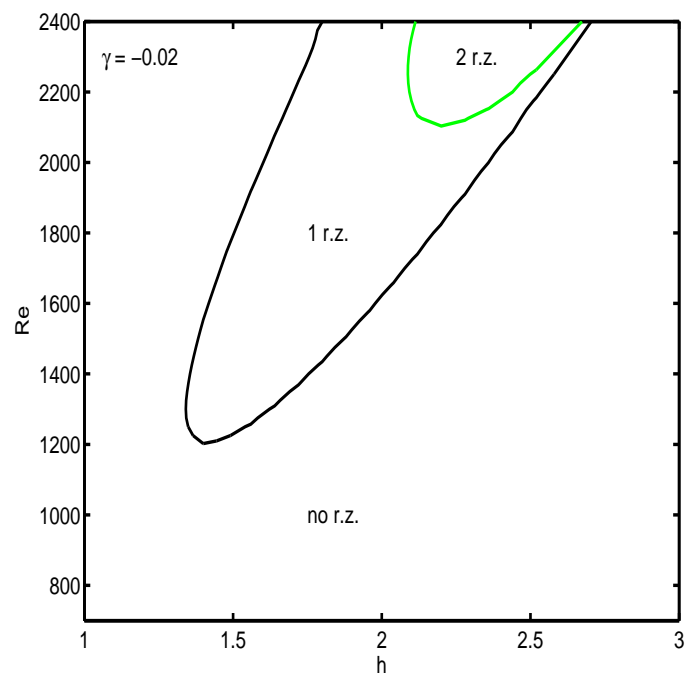


Figure 3.30: Numerically obtained bifurcation diagram for $\gamma = -0.02$.

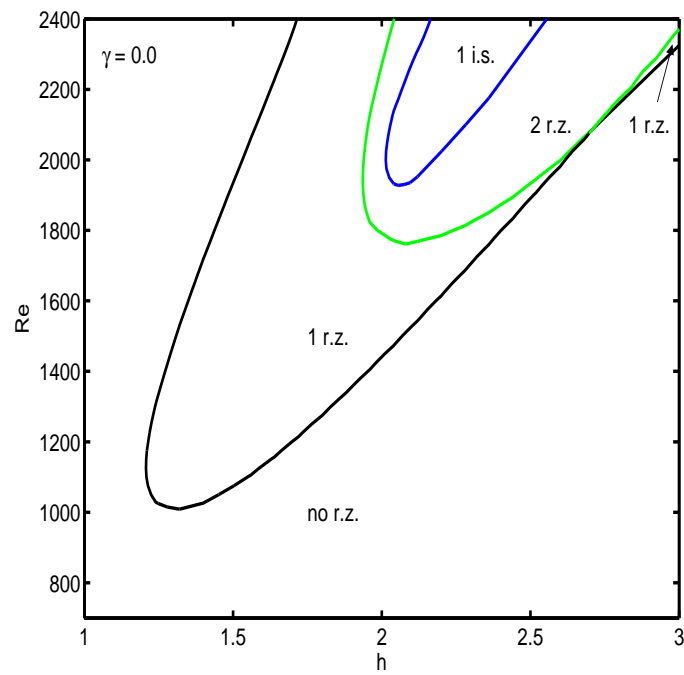


Figure 3.31: Numerically obtained bifurcation diagrams for $\gamma = 0.0$.

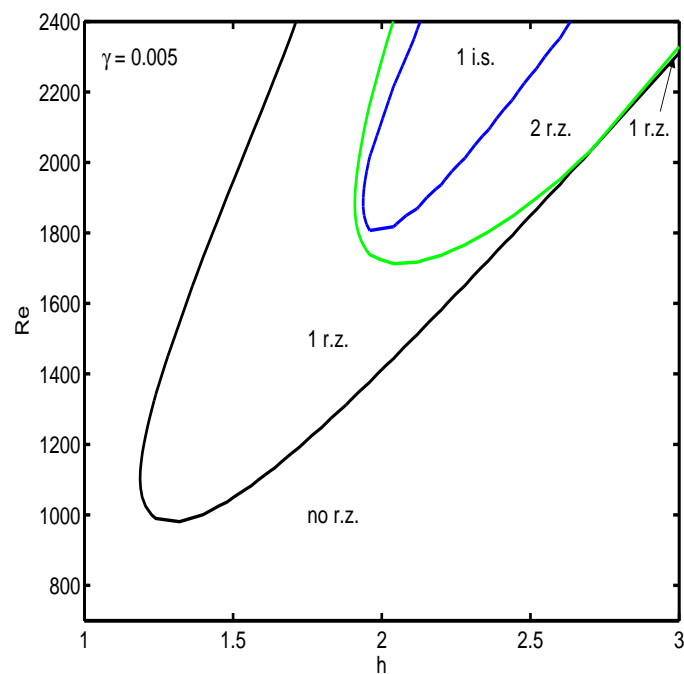


Figure 3.32: Numerically obtained bifurcation diagram for $\gamma = 0.005$.

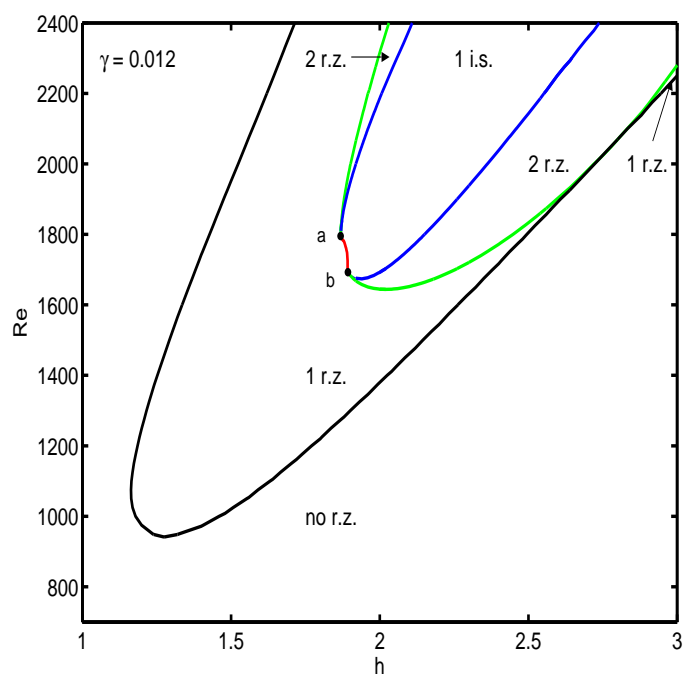


Figure 3.33: Numerically obtained bifurcation diagram for $\gamma = 0.012$.

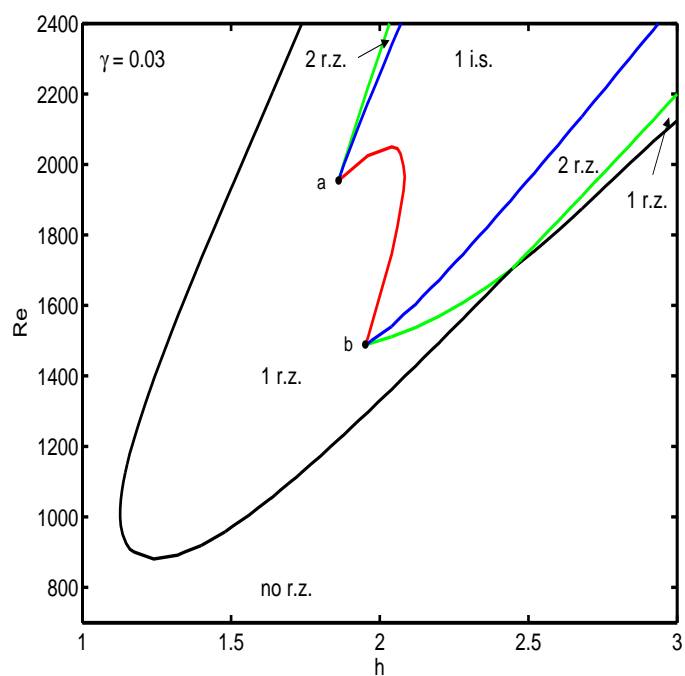


Figure 3.34: Numerically obtained bifurcation diagram for $\gamma = 0.03$

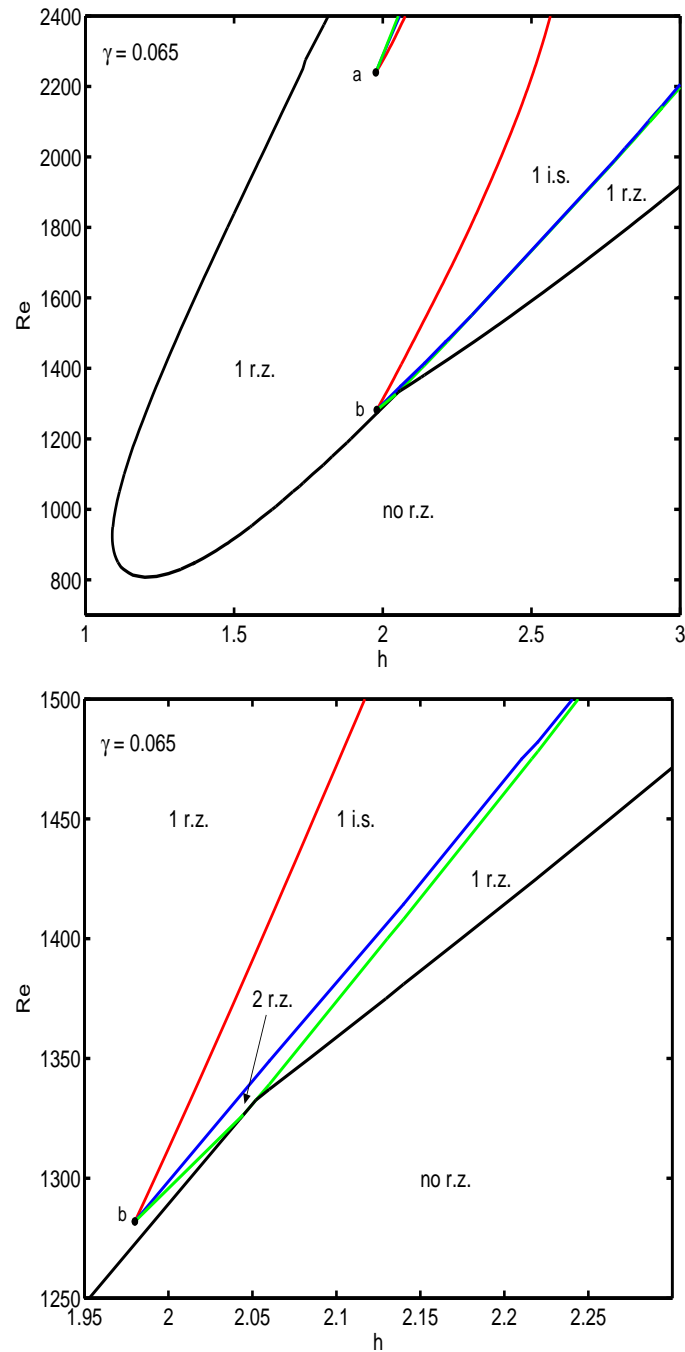


Figure 3.35: Top panel: Numerically obtained bifurcation diagram for $\gamma = 0.065$. Bottom panel: Close-up of part of the bifurcation diagram for $\gamma = 0.065$.

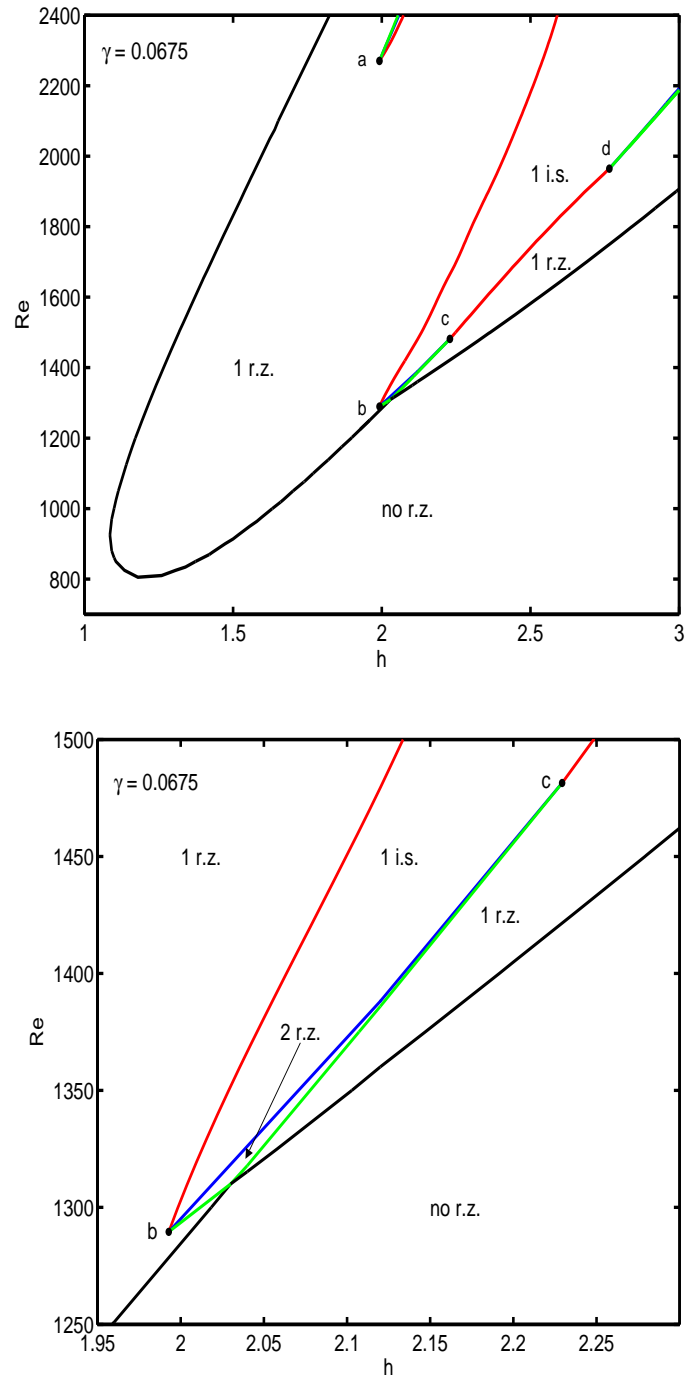


Figure 3.36: Top panel: Numerically obtained bifurcation diagram for $\gamma = 0.0675$. Bottom panel: Close-up of part of the bifurcation diagram for $\gamma = 0.0675$.

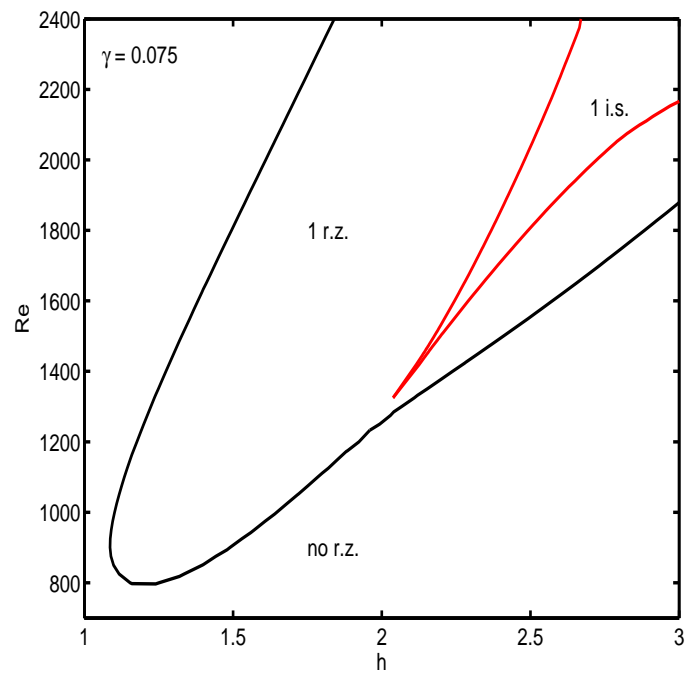


Figure 3.37: Numerically obtained bifurcation diagram for $\gamma = 0.075$.

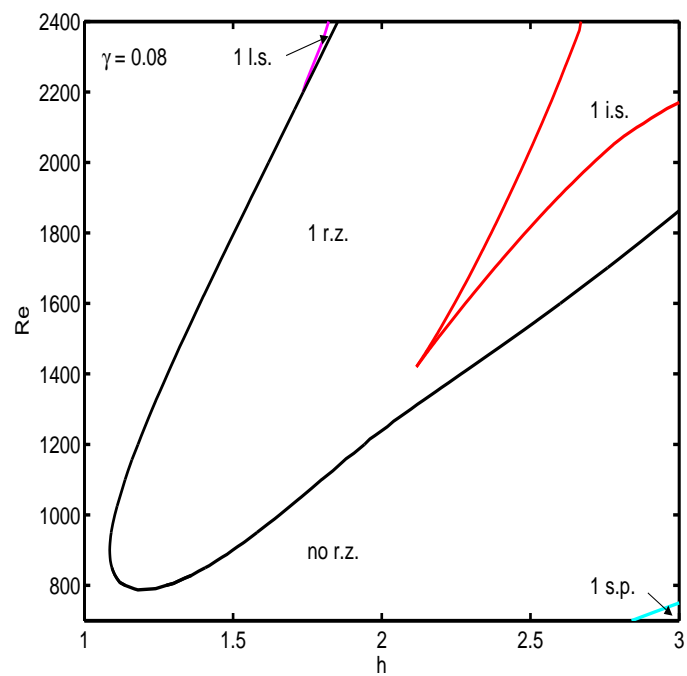


Figure 3.38: Numerically obtained bifurcation diagram for $\gamma = 0.08$.

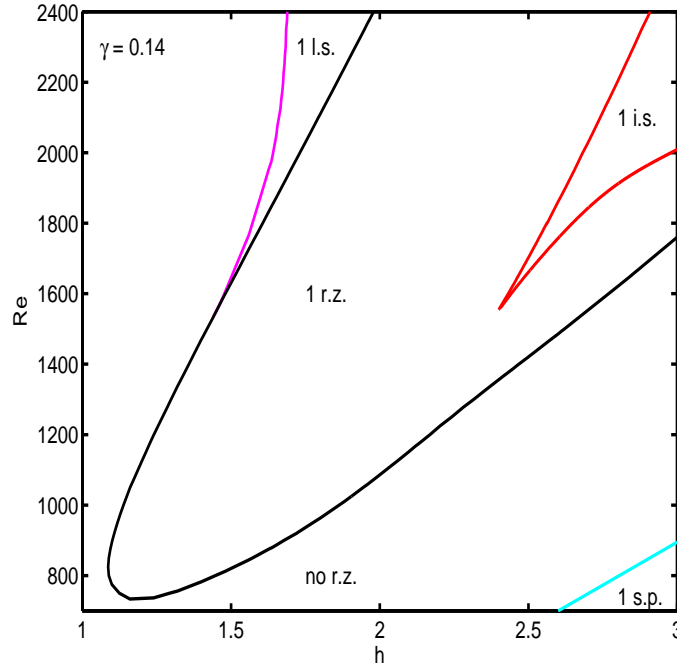


Figure 3.39: Numerically obtained bifurcation diagram for $\gamma = 0.14$.

This recirculation zone is formed by the black creation bifurcation curve. The bifurcation diagram in figure 3.29 for $\gamma = -0.03$ shares qualitatively the same structure as the previous bifurcation diagram, except now the domain where only one recirculation zone exists situated in the center part has moved downwards and increased in area. Thus the area where only one recirculation zone exists has increased with increasing γ -value. One would then expect that the domain where only one recirculation zone exists would decrease with decreasing γ -value and this shows to hold true. For the case of $\gamma = -0.05$ we have found no recirculation zones for the set of parameter values $h \in [1.0; 3.0]$ and $Re \in [700; 2400]$. We do not show the diagram for $\gamma = -0.05$.

The next bifurcation diagram is found in figure 3.30. It shows the bifurcation curves for the case of $\gamma = -0.02$. The area where only one recirculation zone exists has again increased and moved downwards in the bifurcation diagram. Embedded in this area a new area in the top center part of the diagram has emerged consisting of two recirculation zones. The new second recirculation zone is formed by crossing the green creation bifurcation curve.

Figure 3.31 shows the bifurcation diagram for $\gamma = 0.0$. Compared to the above diagram for $\gamma = -0.02$ we see that now a domain consisting of an inner structure recirculation zone has appeared as well in the top center part of the diagram. The new area of the inner structure recirculation zone is embedded in the area consisting of two recirculation zones. The inner structure recirculation zone is formed by crossing the blue merging bifurcation curve.

The bifurcation diagram for $\gamma = 0.005$ shown in figure 3.32 is qualitatively similar to the diagram for $\gamma = 0.0$. The quantitative difference is that now the green creation bifurcation curve and the blue merging bifurcation curve have moved much closer towards each other and are close to being tangent in the center part of the diagram.

In figure 3.33 for $\gamma = 0.012$ we see that a qualitative change has taken place. Two codimension 2 points and a red cusp bifurcation curve have emerged. The red cusp curve meets the two green

creation bifurcation curves and two blue merging bifurcation curves in the two codimension 2 points. We have denoted the codimension 2 points a and b respectively. Thus for a γ -value between $\gamma = 0.0$ and $\gamma = 0.012$ a codimension 3 point must have appeared changing the topology of the bifurcation diagram. One might speculate that this codimension 3 point appears at the γ -value where the green creation and the blue merging bifurcation curves are tangent. We will return to this issue in section 3.3.9. The examples of the creation, merging and cusp bifurcations as given in the figures 3.13, 3.14, 3.15 and 3.24 were chosen using the bifurcation diagram for $\gamma = 0.012$.

The bifurcation diagram in figure 3.34 for $\gamma = 0.03$ is qualitatively similar to the diagram for $\gamma = 0.012$. We notice however that the red cusp bifurcation curve has extended more upwards in the diagram and the distance between the two codimension 2 points a and b has increased.

Continuing to the diagram in the top panel of figure 3.35 which is for $\gamma = 0.065$ we see that no qualitative changes have occurred compared to the above diagram for $\gamma = 0.012$. But quantitatively the red cusp curve has extended further up and out of the considered parameter range. Furthermore the codimension 2 point b has moved significantly closer to the black creation bifurcation curve. Also the green creation and blue merging bifurcation curves have become almost parallel and have moved extremely close to each other as seen in the enlargement of a part of the bifurcation diagram in the bottom panel of figure 3.35.

Another qualitative change in topology of the bifurcation diagrams is shown for $\gamma = 0.0675$ in the top panel of figure 3.36. Two new codimension 2 points denoted c and d and yet a red cusp bifurcation curve have emerged in the leftmost part of the diagram. The type of bifurcation scenario resulting in the codimension 2 points c and d resembles the bifurcation scenario taking place for the formation of the points a and b . The bottom panel of figure 3.36 shows an enlargement of a part of the bifurcation diagram. The close up shows the bifurcation curves ending at the two codimension 2 points b and c . These bifurcation curves together with the points b and c form a swallow-tail like structure.

Again in the next bifurcation diagram seen in figure 3.37 for $\gamma = 0.075$ a qualitative change in topology of the bifurcation diagrams has taken place. The point a has moved upwards and out of the diagram. The point d has moved leftwards and also out of the diagram. Further we see that the blue and green bifurcation curves together with the points b and c have vanished in a bifurcation taking place between $\gamma = 0.0675$ and $\gamma = 0.075$. A sharp cusp has been formed on the red cusp bifurcation curve instead. The terminology might inconveniently cause some confusion. The cusp bifurcation has been introduced in figure 3.8 and the red bifurcation curve shows where this cusp bifurcation takes place when traversing parameter space (h, Re) . Now, as it turns out, the red curve of cusp bifurcations happens in it self to form a cusp. The bifurcation scenario taking place has presumably involved a codimension 3 point. The two points b and c have very likely moved closer to each other as the γ -value has been increased from $\gamma = 0.0675$. The codimension 3 point has occurred for a γ -value between $\gamma = 0.0675$ and $\gamma = 0.075$ where the two points b and c have coalesced. We consider an explanation of this bifurcation scenario in section 3.3.9.

In the bifurcation diagram seen in figure 3.38 for $\gamma = 0.08$ two new domains appear. One in the top left part corresponding to the domain where the loop structure *l.s.* exists. The loop is created via the cusp bifurcation by crossing the magenta line from the left. The loop attaches to the center axis at the black bifurcation line forming a recirculation zone. The other domain appears in the bottom left part of the diagram. In this domain the saddle point *s.p.* exists. Crossing the cyan bifurcation curve from below the saddle point crosses the top left corner of the meridional plane and appears on the cylinder lid. In figure 3.38 for $\gamma = 0.14$ the two new domains have increased in area.

We have now commented on the numerically obtained bifurcation diagrams. The changes

in topology of the bifurcation diagrams are seen to be extremely sensitive to changes in the γ -parameter. Further, two types of bifurcation scenarios were encountered. The first type occurred between the γ -values $\gamma = 0.005$ and $\gamma = 0.012$ and again between $\gamma = 0.065$ and $\gamma = 0.0675$. The second type took place between the γ -values $\gamma = 0.0675$ and $\gamma = 0.075$. A loop appears for $\gamma = 0.08$ and creates a recirculation zone by attaching to the center axis.

3.3.9 Interpreting the bifurcation scenarios

We here explain qualitatively the first two types of bifurcation scenarios encountered in section 3.3.8. An important reason to seek a theoretical understanding of the numerical bifurcation diagrams is that this will ensure us that we have captured all the quantitative different topologies in the series of diagrams.

The numerical bifurcation diagrams were constructed by keeping γ constant in parameter space (h, Re, γ) . Thus the bifurcation curves are the traces where the plane surface for a fixed γ intersects the bifurcation surfaces embedded in (h, Re, γ) . In a similar manner we construct theoretical bifurcation curves by considering a surface intersecting the bifurcation surfaces of the normal form bifurcation diagrams.

The two numerical bifurcation scenarios are at least of codimension 3 as it takes all three of the bifurcation parameters h , Re and γ to unfold them. Furthermore the two scenarios each involve two codimension 2 points. The scenarios indicate that these two codimension 2 points merge in what has to be a codimension 3 point. As both types of scenarios involve the creation bifurcation, the merging bifurcation and the cusp bifurcation the qualitative explanation needs to be based on a normal form having an unfolding which contains these bifurcations. This implies that neither the linear form (3.15) nor the second order normal form (3.77) are suitable. But the third order normal form (3.78) and the fourth order normal form (3.79) are valid candidates.

The first type of numerical bifurcation scenario corresponds to the formation of the two codimension 2 points a and b and the formation of the two codimension 2 points c and d and can be understood qualitatively by virtue of the normal form (3.78) with bifurcation diagram seen in figure 3.8. For the normal form we found that the creation bifurcation curve is given by

$$\mu - \frac{2}{3}\sqrt{c_1^3} = 0 \quad (3.105)$$

and the merging bifurcation curve is given for

$$\mu + \frac{2}{3}\sqrt{c_1^3} = 0. \quad (3.106)$$

The cusp bifurcation curve is given for $c_1 = 0$ and $\mu < 0$ which can also be written as

$$c_1\sqrt{-\mu} = 0 \quad \text{for} \quad \mu < 0. \quad (3.107)$$

We assume that the normal form parameters μ and c_1 and the parameters h , Re and γ relate, locally near a codimension 2 point (Re^*, h^*, γ^*) as

$$c_1 = (Re - Re^*) \quad \text{and} \quad \mu = -(Re - Re^*) + (h - h^*)^2 - (\gamma - \gamma^*) \quad (3.108)$$

corresponding to a quadratic degeneracy in the dependence of μ as a function of h . Setting $\bar{Re} = (Re - Re^*)$, $\bar{h} = (h - h^*)$, $(\bar{\gamma} = \gamma - \gamma^*)$ and keeping $\bar{\gamma} = \bar{\gamma}_0$ fixed we have that the bifurcation

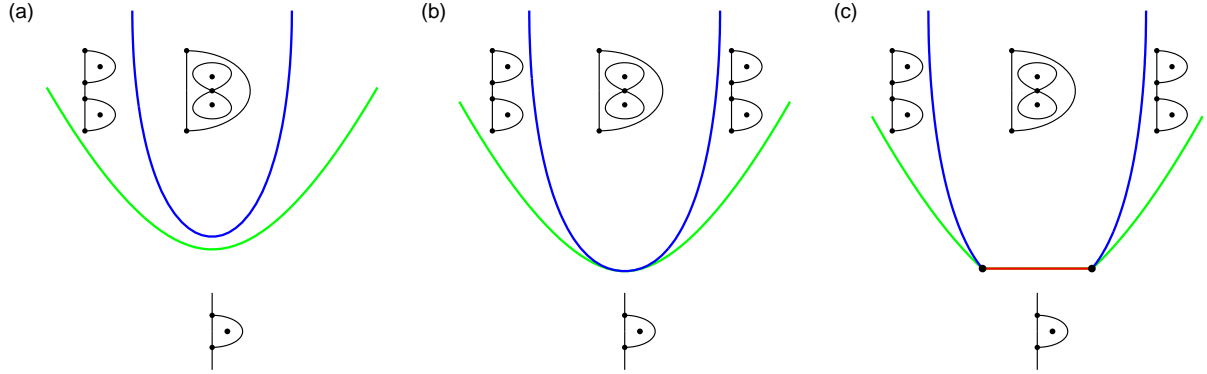


Figure 3.40: Bifurcation scenario obtained by inserting the second order folded surface (3.108) into the normal form (3.78). The scenario has been obtained by varying $\bar{\gamma}_0$.

diagrams for (3.108) can be found by inserting (3.108) into (3.105), (3.106) and (3.107) yielding the creation bifurcation curve given by

$$-\bar{R}e + \bar{h}^2 - \bar{\gamma}_0 - \frac{2}{3}\sqrt{\bar{R}e^3} = 0 \quad (3.109)$$

and the merging bifurcation curve given as

$$-\bar{R}e + \bar{h}^2 - \bar{\gamma}_0 + \frac{2}{3}\sqrt{\bar{R}e^3} = 0. \quad (3.110)$$

The cusp bifurcation curve is given for

$$\bar{R}e\sqrt{\bar{R}e - \bar{h}^2 + \bar{\gamma}_0} = 0. \quad (3.111)$$

Choosing $\bar{\gamma}_0 = -0.1$ and solving (3.109), (3.110) and (3.111) results in the bifurcation diagram (a) seen in figure 3.40. For $\bar{\gamma}_0 = 0$ we find the bifurcation diagram (b) and finally the choice $\bar{\gamma}_0 = 0.1$ results in the bifurcation diagram (c) of figure 3.40. In (b) the green creation and blue merging bifurcation curves are tangent. The point in which they are tangent constitutes a codimension 3 point.

We see that the topology of the bifurcation diagrams in panel (a) and (c) of figure 3.40 are topologically equivalent to the numerical bifurcation diagrams in figure 3.32 and figure 3.33 involving the formation of the codimension 2 points *a* and *b*. The bifurcation diagrams (a) and (c) are also topologically equivalent to the numerical bifurcation diagrams in figure 3.35 and figure 3.36 involving the formation of the codimension 2 points *c* and *d*.

The second type of bifurcation scenario corresponding to the coalescence of the two codimension 2 points *b* and *c* seen in figure 3.36 can be understood qualitatively by virtue of the bifurcation diagram for the normal form (3.79) intersected by a plane. This is illustrated in figure 3.41. Varying continuously the orientation of the intersecting surface we can obtain the bifurcation scenario shown in figure 3.42. The bifurcation curves are the traces formed by the intersecting surface with the bifurcation surfaces. In panel (a) of figure 3.42 the bifurcation diagram contains a black creation bifurcation curve and a red cusp bifurcation curve characterized by having a cusp point. This cusp point of the red cusp bifurcation curve touches the black creation bifurcation curve in a codimension 3 point in panel (b). In panel (c) a swallow-tail like structure has unfolded with two codimension

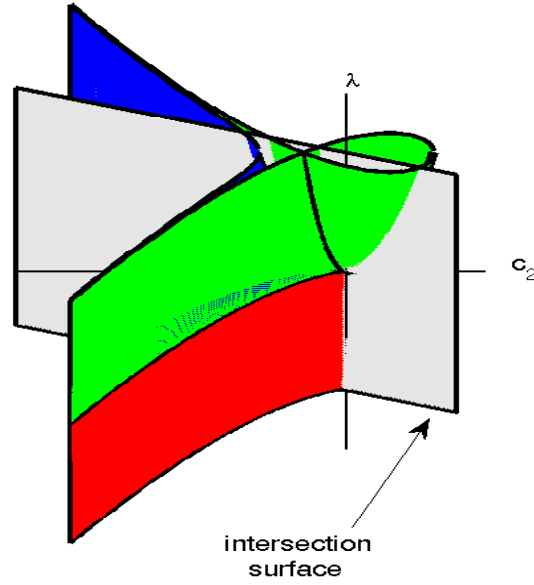


Figure 3.41: Bifurcation surfaces for the normal form (3.79). The intersection plane has normal vector $(n_1, n_2, n_3)^T = (-0.01, 1.0, 0.8)^T$ going through the point $(\lambda_0, c_{20}, c_{10}) = (-0.5, -0.6, 0.5)$.

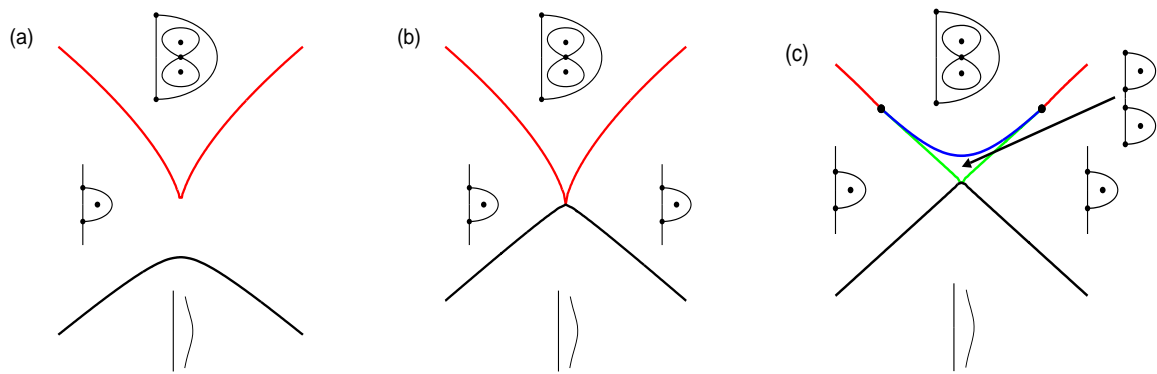


Figure 3.42: Bifurcation scenario of the normal form (3.79) for $N = 4$. The bifurcation diagrams are obtained by intersection of the bifurcation surfaces by a plane surface having normal vector $(0, -1, -1)^T$. In case (a) the plane surface goes through the point $(0, 0, 0.5)$. In case (b) and (c) the plane goes through the points $(0, 0, 0)$ and $(0, 0, -0.5)$ respectively.

2 points. It is seen that the swallow-tail like bifurcation structure involving the two codimension 2 points b and c and the bifurcation curves ending at b and c in figure 3.36 is topologically equivalent to the right bifurcation diagram in figure 3.42. The bifurcation diagram in figure 3.37 involving the cusp found on the red cusp bifurcation curve and the black creation bifurcation curve is topologically equivalent to the left panel of figure 3.42. Qualitatively the second type of numerical bifurcation scenario can be understood by the bifurcation scenario in figure 3.42.

3.4 Conclusions

In this chapter we apply the codimension 1 condition first found in Brøns (1999). The codimension 1 condition is derived by using normal form theory to the streamfunction at the cylinder axis of the cylinder with rotating end-covers. When the codimension 1 condition is fulfilled a creation or merging bifurcation takes place on the center axis. Further the normal form analysis shows that cusp bifurcations can occur. We have devised an isocline method to locate a cusp bifurcation.

The codimension 1 conditions and the isocline method were implemented in a post process procedure and applied to direct numerical simulations of the cylinder with rotating end-covers. From this, bifurcations diagrams were constructed and two types of bifurcation scenarios involving codimension 3 points were found and interpreted. These scenarios show how one or two recirculation zones may be formed from stagnation points on the center axis and how they may interact. Further a third type of bifurcation scenario was observed corresponding to an unfolding of the non-simple degenerate codimension two bifurcation. In this scenario a recirculation zone is formed as an in-flow loop attaches to the center axis. The loop is created by a cusp bifurcation taking place close to the axis. This scenario has not, to our knowledge, been reported in the literature before. We consider this a new way in which vortex breakdown may occur.

The numerically obtained bifurcation diagrams were constructed by using the codimension 1 condition. Thus one may wonder why it is necessary to derive the codimension 2 and 3 conditions together with the affiliated bifurcations diagrams. But these bifurcation diagrams for the higher order of codimension show invaluable in assisting us in the interpretation of the numerical obtained bifurcations diagrams.

Further we must note that the bifurcation diagrams constructed in this chapter only show bifurcations taking place on the center axis or close to as is the cases of the cusp bifurcations considered. We have not investigated bifurcations taking place on the top or bottom lid. Hence for the same values of the parameters Re , h or γ as give in the bifurcation diagrams lid or bottom bifurcations might occur and corresponding bifurcation diagrams have to be overlayed the diagrams shown here.

It was observed that changes in topology of the numerical bifurcation diagrams are extremely sensitive to changes in the γ -parameter. Further the three codimension 3 points are occurring very close to each other in parameter space. Thus it seems likely that if new bifurcation parameters were introduced for instance by changing the system geometry or by not keeping the system temperature constant one could imagine that in parameter space these three codimension 3 points could coalesce into a codimension 5 point, which would probably lead to even more complicated bifurcation diagrams. One could change the system geometry by considering a frustum of a right circular cone instead of a cylinder which would introduce a varying radius in the parameter space. Further if the temperature were not kept constant one would need to consider the energy equation along side the Navire-Stokes equation, which would also introduce parameters.

In section 3.3.8 we noted that for small values of γ slightly below $\gamma = -0.04$ there were no

recirculation zones on the cylinder axis for the considered parameter range as the creation bifurcation curve moves up and out of the bifurcation diagram. Thus the γ -parameter can be considered a control parameter. If one desires to study the cylinder with rotating end-covers but wishes to avoid the vortex breakdown one can do so by controlling γ .

The post process technique might be applied to other systems, for instance the axisymmetric annulus as investigated via direct numerical simulations by Tsitverblit and Kit (1996).

4

Laminar Flow Topology of the Cylinder Wake

It is only fair to say that the fluid flow in the wake of the cylinder is the classical study of fluid flows behind bluff bodies and in particular the incompressible flow around the circular cylinder has become the canonical prototype for investigating bluff body wakes. The one phenomenon that has motivated and created a massive bulk of investigations over great many decades is the formation and shedding of vortices. Recordings of observation and fascination of vortices dates as far back as to the sixteenth century where Leonardo da Vinci (1509) made his studies and drawings on the nature of water. Some of his drawings show surface flows past obstacles forming vortices.

Since the observations of da Vinci many researchers have made both experiments and theoretical studies and within the last two to three decades computer simulations have complemented experiment and theory in helping researchers gaining better understanding. Modern experimental investigations of flow wakes starts among others with the flow visualizations by Prandtl. Prandtl published photos of the flow around the circular cylinder in 1905, see sketches and references in Acheson (1996). Together with co-workers Prandtl made as early as in the 1920s movie recordings and their results have been not only cited but used as recent as in the work of Perry et al. (1982) which shows the refinement of the experimental techniques that Prandtl devised. For more on Prandtl, see for instance Oswatitsch and Wiegardt (1987).

Apart from Prandtl, numerous research groups have made flow visualizations and a catalogue has been collected in “An Album of Fluid Flows” by van Dyke (1982). In figure 4.1 we show four photos taken from this album. The photos show the flow around the circular cylinder at different Reynolds numbers. For the flow around the circular cylinder the Reynolds number Re is given as $Re = DU_\infty/\nu$ where U_∞ is the free stream or parallel oncoming flow velocity, D is the diameter of the cylinder and ν is the kinematic viscosity of the fluid. In the top left panel of figure 4.2 a sketch shows the parallel oncoming flow velocity U_∞ , the diameter D of the cylinder as well as the coordinate system to impose on the photos in figure 4.1. The x - y coordinate system defined in figure 4.2 is fixed at the cylinder and later we shall refer to it as the cylinder system. In all four of the photos in figure 4.1 the view point is along the center axis of the cylinder.

If a fixed position in the flow is considered over time and lines are joined between the particles passing this position then these lines are the streaklines. Hence, a streakline shows the instantaneous result of following tracer particles released from a fixed point. The photos in figure 4.1 show

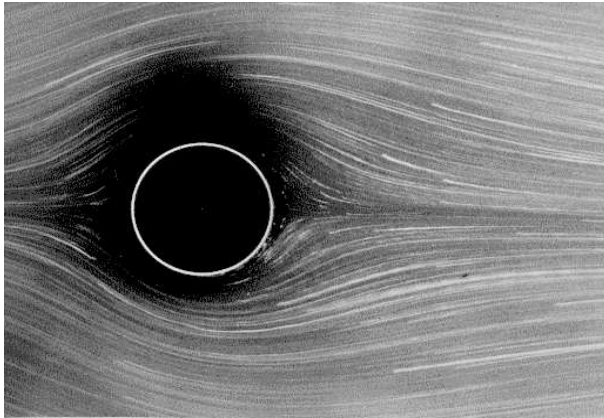
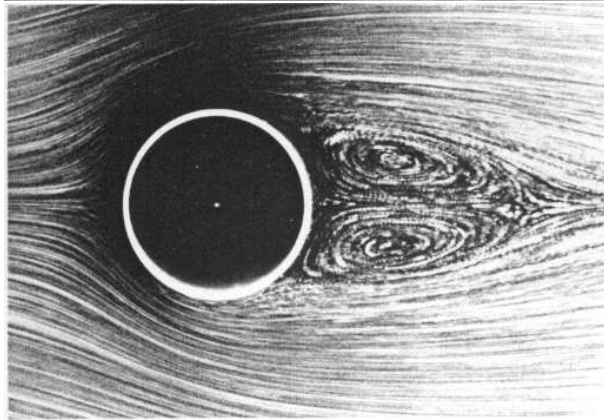
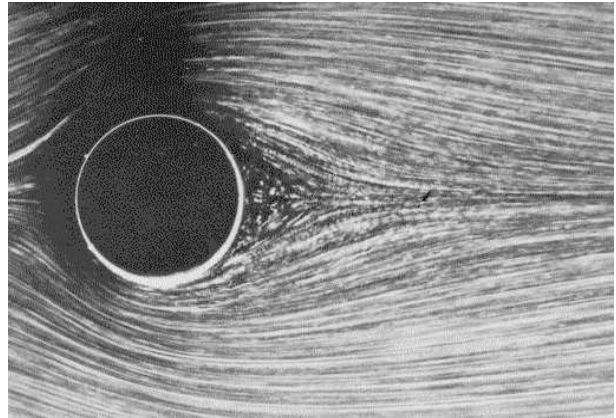
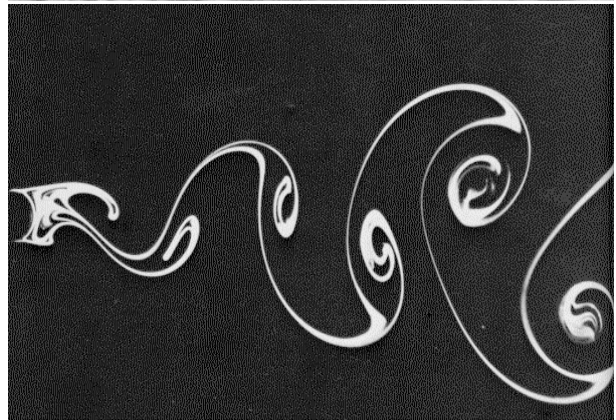
$Re = 1.54$  $Re = 9.6$  $Re = 26$  $Re = 140$

Figure 4.1: The above experimentally recorded photos from van Dyke (1982) show different stages of the vortex shedding process taking place in the wake of the circular cylinder. The top left photo shows the streamline pattern for the steady creeping flow for a Reynolds number of $Re = 1.54$. No vortical structures are observed. Next follows a streamline recording for $Re = 9.6$ and we see that a wake cavity has developed in the steady wake. The cavity is seen to be symmetric. For the case of $Re = 26.0$ the wake is still steady but the symmetric cavity has become more pronounced. The last photo for a Reynolds number of $Re = 140.0$ shows the streakline pattern. The streaklines help visualizing the von Kármán vortex street in the now unsteady wake.

streaklines for various Reynolds numbers.

Streamlines on the other hand are at a given instant in time tangential to the velocity field at every point in the flow. The streamlines therefore show in which direction a fluid parcel moves in that very instant. In a flow with steady velocity field the streamlines are consequently stationary and for this special situation the streamlines coincide with the streaklines and traces out the trajectory which a fluid parcel takes in the fluid flow. To make streamlines in a flow appear on photos small particles are introduced into the flow. The particles are then illuminated using a sheet of laser light and the streamlines can then be recorded on a film by using short time exposure approximating an infinitesimal time instant.

The flow in the first photo in figure 4.1 for $Re = 1.54$ is steady and therefore shows the streamlines. We observe that the flow, coming from the left, follows or creeps around the cylinder and leaves almost undisturbed behind the cylinder. No vortices are seen.

The second photo shows the flow for the Reynolds number $Re = 9.6$. At this Reynolds number

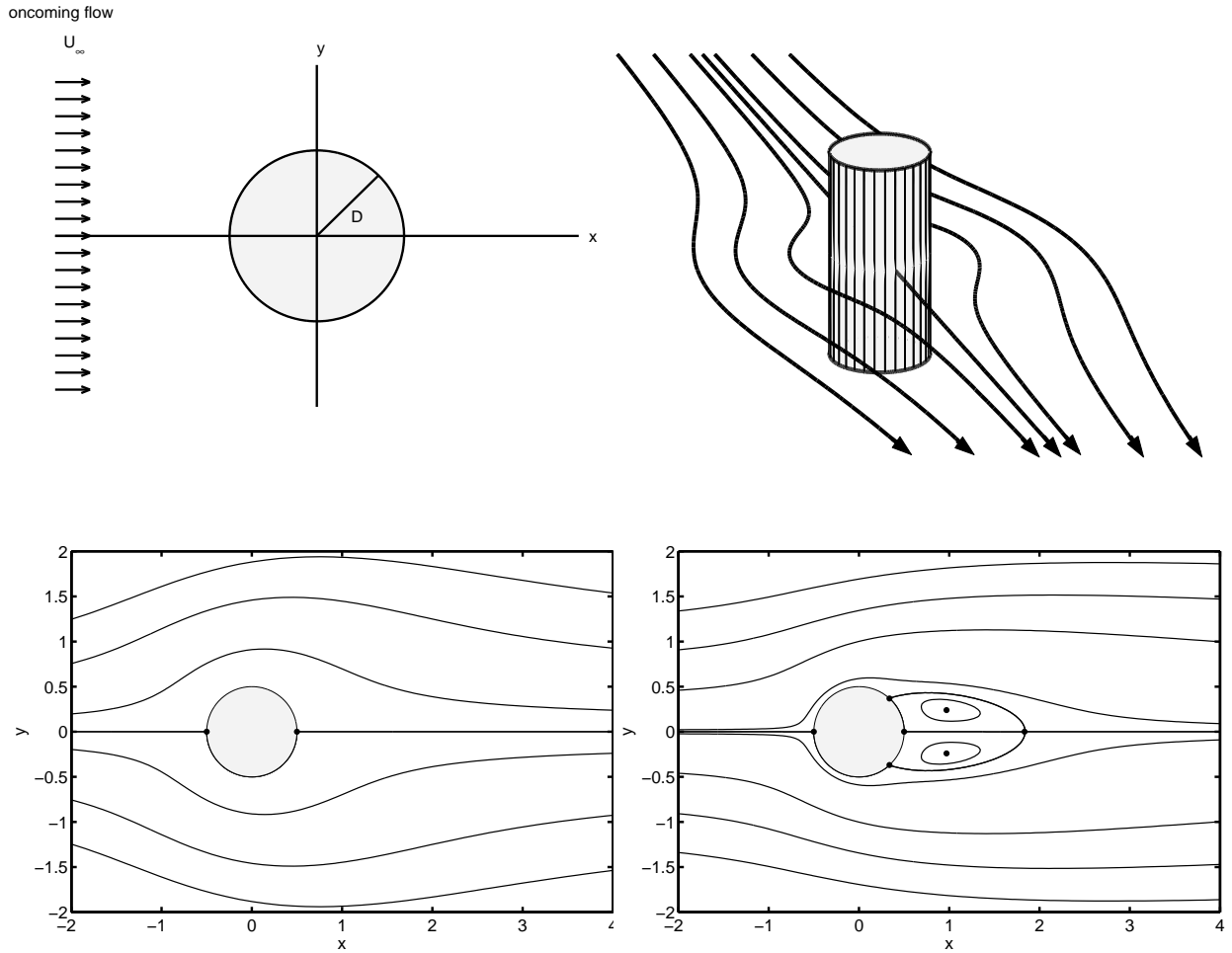


Figure 4.2: The top left sketch shows the oncoming flow with free stream velocity U_∞ . The gray-shaded circle represents a side view of the cylinder. Further is shown the x - y coordinate system to impose on the photos in figure 4.1. We denote the x - y system the cylinder system which is fixed at the cylinder center. The top left panel shows how to perceive the parallel shedding flow in three dimensions. In the two bottom panels we show two simulations of the streamfunction. The lower left panel for $Re = 1.54$ and lower right panel for $Re = 26.0$. In the lower left panel no cavity has been formed whereas this is the case in the lower right panel. The simulations agree with the corresponding observations in figure 4.1. In section 4.7 we compare quantitatively simulation and experiment.

the flow is as in the previous case still steady but comparing with the previous case we now notice a development in the flow pattern. Behind the cylinder a small cavity has been formed. The cavity seems to be symmetric and is hence called the symmetric cavity or bubble in the literature.

The cavity has become more pronounced in the third photo, which shows the streamlines for the flow pattern at Reynolds number $Re = 26$. For this Reynolds number the flow is still steady. In this case it becomes a bit more evident that the cavity is symmetric and further we more clearly see the inner structure of the cavity. From a close inspection an interpretation on the topology of the cavity indicates that the cavity consists of three separation points at the cylinder wall with two centers and a saddle point in the near wake.

In the last photo in figure 4.1 for Reynolds number $Re = 140$ the flow is unsteady, in fact periodic and shows the streaklines in the flow. The streaklines were achieved using dye as an indicator. The dye traces we see on the photo were formed by introducing dye close to the cylinder

boundary at two places, one position near the top part of the cylinder and one near the lower part of the cylinder boundary. The dye traces in the wake are seen to form a trailing series of whirling structures known in the literature as the von Kármán vortex street. Movie recordings of the periodic wake show vortex shedding.

Experiments show that for low Reynolds numbers the vortex shedding is orthogonal to the cylinder center axis and parallel with the free stream. Further the vortex shedding is translation invariant in the direction of the center axis of the cylinder, that is, in the direction of the z -axis orthogonal to the x - y plane shown in the top left panel of figure 4.2. Due to this observed translation invariance parallel vortex shedding can be considered a two dimensional phenomenon.

In the instantaneous streamline sense figure 4.1 summarizes the following experimentally observed scenario given with respect to the Reynolds number Re :

For $Re < \sim 6$: The steady two dimensional flow creeps around the cylinder and no whirling structures are observed in the wake.

For $6 < Re < \sim 49$: The steady two dimensional flow has developed a symmetric cavity with two centers and a saddle point in the near wake. The two centers are typically termed vortices in the literature.

For $49 < Re < \sim 180$: A transition has taken place at $Re = \sim 49$ leaving the two dimensional flow with a periodically oscillating wake. The transition is due to a Hopf bifurcation causing a symmetry breaking of the cavity.

For $Re > 180$: The periodic flow turns three dimensional and several three dimensional shedding modes appear in the range of $180 < Re < 230$. For even higher Reynolds numbers the flow becomes turbulent.

The above overview of experimental facts is only a small part of the overview given in the review article by Williamson (1996). The article contains an overview of the vortex shedding process for the Reynolds number in the range of $Re = 0$ and up to a value of several hundred thousands. Further Williamson (1996) contains an elaborate list of references to earlier reviews. It has been proven numerically that the transition turning the velocity field periodic comes about by virtue of a Hopf bifurcation, see for instance Provansal et al. (1987), Noack and Eckelmann (1994) and Zhang et al. (1995). In the fluid mechanics literature the Hopf bifurcation is often analyzed by a Stuart-Landau equation. The normal form for the Hopf bifurcation and the Stuart-Landau equation are equivalent. The Stuart-Landau equation comes about by a complex formulation of the Hopf bifurcation normal form.

Numerical simulations have during the past decade become so involved that three dimensional numerical investigations of bluff body wakes have become feasible. For instance in the work of Zhang et al. (1995) three dimensional numerical investigations have been compared to experiments and reports on the observation of several three dimensional laminar shedding modes breaking the translation invariance mentioned above. The debate in the article Zhang et al. (1995) contributes to clarifying and classifying the various shedding modes. In spite of the newly started work on the three dimensional wake active interest is still taken on the two dimensional laminar vortex shedding. For instance the classical Strouhal-Reynolds number relationship of Rosko (1954) has recently been revised in the work of Fey et al. (1998). Furthermore the issue of controlling the wake has received recent interest in the works of Hernández and Baudet (2000) and Hernández

and Pacheco (2002) where two dimensional numerical simulations and experimental results have demonstrated the feasibility of a new procedure for controlling and preventing laminar vortex shedding.

The phenomenon of vortex shedding has not only been studied due to the pure fascination and wonder it captures us with. It has shown necessary to understand the phenomenon closer in an engineering context as well. For instance the erosion of sediment under oil and gas pipe lines situated on the sea bed may create complex vortex shedding which again might cause huge loads on the pipe lines. Ocean oil platforms supported by huge cylinder shaped structures standing on the sea bed are also real world examples of cylinders submerged into water flows and we have all on a windy day heard the singing of a flagpole halyard.

In this chapter we will confine ourself to study the above described laminar two dimensional parallel vortex shedding scenario. The article of Perry et al. (1982) has initiated this and the works of Hartnack (1999b), Petersen (2002) and Niss and Jakobsen (2002). Bakker (1991) also studies the steady flow along a wall, although the work omit applying the normal form technique. All of the mentioned references take on a topological fluid dynamics viewpoint in the framework of dynamical systems theory and we shall be doing the same here. Above we introduced the coordinate system x - y in which the two dimensional shedding process takes place. The flow velocity $\mathbf{v}(x, y)$ thus consists of the two velocity components $\mathbf{v} = (u, v)^T$. Further as we consider the flow incompressible the velocity field is divergence free $\nabla \cdot \mathbf{v} = 0$ implying that a streamfunction $\psi(x, y)$ can be introduced and the dynamical system we will consider is given as

$$\dot{x} = u = \frac{\partial \psi}{\partial y}, \quad \dot{y} = v = -\frac{\partial \psi}{\partial x}.$$

The shedding scenario has been investigated in numerous of articles but we still believe that there are questions to be considered and previous answers to clarify upon. In Perry et al. (1982) the topology of the instantaneous streamlines for the parallel vortex shedding has been interpreted on the basis of experimental observations, among others the above mentioned movie recordings of Prandtl. These interpretations resulted in the proposal of a qualitative explanation model collected in the figure 2 of Perry et al. (1982). The figure is reproduced here in figure 4.3 for reference. The model seeks to give an explanation of the topology of the instantaneous streamlines as they develops through one cycle of the periodic wake. Only the essential streamlines namely the saddle separatrices are shown in the figure. It is seen that the topology in the proposed model is made up of a recirculation zone or bubble and a separation line emanating from three saddle points situated on the rear part of the cylinder wall together with loops in the wake. A loop consists of a homoclinic saddle connection surrounding a center. In a homoclinic saddle connection two of the separatrices emanating from a saddle point are connected. The loops are thought to be created in a bifurcation process taking place at the rear of the cylinder wall but figure 4.3 does not explicitly show the particular bifurcation assumed to take place. But it is believed that the creation of the loops in the Perry et al. model takes place when the recirculation zone and the separation line coalesces and a loop lifts off the wall. Hartnack (1999b) sets out to put this bifurcation process on firm theoretical ground and it was shown that in terms of the streamfunction ψ analyzed through normal form theory the bifurcation scenario at the cylinder wall could be explained. But, as it turns out, numerical simulations conducted by Petersen (2002) indicated a disagreement with the proposed model shown in figure 4.3. As mentioned Hartnack (1999b) found that the qualitative model proposed by Perry et al. consistently complies with bifurcation theory. But, as we shall see in section 4.2, in the bifurcation analysis assumptions are made and the choice of these assumptions influences the bifurcation scenario found. One can make different assumptions and obtain a different

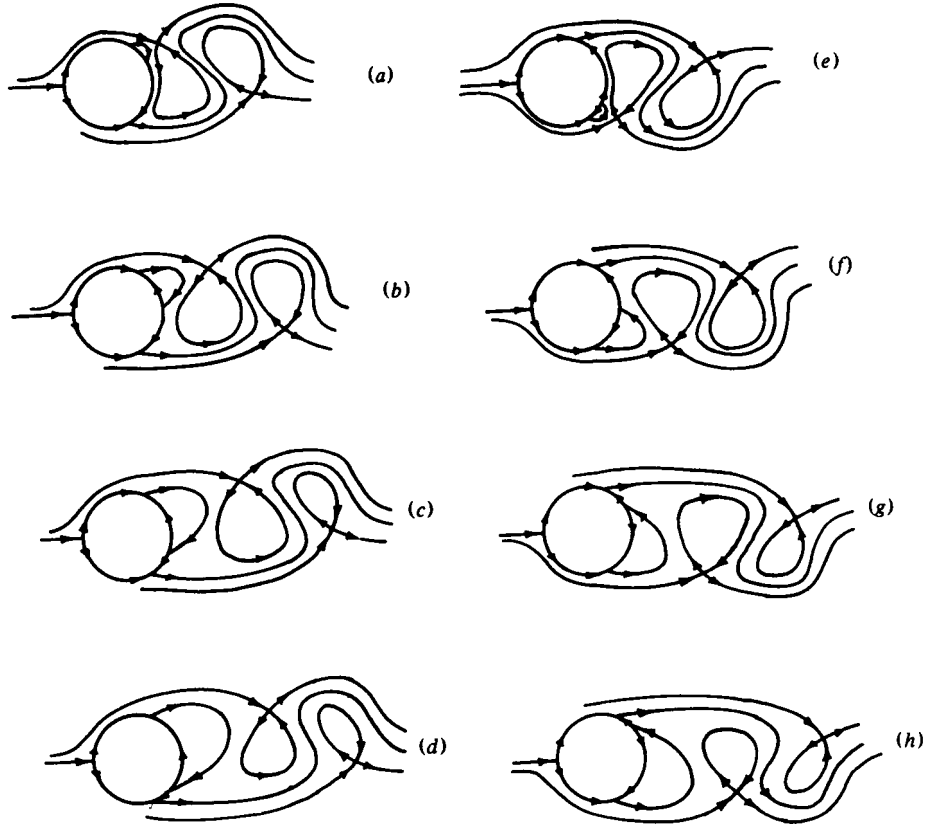


Figure 4.3: The proposed explanation model by Perry et al. (1982) of the instantaneous streamlines for the parallel vortex shedding. Only separatrices are shown. The shedding sequence is from *a* to *h*.

bifurcation scenario. It is this fact and the discovered disagreement with numerical simulations that has motivated the study by Niss and Jakobsen (2002). As we saw in the photos in figure 4.1 and as mentioned in the above overview a symmetric cavity has been formed in the steady wake. One might get the idea that the Hopf bifurcation turning the wake periodic acts as a perturbation of the symmetric cavity leading to a periodically repeating bifurcation scenario and that it is this scenario that has been observed in the numerical simulations by Petersen (2002). The model of Perry et al. and the subsequent analysis of Hartnack (1999b) does not take the symmetry of the cavity into consideration. Niss and Jakobsen (2002) set out to investigate this idea on the symmetric cavity using a theoretical approach similar to the one used in Hartnack (1999b) but now with the different purpose of determining a set of new assumptions to impose on the streamfunction such that the symmetric cavity turns up in the bifurcation analysis. Niss and Jakobsen (2002) succeeded in determining such a set of assumptions and furthermore they showed that an unfolding in parameter space of the streamfunction comply quantitatively with the scenario observed by Petersen (2002). We can further make the remark that the numerical simulations done by Petersen (2002) does not contradict the experimental photos shown in Perry et al. Even though Perry et al. did not get the completely correct qualitative model there is no doubt that the work and the important results of Perry et al. (1982) has set in motion the application of the topological fluid dynamics approach in the quest of understanding the vortex shedding process.

As accounted for above the parallel vortex shedding is sought to be explained on the basis of

the topology of streamline patterns. Further it has shown fruitful to conduct numerical simulations with this topological point of view in mind to complement the experimental observations. The work in Petersen (2002) was limited to the Reynolds number interval $0 \leq Re \leq \sim 50$ and the exact Reynolds numbers at which the various bifurcations take place were not determined. Further some initial investigations on the vorticity field showed too coarse leaving out details thus not suitable to be used as a basis for further conclusions. Moreover in Perry et al. the vorticity field of the parallel shedding process was analyzed in the framework of potential theory. We believe that the conclusions on the vorticity field made on the basis of potential theory can be supplemented by numerical simulations. Hence we have come to the conclusion that a more detailed numerical investigation would be beneficial to complement earlier work and the study conducted here is meant to be a continuation along the lines of Petersen (2002) as well as Niss and Jakobsen and it aims at a descriptive understanding. Thus we will here conduct direct numerical simulations in the range of $Re = [0; 300]$ with the objective to gain an overview of and to clarifying with certainty the instantaneous streamline scenarios taking place. Further we will consider the flow topology in the free stream coordinate system which is fixed relative to the free stream. Lastly we will follow the development of the topology of vorticity field in the same Reynolds number interval. Moreover it has been our aim to precisely determine the values of the Reynolds number in connection with the transition making the velocity field periodic. For instance we determine the Reynolds number Re_{c_1} where the symmetric cavity starts to develop as well as the value Re_{c_2} at which the Hopf bifurcation occurs. We observe and report on other topological bifurcations of the flow field for Reynolds numbers greater than Re_{c_2} . This again to draw comments on conclusions made in Perry et al. where it is believed that the proposed model of figure 4.3 is valid in a much larger parameter interval than the one considered here - a claim that can be true with certain modifications.

The direct numerical simulations we have done are conducted via the code EllipSys2D developed by Michelsen (1992) and Sørensen (1995) and made available to us by Professor J. N. Sørensen at The Department of Mechanical Engineering, The Technical University of Denmark. In validating the simulation code we have compared our simulations with experiments through an experimentally obtained Strouhal number relationship. Furthermore we have made simulations on what we call the normal grid size and the fine grid size. This is to ensure that our simulations show grid independence, for details see section 4.7.

4.1 Modelling

We will consider the fluid flowing around the circular cylinder, as incompressible, laminar and two dimensional. Hence the velocity field $\mathbf{v}(\mathbf{x}, t)$ consists of the two components $\mathbf{v}(\mathbf{x}, t) = (u(\mathbf{x}, t), v(\mathbf{x}, t))^T$ and depends on time t and the spatial coordinates $\mathbf{x} = (x, y)^T$. The coordinate system x - y is having origin fixed at the cylinder center as explained in figure 4.2. We assume that the far field velocity \mathbf{v}_∞ is given as the free stream velocity $\mathbf{v}_\infty = (U_\infty, 0)^T$. The boundary conditions at the cylinder are the no-slip and no-flux conditions. The mathematical model for the incompressible flow around the cylinder consists of the Navier-Stokes equations and the conservation of mass. Due to the incompressibility and the conservation of mass assumption the flow is divergence free. Hence we have

$$\frac{\partial \mathbf{v}}{\partial t} + (\mathbf{v} \cdot \nabla) \mathbf{v} = -\frac{1}{\rho} \nabla p + \nu \nabla^2 \mathbf{v}, \quad \nabla \cdot \mathbf{v} = 0, \quad (4.1)$$

where ν is the kinematic viscosity and ρ the constant fluid density. To non-dimensionalize (4.1) we introduce the following scalings

$$\tilde{x} = \frac{x}{D}, \quad \tilde{y} = \frac{y}{D}, \quad \tilde{t} = \frac{U_\infty}{D}t, \quad \tilde{p} = \frac{p}{p_0}$$

with the characteristic pressure constant chosen to be $p_0 = \rho U_\infty^2$. From the above scalings we get the non-dimensional velocity $\tilde{\mathbf{v}} = \frac{1}{U_\infty} \mathbf{v}$ and especially the non-dimensional far field velocity becomes $\tilde{\mathbf{v}}_\infty = (1, 0)^T$. Inserting the non-dimensional variables into (4.1) and leaving out the tilde notation we get the non-dimensional Navier-Stokes and conservation of mass equations

$$\frac{\partial \mathbf{v}}{\partial t} + (\mathbf{v} \cdot \nabla) \mathbf{v} = -\nabla p + \frac{1}{Re} \nabla^2 \mathbf{v}, \quad \nabla \cdot \mathbf{v} = 0, \quad (4.2)$$

with the non-dimensional Reynolds number $Re = \frac{DU_\infty}{\nu}$.

As the flow is two dimensional and divergence free we can introduce a streamfunction $\psi(x, y)$ via the dynamical system

$$\dot{x} = u = \frac{\partial \psi}{\partial y}, \quad \dot{y} = v = -\frac{\partial \psi}{\partial x}. \quad (4.3)$$

The two equations (4.2) and (4.3) together constitute the flow. Each of the two equations can be regarded as a level of description. The first level (4.2) is the Eulerian field description which focuses on the over-all properties of the flow via vector fields depending on time t and space \mathbf{x} . The first level, the Navier-Stokes equation, is a distributed dynamical system formulated as a set of coupled partial differential equations. The second level (4.3) is the Lagrangian description which gives attention to a single fluid parcel in the flow. Given the fluid parcels initial placement or condition in the flow and solving (4.3) gives information on the parcel trajectory as time goes by. The second level consists of a dynamical system formulated as a set of coupled ordinary differential equations. Thus each level is described by a dynamical system. In each of the dynamical systems bifurcations can occur. We will denote a bifurcation occurring in (4.2) as a velocity field bifurcation. The best example here is of course the Hopf bifurcation that turns the velocity field periodic. A bifurcation taking place in (4.3) regarding the streamline topology will be termed a topological bifurcation. The formation of the symmetric cavity is an example of a topological bifurcation. Furthermore this example shows that topological bifurcations do not in general coincide with velocity field bifurcations.

In analyzing (4.3) we assume that the streamfunction ψ is analytical and hence we can conduct a Taylor expansion in a suitable neighbourhood of a chosen expansion point (x_0, y_0) . Through a canonical normal form transformation of the Taylor expansion we can conduct a bifurcation analysis. During the cause of the Taylor expansion and subsequent canonical normal form transformation we have certain choices to make deciding on the level of degeneracy through a set of degeneracy condition to impose on the normal form expansion coefficients. As mentioned, the first choice to be made will be to choose an appropriate expansion point. As we have set out to explore the bifurcation scenario taking place at the rear wake of the cylinder it will be natural to choose $(x_0, y_0) = (1/2, 0)$ on the rear part of the cylinder wall. Next, to ease our effort in analyzing the streamfunction the curved cylinder wall can be transformed into a plane. In doing so, we introduce the coordinate system $(x_1, y_1) = (-y, x - 1/2)$, see the left illustration in figure 4.4, and locally describe the curved cylinder wall by $y_1 = f(x_1)$, see the middle illustration in figure 4.4. Now by considering the transformation

$$(x_2, y_2) = (x_1, y_1 - f(x_1)) \quad (4.4)$$

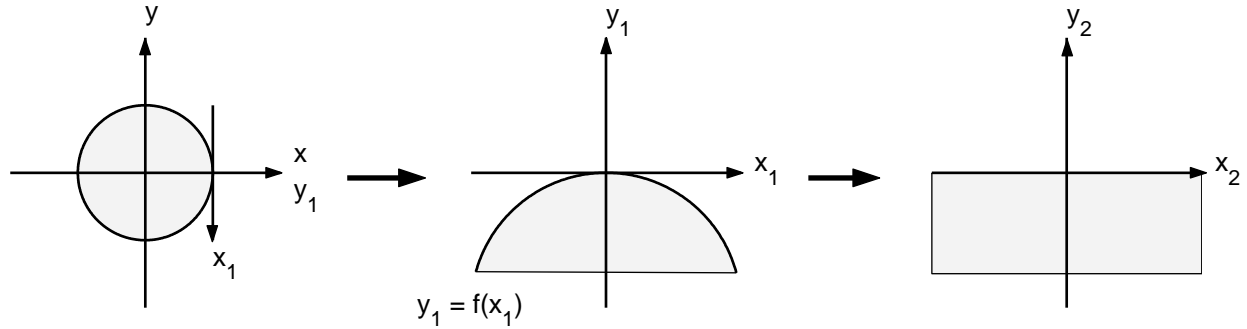


Figure 4.4: In order to ease the analysis of the streamfunction in the near wake of the cylinder the curved cylinder wall can locally be mapped into the plane. To conduct the mapping the coordinate systems (x_1, y_1) and (x_2, y_2) together with the canonical transformation (4.4) are introduced. In the left panel we see the physical cylinder system (x, y) together with (x_1, y_1) . The middle panel shows locally the rear of the cylinder wall represented by the expansion $y_1 = f(x_1)$. The right panel shows the effect of the transformation (4.4) mapping the curved wall into the plane.

we can locally consider the flow along a plane wall as shown in the rightmost illustration of figure 4.4. We note that the transformation is canonical¹ implying that the streamfunction ψ is preserved under (4.4). With the coordinates (x_1, y_1) and the transformation (4.4) the streamfunction $\psi(x, y)$ becomes

$$\psi(x, y) = \psi(y_1 + 1/2, -x_1) = \psi_1(x_1, y_1) = \psi_1(x_2, y_2 + f(x_2)) = \psi_2(x_2, y_2). \quad (4.5)$$

In the following we will for convenience rename the variables $(x_2, y_2) \mapsto (x, y)$ together with $\psi_2 \mapsto \psi$ hoping that this will not disturb the reader. We now consider the flow given through the local streamfunction ψ in the case of the plane wall as shown in the rightmost illustration in figure 4.4. As we have assumed that the streamfunction is analytic we can conduct a Taylor expansion

$$\psi(x, y) = \sum_{i+j=0} \psi_{i,j} x^i y^j \quad (4.6)$$

of the local streamfunction with expansion coefficients $\psi_{i,j}$ where we choose to set $\psi_{0,0} = 0$.

The local streamfunction ψ generates a velocity field $\mathbf{v} = (u, v)^T$ through

$$\dot{x} = u = \frac{\partial \psi}{\partial y}, \quad \dot{y} = v = -\frac{\partial \psi}{\partial x}. \quad (4.7)$$

and inserting (4.6) into (4.7) we get

$$\dot{x} = u = \sum_{i+j=0} (j+1) \psi_{i,j+1} x^i y^j, \quad \dot{y} = v = - \sum_{i+j=0} (i+1) \psi_{i+1,j} x^i y^j. \quad (4.8)$$

We impose further constraints on the streamfunction and hence on the expansion coefficients $\psi_{i,j}$ via the flow conditions at the wall where the flow has to fulfill the no-slip condition and the

¹Considering the generating function $S(y_1, x_2) = y_1 x_2 + x_2 f(x_1)$ the transformation (4.4) is given as $x_1 = \frac{\partial S}{\partial y_1} = x_2$ and $y_2 = \frac{\partial S}{\partial x_2} = y_1 - f(x_1)$. The generating function S fulfills the requirement $\frac{\partial^2 S}{\partial y_1 \partial x_2} = 1 \neq 0$.

impermeability or no-flux condition. If the wall is translated with the constant velocity $\mathbf{v}_w = (u_w, v_w)^T$ then the no-slip condition reads $u(x, 0) = u_w$ and the no-flux condition is given as $v(x, 0) = v_w$. Inserting these two conditions into (4.8)

$$u(x, 0) = u_w = \sum_{i+j=0} (j+1)\psi_{i,j+1}x^i0^j, \quad v(x, 0) = v_w = - \sum_{i+j=0} (i+1)\psi_{i+1,j}x^i0^j. \quad (4.9)$$

we find the no-slip constraint:

$$\psi_{0,1} = u_w \text{ and } \psi_{i,1} = 0 \text{ for } i = 1, 2, 3, \dots \quad (4.10)$$

together with the no-flux constraint:

$$\psi_{1,0} = -v_w \text{ and } \psi_{i,0} = 0 \text{ for } i = 2, 3, \dots \quad (4.11)$$

Inserting the no-slip constraint (4.10) together with the no-flux constraint (4.11) into the Taylor expansion (4.6) we obtain

$$\psi(x, y) = -v_w x + u_w y + y^2 \left(\sum_{i+j=0} \psi_{i,j+2} x^i y^j \right). \quad (4.12)$$

A stationary cylinder can through the transformation (4.4) be modelled as a non-moving wall. To mimic a stationary cylinder we set $u_w = v_w = 0$ in the streamfunction given in (4.12). The objective of the next section will be to analyse this case. But before we do so we note that in the setting of the streamfunction in (4.12) a cylinder rotating around the cylinder center axis with a non-dimensional angular velocity Ω and a chosen non-dimensional diameter of unity can be treated by letting $u_w = \Omega/2 \neq 0$ while $v_w = 0$.

We make one last remark before we close this section. We have applied here the transformation (4.4) to a locally perfectly circular curved wall, but we may note that the transformation is a little more general than that. We can for instance apply the transformation to any locally smooth curved wall such as a locally elliptically curved wall and of course the case of a locally plane wall etc. Hence we can expect that the analysis we conduct below will not only model the topology of the streamfunction in the wake of the circular cylinder but may apply equally well to the wake of an ellipse for example.

4.2 The stationary cylinder and topological classification

In this section we will, on the basis of the streamfunction (4.12) take a closer look at the streamline and vorticity topology on or in a vicinity of the wall. In the first two sections we take a look at the topology of the streamfunction and in the third section we analyse the possible vorticity topology. In the last section before we turn to the numerical simulations we comment briefly on the connection between the streamline topology and the Hopf bifurcation.

4.2.1 Symmetric unfolding of the streamfunction

In the figures 4.1 and 4.2 we notice for low Reynolds number that the velocity field is symmetric around the downstream flow direction. Further we see that a rear separation point exists. Also it is observed how the rear separation point bifurcates into a symmetric cavity, still with a symmetric velocity field. Motivated by this experimental fact, the idea is to first investigate whether degeneracy conditions on the streamfunction coefficients $\psi_{i,j+2}$ for $i, j \in \mathbb{N}_0$ adhering to the observed velocity field symmetry can be found such that a separation point exists on the wall. The next step is then to make an unfolding of the streamfunction that respects the symmetry to see whether the above found stagnation point under the unfolding bifurcates into a symmetric cavity. Then finally the idea is to relax the symmetry condition and consider a full unfolding of the streamfunction which can be perceived as an asymmetric perturbation of the symmetric cavity. The hypothesis is that the Hopf bifurcation mentioned in the introduction is linked to such an asymmetric perturbation of the symmetric cavity which is then perturbed in a periodic manner. We will comment further on this in section 4.2.4.

To fulfill the symmetry condition the velocity field must be symmetric around the y -axis. This symmetry requirement corresponds to the following two constraints

$$v(x, y) = v(-x, y), \quad u(x, y) = -u(-x, y). \quad (4.13)$$

We note that under this requirement $u(x, y)$ is an odd function in x . This implies that the expansion of $u(x, y)$ in (4.8) can not contain any even terms in x , thus $\psi_{i,j+1} = 0$ for even i . In a similar fashion $v(x, y)$ is seen to be an even function in x and the expansion of $v(x, y)$ in (4.8) can not contain any odd terms in x and $\psi_{i+1,j} = 0$ for odd i . Thus coefficients $\psi_{i,j}$ with i even must be vanishing and we obtain the symmetry constraint:

$$\psi_{2i,j} = 0 \text{ for } i, j = 1, 2, 3, \dots \quad (4.14)$$

on the streamfunction coefficients.

Introducing the symmetry constraint (4.14) into (4.12) we have the streamfunction

$$\psi(x, y) = y^2 (\psi_{1,2}x + \psi_{1,3}xy + \psi_{3,2}x^3 + \psi_{1,4}xy^2) + O(|(x, y)|^6). \quad (4.15)$$

which inserted into (4.7) yields the dynamical system

$$\begin{pmatrix} \dot{x} \\ \dot{y} \end{pmatrix} = y \begin{bmatrix} 2\psi_{1,2} & 0 \\ 0 & -\psi_{1,2} \end{bmatrix} \begin{pmatrix} x \\ y \end{pmatrix} + y \begin{pmatrix} 3\psi_{1,3}xy + 2\psi_{3,2}x^3 + 4\psi_{1,4}xy^2 \\ -\psi_{1,3}y^2 - 3\psi_{3,2}x^2y - \psi_{1,4}y^3 \end{pmatrix} + O(|(x, y)|^5). \quad (4.16)$$

We notice that for $y = 0$ for all x we find that $(\dot{x}, \dot{y}) = (0, 0)$ in (4.16) thus all points on the wall are critical points. This comes as a natural fact due to the no-slip condition. But not all critical points on the wall are interesting from a topological point of view. To draw out the inherent topological information we refer to Definition 2.7 and Theorem 2.6, see Chapter 2. The theorem shows that a scaling $t \mapsto yt$ of time in (4.16) for $y > 0$ leads to a dynamical system

$$\begin{pmatrix} \dot{x} \\ \dot{y} \end{pmatrix} = \begin{bmatrix} 2\psi_{1,2} & 0 \\ 0 & -\psi_{1,2} \end{bmatrix} \begin{pmatrix} x \\ y \end{pmatrix} + \begin{pmatrix} 3\psi_{1,3}xy + 2\psi_{3,2}x^3 + 4\psi_{1,4}xy^2 \\ -\psi_{1,3}y^2 - 3\psi_{3,2}x^2y - \psi_{1,4}y^3 \end{pmatrix} + O(|(x, y)|^4) \quad (4.17)$$

which is topologically equivalent to (4.16) above the wall. From (4.17) it is seen that the origin is a no-slip critical point. Furthermore the linear part evaluated at the origin has the eigenvalues $\lambda_{1,2} = 2\psi_{1,2}, -\psi_{1,2}$ implying that the system (4.17) is governed by the linear terms and has a

hyperbolic saddle point at the origin for $\psi_{1,2} \neq 0$. Thus no symmetric cavity can emerge from a bifurcation of the saddle point. Hence we need to consider the unfolding of the degeneracy condition $\psi_{1,2} = 0$ by letting $\psi_{1,2}$ be a small parameter $\epsilon_{1,2} = \psi_{1,2}$ leading to the streamfunction

$$\psi(x, y) = y^2 (\epsilon_{1,2}x + \psi_{1,3}xy + \psi_{3,2}x^3 + \psi_{1,4}xy^2) + O(|(x, y)|^6). \quad (4.18)$$

which still fulfills the symmetry condition. The streamfunction (4.18) can be transformed to a simpler normal form via the application of a canonical near-identity transformation based on a generating function. As the streamfunction (4.18) involves a small parameter $\epsilon_{1,2}$, the canonical transformation must be parameter dependent. In Chapter 3 we derived the near-identity transformation (3.33), rewritten here for convenience

$$x = \xi + \frac{\partial S_l(\epsilon_{1,2})}{\partial y}(\eta, \xi) + O(|(\xi, \eta)|^l), \quad y = \eta - \frac{\partial S_l(\epsilon_{1,2})}{\partial \xi}(\eta, \xi) + O(|(\xi, \eta)|^l) \quad (4.19)$$

where S_l is a monomial of order l on the form

$$S_l(y, \xi; \epsilon_{1,2}) = s_{l,0}(\epsilon_{1,2})y^l + s_{l-1,1}(\epsilon_{1,2})y^{l-1}\xi + \dots + s_{1,l-1}(\epsilon_{1,2})y\xi^{l-1} + s_{0,l}(\epsilon_{1,2})\xi^l \quad (4.20)$$

Inspection shows that to simplify (4.18) it is sufficient to consider the second order terms in the canonical transformation, thus from (4.19) and (4.20) we have

$$x = \xi + 3s_{3,0}(\epsilon_{1,2})\eta^2 + 2s_{2,1}(\epsilon_{1,2})\eta\xi + s_{1,2}(\epsilon_{1,2})\xi^2 + O(|(\xi, \eta)|^3) \quad (4.21)$$

$$y = \eta - s_{2,1}(\epsilon_{1,2})\eta^2 - 2s_{1,2}(\epsilon_{1,2})\eta\xi - 3s_{0,3}(\epsilon_{1,2})\xi^2 + O(|(\xi, \eta)|^3) \quad (4.22)$$

It is desirable to have the normal form of (4.18) fulfilling a corresponding symmetry condition, thus we choose to let (4.21) be an odd function of ξ so we set $s_{3,0} = s_{1,2} = 0$. Furthermore by letting $\eta = 0$ implying $y = 0$ in (4.22) we can perceive $\eta = 0$ for all ξ as the wall for the normal form, hence we choose to set $s_{0,3} = 0$. With the above choices of coefficients in the canonical transformation we have

$$x = \xi + 2s_{2,1}(\epsilon_{1,2})\eta\xi + O(|(\xi, \eta)|^3) \quad (4.23)$$

$$y = \eta - s_{2,1}(\epsilon_{1,2})\eta^2 + O(|(\xi, \eta)|^3).$$

Before we insert (4.23) in (4.18) we Taylor expand the parameter dependent coefficient $s_{1,2}$ to second order in $\epsilon_{1,2}$

$$s_{2,1}(\epsilon_{1,2}) = s_{2,1,0} + O(|\epsilon_{1,2}|). \quad (4.24)$$

which together with (4.23) inserted into (4.18) yields

$$\psi(\xi, \eta) = \eta^2 (\epsilon_{1,2}\xi + \psi_{1,3}\xi\eta + \psi_{3,2}\xi^3 + (\psi_{1,4} - s_{2,1,0}\psi_{1,3})\xi\eta^2) + O(|(\xi, \eta)|^6) + O(|\epsilon_{1,2}|^2) \quad (4.25)$$

We note here that to fifth order in the normal form (4.25) only the zero order term $s_{2,1,0}$ plays a rôle in the Taylor expansion (4.24) of the coefficient $s_{2,1}(\epsilon_{1,2})$.

By assuming the non-degeneracy conditions $\psi_{1,3} \neq 0$ and $\psi_{3,2} \neq 0$ and then choosing

$$s_{2,1,0} = \frac{\psi_{1,4}}{\psi_{1,3}}, \quad \tilde{\psi}_{3,2} = \frac{\psi_{1,3}}{\psi_{3,2}} \quad \text{and} \quad c_{1,2} = \frac{\epsilon_{1,2}}{\psi_{3,2}} \quad (4.26)$$

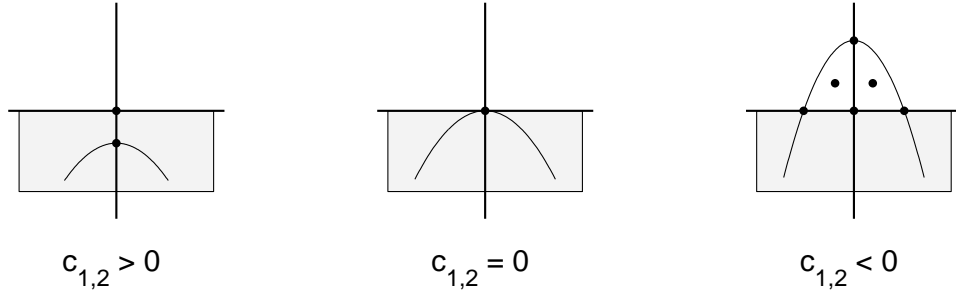


Figure 4.5: Bifurcation diagram for the normal form (4.27) truncated to fifth order. The diagram shows the formation of the symmetric cavity for the symmetric unfolding of the streamfunction. For $c_{1,2} > 0$ a saddle point exists on and below the wall. The saddle point below the wall is not physically relevant. For $c_{1,2} \leq 0$ the cavity bifurcates from the saddle point on the wall and emerges above the wall.

we can simplify (4.25) and finally arrive at the normal form

$$\psi(\xi, \eta) = \eta^2 \left(c_{1,2} \xi + \tilde{\psi}_{1,3} \xi \eta + \xi^3 \right) + O(|(\xi, \eta)|^6) + O(\epsilon_{1,2}^2). \quad (4.27)$$

We note here that if the non-degeneracy conditions $\psi_{1,3} \neq 0$ and $\psi_{3,2} \neq 0$ were not to hold we would have to include higher order terms in the normal form.

Now truncate the normal form (4.27) keeping fifth order terms. An inspection of (4.27) shows that mapping $\tilde{\psi}_{1,3} \mapsto -\tilde{\psi}_{1,3}$ has the same effect as mirroring $\eta \mapsto -\eta$. Thus in analyzing (4.27) it will be sufficient to only consider one sign of $\tilde{\psi}_{1,3}$ we choose here $\tilde{\psi}_{1,3} > 0$ and consequently the topology for $\eta > 0$ will correspond to the physically relevant topology in the near cylinder wake. A scaling of time by $t \mapsto \eta t$ in the truncated normal form gives the dynamical system

$$\begin{pmatrix} \dot{\xi} \\ \dot{\eta} \end{pmatrix} = \begin{bmatrix} 2c_{1,2} & 0 \\ 0 & -c_{1,2} \end{bmatrix} \begin{pmatrix} \xi \\ \eta \end{pmatrix} + \begin{pmatrix} 3\tilde{\psi}_{1,3}\xi\eta + 2\xi^3 \\ -\tilde{\psi}_{1,3}\eta^2 - 3\xi^2\eta \end{pmatrix} \quad (4.28)$$

The stagnation points to (4.28) are

$$(\xi, \eta) = (0, 0) \quad (4.29)$$

$$(\xi, \eta) = \left(0, -\frac{c_{1,2}}{\tilde{\psi}_{1,3}} \right) \quad (4.30)$$

$$(\xi, \eta) = (\pm \sqrt{-c_{1,2}}, 0) \quad (4.31)$$

$$(\xi, \eta) = \left(\pm \sqrt{\frac{-c_{1,2}}{7}}, -\frac{4}{7} \frac{c_{1,2}}{\tilde{\psi}_{1,3}} \right) \quad (4.32)$$

There is always a stagnation point (4.29) in origo and a stagnation point (4.30) on the η -axis. For $c_{1,2} > 0$ (4.30) is below the wall whereas for $c_{1,2} \leq 0$ the stagnation point (4.30) is on or above the wall. For $c_{1,2} \leq 0$ two more stagnation points (4.31) bifurcates and exists on the ξ -axis. Furthermore for $c_{1,2} \leq 0$ two in-flow stagnation points (4.32) bifurcates and exists above the wall $\eta > 0$. All in all this leads to the bifurcation diagram shown in figure 4.5. The figure shows that the symmetric unfolding (4.27) is able, from a no-slip critical point on the wall to form a symmetric cavity sharing the same topology as the experimental observed symmetric cavity seen in figure 4.1 for Reynolds numbers $Re = 9.6$ and $Re = 26.0$. This motivates in the next section a further analysis of the streamfunction (4.18) subject to an asymmetric perturbation breaking the symmetry of the cavity.

4.2.2 Full unfolding of the streamfunction

The following analysis of asymmetric perturbation of the symmetric cavity follows Niss and Jakobsen (2002). The asymmetric perturbation is conducted by a breaking of the symmetry condition via a full unfolding of the streamfunction (4.18) by consider all the coefficients

$$\epsilon_{0,2} = \psi_{0,2}, \quad \epsilon_{0,3} = \psi_{0,3}, \quad \epsilon_{1,2} = \psi_{1,2}, \quad \epsilon_{2,2} = \psi_{2,2}, \quad \epsilon_{0,4} = \psi_{0,4}, \quad \epsilon_{2,3} = \psi_{2,3}, \quad \epsilon_{0,5} = \psi_{0,5} \quad (4.33)$$

stemming from (4.14), together with $\epsilon_{1,2}$ as small parameters. Thus introducing (4.33) into (4.12) gives

$$\begin{aligned} \psi(x, y) = & \epsilon_{0,2}y^2 + \epsilon_{1,2}xy^2 + \epsilon_{0,3}y^3 + \epsilon_{2,2}x^2y^2 + \psi_{1,3}xy^3 + \epsilon_{0,4}y^4 \\ & + \psi_{3,2}x^3y^2 + \epsilon_{2,3}x^2y^3 + \psi_{1,4}xy^4 + \epsilon_{0,5}y^5 + O(|(x, y)|^6). \end{aligned} \quad (4.34)$$

The unfolding (4.34) can be transformed to normal form in a similar manner as above. The second order canonical transformations (4.21) and (4.22) are still adequate. We choose to set $s_{0,3} = 0$ implying that $\eta = 0$ maps to $y = 0$ in (4.22) such that $\eta = 0$ for all ξ represents the wall in the normal form. The coefficients $s_{3,0}$, $s_{2,1}$ and $s_{1,2}$ must depend on the vector $\epsilon = (\epsilon_{0,2}, \epsilon_{0,3}, \epsilon_{1,2}, \epsilon_{2,2}, \epsilon_{0,4}, \epsilon_{2,3}, \epsilon_{0,5})^T$ of small parameters such that the canonical transformation becomes

$$x = \xi + s_{3,0}(\epsilon)\eta^2 + 2s_{2,1}(\epsilon)\eta\xi + s_{1,2}(\epsilon)\xi^2 + O(|(\xi, \eta)|^3) \quad (4.35)$$

$$y = \eta - s_{2,1}(\epsilon)\eta^2 - 2s_{1,2}(\epsilon)\eta\xi + O(|(\xi, \eta)|^3).$$

Inserting (4.35) in (4.34), Taylor expanding the coefficients in ϵ and simplifying terms one arrives at the unfolded normal form

$$\psi(\xi, \eta) = \eta^2(c_{0,2} + c_{1,2}\xi + c_{0,3}\eta + \psi_{1,3}\xi\eta + \xi^3) + O(|(\xi, \eta)|^6) + O(|\epsilon|^2). \quad (4.36)$$

with the non-degeneracy conditions

$$\psi_{1,3} \neq 0 \text{ and } \psi_{3,2} \neq 0. \quad (4.37)$$

The normal form parameters are given as

$$c_{0,2} = \frac{\epsilon_{0,2}}{\psi_{3,2}}, \quad c_{1,2} = \frac{\epsilon_{1,2}}{\psi_{3,2}}, \quad c_{0,3} = \frac{\epsilon_{0,3}}{\psi_{3,2}} - 2\frac{\psi_{1,4}\epsilon_{0,2}}{\psi_{3,2}\psi_{1,3}} - \frac{1}{3}\frac{\psi_{1,3}\epsilon_{2,2}}{\psi_{3,2}^2} \quad (4.38)$$

with $\tilde{\psi}_{1,3} = \psi_{1,3}/\psi_{3,2}$.

The bifurcation diagram of (4.36) has been investigated in great detail in Niss and Jakobsen (2002). Here we will merely show, in figure 4.6 for $c_{1,2} < 0$, the physically relevant part of the diagram. The bifurcation diagram shows how the symmetric cavity, seen at $(c_{0,2}, c_{0,3}) = (0, 0)$ at the bifurcation curve denoted I can be perturbed for instance into a single recirculation zone and a loop shown in the regions denoted a and a' . Changing the parameters $c_{0,2}$ and $c_{0,3}$ further the loop might disappear in the cusp bifurcation taking place at the bifurcation curves II and II' such that only the recirculation zone in region b or b' is left. We will comment on figure 4.6 in connection with the aforementioned link between the Hopf bifurcation and a perturbation of the symmetric cavity in section 4.2.4. But before we do so we will consider the possibility of bifurcations in the vorticity topology.

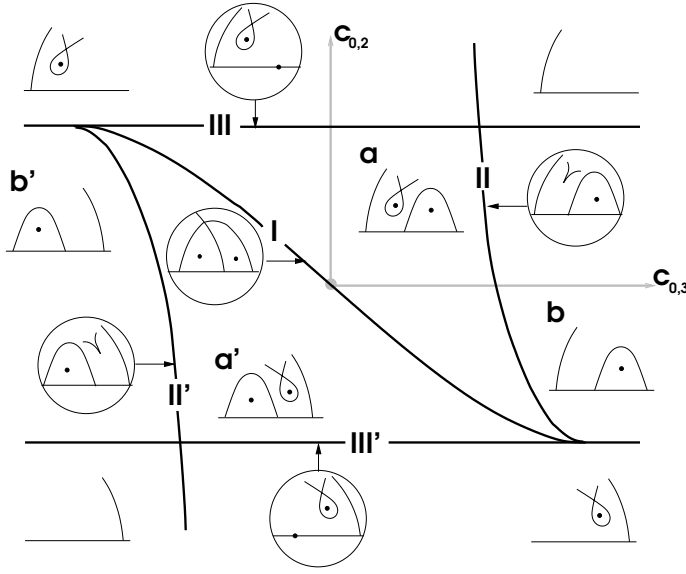


Figure 4.6: The diagram, adapted from Niss and Jakobsen (2002) shows for $c_{1,2} < 0$ the physically relevant part of the complete bifurcation diagram for the full unfolded normal form (4.36). We refer to Niss and Jakobsen (2002) for the complete bifurcation diagram for both $c_{1,2} < 0$ and $c_{1,2} \geq 0$. The bifurcation diagram shows the topologies that arise when the cavity is perturbed by asymmetric perturbations.

4.2.3 Bifurcations in the vorticity topology

Having discussed the bifurcation diagram showing the possible streamline topologies for the unfolding of the symmetric cavity we focus in this section on an investigation of the corresponding vorticity topology. It turns out that a direct analysis of the vorticity function based on (4.34) will suffice, no normal form simplification of the vorticity function will be necessary. The vorticity ω can be found via the streamfunction ψ by

$$\omega = -\Delta\psi = -\frac{\partial^2\psi}{\partial x^2} - \frac{\partial^2\psi}{\partial y^2}. \quad (4.39)$$

To base the analysis of the vorticity topology on the same assumptions as the streamfunction we insert (4.34) into (4.39) and find

$$\begin{aligned} \omega = & -2\epsilon_{0,2} - 2\epsilon_{1,2}x - 6\epsilon_{0,3}y - 2\epsilon_{2,2}x^2 - 6\psi_{1,3}xy - 2(\epsilon_{2,2} + 6\epsilon_{0,4})y^2 - 2\psi_{3,2}x^3 \\ & - 6\epsilon_{2,3}x^2y - 6(2\psi_{1,4} + \psi_{3,2})xy^2 - 2(\epsilon_{2,3} + 10\epsilon_{0,5})y^3 + O(|(x,y)|^4). \end{aligned} \quad (4.40)$$

First we consider the degenerate case where all the small parameters are set to zero i.e.

$$\epsilon_{0,2} = \epsilon_{0,3} = \epsilon_{1,2} = \epsilon_{2,2} = \epsilon_{0,4} = \epsilon_{2,3} = \epsilon_{0,5} = 0 \quad (4.41)$$

which leaves us with the degenerate vorticity function ω_0 on the form

$$\omega_0 = -6\psi_{1,3}xy - 2\psi_{3,2}x^3 - 6(2\psi_{1,4} + \psi_{3,2})xy^2 + O(|(x,y)|^4). \quad (4.42)$$

Inserting $(x_{c_0}, y_{c_0}) = (0, 0)$ into the gradient of ω_0 gives $\nabla\omega_0(0, 0) = 0$ which shows that $(x_{c_0}, y_{c_0}) = (0, 0)$ is a critical point of the degenerate vorticity function ω_0 . The type of this critical point can be established by the eigenvalues to the Hessian $\mathbf{H}(x, y)$ of ω_0 evaluated at $(x_{c_0}, y_{c_0}) = (0, 0)$. We find that

$$\mathbf{H}(0, 0) = \begin{bmatrix} 0 & 6\psi_{1,3} \\ -6\psi_{1,3} & 0 \end{bmatrix}$$

with the eigenvalues $\lambda_{\mathbf{H}(0,0)} = \pm 6\psi_{1,3}$. As we assume $\psi_{1,3} \neq 0$, see (4.37), we have that the origin is a non-degenerate saddle point. Hence for the case in (4.41) a saddle point in the vorticity is situated exactly on the wall. A non-degenerate saddle point shows structural stability. Therefore the saddle point will continue to exist even when the small parameters in (4.41) are no longer zero. Thus in a vicinity of the origin the vorticity function (4.40) will have a saddle point. As the small parameters are varied away from zero the saddle point will persist and will merely change position slightly away from the origin on the wall. In this connection we need to know whether the saddle point will move below the wall $y < 0$ or above the wall $y > 0$ and into the flow. The latter is the physical relevant case that we will be interested in. As the critical point (x_c, y_c) of ω moves smoothly with the small parameters we consider the first order approximations

$$x_c = \alpha_{0,2}\epsilon_{0,2} + \alpha_{0,3}\epsilon_{0,3} + \alpha_{1,2}\epsilon_{1,2} + \alpha_{2,2}\epsilon_{2,2} + \alpha_{0,4}\epsilon_{0,4} + \alpha_{2,3}\epsilon_{2,3} + \alpha_{0,5}\epsilon_{0,5} \quad (4.43)$$

$$y_c = \beta_{0,2}\epsilon_{0,2} + \beta_{0,3}\epsilon_{0,3} + \beta_{1,2}\epsilon_{1,2} + \beta_{2,2}\epsilon_{2,2} + \beta_{0,4}\epsilon_{0,4} + \beta_{2,3}\epsilon_{2,3} + \beta_{0,5}\epsilon_{0,5} \quad (4.44)$$

Insert (4.43) and (4.44) into $\nabla\omega(x_c, y_c) = 0$ we obtain to first order

$$\begin{aligned} \frac{\partial\omega}{\partial x} &= -6\psi_{1,3}\beta_{0,2}\epsilon_{0,2} - 6\psi_{1,3}\beta_{0,3}\epsilon_{0,3} - (2 + 6\psi_{1,3}\beta_{1,2})\epsilon_{1,2} \\ &\quad - 6\psi_{1,3}\beta_{2,2}\epsilon_{2,2} - 6\psi_{1,3}\beta_{0,4}\epsilon_{0,4} - 6\psi_{1,3}\beta_{2,3}\epsilon_{2,3} - 6\psi_{1,3}\beta_{0,5}\epsilon_{0,5} = 0 \end{aligned} \quad (4.45)$$

and

$$\begin{aligned} \frac{\partial\omega}{\partial y} &= -6a_{1,3}\alpha_{0,2}\epsilon_{0,2} - (6a_{1,3}\alpha_{0,3} - 6)\epsilon_{0,3} - 6a_{1,3}\alpha_{1,2}\epsilon_{1,2} \\ &\quad - 6a_{1,3}\alpha_{2,2}\epsilon_{2,2} - 6a_{1,3}\alpha_{0,4}\epsilon_{0,4} - 6a_{1,3}\alpha_{2,3}\epsilon_{2,3} - 6a_{1,3}\alpha_{0,5}\epsilon_{0,5} = 0 \end{aligned} \quad (4.46)$$

solving (4.45) and (4.46) for the expansion coefficients $\alpha_{i,j}$ and $\beta_{i,j}$ gives that all coefficients are equal to zero except $\alpha_{0,3} = -1/\psi_{1,3}$ and $\beta_{1,2} = -1/(3\psi_{1,3})$. To first order we have that

$$y_c = -\frac{\epsilon_{1,2}}{3\psi_{1,3}} \quad (4.47)$$

Thus if $\epsilon_{1,2}$ and $\psi_{1,3}$ have opposite sign we have that $y_c > 0$ and the saddle point is above the wall and thus in the flow. If $\epsilon_{1,2}$ and $\psi_{1,3}$ have the same sign the saddle point is below the wall which is not physically relevant. The formation or bifurcation of the saddle point into the flow therefore takes place for $\epsilon_{1,2} = 0$. All we need now is to tie together (4.47) to the normal form coefficients given in (4.38). From (4.38) we find that

$$c_{1,2} = \tilde{\psi}_{1,3} \left(\frac{\epsilon_{1,2}}{\psi_{1,3}} \right) = -3\tilde{\psi}_{1,3}y_c \quad (4.48)$$

where we remind the reader of the assumption $\tilde{\psi}_{1,3} > 0$. From (4.48) we can conclude that for $c_{1,2} > 0$ no saddle point exists in the flow. At $c_{1,2} = 0$ a saddle point is formed on the wall which for $c_{1,2} < 0$ has moved into the flow. This bifurcation of a saddle point for the vorticity is shown in figure 4.7.

4.2.4 Streamline and vorticity topology together with the Hopf bifurcation

Before we can turn to the numerical investigations we first need, in very brief overview, to highlight the results found in the analysis of Marsden and McCracken (1976) and Niss and Jakobsen (2002).

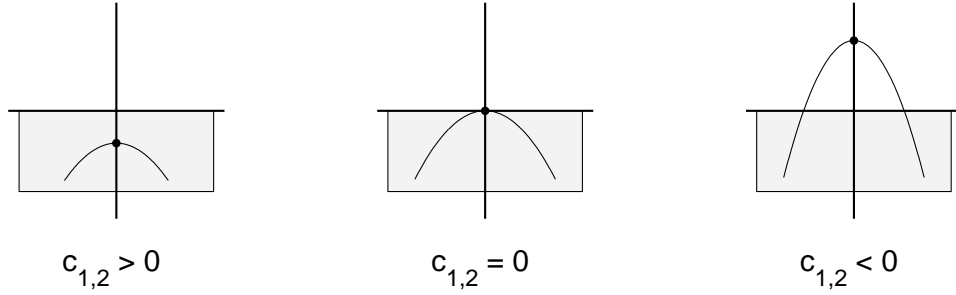


Figure 4.7: Vorticity bifurcation diagram showing the formation of the symmetric cavity. For $c_{1,2} > 0$ a saddle point exists below the wall. This case is not physically relevant. For $c_{1,2} \leq 0$ the saddle point moves on and above the wall.

In Marsden and McCracken (1976) the Hopf bifurcation is applied to partial differential equations and in Niss and Jakobsen (2002) a detailed treatment shows under the assumption that a Hopf bifurcation takes place in the velocity field, how to tie together the topological streamfunction bifurcations we analyzed in the previous sections and the Hopf bifurcation. To correspond with later notation we assume that the Hopf bifurcation is taking place at $Re = Re_{c_2}$. Niss and Jakobsen (2002) shows that in a neighborhood of the Hopf bifurcation a first order approximation of the streamfunction after the Hopf bifurcation can be written as

$$\psi(\mathbf{x}, t) \simeq \psi_0(\mathbf{x}) + \sqrt{Re - Re_{c_2}} \left(e^{i\beta_0 t} \psi_1(\mathbf{x}) + e^{-i\beta_0 t} \psi_1^*(\mathbf{x}) \right) + O(|\sqrt{Re - Re_{c_2}}|^2) \quad (4.49)$$

where ψ_0 is the steady state from which ψ bifurcates from. As we have assumed that the streamfunction (4.6) is analytic we can Taylor expand the various terms in (4.49) into

$$\begin{aligned} \psi(x, y) &= \sum_{i+j=0}^n \psi_{i,j} x^i y^j + O(|(x, y)|^{n+1}) \\ \psi_0(x, y) &= \sum_{i+j=0}^n a_{i,j} x^i y^j + O(|(x, y)|^{n+1}) \\ \psi_1(x, y) &= \sum_{i+j=0}^n b_{i,j} x^i y^j + O(|(x, y)|^{n+1}) \end{aligned} \quad (4.50)$$

from which together with (4.49) we have the following relationship

$$\psi_{i,j} \simeq a_{i,j} + \sqrt{Re - Re_{c_2}} \left(e^{i\beta_0 t} b_{i,j} + e^{-i\beta_0 t} b_{i,j}^* \right) \quad (4.51)$$

between the coefficients. The relation (4.51) shows how the streamfunction coefficients may vary with time $\psi_{i,j} = \psi_{i,j}(t)$ after the Hopf bifurcation has occurred. As we have seen there is a direct relation between the streamfunction coefficients $\psi_{i,j}$ and the normal form coefficients given in (4.38). Thus the normal form coefficients will also vary with time resulting in a time dependent periodic perturbation of the symmetric cavity. The periodic perturbation is traversing the parameter space and can be understood or pictured as closed curves superimposed the bifurcation diagram in figure 4.6. This is illustrated in figure 4.8.

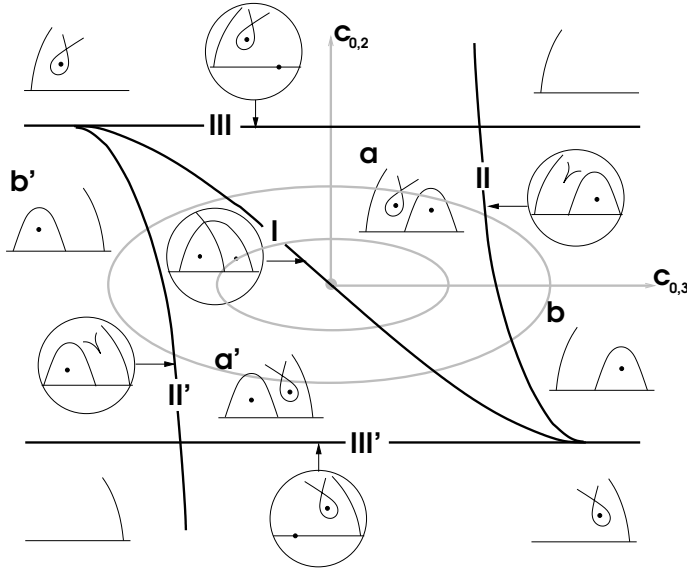


Figure 4.8: Two closed curves are superimposed the bifurcation diagram in figure 4.6. The closed curves are illustrations of how periodic perturbations can traverse the parameter space of the normal form (4.36).

Right after the Hopf bifurcation the amplitude of the periodic oscillation is small but increases with increasing Reynolds number Re . Therefore it is expected that an increase of Re right after the Hopf bifurcation will yield an increase of the close curve thereby spanning a wider range in the parameter space. This is illustrated by the two closed curves superimposed the bifurcation diagram in figure 4.8. The smaller curve represents a possible bifurcation scenario just after the Hopf bifurcation and following the smaller curve traversing parameter space yields the following sequence of a possible first topological bifurcation scenario.

$$\dots a \mapsto I \mapsto a' \mapsto I \mapsto a \dots \quad (4.52)$$

An increase in the system parameters opens up for the possibility of a second topological bifurcation scenario having the sequence

$$\dots a \mapsto II \mapsto b \mapsto II \mapsto a \mapsto I \mapsto a' \mapsto II' \mapsto b' \mapsto II' \mapsto a' \mapsto I' \mapsto a \dots \quad (4.53)$$

There might be other possible sequences than (4.52) and (4.53). For instance one could imagine a sequence involving the bifurcations III and III' instead of II and II' in (4.53). But the numerical investigations which we will turn to in the next section reveals that the two possible topological bifurcation scenarios (4.52) and (4.53) corresponds to and describes the streamfunction topologies observed in the simulations of the near wake of the cylinder.

4.3 Numerical investigations

We have now modelled the streamline topology for the laminar two dimensional cylinder wake via the streamfunction and subsequently conducted a bifurcation analysis based on a derived normal form thereof. Next we wish to compare the theoretical obtained bifurcation study with numerical simulations for the stationary cylinder. This has a twofold inherently intertwined purpose. Firstly we can confirm through the numerical simulations whether we have chosen to analyse the right degeneracy conditions based on the idea to unfold the normal form of the streamfunction on the

basis of the symmetric cavity. Secondly we lean on the theoretical bifurcation catalogue of the various streamfunction topologies to help us look for, in an organized manner, bifurcations which we might otherwise miss in the numerical investigation of the streamline topology.

4.3.1 The computational domain and simulation code

The simulations lying behind the numerical topological streamline and vorticity investigations we are about to conduct are based on the code EllipSys2D. EllipSys2D has been developed by Michelsen (1992) and Sørensen (1995) and is capable of solving time dependent two dimensional spatial flow problems. The code is a finite volume method, see Versteeg and Malalasekera (1995) and is based on the incompressible isothermal Navier-Stokes equations and therefore suitable for the flow problem we have been studying.

Via EllipSys2D we have access to, among other non-dimensionalized quantities, the streamfunction ψ , the velocity field $\mathbf{v} = (u, v)^T$ and the vorticity field ω . The input to EllipSys2D has to be the initial condition \mathbf{v}_{init} of the velocity field at time $t = 0$, the velocity far field \mathbf{v}_∞ together with numerical values of the various geometric and fluid parameters.

The code can both integrate steady and unsteady or transient flow problems. Depending on the considered flow problem, it is possible to choose an adequate numerical integration scheme. For steady simulations we have used a second order upwind difference scheme (suds) whereas for unsteady simulations we have chosen the central difference scheme (cds). For the pressure-velocity coupling we have for the pressure correction used the SIMPLE-algorithm at steady simulations and the PISO-algorithm for unsteady simulations. We have chosen to set the relaxation parameters r for the velocity and pressure corrections to $r_u = 0.7$, $r_v = 0.7$ and $r_p = 0.3$ for steady simulations and $r_u = 0.8$, $r_v = 0.8$ and $r_p = 0.8$ for unsteady simulations in order for EllipSys2D to converge. Based on experience the convergence criteria for the velocity components has been set to $\Delta = 1.0 \cdot 10^{-5}$. and the convergence criteria for the pressure correction has been set to $\Delta_p = 1.0 \cdot 10^{-5}$.

EllipSys2D computes the flow field on a structured mesh or grid. A structured grid is characterized by a direct correspondence between points in the physical computational domain and the point index domain. This means that points situated next to each other in the computational domain have neighbor indices. Structured grids in themselves are not so versatile in handling a complex physical geometry. To circumvent this drawback EllipSys2D allows for block structured grids. Thus the physical domain is decomposed into simpler blocks that each can be discretized as a structured grid. EllipSys2D then patches together these blocks. For the flow around the circular cylinder we have chosen to use an annulus as computational domain. The annulus is then decomposed down to four blocks, see the sketch found in the right panel of figure 4.9. Within each block the structured grid is polar. The polar grid in one of the blocks is generated by a discretization in the radial and tangential direction respectively. The distribution of grid points in both the radial and tangential component is done by stretching. We will not go into the details of the stretching procedure, but can briefly mention that the radial stretching is performed by a growth factor calculated from the compound interest principle. For the tangential direction the stretching depends on the cosine of the relative index of the tangential grid point. The relative index is the ratio of index to total number of points in the tangential direction. In the left panel of figure 4.9 we have shown an example of a grid decomposed into four structured blocks. Each block has been discretized into a 32×32 grid with 32 grid points in both the radial direction and in the tangential direction. The grid consisting of the four 32×32 blocks has a total of 4096 grid points. As seen in the figure, the advantage of this grid generation is that the grid points are distributed more densely in the wake of the cylinder around the x -axis whereas the computational domain is

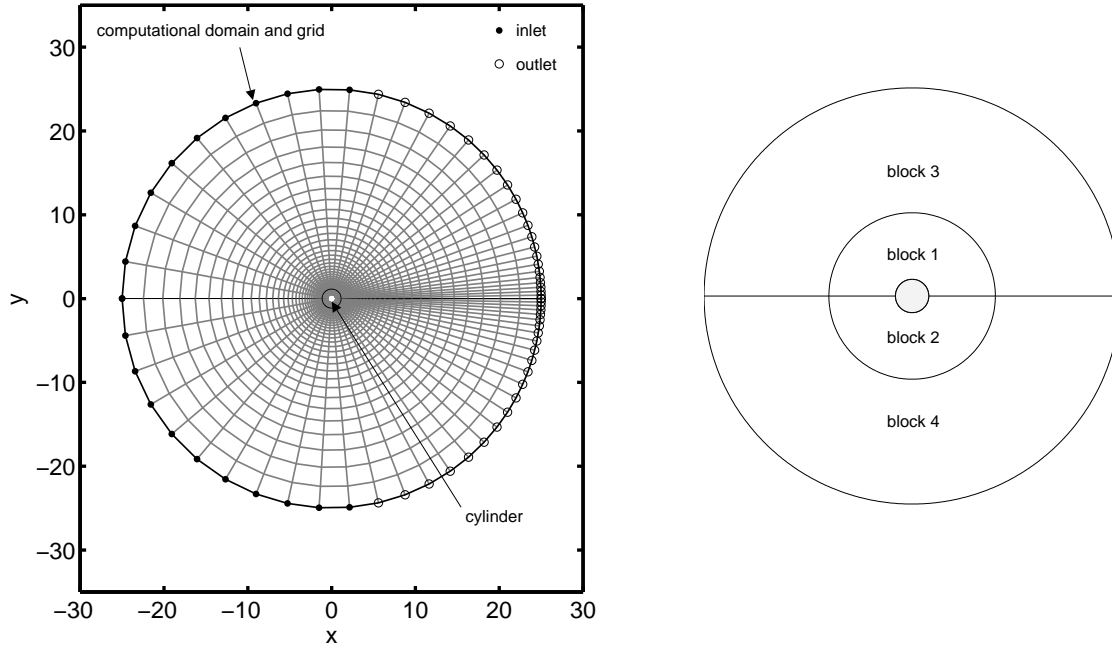


Figure 4.9: The computational domain is a circular annulus divided into four blocks. To the left we show the computational domain and the grid 32×32 . The panel in the right shows a sketch of the decomposition of the computational domain into four blocks.

more sparsely filled relatively speaking, in the vicinity of the front, top and bottom of the cylinder. Further it is clearly seen that the density of grid points increases as we move closer towards the cylinder. The grid has been constructed in this way as it is expected that the fluid flow will be more detailed in the wake around the x -axis. The block decomposition includes the possibility of having different stretching factors in the grid of each block, but here we have found it adequate to operate with the same stretching factor in all the blocks.

4.3.2 The simulations

In the numerical simulations the computational domain has naturally to be finite hence we need to set some finite distance to what we regard as far field. We have chosen the computational domain to be 50 times greater than the diameter D of the cylinder. As $D = 1.0$ the annulus shaped computational domain has an outer diameter of 50.

We have in our calculations mainly used a grid composed of four 64×64 blocks, we call this the normal grid. We have chosen the first cell height in the grid to be $D/400 = 0.0025$.

In all the simulations we have chosen to set the initial condition of the velocity field to $\mathbf{v}_{init} = (1, 0)^T$ in all of the computational domain. Further we have chosen to set the circular cylinder diameter to $D = 1m$, the free stream velocity to $U_\infty = 1m/s$ and the absolute viscosity to $\mu = 1Pa \cdot s$. Remembering that the kinematic viscosity is $\nu = \mu/\rho$, where ρ is the fluid density, we have in our simulations that the Reynolds number is given as $Re = DU_\infty/\nu = \rho \cdot m^3/Kg$. Thus in the simulations we set the Reynolds number Re via the numerical value of the fluid density ρ . The velocity far field is set to the free stream boundary condition $\mathbf{v}_\infty = (U_\infty, 0) = (1, 0)$.

The Reynolds number Re is the only free system parameter for the stationary cylinder. We

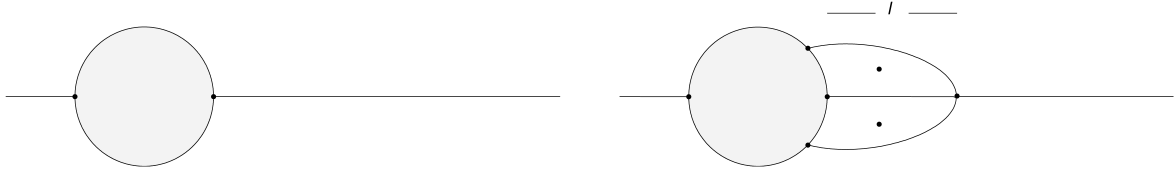


Figure 4.10: The left panel shows the essential streamlines for Reynolds number $Re = 1.0$. The right panel shows the essential streamlines for $Re = 20.0$. In the two panels the cylinder is grey shaded. A bullet (•) marks the placement of a stagnation point. Only the essential streamlines or separatrices to the stagnation points of saddle type are shown. The figure shows that a formation of a symmetric double recirculation zone or cavity takes place in the wake of the cylinder. The symmetric recirculation zone does not appear for the case of $Re = 1.0$ but has been formed for $Re = 20.0$. Thus the emergence or bifurcation of the recirculation zone must take place in the interval $Re \in [1.0; 20.0]$. In the left panel we show how the length l of the symmetric double recirculation zone is measured.

will in the following regard the Reynolds number as a bifurcation parameter. For the Reynolds number interval $Re = [0 : 300]$ we report on the various topologies we find for the streamfunction and the vorticity field. We consider the topology of the streamfunction in two different coordinate systems. First we consider the coordinate system with origo fixed at the cylinder center axis, that is, a coordinate system where the observer follows the cylinder. This cylinder system is described in figure 4.2. The second coordinate system we consider is the free stream system where the cylinder is translated with constant velocity \mathbf{v}_{cyl} passing by the observer. We have chosen to look at the case where the translated coordinate system moves with the negative value of the free stream velocity $\mathbf{v}_{\infty} = (1, 0)^T$, that is $\mathbf{v}_{cyl} = (-1, 0)^T$. Next we report on the vorticity field. The vorticity field has by virtue of definition the same topology in a fixed as well as a translated coordinate system.

The stagnation points observed in a streamline pattern occurring at time $t = t_0$ are identified by inspecting the 0-isoclines and the ∞ -isoclines of the velocity field at time $t = t_0$. The set of 0-isoclines and ∞ -isoclines in \mathbf{x} are found by solving for the zero level contours $v(\mathbf{x}, t_0) = 0$ and $u(\mathbf{x}, t_0) = 0$ respectively. The stagnation points appear where the two sets of isoclines intersect.

4.4 Bifurcations in the streamline topology

We start out by reporting in this section on numerical investigations of the streamline topology in the fixed coordinate system x - y with origo centered at the cylinder center axis. We report on the symmetric cavity bifurcation occurring at the Reynolds number Re_{c_1} , the Hopf bifurcation taking place at Re_{c_2} followed by two topological bifurcations involving cusp bifurcations. The two topological bifurcations take place at Re_{c_3} and Re_{c_4} respectively.

4.4.1 The steady wake and the first topological bifurcation

In figure 4.10 we have shown two numerical simulations. In the left panel we show the streamline topology for the case of $Re = 1.0$. The right panel shows the streamline topology at a Reynolds number of $Re = 20.0$. Now comparing the two panels in figure 4.10 to the two bottom panels in figure 4.2 we see that in figure 4.10 we have omitted some of the streamlines and have only presented what we denote as the essential streamlines. The essential streamlines are the set of separatrices either emanating from saddle points or cusp points in the wake of the cylinder or separatrices emanating from separaiton points situated on the cylinder wall. Together with the saddle and center points the essential streamlines sum up the essentials of a streamline topology.

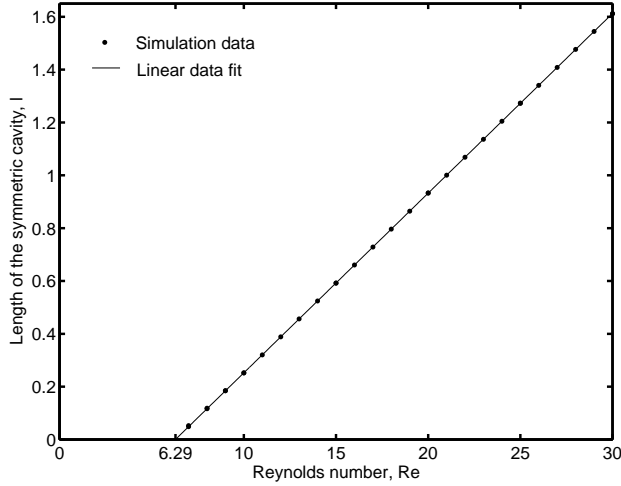


Figure 4.11: Length l of the symmetric cavity as function of the Reynolds number Re . The graph suggests a linear dependence. A linear data fit of the shown simulation data yields $l_{fit} = 0.068Re - 0.428$. From the data fit we estimate that the emergence or bifurcation of the symmetric cavity takes place for $Re_{c1} = 6.29$.

The placement of critical points in the flow and separation points on the cylinder wall are in figure 4.10 and the figures to come illustrated by using bullets.

Returning to figure 4.10 we see that a symmetric cavity has emerged or bifurcated in the wake of the cylinder. The symmetric cavity does not appear for the case of $Re = 1.0$ where as it has long been formed for $Re = 20.0$. The wake and hence the velocity field in the two cases are steady, this has not changed - we have not shown any figures of the transient taking place from the initial velocity condition to the steady velocity field but we will make a comment on this in the next section. As we noticed above, the wake is still steady but the topology of the wake has changed. Therefore a so-called topological bifurcation has taken place. A topological bifurcation is a bifurcation in the streamfunction. The bifurcation of the cavity must have taken place in the Reynolds number interval $Re \in [1.0; 20.0]$. To determine when the bifurcation takes place we have for a number of numerical simulations measured the length l in the direction of the x -axis of the symmetric cavity. The length l is shown in the left panel of figure 4.10. In figure 4.11 we have mapped the measured length l against the Reynolds number Re . The graph suggests a linear dependence between the cavity length and the Reynolds number thus we have made a linear data fit l_{fit} of l as a function of Re . The linear fit gives the relation $l_{fit} = 0.068Re - 0.428$ and is shown on top of the numerically measured Re - l relation in figure 4.11. We have not shown the residue $l - l_{fit}$ between the measured data and the data fit but the norm of the residue has the value $||l - l_{fit}|| = 0.0018$. From the linear data fit we estimate that $l_{fit} = 0$ at $Re = 6.29$ meaning that the topological bifurcation of the symmetric cavity takes place for $Re_{c1} = 6.29$.

In Koromilas and Telionis (1980) the length l_{exp} of the symmetric cavity of a circular cylinder has been measured experimentally in a channel flow. The measured values of length l_{exp} has been fitted to a linear dependence of the Reynolds number and $l_{exp} = 0$ for the Reynolds number $Re_{c1,exp} = 5.2$. This value deviates from the numerically obtained value $Re_{c1} = 6.29$. The reason to this deviation might be that the numerical simulations are not conducted in a channel flow but in a free stream flow thus the boundary conditions are different. But the order of magnitude of the values Re_{c1} for the numerical simulations and $Re_{c1,exp}$ for the experiments are comparable. Furthermore the dependence of the cavity length to the Reynolds number are in both cases linear.

4.4.2 The periodic wake and the Hopf bifurcation

The fluid flow for the Reynolds number in the interval $Re \in [0; 30]$ investigated in the previous section all had a steady wake. For low Reynolds number, the transient from initial velocity condition to the steady velocity field have time series showing purely exponential decay. For Reynolds numbers of about $Re \geq 30.0$ the transient towards the steady velocity field has changed behaviour and clearly has time series showing sinusoidal oscillations with an exponentially decaying envelope function. Thus the steady state of the velocity field is a focus. An example of a transient is shown for the case of $Re = 41.0$ in the top left panel of figure 4.12. In the panel we see the time development of the v -component of the velocity field at the wake position $(x_1, y_1) = (2.09, -0.01)$ in the time interval $t = [0; 375]$. The v -component approaches the steady value $v_f = 0.364 \cdot 10^{-3}$ as time goes by.

It is believed according to the literature that a supercritical Hopf bifurcation is the cause for the velocity field turning periodic. Together with the fact that the transient towards the steady state of the velocity field has become a focus which might be an indication of a Hopf bifurcation soon to occur, we will in the following assume that a Hopf bifurcation will take place. The question that arises is, at which Reynolds number, which we denote Re_{c_2} will the Hopf Bifurcation occur. In determining Re_{c_2} we will, using a similar approach as Hernández and Baudet (2000) apply the theoretical characteristics of the supercritical Hopf bifurcation, therefore we summarize these below.

The supercritical Hopf bifurcation is characterized by the existence of a steady hyperbolic focus $\mathbf{v}_f(\mathbf{x})$ turning instable at the Hopf bifurcation point while at the same time the formation of a steady limit cycle takes place. To the hyperbolic focus is associated a complex conjugated pair of eigenvalues $\lambda(Re)$ and $\lambda^*(Re)$ and a pair of complex conjugated eigenfunctions $\mathbf{v}_t(\mathbf{x}; Re)$ and $\mathbf{v}_t^*(\mathbf{x}; Re)$ all depending on the Reynolds number Re with $\lambda(Re) = \alpha(Re) + i\omega(Re)$ where α and ω are real. This complex set of eigenvalues and eigenfunctions stems from a linearization of the Navier-Stokes equations around the hyperbolic focus. During the course of the bifurcation the real part $\alpha(Re)$ of the complex conjugated pair of critical eigenvalues changes from being negative to becoming positive as the Reynolds number is varied. At the bifurcation point Re_{c_2} we have that $\alpha(Re_{c_2}) = 0$. Thus one way of locating the bifurcation point would be to estimate when the real part of the eigenvalues is zero. This can be done by considering the velocity field transient $\mathbf{v}_t(\mathbf{x}, t)$ approaching the stable hyperbolic focus $\|\mathbf{v}_t(\mathbf{x}, t) - \mathbf{v}_f(\mathbf{x})\| = 0$ for $t \rightarrow \infty$ for a set of Reynolds numbers where the Reynolds number is increased from below towards the bifurcation point Re_{c_2} . At each Reynolds number $\alpha(Re)$ is determined. To accompany us in this task we write up the first order approximation

$$\begin{aligned} \mathbf{v}_t(\mathbf{x}, t) &= \mathbf{v}_f(\mathbf{x}) + \left(C e^{\lambda t} \mathbf{v}_t(\mathbf{x}) + C^* e^{\lambda^* t} \mathbf{v}_t^*(\mathbf{x}) \right) \\ &= \mathbf{v}_f(\mathbf{x}) + \mathbf{c}(\mathbf{x}) e^{\alpha t} \sin(\omega t + \psi(\mathbf{x})) \end{aligned} \quad (4.54)$$

of the transient where C is a complex constant and $\mathbf{c}(\mathbf{x})$ a real valued vector function depending on C and the eigenfunction $\mathbf{v}_t(\mathbf{x})$. Considering a fixed location $\mathbf{x} = \mathbf{x}_1$ in (4.54) leaves us with the time dependent expression

$$\mathbf{v}_t(t) = \mathbf{v}_f + \mathbf{c} e^{\alpha t} \sin(\omega t + \psi) \quad (4.55)$$

composed of an exponential envelope function $e^{\alpha t}$ and a sinusoidal function $\sin(\omega t + \psi)$ where $\mathbf{v}_t(\mathbf{x}_1, t) = \mathbf{v}_t(t)$, $\mathbf{v}_f(\mathbf{x}_1) = \mathbf{v}_f$, $\mathbf{c}(\mathbf{x}_1) = \mathbf{c} = (c_u, c_v)^T$ and $\psi(\mathbf{x}_1) = \psi$. Our objective is to fit (4.55) to a numerically given time series for a fixed location in the cylinder wake. Figure (4.12) explains how we have done this data fitting. We only need the time series for one of the velocity

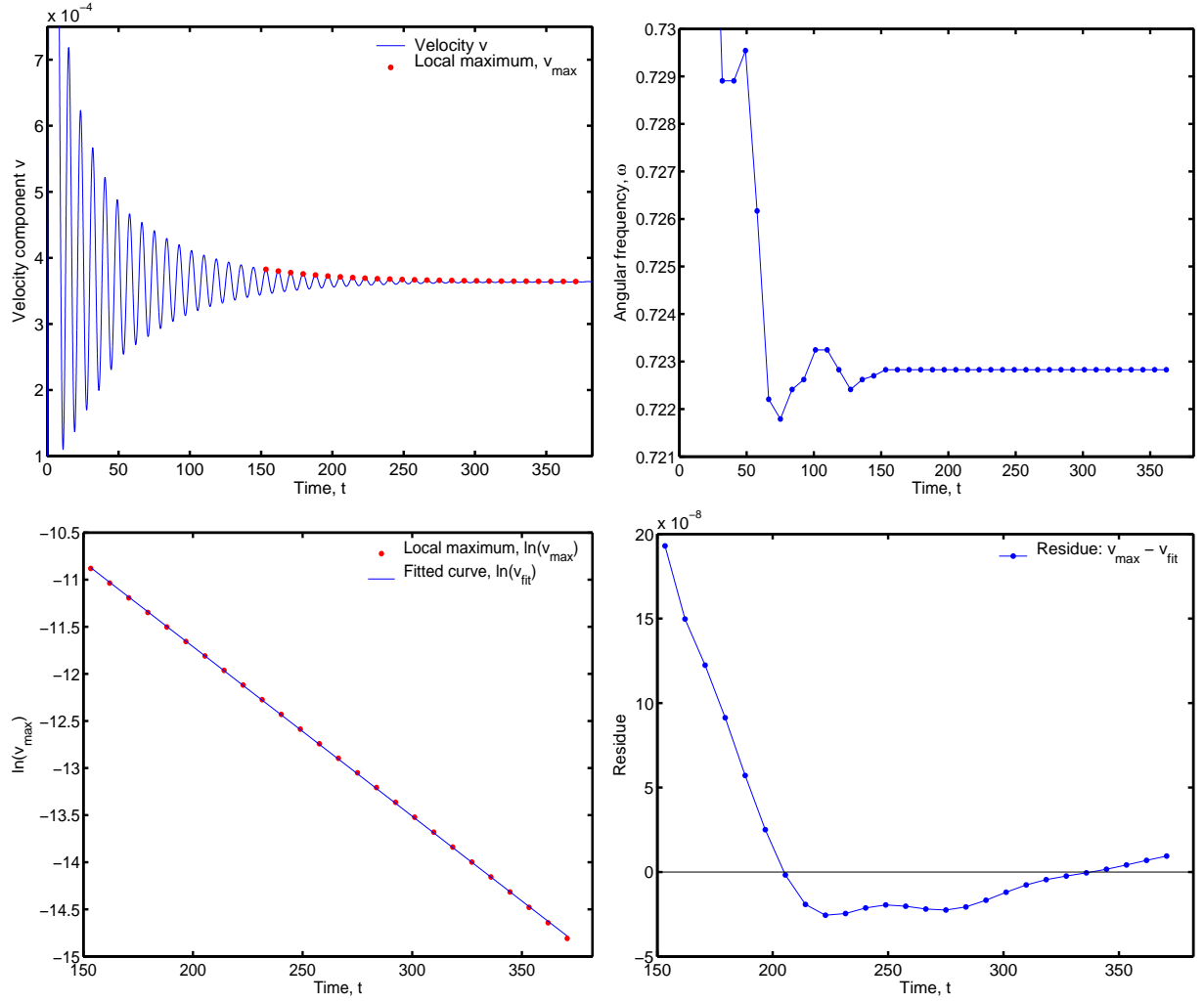


Figure 4.12: Top left panel shows the time series for the velocity component v at position $(x_1, y_1) = (2.09, -0.01)$ for $Re = 41.0$. Local maximum values v_{max} of v are indicated. In the right top panel the angular frequency ω as a function of time between subsequent v_{max} is shown. It is seen that $\omega = 0.7228$ from $t \geq 153.34$. The maximum values v_{max} are shown fitted to the expression (4.56) in the bottom left panel and the bottom right panel shows the residue between the fitted values v_{fit} and the maximum values v_{max} . From the slope in the bottom left panel we find that $\alpha = -0.0180$.

components $\mathbf{v}_t(t) = (u_t(t), v_t(t))$. We have chosen the v -component and in the figure we show the numerically obtained transient time series for the case of $Re = 41.0$ at the wake location $\mathbf{x}_1 = (x_1, y_1) = (2.09, -0.01)$. The top left panel shows the transient $v_t(t)$ towards a stable steady state with $v_f = 0.364 \cdot 10^{-3}$ in the time interval $t \in [0 : 375]$. As we mentioned above we notice that the numerically obtained time series is oscillating but damped via a presumably exponential decaying envelope function - a qualitative behaviour similar to the time dependent expression in (4.55). In the top left panel we have furthermore marked the set of maxima $v_{t,max}$ in the time interval $t \in [153.34; 375]$. In the top right panel we have measured the angular frequency ω as a function of time t between subsequent maxima $v_{t,max}$ found in the top left panel. In (4.55) the angular frequency ω is a constant, thus for the transient $v_t(t)$ to be described via (4.55) we have to determine the time interval for the transient in the top left panel of figure 4.12 at which ω has become constant. It is seen in the top right panel that the angular frequency has taken on a constant value $\omega = 0.7228$ for $t \geq 153.34$. We will use this as an estimate of the angular frequency ω in (4.55). Having estimated the angular frequency we can go on fitting the extracted maxima values $v_{t,max}$ to the exponential envelope function in the time interval where the angular frequency has shown to be constant i.e. in the time interval $t \in [153.34; 375]$. From (4.55) we obtain the linear relationship

$$\ln(v_{t,max} - v_f) = \alpha t + \ln(c_v). \quad (4.56)$$

The linear data fit $v_{t,fit}$ of $v_{t,max}$ to the expression (4.56) is shown in the bottom left panel of figure 4.12. The residue $v_{t,max} - v_{t,fit}$ in the time interval $t \in [153.34; 375]$ is shown in the bottom right panel with $\|v_{t,max} - v_{t,fit}\| = 3.0 \cdot 10^{-7}$. We have found this value of the residue satisfactory. To conduct the data fitting we have performed a linear fit of the $v_{t,max}$ data to the expression (4.56). The two constants α and c_v in the linear fit have been found via the least squares method. From the slope of the linear data fit we estimate for $Re = 41.0$ the value $\alpha_{est} = -0.0018$.

In a similar manner as described above we have for the same wake location $\mathbf{x}_1 = (2.09, -0.01)$ estimated the $\alpha_{est,1}$ -values for a set of Reynolds numbers in the interval $Re = [36; 46]$. The results are collected in the middle panel of figure 4.13. We have made a linear fit $\alpha_{fit,1}$ of the set of estimated $\alpha_{est,1}$ -values as function of the Reynolds number. From this fit we have estimated that $\alpha_{fit,1} = 0$ for the Reynolds number $Re_1 = 45.22$ with a residue of $\|\alpha_{est,1} - \alpha_{fit,1}\| = 0.004$.

To back up this estimate and to make sure that the above series of data fits are wake position independent we have repeated the above data fitting procedure for a second wake location $\mathbf{x}_2 = (7.42, 0.48)$. To give a qualitative impression of the placement of \mathbf{x}_1 and \mathbf{x}_2 in the cylinder wake we have in the top panel of figure 4.13 for Reynolds number $Re = 41.0$ marked the position of \mathbf{x}_1 together with \mathbf{x}_2 . It is seen that location \mathbf{x}_1 is situated more or less at the x -axis close to the rear of the cylinder within the symmetric cavity whereas \mathbf{x}_2 is situated further down stream outside the symmetric cavity off the x -axis.

The result of the fit $\alpha_{fit,2}$ of $\alpha_{est,2}$ as a function of Re for the second wake position \mathbf{x}_2 is seen in the bottom panel of figure 4.13 and it was found that $\alpha_{fit,2} = 0$ for the Reynolds number $Re_2 = 45.08$ with a residue of $\|\alpha_{est,2} - \alpha_{fit,2}\| = 0.005$.

The two Reynolds numbers $Re_1 = 45.22$ and $Re_2 = 45.08$ have been determined with residues of the same order of magnitude. Thus we will regard the average value of Re_1 and Re_2 , which is $Re_{c_2} = 45.15$, as the Reynolds number where the Hopf bifurcation occurs.

Channel flow experiments, see Williamson (1996) show that the Hopf bifurcation takes place near $Re_{c_2,exp} = 49.0$ whereas the channel flow simulations by Hernández and Pacheco (2002) has been determined to take place for approximately $Re_{c_2,her} = 56.8$. These results are in the same range as the numerical estimate $Re_{c_2} = 45.15$ we have found here. The discrepancy is believed as in

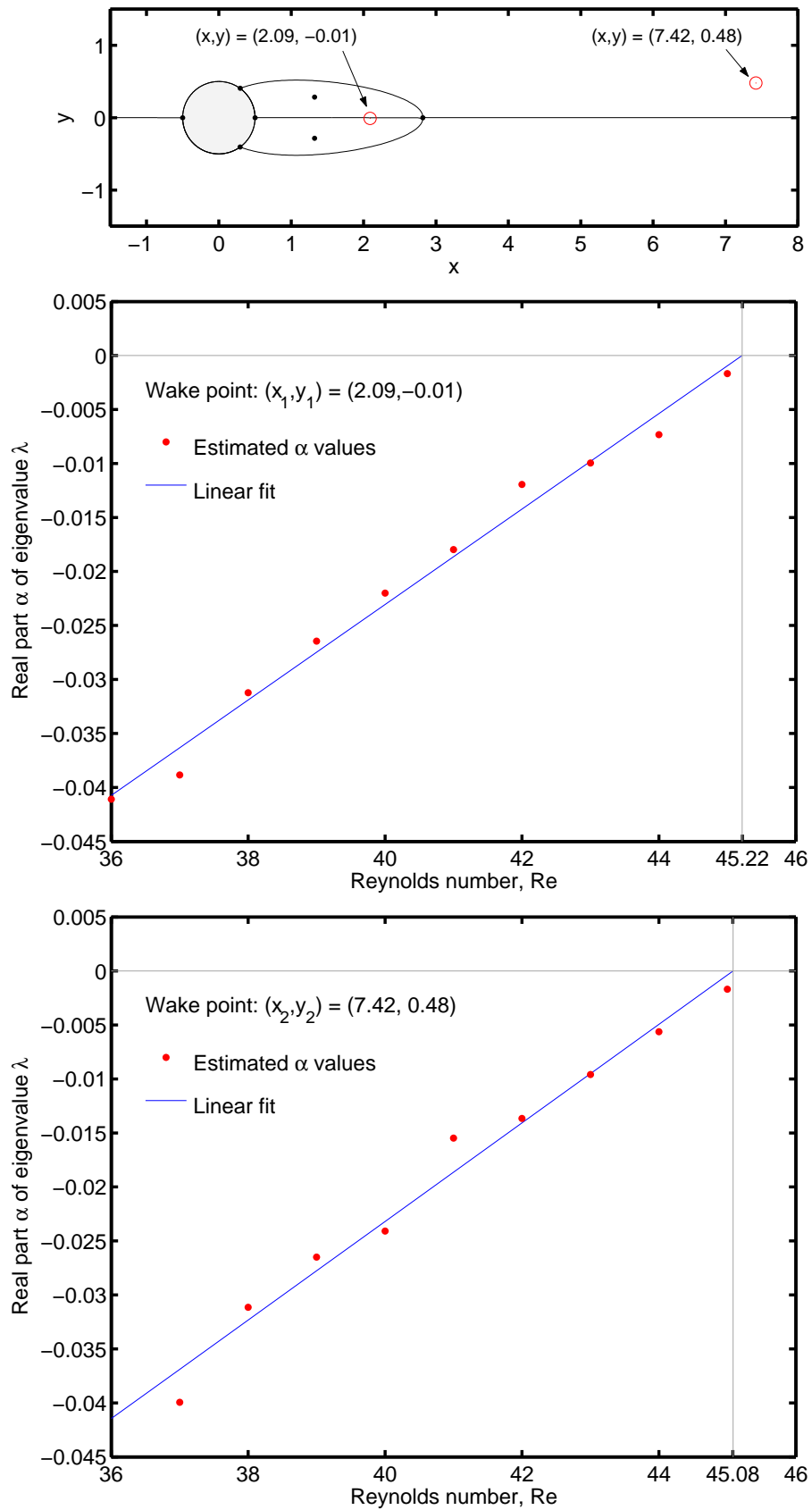


Figure 4.13: Estimation of α as function of the Reynolds number Re .

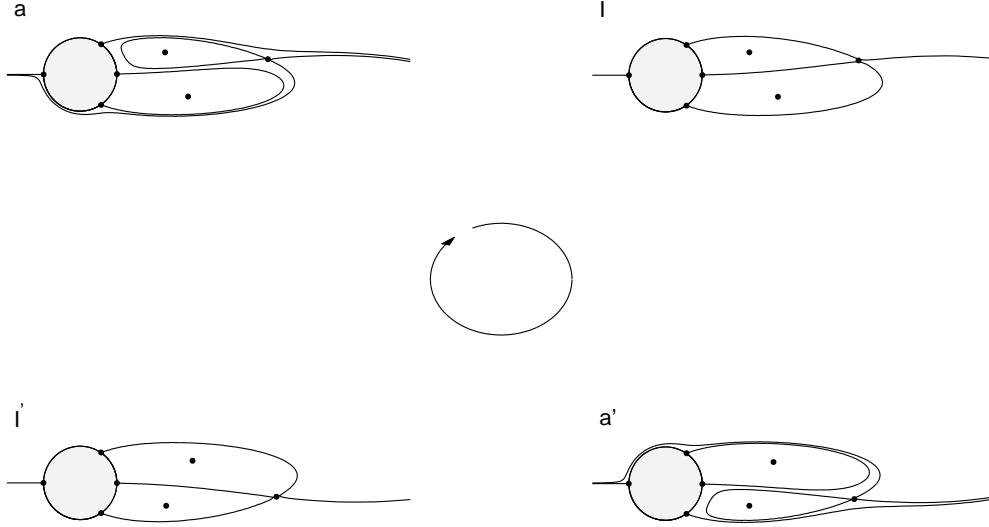


Figure 4.14: Numerically obtained bifurcation scenario taking place for $Re = 45.6$ right after the Hopf bifurcation at $Re = 45.15$. The period of the bifurcation scenario is $T = 8.57$ where the first topological bifurcation I takes place for $T_I = 3.34$ and the second topological bifurcation I' takes place for $T_{I'} = 7.63$.

section 4.4.2 to be caused by the different boundary conditions between the numerical simulations of the free stream flow and the channel flow simulations and experiments.

4.4.3 Streamline topology after the Hopf bifurcation

Now we have seen that the wake has turned periodic at Re_{c_2} . The limit cycle occurring right at the Hopf bifurcation point has zero amplitude, therefore to see whether the Hopf bifurcation have had any influence on the topology of the streamline topology we need to conduct a simulation at a Reynolds number Re slightly higher than Re_{c_2} . The streamline topology scenario for $Re = 45.6 > Re_{c_2} = 45.15$ for instance, is illustrated in figure 4.14. As seen in the figure the Hopf bifurcation turning the wake periodic with period T leads to a continuously cyclic repeating change in the topology of the streamline pattern. Two new topologies denoted a and a' in figure 4.14 have emerged and the wake is periodically changing between these two topologies through the two topological bifurcations I and I' . In the course of time t the scenario repeats itself all over in the sequence

$$\dots a \mapsto I \mapsto a' \mapsto I' \mapsto a \dots \quad (4.57)$$

In the periodic cycle topology a is present in the time interval $t \in [0 : T_I] \cup [T_{I'} : T]$. The topological bifurcation I takes place at time $t = T_I$. Then a' is present for $t \in [T_I : T_{I'}]$ followed by the topological bifurcation I' at time $t = T_{I'}$ leading back to the topology a . For $Re = 45.6$ the period of the sequence is $T = 8.57$. The topological bifurcation I happens at time $t = T_I = 3.34$ and I' takes place at $t = T_{I'} = 7.63$. We further note that as $T_{I'} - T_I = 4.29 = T/2$ there is half period between the two topological bifurcations I and I' .

The topologies a and a' are mirror images of each other. Topology a mirrored in the x -axis maps to the topology a' occurring half a period later on in the cycle. In a similar manner the topological bifurcation I maps to I' when mirrored in the x -axis. We further note that the two topologies I and I' are actually cavities in the wake like the symmetric cavity but the velocity field

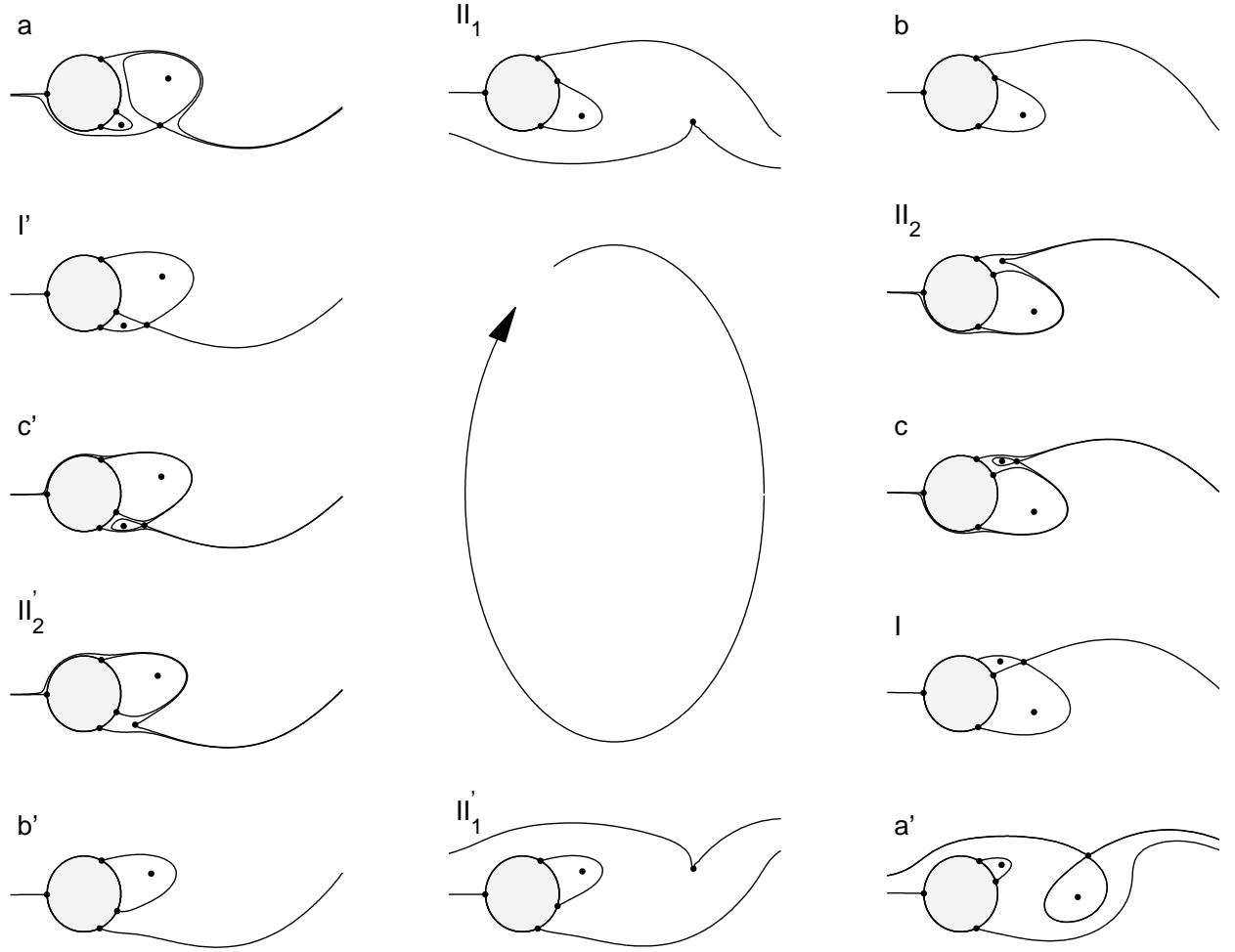


Figure 4.15: Numerically obtained bifurcation scenario taking place for $Re = 100.0$.

bifurcation has caused a symmetry breaking of the cavities compared to the symmetric cavity. The topology a and bifurcation I together with the mirror images correspond to I and a in (4.52).

The sequence (4.57) is seen to correspond to the sequence (4.52) found in the bifurcation diagram for the full unfolding of the normal form (4.36). Thus it seems that an fifth order normal form shows sufficient richness to give a theoretical understanding of the topological bifurcation scenario observed right after the Hopf bifurcation has occurred.

4.4.4 The periodic wake and the second topological bifurcation

In the previous section we found the cyclicly repeating sequence (4.57) for $Re = 45.6$. It turns out that we do not have to increase the Reynolds number much above $Re = 45.6$ to discover that a second topological bifurcation takes place. The first topological bifurcation was the bifurcation of the symmetric cavity for the steady wake taking place at $Re_{c1} = 6.29$. The observed second topological bifurcation sequence is shown in figure 4.15 for a Reynolds number of $Re = 100.0$. In figure 4.17 we find that this new second topological bifurcation occurs for $Re_{c3} = 45.68$. Below we

will further comment on figure 4.17 and show how we have determined Re_{c3} . In this new bifurcation scenario a set of new streamline topologies have emerged. The wake is still periodic meaning that this new set of topologies are, as in figure 4.14, repeated over and over again. Comparing to (4.57) the sequence of topologies is now

$$\dots a \mapsto II_1 \mapsto b \mapsto II_2 \mapsto c \mapsto I \mapsto a' \mapsto II'_1 \mapsto b' \mapsto II'_2 \mapsto c' \mapsto I' \mapsto a \dots \quad (4.58)$$

In comparison with figure 4.14 and the sequence (4.57) we seen that two new topological bifurcations II_1 and II_2 together with the morror images II'_1 and II'_2 are now present. The bifurcations are topologically equivalent and corresponds to the bifurcation II in the sequence (4.53). The indices on II_1 and II_2 indicates that II_1 appears before II_2 in time in the sequence (4.58). Further they only differs in the placement of the cusp bifurcation in the wake. The cusp bifurcation for II_2 appears closer to the cylinder than the cusp bifurcation for II_1 . In the bifurcations a saddle-centre or loop is created via a cusp bifurcation in the wake. In the sense of direction shown in the sequence (4.58) following the course of time in the periodic wake the bifurcations II_1 and II'_1 are supercritical meaning that a loop has been created whereas the two bifurcations II_2 and II'_2 are subcritical and a loop disappears in a cusp bifurcation.

The new topologies are b and c together with the mirror images b' and c' . Topologically a and c are equivalent whereas b introduces a new topology. A similar remark hold for the mirror images a' and c' together with b' . The topologies a , b and c correspond to the topologies a and b in (4.53). Even though a and c are topologically equivalent the actual placement of the saddle-centre or loop in the wake of a and c is different. The shift between topology a and b is taking place via the topological bifurcation II_1 and the change of topology b to topology c occurs via the topological bifurcation II_2 . The mirror images of II_1 , that is II'_1 is the corresponding topological bifurcation between a' and b' . Similar for II'_2 which makes b' bifurcate into c' .

For $Re = 100.0$ the period is $T = 6.03$. In figure 4.16 we have shown the time series transient towards the periodic limit cycle. The bottom left panel shows one period T of the limit cycle and with respect to an arbitrarily chosen reference phase ϕ the first bifurcation II_1 in the sequence (4.58) takes place for $T_{II_1} = 2.29$. Next follows the bifurcation II_2 for $T_{II_2} = 2.8125$. Then at $T_I = 2.97$ we have I occurring. After I follows II'_1 at $T_{II'_1} = 5.31$ again followed by II'_2 at $T_{II'_2} = 5.85$. Then finally the bifurcation I' happens for $T_{I'} = 5.985$. The various time measurements for the occurrence of the topological bifurcations above have been conducted with a time resolution of $T_{res} = 0.0225$ and as the period is $T = 6.03$ this means that we have been using 268 time frames of streamline phase space plots to cover one limit cycle period where twelve of these streamline phase space plots are shown in figure 4.15. Within the time resolution each bifurcation and the corresponding mirror image differs in appearance by a half period $T/2 = 3.015$. For instance we notice that $T_{II'_1} - T_{II_1} = 3.0375$ which differs from $T/2$ with exactly the time resolution.

As for the streamline topologies in figure 4.14 topology a' , b' and c' are mirror images of a , b and c respectively. The mirror images come about by mirroring the topologies in the x -axis together with a time delay of half a period.

Above we saw that II_1 and II_2 together with the mirror bifurcations forms the set of new topological bifurcations that emerges in the second topological bifurcation scenario. One way to locate the parameter value Re_{c3} for which the the second topological bifurcation occurs is to monitor either the time difference $\Delta T = T_{II_2} - T_{II_1}$ or $\Delta T' = T_{II'_2} - T_{II'_1}$ for a suitable interval of Reynolds numbers. As we approach the bifurcation value Re_{c3} from above the time differences ΔT and $\Delta T'$ will decrease and at some Reynolds number Re_{c3} they will become zero which then establishes the bifurcation point. We have recorded both ΔT and $\Delta T'$ and in the top panel of figure 4.17 we show

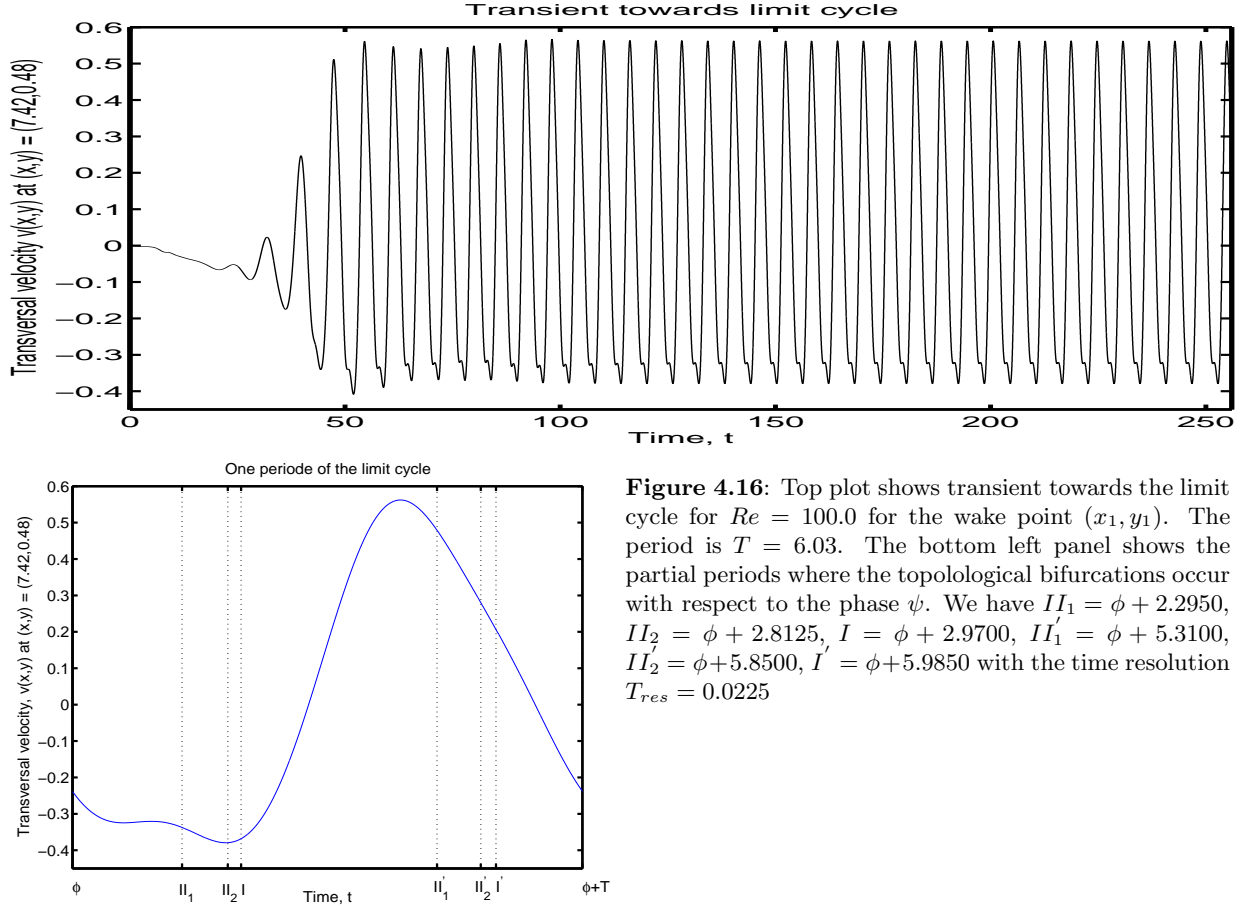


Figure 4.16: Top plot shows transient towards the limit cycle for $Re = 100.0$ for the wake point (x_1, y_1) . The period is $T = 6.03$. The bottom left panel shows the partial periods where the topological bifurcations occur with respect to the phase ψ . We have $II_1 = \phi + 2.2950$, $II_2 = \phi + 2.8125$, $I = \phi + 2.9700$, $II'_1 = \phi + 5.3100$, $II'_2 = \phi + 5.8500$, $I' = \phi + 5.9850$ with the time resolution $T_{res} = 0.0225$

both ΔT and $\Delta T'$ together with the average value $\langle T \rangle = |\Delta T - \Delta T'|/2$ as a function of the Reynolds number in the interval of $Re = [45.5; 50]$. We notice that the time difference average $\langle T \rangle$ decreases significantly from a value of approximately $\langle T \rangle = 0.7$ towards $\langle T \rangle = 0$ in the interval $Re = [45.5; 46.5]$. Thus we expect to find the bifurcation point Re_{c_3} within this interval.

To get an idea on how the time difference average $\langle T \rangle$ tends to zero as a function of the Reynolds number Re we refer back to figure 4.8 and to figure 4.18. It is assumed that the spanning of the closed curves traversing the parameter space in figure 4.8 depends on the Reynolds number. Thus as the Reynolds number is increased from the Hopf bifurcation taking place at Re_{c_2} towards Re_{c_3} the spanning of the closed curve will increase and at Re_{c_3} the curve will be tangent to the bifurcation curves II and II' . In a neighborhood of the point where the closed curve is tangent to II and II' the traversing curve will approximately be of second order. In keeping $c_{1,2} < 0$ constant it is assumed that the normal form parameters $c_{0,2}$ and $c_{0,3}$ depends on the Reynolds number Re as well. At the point where the closed curve is tangent to say II we introduce the local coordinates $\tilde{c}_{0,2}$ and $\tilde{c}_{0,3}$ for the normal form parameters which we then expand to second order obtaining the approximation

$$\tilde{c}_{0,3} = A(\tilde{c}_{0,2} - \bar{c}_{0,2})^2 - (Re - Re_{c_3}) \quad (4.59)$$

where $(\bar{c}_{0,2}, Re_{c_3})$ corresponds to the point where the closed curve is tangent to I . Setting $\tilde{c}_{0,3} = 0$ in (4.59) we find the intersection points $\tilde{c}_{0,2\pm} = \bar{c}_{0,2} \pm \sqrt{(Re - Re_{c_3})/A}$ and we have that $\tilde{c}_{0,2+} - \tilde{c}_{0,2-} = 2\sqrt{(Re - Re_{c_3})/A}$. Furthermore assuming that the velocity v it takes to traverse the sequence

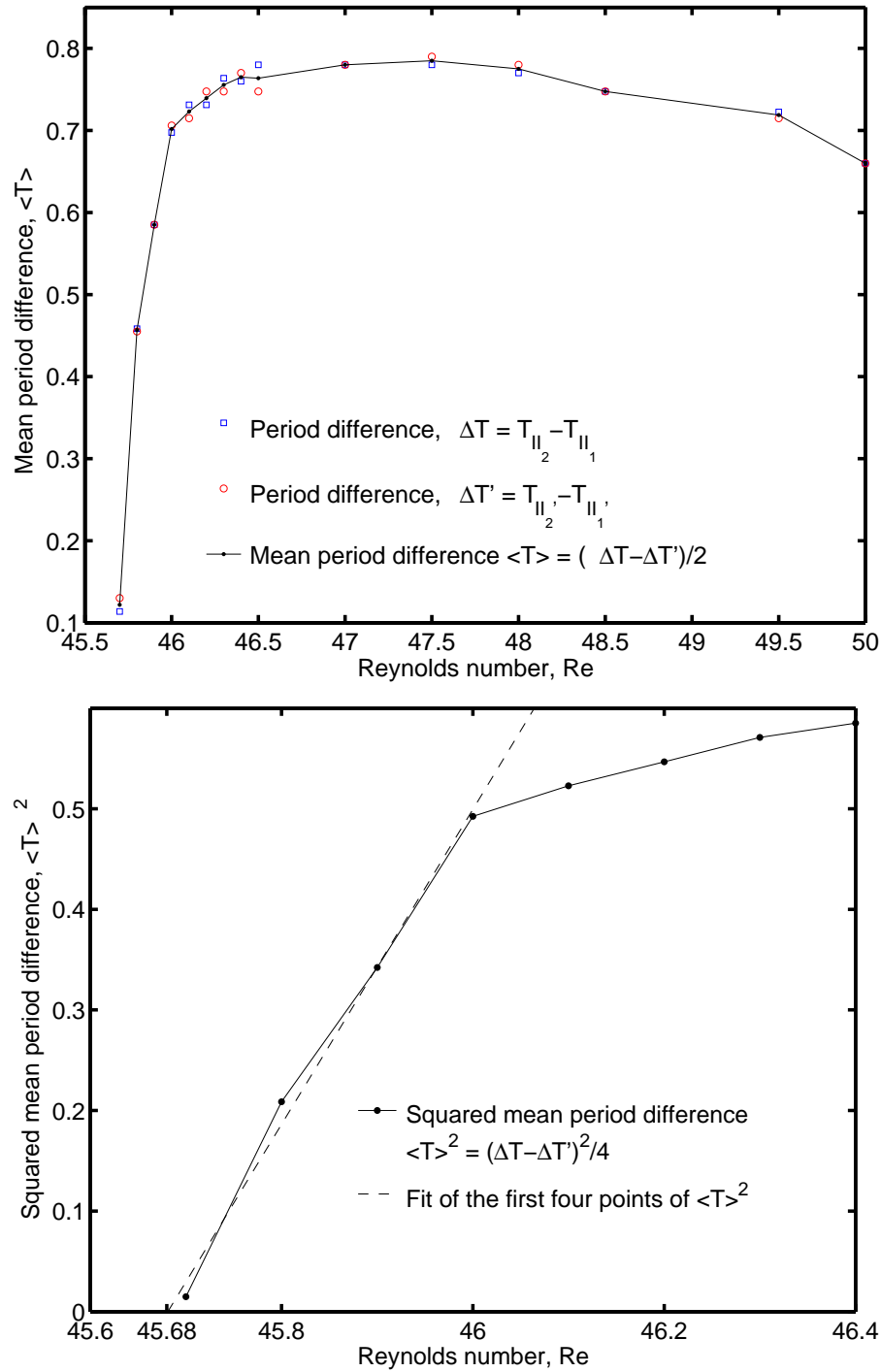


Figure 4.17: The top panel shows the period differences ΔT , $\Delta T'$ and the average $\langle T \rangle = (\Delta T - \Delta T')/2$ as function of the Reynolds number Re . The period differences are the time between the occurrence of the bifurcations II_1 and II_2 or II_1' and II_2' in the bifurcation scenario seen in figure 4.15. At $\langle T \rangle = 0$ for some Re_{c_3} marks the occurrence of the second topological bifurcation after the Hopf bifurcation. It is expected that in a neighborhood of Re_{c_3} after the occurrence of the second topological bifurcation the average $\langle T \rangle$ will be described by the expression $\langle T \rangle = K\sqrt{Re - Re_{c_3}}$ which squared yields $\langle T \rangle^2 = K^2 Re - K^2 Re_{c_3}$. The bottom panel shows a plot of $\langle T \rangle^2$ together with a linear data fit of the first four data points of $\langle T \rangle^2$. The fit yields the constants $K = 1.25$ and $Re_{c_3} = 45.68$ hence $\langle T \rangle = 0$ at $Re_{c_3} = 45.68$.

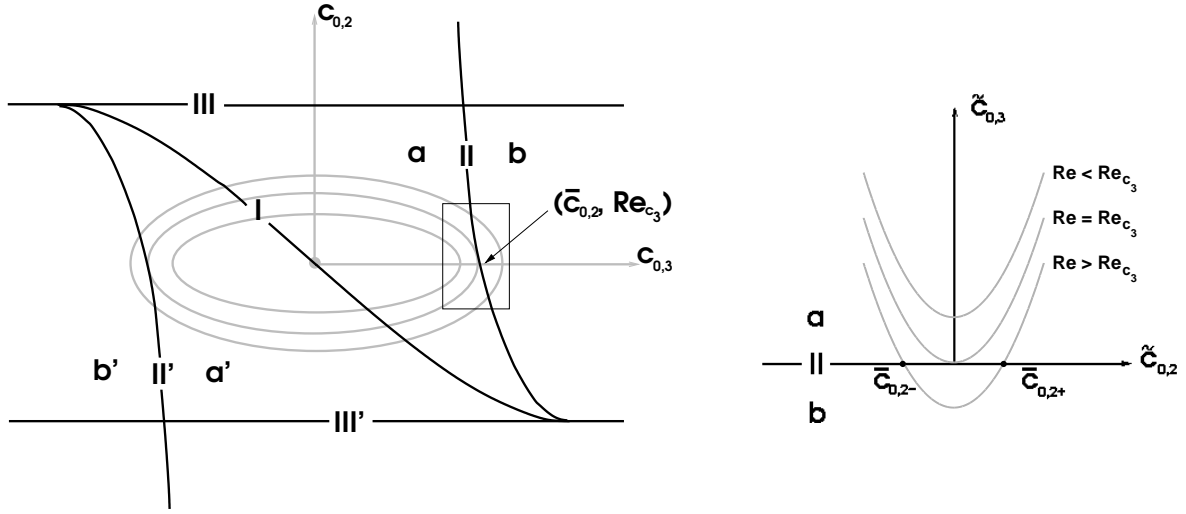


Figure 4.18: The left panel illustrates how the spanning of the closed curve will increase with the Reynolds number from the Hopf bifurcation at Re_{c_2} towards Re_{c_3} . For $Re = Re_{c_3}$ the curve will be tangent to the bifurcation curves II and II' . In a neighborhood of the point $(\bar{c}_{0,2}, Re_{c_3})$ where the closed curve is tangent to II and II' the traversing curve will approximately be of second order. At $(\bar{c}_{0,2}, Re_{c_3})$ we introduce the local coordinates $\tilde{c}_{0,2}$ and $\tilde{c}_{0,3}$, as shown in the right panel.

$II_1 \mapsto b \mapsto II_2$ in parameter space right after the second topological bifurcation is close to being constant we can write up the approximation

$$t \approx \frac{(\tilde{c}_{0,2+} - \tilde{c}_{0,2-})}{v} = \frac{2}{v\sqrt{A}} \sqrt{Re - Re_{c_3}}. \quad (4.60)$$

where t is the time it takes to go from one intersection to another. Taking the square of (4.60) we find that

$$t^2 \approx \frac{4}{v^2 A} (Re - Re_{c_3}). \quad (4.61)$$

The relation (4.61) shows how the square of time t approximately depends linearly on the Reynolds number in a vicinity of the bifurcation point Re_{c_3} .

Now we expect that the time difference average $\langle T \rangle$ will fulfill a relation similar to (4.61) close to the bifurcation point $Re = Re_{c_3}$, thus we write

$$\langle T \rangle^2 \approx K(Re - Re_{c_3}) \quad (4.62)$$

with K being a constant. The relation (4.62) can hence be regarded as a model for how $\langle T \rangle$ tends towards zero as the Reynolds number Re tends towards Re_{c_3} from above. In the bottom panel of figure 4.17 we have therefore mapped the square $\langle T \rangle^2$ of the time difference average as a function of the Reynolds number Re in the interval $[45.6; 46.4]$. We see that the first four data points counting from the left closely follows a linear dependence. After the first four data points follows a more flat saturation of the $\langle T \rangle^2$ -curve a way from this linear dependence. This is what to expect as (4.62) only holds true in a neighborhood of the bifurcation point. A linear data fit of these first four points to the relation (4.62) yields the values $K = 1.25$ and $Re_{c_3} = 45.68$ for the constants. The linear data fit is also shown as a dashed line in the bottom panel of figure 4.17. Thus to sum up, the third topological bifurcation takes place at a Reynolds number of $Re_{c_3} = 45.68$.

We note here that the Reynolds numbers $Re_{c_2} = 45.15$ and $Re_{c_3} = 45.68$ appear quite close to each other. It is expected that in experiments it will be impossible to observe the bifurcation scenario situated in the interval $Re \in [Re_{c_2}; Re_{c_3}]$ thus corresponding to the scenario seen in figure 4.14. The reason being that the experimental resolution of the Reynolds number cannot resolve this narrow Reynolds number interval.

One last comment before we close this section. We remind the reader that topology a and topology c seen in figure 4.15 are equivalent. When taking this into account the sequence (4.58) is seen to correspond topologically to the sequence (4.53). Thus the full unfolding of the fifth order normal form (4.36) again shows sufficient to give a qualitative understanding of the topological bifurcation scenario observed in the numerical simulation after the Hopf bifurcation even when the Reynolds number is increased substantially above the Reynolds number $Re_{c_3} = 45.68$ as in the case for $Re = 100.0$ in figure 4.15.

4.4.5 The periodic wake and the third topological bifurcation

Having determined the topological scenario of the second topological bifurcation we continue to increase the Reynolds number. In figure 4.19 we show an addition to the bifurcation scenario found in figure 4.15. The particular scenario in figure 4.19 is given here for a Reynolds number of $Re = 290.0$. The scenario involves quite a few new topologies which makes it somewhat tedious to present graphically. Consequently we have not shown the whole of the third bifurcation scenario but merely half of the new sequence. This third bifurcation scenario involves new topologies emerging right in between topology a and topology b and similarly new mirror images occurring in between a' and b' where we know a , b and c and a' , b' and c' together with II_1 , II_2 , II'_1 , and II'_2 from the second bifurcation scenario seen in figure 4.15 and in the sequence (4.58). In figure 4.19 we only illustrate the particular part of the new third scenario which comes in between a and b . The third sequence is as follows

$$\begin{aligned} \dots a \mapsto A_1 \mapsto a_2 \mapsto A_3 \mapsto a_4 \mapsto II_1 \mapsto b_{-2} \mapsto B_{-1} \mapsto b \mapsto II_2 \mapsto c \mapsto I \mapsto \\ a' \mapsto A'_1 \mapsto a'_2 \mapsto A'_3 \mapsto a'_4 \mapsto II'_1 \mapsto b'_{-2} \mapsto B'_{-1} \mapsto b' \mapsto II'_2 \mapsto c' \mapsto I' \mapsto a \dots \end{aligned} \quad (4.63)$$

At topology a we have one loop in the near wake of the cylinder and one recirculation zone at the cylinder wall. Then at topology A_1 one further stagnation point bifurcates on the wall above the already existing recirculation zone. In topology a_2 this new stagnation point has developed into a recirculation zone such that two recirculation zones exists at the cylinder wall. In A_3 these two recirculation zones merge in a bifurcation forming one recirculation zone with inner structure which we see in topology a_4 . Then at II_1 the loop in the near wake disappears in a cusp bifurcation and we have topology b_{-2} . At B_{-1} the inner structure in the recirculation zone at the cylinder wall disappears in a cusp bifurcation leaving us with one recirculation zone in topology b . A similar scenario takes place for the corresponding mirror topologies found in the sequence (4.63).

The new additional sequence might be viewed merely as an intermezzo as at topology a we have one recirculation zone which is also the case at topology b . The numerical simulations show one quantitative difference though, the recirculation zone at topology b is greater than the recirculation zone at topology a .

We have made no attempts to determine the exact Reynolds number Re_{c_4} at which this third topological bifurcation takes place. But to do so an approach similar to the way we determined the bifurcation point $Re_{c_3} = 45.68$ for the second topological bifurcation could be used. We have observed this third scenario in the interval $Re = [210; 300]$.

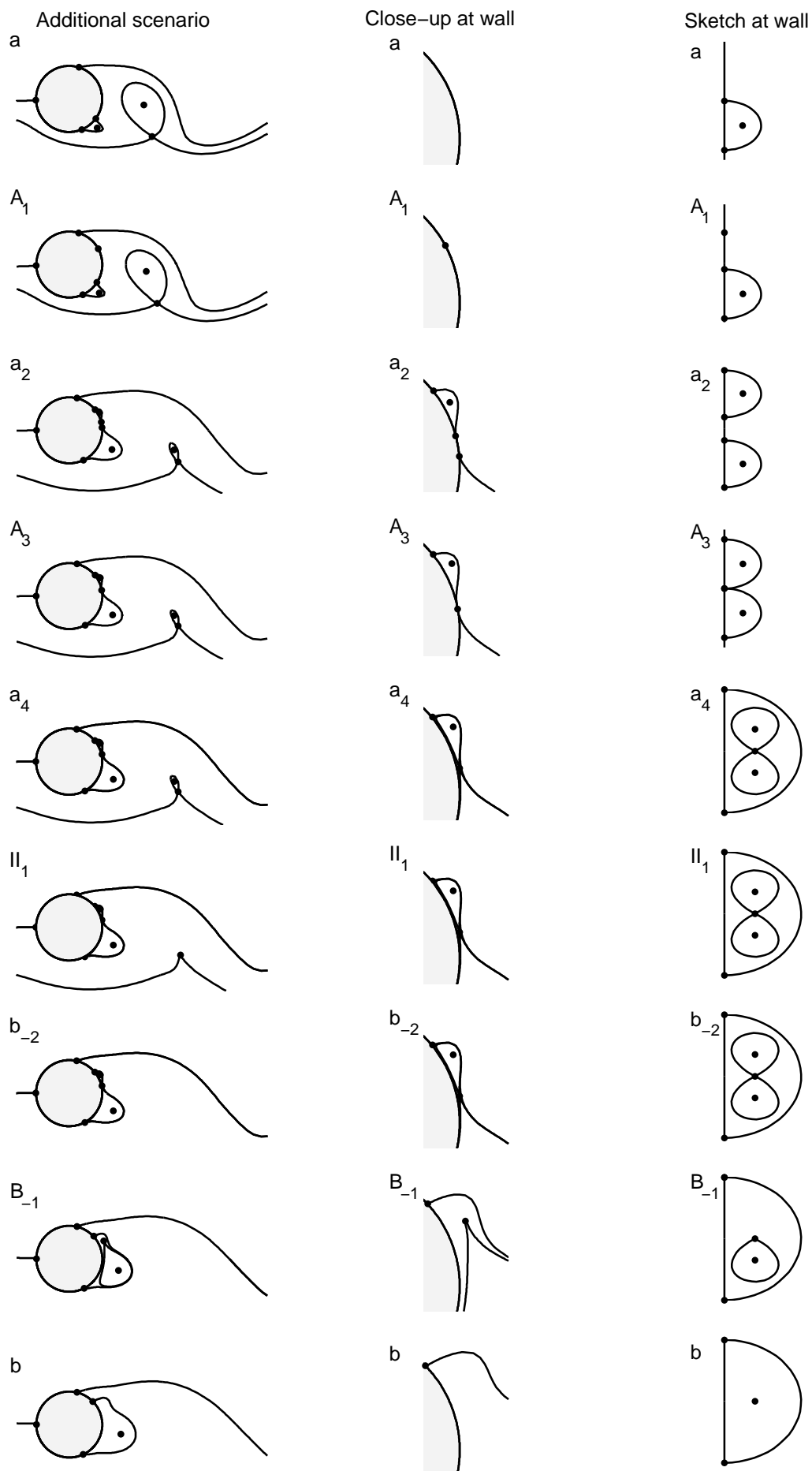


Figure 4.19: Additional numerically obtained bifurcation scenario shown here for $Re = 290.0$.

We note that the normal form analysis in section 4.2.2 does not capture this bifurcation scenario. This could not be expected as the normal form is valid only locally near the first topological bifurcation and the present Reynolds number range is far from this.

4.5 Bifurcations in the translated streamline topology

We have until now in our numerical investigations reported on the streamline topology in the cylinder system. This moving coordinate system has origo fixed at the cylinder center axis. To picture this one can imagine being an observer following or sitting on the cylinder watching the streamline topology.

Contrary to this we will in this section translate the coordinate system and consider a coordinate system which is fixed relative to the free stream flow, the so-called free stream system and let the cylinder move with constant velocity \mathbf{v}_{cyl} . An observer standing still at a fixed position in space will experience the cylinder passing by with constant velocity. We have chosen the cylinder velocity to be opposite the free stream velocity $\mathbf{v}_{cyl} = -(U_\infty, 0)^T$ thus in the free stream system the velocity field \mathbf{v}_T is translated via

$$\mathbf{v}_T = \mathbf{v} - (U_\infty, 0)^T \quad (4.64)$$

where \mathbf{v} is the velocity field given in the cylinder system. The topology of the free stream system and the cylinder system will be different. For instance, a critical point $\mathbf{v} = (0, 0)^T$ in the cylinder system will not be a critical point in the free stream system $\mathbf{v}_T = (-U_\infty, 0)^T$.

One can picture the translation (4.64) by imagine being an observer standing still watching the cylinder coming from the left, passing the observer and moving away to the right. We have seeked to illustrate this in figure 4.20. In the top panel we have shown the streamline topology in the free stream system for a Reynolds number of $Re = 1.54$. In the bottom panel of the figure we have shown schematically what an observer in a fixed spatial position in the free stream system will see at three different time instances $t_1 < t_2 < t_3$. We will comment on this in the following. When comparing the top panel in figure 4.20 to the bottom left panel of figure 4.2 with streamline topology in the cylinder system also shown for $Re = 1.54$ we notice a significant difference between the streamline topology in the free stream system and cylinder system. In the cylinder system, figure 4.2, we notice that the streamlines follows the boundary around the cylinder which has to be understood as fluid passing or flowing by the cylinder. Far away from the cylinder the streamlines becomes parallel signifying that the fluid is flowing downstream with the free stream velocity $\mathbf{v} = (U_\infty, 0)^T$ virtually undisturbed by the cylinder. In the free stream system the fluid far away is non-moving whereas the fluid which is coming close to the cylinder as the cylinder moves through the domain is disturbed and the fluid in front of the moving cylinder is forced or pushed aside thus the bending streamlines seen in the front part of the cylinder. In the bottom panel of figure 4.20 we see that at different moments, for instance at time t_1 , t_2 and t_3 the cylinder has moved from the right to the left but the streamline topology for this low Reynolds number $Re = 1.54$ has not changed, the observer sees the same streamline topology. The streamline topology at time t_2 looks and is the same as the time instant before at time t_1 for instant. For low Reynolds numbers the streamline topology is constant or steady for the moving cylinder. This is still true if we increase the Reynolds number. In figure 4.21 we show the steady topology of the streamlines for three different values of the Reynolds number. We show only what we have chosen to denote the essential streamlines, that is the streamlines which are the corresponding separatrices to saddle points or loops. We have further shown the streamline where the streamfunction is zero. For instance this is the only streamline included in the top panel of figure 4.21 which is again the case of $Re = 1.54$ that we

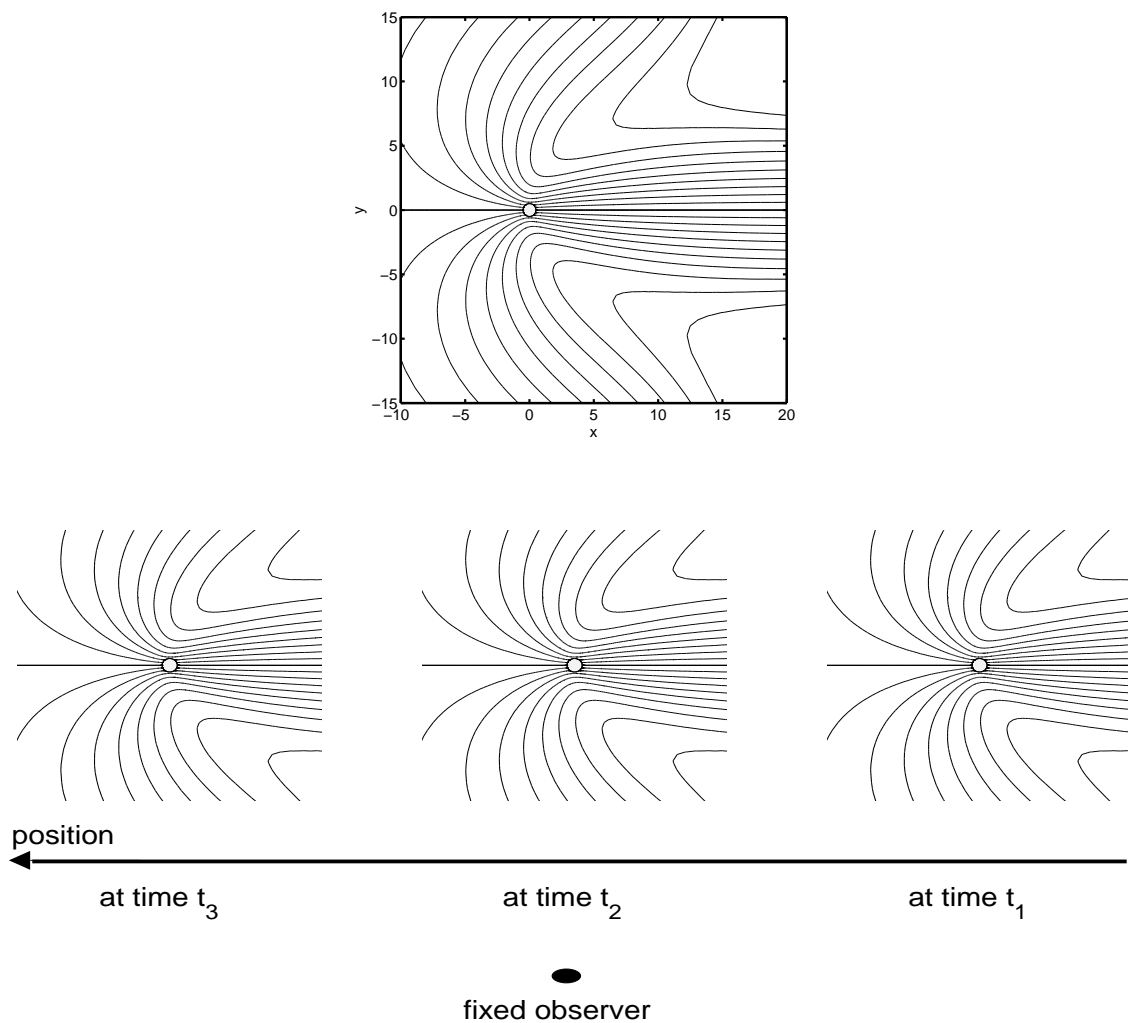


Figure 4.20: The moving streamfunction topology for Reynolds number $Re = 1.54$. The observer stays fixed at one position in space while the cylinder is passing by the observer.

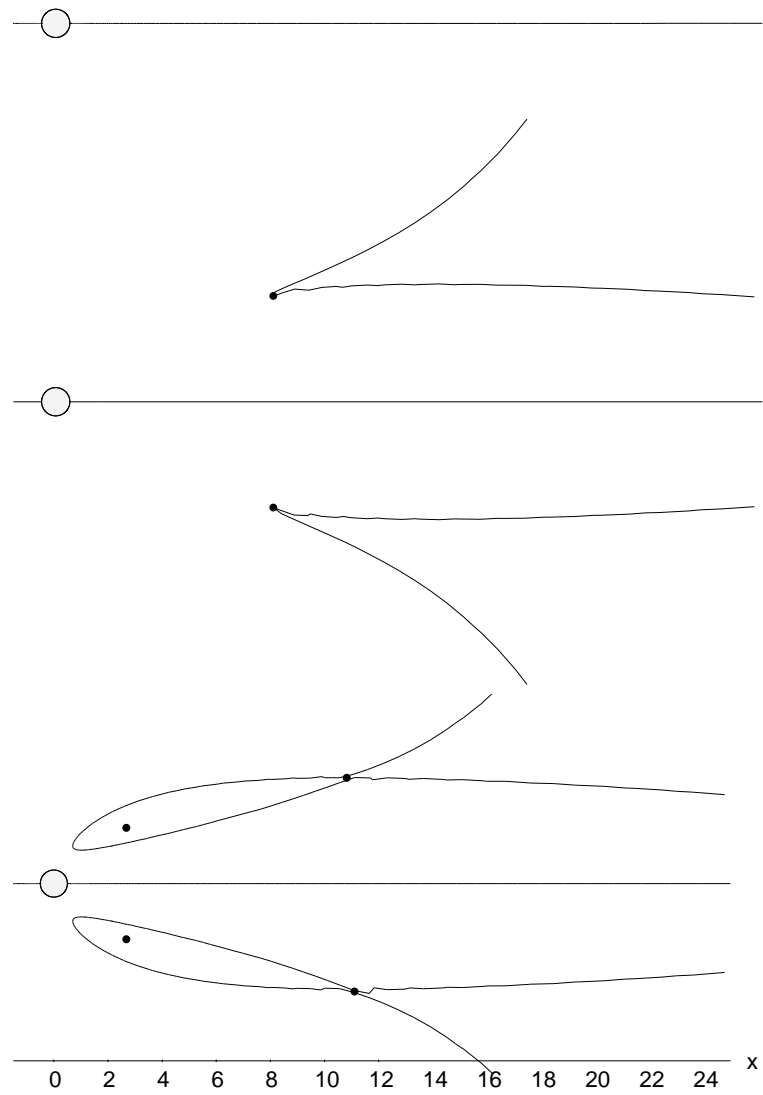


Figure 4.21: The moving streamline topology for Reynolds number $Re = 1.54$, $Re \simeq 6.0$ and $Re = 10.0$

already have shown in full in the top panel of figure 4.20. In the middle panel of figure 4.21 for approximately $Re \simeq 6.0$, we observe that two cusp bifurcations take place at $(x, y) = (7.8, \pm 3.9)$ away from the cylinder. The two cusp bifurcations are symmetrically located around the x -axis. We note that no connection to the cusp bifurcations at $Re \simeq 6.0$ and the emergence of the symmetric cavity at $Re_{c_1} = 6.29$ is expected. For higher Reynolds numbers the two cusp bifurcations develop into two loops also placed symmetrically around the x -axis. For instance in the bottom panel of figure 4.21 we see these two loops in the streamline topology for $Re = 10.0$. As we mentioned above, these three streamline topologies are all steady. But this picture changes when we consider even higher values of the Reynolds number. In the figures 4.22 through 4.23 we show the sequence of streamline topologies in the free stream system for a Reynolds number of $Re = 100.0$. Again only the essential streamlines are shown. The streamline topology has now from being steady turned periodic. Actually we have observed this transition to take place at $Re = Re_{c_2} = 45.6$ and this scenario we have observed to hold through the interval $Re = [45.6; 300]$ without any further topological changes. In the figures 4.22 and 4.23 we see the topological sequence

$$\dots a \mapsto I_l \mapsto b \mapsto I_u \mapsto a \dots \quad (4.65)$$

repeating all over as the cylinder moves through the domain. The sequence is repeating itself with period $T = 6.03$, the same period as for the scenario we have seen for the streamline topology in the moving coordinate system shown in figure 4.15, also for $Re = 100.0$.

Contrary to the steady topologies seen in figure 4.21 we see that in the periodic case in the figures 4.22 and 4.23 the topology has become much more complex. Now we observe double loops embedded in double loops embedded in double loops etc. repeating apparently endlessly downstream on each side of the zero streamline. A new double loop in the wake of the cylinder is created in a cusp bifurcation. In the lower half of the domain the cusp bifurcation I_l is seen emerging in the bottom panel of figure 4.22 at position $(x, y) = (0.95, -0.86)$. Half a period later a new double loop is created through the cusp bifurcation I_u in the upper half of the domain at $(x, y) = (0.95, 0.86)$, which is seen in the bottom panel of figure 4.23. We note that the cusp bifurcations I_u and I_l have moved closer to the cylinder compared to the steady cusp bifurcation for $Re \simeq 6.0$.

While new loops are created via the cusp bifurcations, loops created periods earlier have moved down stream.

4.6 Bifurcations in the vorticity topology

In this section we will consider the vorticity ω and the vorticity topology. The vorticity is defined as $\omega = \nabla \times \mathbf{v}$. Due to the fact that we here consider the parallel vortex shedding two-dimensional velocity field is, as we previously stated, given as $\mathbf{v} = (u, v)^T$ in the domain (x, y) . Inserting this two-dimensional velocity field into the definition of vorticity leaves us with only one non-zero vorticity component namely $\omega = (0, 0, \omega)^T$ where ω is given as

$$\omega = -\Delta\psi = \frac{\partial v}{\partial x} - \frac{\partial u}{\partial y}. \quad (4.66)$$

The vorticity topology is constituted by the lines of equal vorticity, the equivorticity lines. The vorticity topology is invariant in translated coordinate systems and therefore independent of the position of the observer. This comes about as from (4.66) we can conclude that a constant term in a velocity translation has no effect on the vorticity due to the partial differentiation of the velocity components u and v .

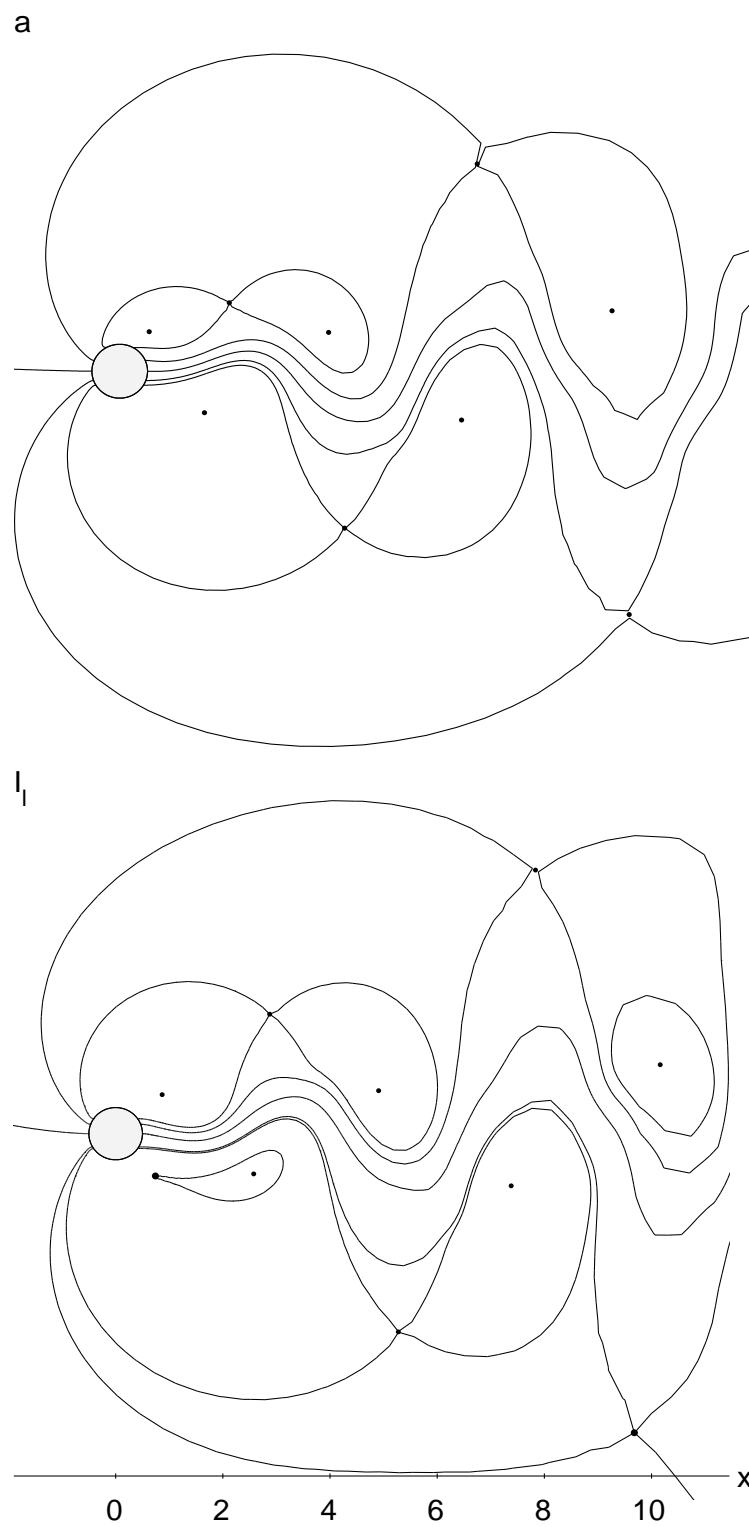


Figure 4.22: The moving streamfunction topology for Reynolds number $Re = 100.0$

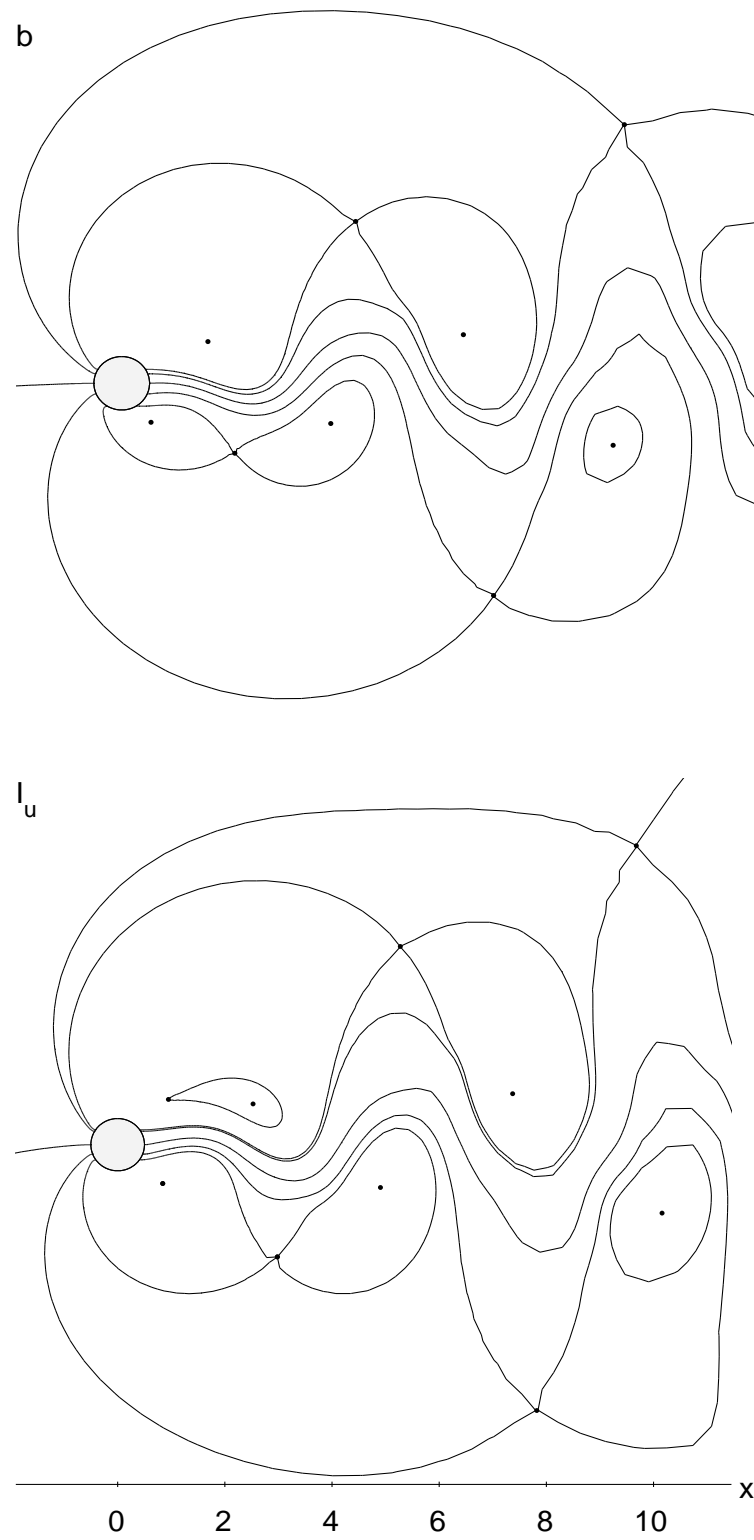


Figure 4.23: Continued from figure 4.22

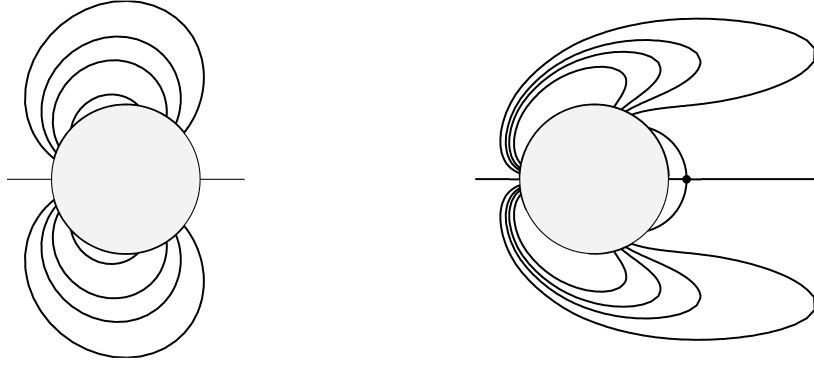


Figure 4.24: The left panel shows the vorticity topology for Reynolds number $Re = 1.54$. The right panel shows the vorticity topology for $Re = 20.0$.

Vorticity is in general governed by two mechanisms; convection and diffusion. This can be seen from the vorticity equation

$$\frac{\partial \omega}{\partial t} + (\mathbf{v} \cdot \nabla) \omega = \frac{1}{Re} \nabla^2 \omega. \quad (4.67)$$

The vorticity equation (4.67) comes about by taking the curl of (4.2). The second term in (4.67) is the convection term and the third term is the diffusion term. For low Reynolds number $Re = DU_\infty/\nu$ we expect the diffusion term to be dominating. A low Reynolds number comes about for a low value of the free stream velocity U_∞ . The convection term has increasing effect as the free stream velocity U_∞ is increased.

In figure 4.24 we show the vorticity topology for two Reynolds numbers. In the left panel we see the vorticity topology for the case of $Re = 1.54$ and in the right panel the vorticity topology is for $Re = 40.0$. Both topologies are steady. In the left panel we notice that the equivorticity lines are more densely collected close to the top and bottom part of the cylinder meaning that the value of vorticity is higher here and decreases into the flow. Hence vorticity is formed at the boundary close to the top and bottom part of the cylinder. We further remark that the vorticity attains opposite values on each side of the x -axis. The vorticity is negative above the x -axis and positive below the x -axis. Furthermore we notice that for low Reynolds numbers the x -axis acts as a symmetry line for the vorticity. In the case of low Reynolds number such as for $Re = 1.54$ the flow is creeping and hardly no convection is taking place. The vorticity is governed by diffusion resulting in this dipole-like vorticity topology. In the right panel of figure 4.24 for $Re = 40.0$ the free stream velocity U_∞ is greater than in the case of $Re = 1.54$ resulting in an increasing effect of the convection term on the vorticity. We notice that the equivorticity lines are swept downstream. Furthermore for $Re = 40.0$ a saddle point in the vorticity topology has been formed in the rear part of the cylinder. This saddle point is actually formed at the Reynolds number $Re = Re_{c1} = 6.29$, see section 4.4.1.

When increasing the Reynolds number further from $Re = 40.0$ to $Re = 45.6$ we obtain the vorticity topology shown in figure 4.25. The vorticity field has now turned periodic and is no longer symmetric around the x -axis. The saddle point at the close rear part of the cylinder still persists. The saddle point is shown in a close up in the bottom right panel of figure 4.25. Additional to the saddle point, loops in the far wake are created periodically via cusp bifurcations. The loops

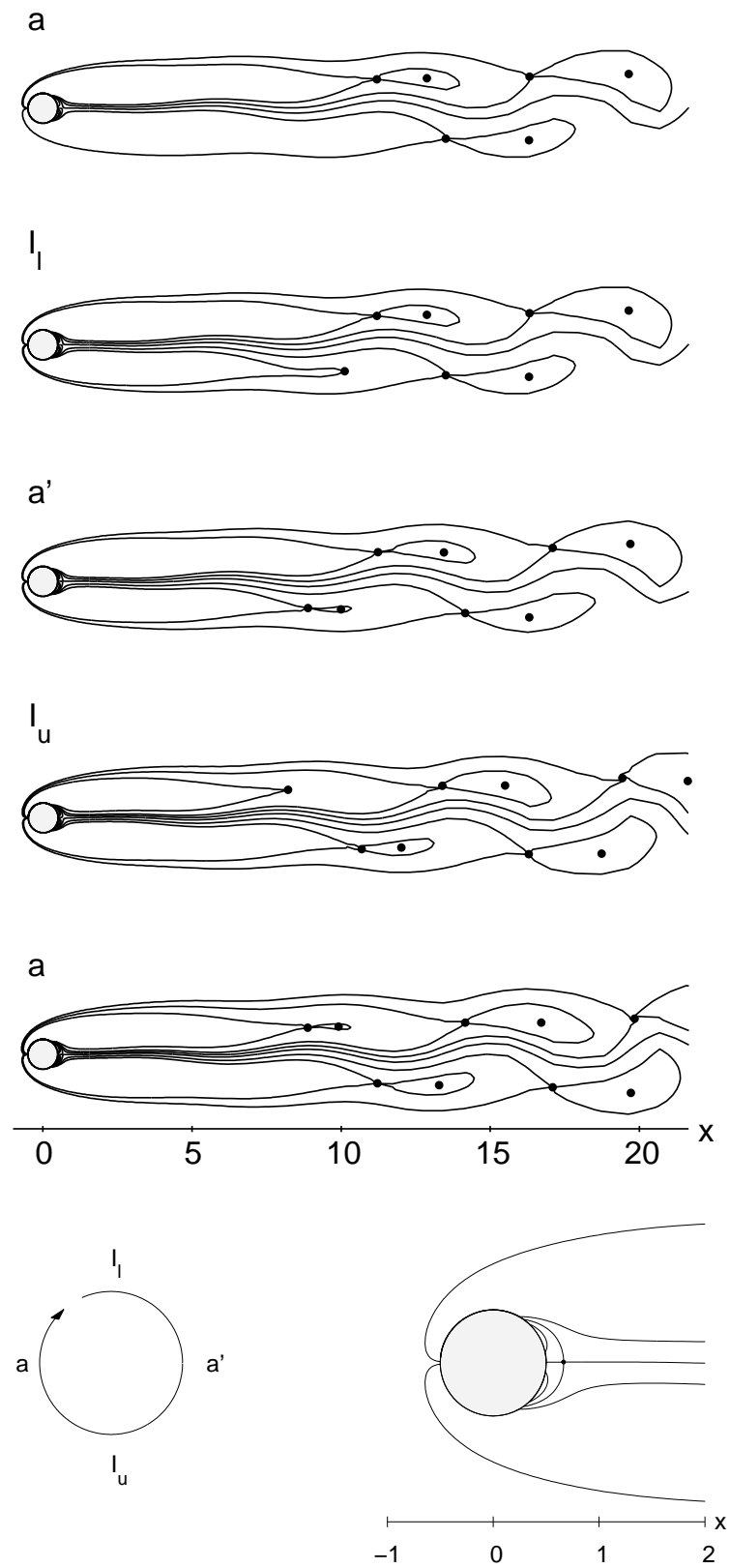


Figure 4.25: The vorticity topology for Reynolds number $Re = 45.6$

are persistent and with time advected downstream. In figure 4.25 we see the sequence

$$\dots a \mapsto I_l \mapsto a' \mapsto I_u \mapsto a \dots \quad (4.68)$$

which is repeating all over with the period $T = 8.57$. For I_l a cusp bifurcation is taking place in the lower half of the domain creating in a' a new loop. For I_u a cusp bifurcation is taking place half a period later creating the new loop we see in a . A new loop in the vorticity topology is seen to be embedded into a loop which has been formed one period before which again is embedded in yet another loop and so forth. No loops are seen intersecting the wavy middle equivorticity line. And we further remark that the loops are being created far down in the cylinder wake away from the saddle point.

When increasing the Reynolds number further to for instance $Re = 150.0$ a bifurcation scenario is taking place involving the saddle point. This bifurcation scenario is partly shown in figure 4.26. The scenario consists of a number of bifurcations and therefore cumbersome to show for a full period. We have only shown half the scenario. The other half manifests itself as mirror images to the topologies shown in figure 4.26 and are occurring with a delay of half a period. Furthermore we only show the wake close to the cylinder as the bifurcation scenario only involves the saddle point and are not influencing the creation of loop we saw in figure 4.25 taking place undisturbed much further downstream.

We have only shown the essential equivorticity lines in figure 4.26. In the topology a we see the saddle point together with the separatrices. The separatrices each form a closed region behind the cylinder. In topology b a saddle point bifurcate on the cylinder boundary embedded in the lower closed region. The newly formed saddle point has moved in to the wake in topology c . In topology d a cusp bifurcation is taking place also in the lower closed region forming the loop we see in topology e . The loop consists of yet a saddle point and a center. In topology f the saddle point has virtually disappeared into the cylinder boundary and left the center behind in the wake together with the two other saddle points. In topology g two of the separatrices of the two saddle points form a heteroclinic connection in a global bifurcation resulting in topology h . In topology i a separatrix of the lower saddle point is tangential to the cylinder wall and lifts off the cylinder wall in topology j . The upper saddle point and the center in the lower region disappears in a cusp bifurcation in topology k and left is only the lower saddle point in topology l . The over-all effect of this bifurcation scenario is apparent to take a saddle point located in the upper half of the domain and move it to the lower half of the domain. The scenario might seem negligible but does show some complexity which one might expect to increase for even higher Reynolds numbers. We have not made any attempt to precisely determine the Reynolds number at which this scenario first bifurcates and further we have not experienced the introduction of any additional bifurcation scenario for a Reynolds number up to $Re = 300.0$. We have observed the bifurcation scenario seen in figure 4.26 in the interval $Re = [130; 300]$.

4.7 Validating the numerical investigations

In this section the numerical simulations be validated. In the validation will we compare the computational grid, the normal grid to a refined grid. The comparison will both be spatial and temporal. Finally the simulations will be compared to experimental data via the Strouhal number.

To ensure grid size independence of our numerical simulations we have chosen to compare the normal grid to a fine grid consisting of four 128×128 blocks. We have made this comparison for one Reynolds number, namely $Re = 100.0$. As we have seen at $Re = 100.0$ the wake has turned

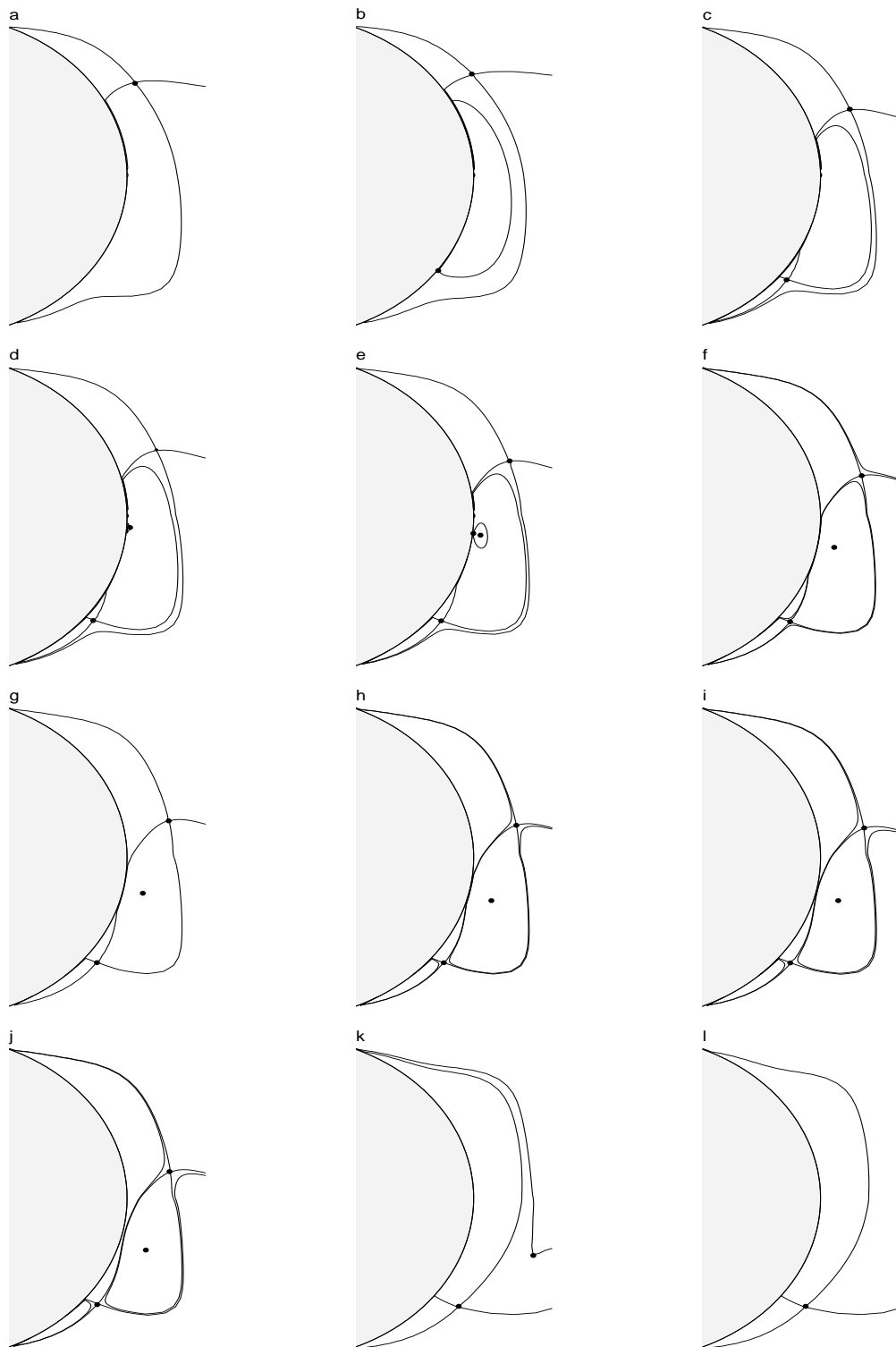


Figure 4.26: The vorticity topology for Reynolds number $Re = 150.0$

periodic with different topologies appearing via topological bifurcations at certain instances in the period, see figure 4.15 and figure 4.16. The periodic wake with the changing topologies gives us the opportunity to compare simulations conducted with the normal grid and the fine grid both in the time development and in the physical domain. We can compare in time for the two grids when a certain topological bifurcation takes place and for at give fixed time instant we can in the physical domain compare whether the stagnation points of a topology comply for the two grids. In figure 4.27 we have located the topological bifurcation I for both of the grids. In the top panel of figure 4.27 we shown for the normal grid an example of how we determine the stagnation points. The stagnation points are found by first calculating the 0-isoclines and the ∞ -isoclines of the velocity field. The stagnation points then appear where the two set of isoclines intersect. In the middle panel of the figure we have imposed on top of each other the essential streamlines and stagnation points for both the normal and the fine grid. Qualitatively we find a reasonable agreement in the over all flow but with a slight disagreement in the down stream flow. A more quantitative comparison is found in the table of figure 4.27. Here we have listed the various positions of the stagnation points. For the case of the lower center point we find a relative error of 0.038 which is the worst case. We find this acceptable.

In figure 4.28 we have compared the time development within one period of the oscillating wake at $Re = 100.0$ for the normal and fine grid. The time development has been conducted with a time resolution of $T_{res} = 0.025$ for both grids. The period for the normal grid has been measured to $T_{normal} = 6.03$ whereas the period for the fine grid is $T_{fine} = 6.04$. Thus the periods disagree with a relative error of 0.002. In the table we have taken the time T_{II_1} at which the first bifurcation II_1 occurs to be the phase reference. With respect to T_{II_1} we have listed the various instances at which the topological bifurcations for the scenario found in figure 4.15 occur as well as the time differences between these. There are some discrepancies but all of then are less than or equal to the time resolution T_{res} . For instance for the normal grid $T_{II_2} = 0.5175$ whereas for the fine grid we find $T_{II_2} = 0.4950$ which gives a deviation of exactly the time resolution.

From both the agreement of the position of the stagnation points for the topological bifurcation I and from the acceptable agreement of the time development that stays within the time resolution we consider the normal grid suitable to our purposes compare to the fine grid.

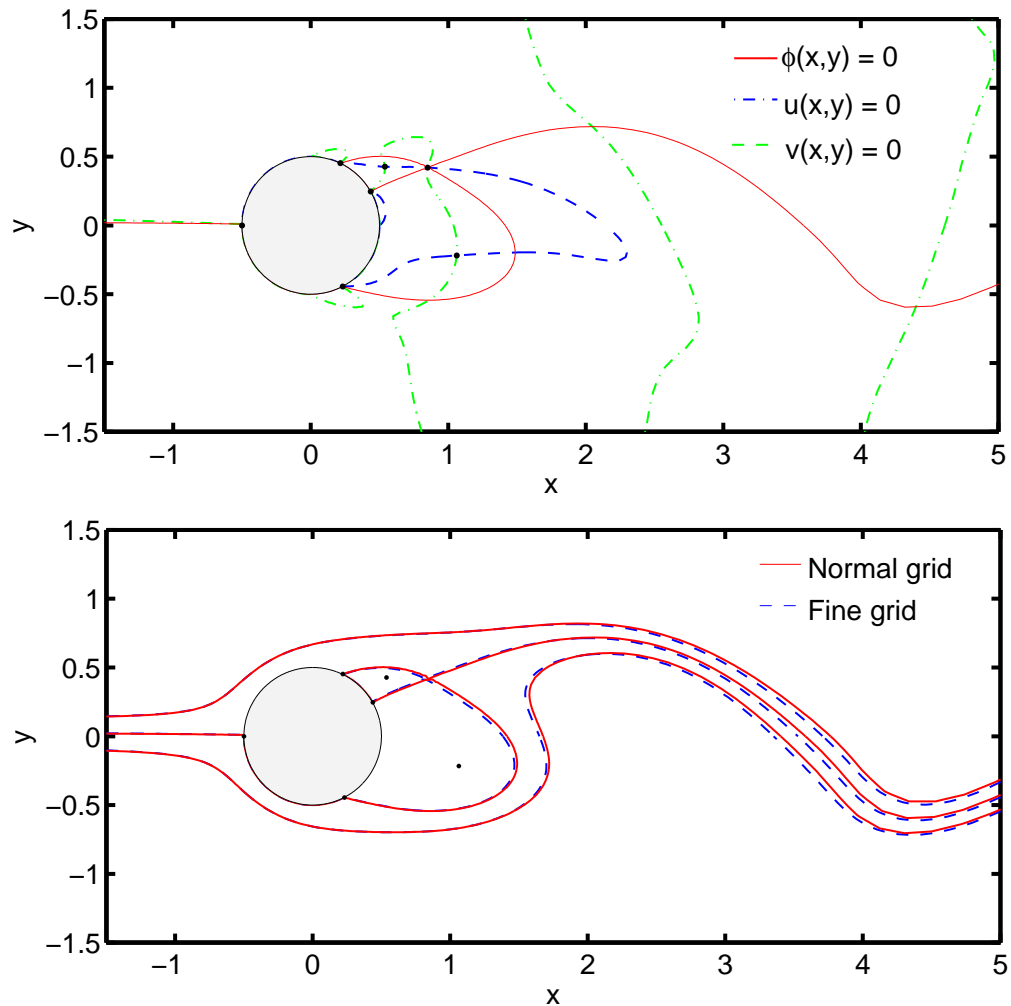
To further validate our numerical simulations we can next hold the simulations against experiments. A possible measure in comparing simulations to experiments is the frequency f with which the vortex shedding takes place. At the Hopf bifurcation occurring for $Re_{c_2} = 45.15$ parallel vortex shedding from the cylinder is initiated. The frequency with which the shedding is taking place can be made dimensionless by introducing the Strouhal number using the diameter D of the cylinder and the far field flow velocity U_∞ . The Strouhal number St is defined as

$$St = \frac{fD}{U_\infty} \quad (4.69)$$

and as we have chosen $D = 1$ and $U_\infty = 1$ gives us in this study the Strouhal number is equal to the frequency.

The Strouhal number St has been recorded in various experiments and has been documented in the literature and is therefore an excellent measure to validate our simulations against simulations in the parallel vortex shedding regime. In a classical study of Rosko (1954) which is also referred to in Fey, König, and Eckelmann (1998) a relation between the Strouhal number St and the Reynolds number Re is suggested and is on the form

$$St(Re) = a_1 + a_2 \frac{1}{Re} \quad (4.70)$$



	normal grid		fine grid		rel. err.
stagnation point	x	y	x	y	
upper center point	0.537	0.428	0.520	0.427	0.020
lower center point	1.063	-0.216	1.022	-0.215	0.038
front middle cylinder point	-0.500	0.000	-0.500	0.000	0.000
back upper cylinder point	0.219	0.452	0.221	0.452	0.002
back middle cylinder point	0.438	0.248	0.436	0.250	0.000
back lower cylinder point	0.232	-0.446	0.229	-0.445	0.004
in-flow saddle point	0.842	0.413	0.814	0.413	0.030

Figure 4.27: Spatial comparison of fine and normal grid at $Re = 100.0$. The top panel shows for the normal grid the 0- and ∞ -isoclines of the velocity field. The intersection of a 0- and ∞ -isocline constitute a critical point and shows how we have determined the position of the critical points. Middle panel shows the comparison of the fine and the normal grid. Only critical points and essential streamlines are shown. The bottom table lists positions of critical points for the normal versus the fine grid together with the relative error on the norm for the critical points. The highest relative error comes for the lower center point.

	normal grid		fine grid	
	time	difference	time	difference
T	6.03	-	6.04	-
T_{II_1}	0		0	
$T_{II_2} - T_{II_1}$		0.5175		0.4950
T_{II_2}	0.5175		0.4950	
$T_I - T_{II_2}$		0.1575		0.1575
T_I	0.6750		0.6525	
$T_{II'_1} - T_I$		2.3400		2.3500
$T_{II'_1}$	3.0150		3.0025	
$T_{II'_2} - T_{II'_1}$		0.5400		0.5400
$T_{II'_2}$	3.5550		3.5425	
$T_{I'} - T_{II'_2}$		0.1350		0.1350
$T_{I'}$	3.6900		3.6775	

Figure 4.28: Temporal comparison of the fine and normal grid at $Re = 100.0$. The table lists and compares the period T together with the partial periods for the bifurcations seen in figure 4.15 for one period in the wake oscillations. Also listed is the time difference between some of the partial periods. The time resolution is $T_{res} = 0.0225$. For instance for the normal grid we have $T_{I',n} - T_{I,n} = 3.0150$ compared to the fine grid where $T_{I',f} - T_{I,f} = 3.0250$. The deviation is within the time resolution.

with the constants $a_1 = a_{1,rosko} = 0.212$ and $a_2 = a_{2,rosko} = -4.5$. The relation is valid in the regular laminar shedding interval $Re \in [47; 180]$ and is seen to be linear in the reciprocal of the Reynolds number. Furthermore in Fey, König, and Eckelmann (1998) a new experimentally based Reynolds-Strouhal number relation different from the Rosko-relation (4.70) for parallel shedding has been obtained and is given on the form

$$St(Re) = b_1 + b_2 \frac{1}{\sqrt{Re}} \quad (4.71)$$

with the constants given as $b_1 = b_{1,exp} = 0.2684$ and $b_2 = b_{2,exp} = -1.0356$ and is valid in the regular laminar shedding interval $Re \in [47; 180]$. It is seen that the FKE-relation (4.71) is linear in the reciprocal to the square root of the Reynolds number. The constants $b_{1,exp}$ and $b_{2,exp}$ have been obtained by linear fitting of experimental data. The linear fit has been conducted on an almost equal distributed set of experimental data which ensures that the data is equally weighted implying that the FKE-relation is valid with good agreement in the whole range of the given interval $Re \in [47; 180]$. In the top left panel of figure 4.29 we show the parallel shedding frequency or Strouhal number St as function of the Reynolds number Re measured from our simulations conducted in the shedding interval $Re \in [45.15; 300]$. In the top right panel of figure 4.29 we show again in the interval $Re \in [47; 180]$ our simulation recordings of the Reynolds-Strouhal number relationship together with the FKE-relation (4.71). Also we show a fit of the simulation data to the functional form (4.71). The fit we have conducted is linear in $(1/\sqrt{Re})$ with almost equally distributed simulation data shown on the figure ensuring that the data is equally weighted over the interval $Re \in [47; 180]$. The constants we obtain for the fit of our simulation data to the form (4.71) have the values $b_1 = b_{1,sim} = 0.2678$ and $b_2 = b_{2,sim} = -1.0168$ in the interval $[47; 180]$. The relative error Δb between the constants $b_{1,exp}$ and $b_{1,sim}$ is $\Delta b_1 = |(b_{1,exp} - b_{1,sim})/b_{1,sim}| = 0.0021$ whereas the relative error between $b_{2,exp}$ and $b_{2,sim}$ amounts to $\Delta b_2 = 0.0184$. This shows a good agreement between our simulation data to the experimentally obtained FKE-relation. One discrepancy must be mentioned though, which can explain the relative deviation, how ever small it might be. In the study Fey, König, and Eckelmann (1998) the Hopf bifurcation point has been found to take place at $Re_{c2,FKE} = 47$ whereas we have for our simulation data determine the Hopf bifurcation to take place at $Re_{c2} = 45.15$. We have not made any attempts to compensate for this discrepancy but as

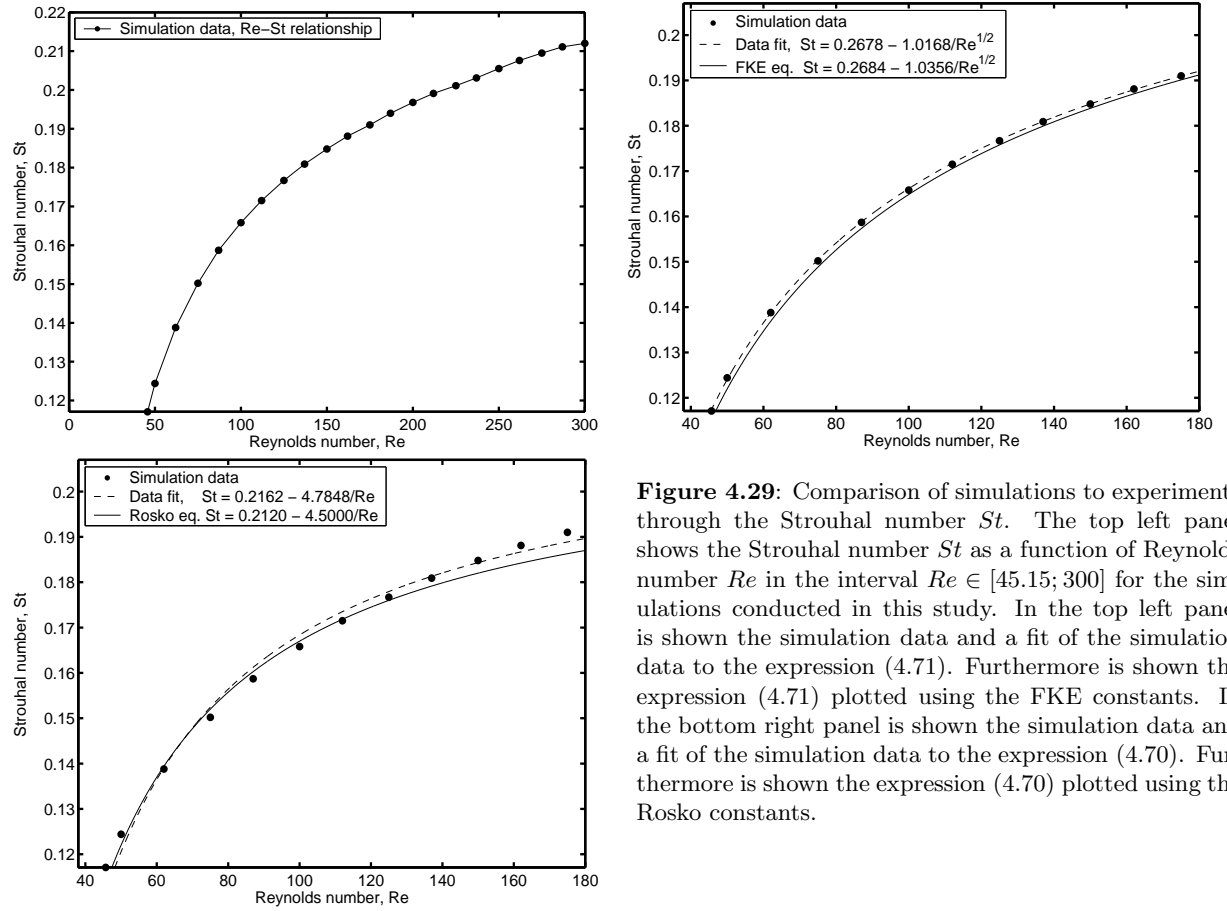


Figure 4.29: Comparison of simulations to experiments through the Strouhal number St . The top left panel shows the Strouhal number St as a function of Reynolds number Re in the interval $Re \in [45.15; 300]$ for the simulations conducted in this study. In the top left panel is shown the simulation data and a fit of the simulation data to the expression (4.71). Furthermore is shown the expression (4.71) plotted using the FKE constants. In the bottom right panel is shown the simulation data and a fit of the simulation data to the expression (4.70). Furthermore is shown the expression (4.70) plotted using the Rosko constants.

the fit shows a good over-all agreement in the range $Re = [47; 180]$ we shall be satisfied with this.

A fit of our simulation data to the Rosko expression on the form (4.70) results in the constants $a_1 = a_{1,fit} = 0.2678$ and $a_2 = a_{2,fit} = -1.0168$ with the relative errors $\Delta a_1 = 0.0184$ and $\Delta a_2 = 0.0021$. The fit is shown together with our simulation data and the Rosko expression in the bottom left panel of figure 4.29.

The fit of our simulation data and the Rosko expression (4.70) have the same order of magnitude all though with some deviation. The over-all agreement of the fit of our simulation data to the Rosko expression (4.70) is not as convincing as the over-all agreement of our simulation data compared to the FKE-relation.

We are satisfied with the agreement of the simulation data compared to the experimental data and therefore consider our numerical simulation validated.

4.8 Conclusions

First of all the purpose of the work in this chapter was to clarify the streamline topology of the cylinder wake close to the Hopf bifurcation and compare the results to the proposed explanation model in figure 4.3 by Perry et al. (1982).

By basing the theoretical analysis on the experimental observation of the symmetric cavity and by assuming that the streamline topology after the Hopf bifurcation results from a periodic

asymmetric perturbation of the symmetric cavity a new explanation model was proposed by Niss and Jakobsen (2002). The new model is shown in figure 4.8. Right after the Hopf bifurcation the model predicts the sequence (4.52). The explanation model furthermore predicts the occurrence of a topological bifurcation, the sequence (4.53) when the Reynolds number is increased further.

The numerical simulations comply and confirms these two theoretically predicted sequences, see figure 4.14 and figure 4.15. Contrary to the Perry et al. (1982) model, the new explanation model does not contain any whirling alley consisting of repeating loops in the streamline topology in the cylinder system. Thus this must be regarded as a misinterpretation in the Perry et al. (1982) model. An alley of repeating loops are instead observed away from the cylinder in the numerical simulations of the streamline topology in the free stream system. Similarly to the streamline topology in the free stream system an alley of repeating vorticity loops away from the cylinder are observed in the vorticity field. The loops are formed by cusp bifurcations. The cusp bifurcations in the streamline topology in the free stream system are not situated at the same positions as the cusp bifurcations taking place in the vorticity field.

For Reynolds numbers higher than Re_{c_2} where the Hopf bifurcation occurs even more complex topologies are observed in the streamline topology in the cylinder system and for the vorticity field.

Bibliography

- Acheson, D. J. (1996). *Elementary Fluid Dynamics*. Clarendon Press, Oxford.
- Andersen, K. M., N. M. Hansen, and A. Sandqvist (1988). *Sædvanlige differentiaalligninger, 6.ed.* (in Danish). Department of Mathematics, Technical University of Denmark.
- Bakker, P. G. (1991). *Bifurcations in Flow Patterns*. Kluwer Academic Publishers.
- Bar-Yoseph, P. Z., A. Solan, and K. G. Roesner (1990). Sekundärstörung in axialsymmetrischen Hohlräumen. *Z. Angew. Math. Mech.* 70, 442–444.
- Barker, V. A. (1997). *The Finite Difference Method for Partial Differential Equations*. Notes, Department for Informatics and Mathematical Modelling, The Technical University of Denmark.
- Brøns, M. (1996). Topological fluid dynamics of interfacial flows. *Phys. Fluids* 6(8), 2730–2737.
- Brøns, M. (1999). "Streamline topology of axisymmetric flows" in *Simulation in Organized Structures in Flows*. Edited by J. N. Sørensen, E. J. Hopfinger and N. Aubry, Kluwer Academic Publishers.
- Brøns, M. (2000). "Streamline patterns and their bifurcations using methods from dynamical systems" in *An Introduction to the Geometry and Topology of Fluid Flows*. Edited by R. L. Ricca, NATO Science Series II Vol 47.
- Brøns, M. and J. N. Hartnack (1999). Streamline topologies near simple degenerate critical points in two-dimensional flow away from boundaries. *Phys. Fluids* 11(3), 314–324.
- Brøns, M., L. K. Voigt, and J. N. Sørensen (1999). Streamline topology of steady axisymmetric vortex breakdown in a cylinder with co- and counter-rotating end-covers. *J. Fluid Mech.* 401, 275–292.
- Brøns, M., L. K. Voigt, and J. N. Sørensen (2001). Topology of vortex breakdown bubbles in a cylinder with a rotating bottom and a free surface. *J. Fluid Mech.* 428, 133–148.
- da Vinci, L. (1509). Studies of Water. <http://www.kfki.hu/~arthp/html/l/leonardo/>.
- Dallmann, U. (1988). Three-dimensional vortex structures and vorticity topology. *Fluid Dynamics Research* 3, 183–189.
- Daube, O. (1991). *Numerical Simulation of Axisymmetric Vortex Breakdown in a Closed Cylinder*, Volume 28. Lectures in Applied Mathematics.
- Escudier, E. P. (1984). Observations of the flow produced in a cylindrical container by a rotating end wall. *Exps. in Fluids* 2, 189–196.
- Escudier, E. P. and L. M. Cullen (1996). Flow of a shear-thinning liquid in a cylindrical container with a rotating end wall. *Expl. Thermal Fluid Sci.* 12, 381–387.
- Fey, U., M. König, and H. Eckelmann (1998). A new Strouhal-Reynolds number relationship for the circular cylinder in the range $47 < Re < 2 \cdot 10^5$. *Phys. Fluids Lett.* 10(7), 1547–1549.
- Gelfat, A. Y., P. Z. Bar-Yoseph, and A. Solan (1996). Steady states and oscillatory instability of swirling flow in a cylinder with rotating top and bottom. *Phys. Fluids* 8, 2614–2625.

- Grimshaw, R. (1990). *Nonlinear Ordinary Differential Equations*. Blackwell Scientific Publications.
- Guckenheimer, J. and P. Holmes (1983). *Nonlinear Oscillations, Dynamical Systems and Bifurcations of Vector Fields*. Springer-Verlag.
- Hartnack, J. N. (1999a). Streamline topologies near a fixed wall using normal forms. *Acta Mechanica* 136, 55–75.
- Hartnack, J. N. (1999b). *Structural Changes in Incompressible Flow Patterns*, Ph.D. Thesis. Department of Mathematics, Technical University of Denmark.
- Hernández, R. H. and C. Baudet (2000). A new perturbation method. Application to the Bénard-von Kármán instability in the subcritical regime. *Europhys. Lett.* 49, 329–335.
- Hernández, R. H. and A. Pacheco (2002). Numerical simulation and experiments of a control method to suppress the Bénard-von Kármán instability. *Euro. Phys. J. B* 30, 265–274.
- Herrada, M. A. and V. Shtern (2003). Control of vortex breakdown by temperature gradients. *Phys. Fluids* 15(11), 3468–3477.
- Hunt, J. C. R., C. J. Abell, J. A. Peterka, and H. Woo (1978). Kinematical studies of the flow around free or surface-mounted obstacles; applying topology to flow visualization. *J. Fluid Mech.* 86, 179–200.
- Jahnke, C. C. and D. T. Valentine (1998). Recirculations zones in a cylindrical container. *Trans. ASME: J. Fluids Engng.* 120, 680–684.
- Koromilas, C. A. and D. P. Telionis (1980). Unsteady laminar separation: An experimental study. *J. Fluid Mech.* 97, 347–384.
- Kuznetsov, Y. A. (1998). *Elements of Applied Bifurcation Theory*, 2. ed. Springer-Verlag.
- Lim, T. and Y. Cui (2005). On the generation of a spiral-type vortex breakdown in an enclosed cylindrical container. *Phys. Fluids* 17, 044105–1 – 044105–9.
- Lopez, J. M. (1990). Axisymmetric vortex breakdown. Part 1. Confined swirling flow. *J. Fluid Mech.* 221, 533–552.
- Lopez, J. M. and J. Chen (1998). Coupling between a viscoelastic gas/liquid interface and a swirling vortex flow. *Trans. ASME: J. Fluids Engng.* 120, 655–661.
- Lopez, J. M. and A. D. Perry (1992). Axisymmetric vortex breakdown. Part 3. Onset of periodic flow and chaotic advection. *J. Fluid Mech.* 234, 449–471.
- Lugt, H. J. (1983). *Vortex Flow in Nature and Technology*. Wiley Interscience.
- Marsden, J. E. and M. McCracken (1976). *The Hopf Bifurcation and Its Applications*. Springer-Verlag.
- MathWorks (2004). *MATLAB 7 Release 14*. www.mathworks.com.
- Michelsen, J. (1992). *Basis3D - A Platform for Development of Multiblock PDE Solvers*. Department of Fluid Mechanics, Technical University of Denmark.
- Mittelbach, F. and M. Goossens (2004). *The L^AT_EX Companion*, 2. ed. Addison-Wesley.
- Mullen, T., J. J. Kobine, S. J. Tavener, and K. A. Cliffe (2000). On the creation of stagnation points near straight and sloped walls. *Phys. Fluids* 12, 425–431.

- Mununga, L., K. Hourigan, M. C. Thompson, and T. Leweke (2005). Confined flow vortex breakdown control using a small rotating disk. *Phys. Fluids* 16, 4750–4753.
- Niss, K. and B. Jakobsen (2002). *Hopfbifurkation og topologi i væskestrømning* (in Danish). IMFUFA Report, IMFUFA, University of Roskilde.
- Noack, B. R. and H. Eckelmann (1994). A global stability analysis of the steady and periodic cylinder wake. *J. Fluid Mech.* 270, 297.
- Olsen, S. M., E. Buch, and M. H. Ribergaard (2005). Hav og klima (in Danish). *Aktuel Naturvidenskab* 2, 23–27.
- Oswatitsch, K. and K. Wiegardt (1987). Ludwig Prandtl and his Kaiser-Wilhelm-Institut. *Ann. Rev. of Fluid Mech.* 19, 1–25.
- Pereira, J. C. F. and J. M. M. Sousa (1999). Confined vortex breakdown generated by a rotating cone. *J. Fluid Mech.* 385, 287–323.
- Perry, A. E. and M. S. Chong (1987). A description of eddying motions and flow patterns using critical-point concepts. *Ann. Rev. Fluid Mech.* 19, 125–155.
- Perry, A. E., M. S. Chong, and T. T. Lim (1982). The vortex-shedding process behind two-dimensional bluff bodies. *J. Fluid Mech.* 116, 77–90.
- Petersen, R. (2002). *Dynamical Systems and Structures in The Flow around a Cylinder*, M.Sc. Thesis. Department of Mathematics, Technical University of Denmark.
- Press, W. H., B. P. Flannery, S. A. Teukolsky, and V. T. Wetterling (1993). *Numerical Recipes in C*. Cambridge University Press.
- Provansal, M., C. Mathis, and L. Boyer (1987). Bénard-von Kármán instability: Transient and forced regimes. *J. Fluid Mech.* 182, 1.
- Roesner, K. G. (1989). "Recirculation Zones in a Cylinder with Rotating Lid". *Proceedings of the IUTAM Symposium on Topological Fluid Mechanics*. Edited by A. Tsinober and H. K. Moffatt. 699–708.
- Rosko, A. (1954). On The Development of Turbulent Wakes from Vortex Streets. Technical report, NACA TN 1191.
- Scott, A. C. (2005). *Encyclopedia of Nonlinear Science*. Routledge, Taylor & Francis Group.
- Smith, B. V. (2002). *Xfig ver. 3.2.4*. file:///usr/unic/share/xfig/3.2.4/html/index.html.
- Sørensen, J. N. (1988). *Et essay om vortex breakdown* (in Danish). Technical Report, Department of Fluid Mechanics, Technical University of Denmark.
- Sørensen, J. N. and E. A. Christensen (1995). Direct numerical simulation of rotating fluid flow in a closed cylinder. *Phys. Fluids* 7(4), 764–778.
- Sørensen, J. N. and T. P. Loc (1989). Higher-order axisymmetric Navier-Stokes code: Description and evaluation of boundary conditions. *International Journal for Numerical Methods in Fluids* 9, 1517–1537.
- Sørensen, N. N. (1995). *General Purpose Flow Solver Applied to Flows over Hills*. Risø National Laboratory, Roskilde, Denmark.
- Spohn, A., M. Mory, and E. J. Hopfinger (1993). Observations of vortex breakdown in an open cylindrical container with a rotating bottom. *Exps. in Fluids* 13, 70–77.

- Spohn, A., M. Mory, and E. J. Hopfinger (1998). Experiments on vortex breakdown in a confined flow generated by a rotating disc. *J. Fluid Mech.* 370, 73–99.
- Thompson, M. C. and K. Hourigan (2003). The sensitivity of steady vortex breakdown bubbles in confined cylinder flows to rotating lid misalignment. *J. Fluid Mech.* 496, 129–138.
- Tobak, M. and D. J. Peak (1982). Topology of three-dimensional separated flows. *Ann. Rev. of Fluid Mech.* 14, 61–85.
- Tsitverblit, N. (1993). Vortex breakdown in a cylindrical container in the light of continuation of a steady solution. *Fluid Dyn. Res.* 11, 19–35.
- Tsitverblit, N. and E. Kit (1996). Numerical study of axisymmetric vortex breakdown in an annulus. *Acta Mechanica* 118, 79–95.
- van Dyke, M. (1982). *An Album of Fluid Motion*. Parabolic Press.
- Versteeg, H. K. and W. Malalasekera (1995). *An Introduction to Computational Fluid Dynamics, The Finite Volume Method*. Longman Scientific and Technical.
- Vogel, H. U. (1968). Experimentelle ergebnisse über die laminäre strömung in einem zylindrischen gehäuse mit darin rotierender schraube. *Bericht 6*. Max-Planck-Institut für Strömungsforschung, Göttingen.
- Westergaard, C., P. Buchhave, and J. N. Sørensen (1993). PIV measurements of turbulent and chaotic structures in a rotating flow using an optical correlator. *Laser Techniques and Applications in Fluid Mechanics*. Edited by R. J. Adrian, Springer-Verlag.
- Wiggins, S. (2003). *Introduction to Applied Nonlinear Dynamical Systems and Chaos*. 2.ed. Springer-Verlag.
- Williamson, C. H. K. (1996). Vortex dynamics in the cylinder wake. *Ann. Rev. of Fluid Mech.* 28, 477–539.
- Xue, S. C., N. Phan-Thien, and R. I. Tanner (1999). Fully three-dimensional, time-dependent numerical simulations of Newtonian and viscoelastic swirling flow in a confined cylinder part 1. Method and steady flows. *J. Non-Newtonian Fluid Mech.* 87, 337–367.
- Zhang, H.-Q., U. Fey, B. R. Noack, M. König, and H. Eckelmann (1995). On the transition of the cylinder wake. *Phys. Fluids* 7, 779–794.